First principles based thermodynamic stability analysis of the secondary structure of proteins

Dissertation
zur Erlangung des akademischen Grades
Doktor der Naturwissenschaften (Dr. rer. nat.)
an der Universität Paderborn

Lars Ismer

Promotionskommision

Vorsitzender	Prof. Dr. phil. Klaus Lischka
Gutachter	Prof. Dr. rer. nat. Wolf Gero Schmidt
Gutachter	Prof. Dr. rer. nat. Jörg Neugebauer

… Was ist zum Beispiel mit Willis Spucke? Seit heute morgen liegt Willis Spucke auf dem Weg. Oder ist es Willi selbst? Willi ist längst nach Hause gegangen. Aber die Spucke ist noch da. Seine Spucke! Allein auf dem Fußweg …

(aus: "Wo bist Du, Willi Wiberg?" von Gunilla Bergström)

Für meinen Sohn Ben Mika Ismer ...

Danksagung

Zuallererst möchte ich den beiden Betreuern dieser Arbeit, Jörg Neugebauer und Joel Ireta danken. Jörg Neugebauer gab die Anregung zum Thema der Arbeit und hat sie über die Jahre hinweg durch entscheidende Hinweise und Fragen auf erfolgreichem Kurs gehalten. Außerdem hat er mich kontinuierlich bestärkt und mir durch seinen Optimismus eine positive Sichtweise auf meine Arbeitsergebnisse ermöglicht. Joel Ireta war für mich in meiner Zeit am Fritz-Haber-Institut in Berlin zu jeder Zeit ansprechbar und hilfsbereit. Unzählige Diskussionen mit Joel und geduldige Denkanstösse seinerseits halfen mir besonders dabei, physikalische Interpretationen für meine Ergebnisse zu finden und Modellvorstellungen zu entwickeln. Jörg Neugebauer und Joel Ireta haben meine wissenschaftliche Denkweise nachhaltig geprägt.

Des weiteren möchte ich Matthias Scheffler danken, durch dessen und Jörg Neugebauers Fürsprache ich in meiner Zeit in Berlin die nötige finanzielle Unterstützung erhielt und der es mir gemeinsam mit Jörg Neugebauer ermöglichte, den Grossteil meiner Doktorarbeit am Fritz-Haber-Institut anzufertigen.

Die Schlussphase meiner Doktorarbeit hat am Max-Planck-Institut für Eisenforschung in Düsseldorf stattgefunden. Die Zusammenarbeit mit den Kollegen dort hat vor allem dem methodischen Aspekt der Arbeit einen weiteren Schub verliehen. Für fruchtbare Diskussionen möchte ich hier besonders Blazej Grabowski danken. Auch möchte ich besonders Tilmann Hickel danken, der sich wie selbstverständlich bereit erklärt hat, meine Arbeit gründlich Korrektur zu lesen. Gleicher Dank gilt Nadia Elghobashi, die meinem Englisch auf die Sprünge geholfen hat. Außerdem möchte ich für das Korrekturlesen Dank aussprechen an Johann von Pezold und Antje Ismer.

Abschließend möchte ich meinen Eltern danken, die mit Ihrer Erziehung und Fürsorge den wichtigsten Grundstein letztendlich auch für das Zustandekommen dieser Doktorarbeit gelegt haben.

Abstract

The existence of locally regular secondary structure motifs, such as helices, sheets, or turns, plays a central role for the biological function of proteins. However, open questions remain the thermodynamic stability of the secondary structure motifs. In particular, the *intrinsic stability* , i.e., the stability in the absence of any environmental effects, has – on the basis of experimental studies – not been acquired yet, even for the most abundant secondary structure motif, the helix. A detailed understanding of the intrinsic stability is in turn fundamental for a systematic theory of protein folding. Accurate theoretical studies of model systems are therefore highly desirable.

Density functional theory (DFT) is a powerful electronic structure method which meets the high requirements on accuracy demanded by these systems. However, existing DFT studies on helices focus on the static stability at the absolute temperature zero point and do not account for the strong thermal vibrations which occur at the biologically relevant temperature range. In this project we have therefore faced the challenge to employ DFT to determine the *temperature dependence* of the intrinsic helix stability.

The study includes all three experimentally observed helix types, i.e, the α-, the π- and the 3_{10}-helix. Further it includes several unfolded conformations, which serve as reference for the stability analysis. A key quantity to address the helix stability is the free energy. In the present study the free energy has been determined from the harmonic phonon spectrum, which in turn is determined from the dynamical matrix. In order to achieve the extreme high numerical accuracy required for this project, we had to extend the established standard methodology for calculating the dynamical matrix by a novel method, consisting of a three-stages refinement scheme. To further refine the results, we then extended the study by explicitly calculating anharmonic effects. We therefore have implemented the thermodynamic integration approach and combined it with an efficient stochastic Langevin dynamics scheme, which shows a dramatic increase in the computational efficiency as compared to common deterministic molecular dynamics schemes.

Employing this novel approach on the poly-L-alanine chain we are able to demonstrate that vibrational entropy plays a key role for the stability of the helix in the biologically relevant temperature range, since it strongly reduces the phase stability of the helices compared to the unfolded states. Nonetheless, we find that the enthalpic contributions arising from the cooperative hydrogen bond network of the α-helix are still sufficiently strong to make it the most stable bulk phase at room temperature, and also stable against unfolding. These results provide a very fundamental conclusion: The α-helix is *intrinsically* stable at room temperature, without the need of environmental effects, such as solvent or pressure. Furthermore, our results reveal trends on the temperature dependence of the *relative* stability between the three helix types. Most important, the π-helix exhibits a significant entropic "penalty" with respect to the two other helix types. By carefully mapping our DFT

data on an analytical model, we show that this trend is almost exclusively driven by the geometric peculiarities of the π-helix as compared to the α-helix and 3_{10}-helix. Since these peculiarities are roughly independent of the specific amino acid sequence and of the environment, they rationalize why the π-helix is in *general* the least common of the three helix types in proteins.

Based on these insights we have studied the impact of the side chain of the amino acids, which constitute the basic building blocks of the proteins, on the helix stability by performing a detailed comparative analysis between chains composed of two different amino acids, glycine and L-alanine. According to the experimental results, glycine is a very weak helix former, whereas L-alanine is a very strong helix former. The origin of this difference has not been clarified yet. By means of our approach we can show that vibrational free energy contributions siginificatly lower the glycine helical propensities compared to L-alanine, which also verifies that helical propensities of the amino acids already exist in the absence of *any* environmental effects.

Zusammenfassung

Die Existenz von lokal geordneten Sekundärstrukturelementen, z.B. Helices oder auch Faltblattstrukturen, ist von zentraler Bedeutung für die biologische Funktion von Proteinen. Dennoch bleiben offene Fragen bezüglich der Stabilität dieser Sekundärstrukturelemente. Insbesondere die *intrinsische Stabilität*, also die Stabilität in Abwesenheit jeglicher äußerer Einflüsse, konnte – basierend auf experimentellen Studien — bisher nicht erfasst werden, nicht einmal für das am häufigsten vorkommende Sekundärstrukturelement, die Helix. Eine detaillierte Kenntnis der intrinsischen Stabilität ist jedoch eine Grundvorraussetzung für ein systematisches, theoretisches Verständnis der Proteinfaltung. Deswegen sind genaue theoretische Studien von idealisierten Helices unersetzlich.

Die Dichtefunktionaltheorie (DFT) ist eine universell einsetzbare, theoretische Methode zur Beschreibung der elektronischen Struktur von poly-atomaren Systemen, welche die hohen Anforderungen, die die Simulation der Helix an die Genauigkeit stellt, grundsätzlich erfüllt. Jedoch konzentrieren sich bisherige DFT-Studien von Helices im Wesentlichen auf die statische Stabilität am absoluten Temperaturnullpunkt und lassen die ausgeprägten thermischen Schwingungen des Systems im biologisch relevanten Temperaturbereich außer Acht. Deshalb haben wir uns im Rahmen dieser Studie der Herausforderung gestellt, die Temperaturabhängigkeit der intrinschen Helix-Stabilität mit Hilfe der DFT zu bestimmen.

Die Studie umfasst alle drei experimentell beobachteten Helix-Typen, d.h., die α-, die π- und die 3_{10}-Helix und außerdem verschiedene ungefaltete Konformationen, die als Referenz für die Stabilitätsanalyse dienen. Eine zenrale Größe für die Bestimmung der Helix-Stabilität ist die freie Energie. Letztere wird in der vorliegenden Studie aus dem harmonischen Phononenspektrum bestimmt, welches seinerseits aus der dynamischen Matrix bestimmt wird. Um die extrem hohe numerische Genauigkeit zu erreichen, die für dieses Projekt nötig war, haben wir die etablierte Standardmethodologie zur Berechnung der dynamischen Matrix um eine neuartige Methode erweitert, die ein dreistufiges Verfeinerungsverfahren beinhaltet. Um die Ergebnisse weiter zu verfeinern, haben wir die Studie außerdem um die Berechnung anharmonischer Effekte erweitert. Hierfür haben wir die Methode der thermodynamischen Integration implementiert und sie mit einem effizienten stochastischen Langevindynamikverfahren kombiniert, was eine drastische Erhöhung der Recheneffizienz im Vergleich zu herkömmlichen, deterministischen Verfahren der Moleküldynamik zur Folge hatte.

Mit Hilfe dieses neuartigen Ansatzes konnten wir für das Beispiel einer poly-L-Alanin Kette zeigen, dass die Entropie der Schwingungszustände die Stabilität der drei untersuchten Helix-Phasen im Vergleich zum ungefalteten Zustand deutlich reduziert uns somit eine zentrale Rolle für die Stabilität der Helix im biologischen relevanten Temperaturbereich spielt. Nichtsdestotrotz haben wir auch ermittelt, dass die stabilisierenden Beiträge, welche durch das kooperative Netzwerk der

Wasserstoffbrücken in der Helix bestimmt werden, immer noch ausreichend groß sind, um die α-Helix bei zur stabilsten thermodynamischen Phase bei Zimmertemperatur zu machen, und sie vor dem Übergang in den Entfalteten Zustand zu bewahren. Diese Ergebnisse lassen eine grundlegende Schlussfolgerung zu: Die α-Helix ist bei Zimmertemperatur *intrinsisch* stabil, ohne die Hilfe von äußeren Einflüssen, also z.B. Lösungsmittel oder Druck. Darüberhinaus liefern unsere Ergebnisse wichtige Trends für die *relativen* Stabilitätsunterschiede zwischen den drei Helix-Typen. Von größter Bedeutung ist ein entropisches "Handicap", das die π-Helix im Vergleich zu den anderen beiden Helix-Typen tragen muss. Indem wir unsere DFT Daten auf ein analystisches Modell abbilden, können wir zeigen, dass dieses "Handicap" fast ausschließlich durch die geometrischen Eigenheiten der π-Helix im Vergleich zur α-Helix und zur 3_{10}-Helix verursacht wird. Da diese Eigenheiten im Wesentlichen unabhängig von der spezifischen Aminosäurenanordnung und der Umgebung sind, erklären sie grundlegend, warum die π-Helix *generell* der am seltensten vorkommende Helix-Typ in Proteinen ist.

Basierend auf diesen Einsichten haben wir den Einfluss der Seitengruppe der Aminosäuren, also der Grundbausteine der Proteine, auf die Helix-Stabilität untersucht, indem wir eine vergleichende Analyse zwischen zwei Peptid-Ketten angestellt haben, wovon die eine aus Peptiden der Aminosäure L-Alanin und die andere aus Peptiden der Aminosäure Glycin zusammengesetzt war. Entsprechend der Resultate von experimentellen Studien lassen sich mit Glycin nur sehr schwer Helices erzeugen, wohingegen L-Alanin sehr stark dazu neigt, Helices auszubilden. Die Ursache für diese Unterschiede ist noch unbekannt. Mit Hilfe unseres Ansatzes können wir zeigen, dass die Schwingungsbeiträge zur freien Energie die Helixpropensität von Glycin im Vergleich zu L-Alanin deutlich verringern, was auch beweist, dass die Aminosäuren schon in der Abwesenheit jeglicher äußerer Einflüsse unterschiedliche Helixpropensitäten aufweisen.

Contents

1 Introduction

1.1 Proteins

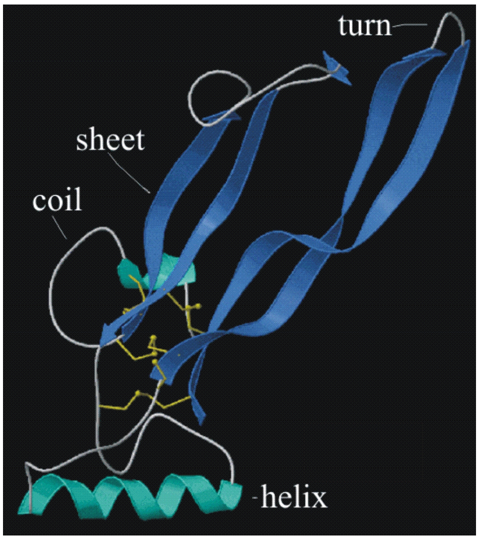

Figure 1.1: Schematic representation of a protein and its secondary structure.

Proteins are essential parts of living organisms that participate in almost all processes taking place in the cells. They are built of 20 different amino acids, which are linked together by the so-called peptide bonds to form a linear peptide chain, known as the primary structure.

The latter is assembled using the information encoded in genes and completely determines the biological function of a protein. However, to be able to carry out their function, proteins must adopt specific three-dimensional, folded conformations, the so called tertiary structure[1]. The tertiary structure is also called folded state and the way how the primary structure transforms to the folded state is denoted as protein folding process. This process and the characteristics of the folded state have raised various important questions in the past decades.

The central question has been, whether protein folding is a thermodynamic or a kinetic process. It was Levinthal [1] who made the "kinetic hypothesis". He recognized that it would be impossible for a protein to find its native state by randomly searching through the entire space of possible conformations and concluded that the folding must follow a specific pathway. This implies that the protein structure possibly gets trapped in a *local* minimum of the free energy surface corresponding to a *meta-stable* thermodynamic state. In contrast, Anfinsen [2] made, based on numerous experimental results, the "thermodynamic hypothesis" and stated that the folded state corresponds to a global free energy minimum. The contradiction between the two hypotheses was partially resolved by the introduction of the "folding funnel" concept [3]. This concept directs the folding of the protein without the need for a definite pathway, thus supports the thermodynamic hypothesis, but also leaves open the possibility for kinetically inaccessible lower-energy states outside of the folding funnel and thus supports the kinetic hypothesis. Recently, also the role of evolution was considered, which possibly facilitates that the free energy minimum in many (but not all) cases corresponds to the bottom of the folding funnel [4]. Nevertheless, it is also known that *some* proteins (in particular large proteins) require the assistance of other proteins (so called chaperones) to maintain their

---

[1] If the protein is assembled with more than one peptide-chain, the folded conformation is called quaternary structure.

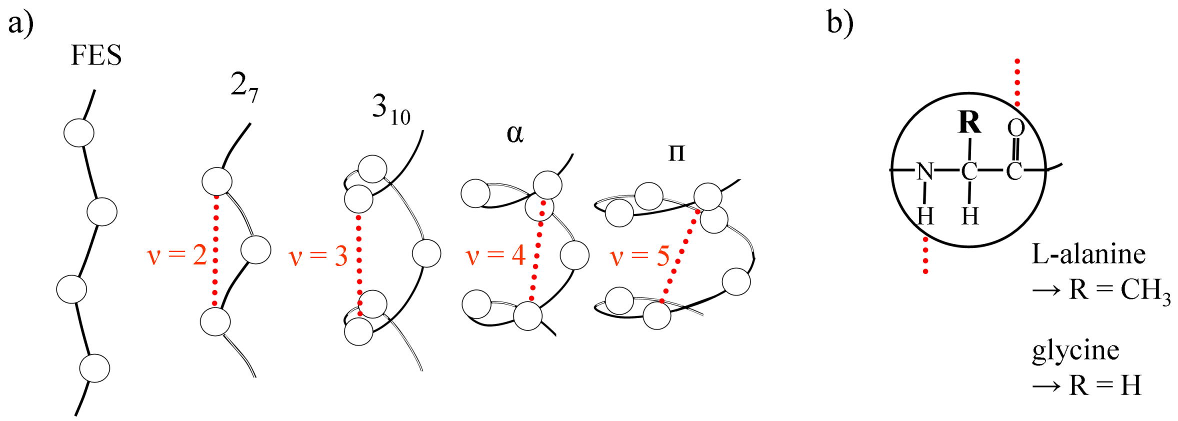

Figure 1.2: a) Helix types and fully extended structure (FES). The red, dotted lines denote intra-chain $\mathrm{N-H\cdots O=C}$ hydrogen bonds. ν denotes the number of peptide units to form a hydrogen bond. b) Amino acid residue (peptide unit). The various amino acids differ in the side chain that is attached to them. For example, for glycine we have $\mathrm{R} = \mathrm{H}$ and for L-alanine $\mathrm{R} = \mathrm{CH_3}$.

functional state [5]. While this fundamental question about the basic mechanism of protein folding seems thus to be answered, a predictive theory of protein folding is, nonetheless, far from being developed.

1.2 Secondary structure

The local spatial arrangement of the peptide chain is called secondary structure. A major part (about 90 % among all proteins) of the secondary structure is found in rather regular structural motifs. Such regular motifs can be either sheets, helices or turns (Fig. 1.1). Every part of the peptide chain which is not in either one of these motifs is called random coil. It is generally accepted that the formation and existence of the regular secondary structure motifs play a central role for both the folding and the biological function of proteins. Serious diseases, such as Altzheimer's disease, Parkinson's disease or the Creuzfeldt-Jacob disease are supposed to be connected to misfoldings in the secondary structure [6]. Thus a detailed understanding of the secondary structure stability both from thermodynamic and kinetic viewpoints is essential to get a predictive understanding of protein (mis)folding and functionality/degeneration.

1.3 Helical conformations

The helix is the most abundant secondary structure motif. It is stabilized by intra-chain hydrogen bonds (Figs. 1.2 and 1.3). Three different helix types have been found in proteins: the α-helix, the 3_{10}-helix, and the π-helix. These three helix types differ in the hydrogen bonding (hb) pattern they form: The hbs are formed between the peptide units i and $i + \nu$, where $\nu = 3$ for the 3_{10}-helix, $\nu = 4$ for the α-helix and $\nu = 5$ for the π-helix (Fig. 1.2). Furthermore, they differ in the number of peptide units per turn and exhibit different geometries: The 3_{10}-helix is more tightly wound than the α-helix, which by itself is more tightly wound than the π-helix. In proteins the α-helix is the predominant helix type, with an occurrence of 80 %, followed by the 3_{10}-helix, with an occurrence of 20 % [7]. In contrast, *extended* π-helices are found only in exceptional cases [8]. However, investigations on the conformations of peptides in solution indicate that π-helical (and 3_{10}-helical) *segments* may be present as defects in α-helices [9, 10, 11].

The discovery of these three helix types [12, 13, 14] has stimulated scientific research for more than 5 decades. Nevertheless, open questions remain regarding their thermodynamic stability, which is a rather delicate balance between the enthalpic and entropic contributions of the peptide chain and those arising from the surrounding environment (e.g. solvent). Here we address three of these questions:

I. Is the helical secondary structure motif intrinsically stable at room temperature?

It is well accepted that the formation of hydrogen bonds between peptide units constitutes an important contribution to the helix stability. However, it is a matter of debate, whether hydrogen bonds on their own are strong enough to stabilize the helical conformation at a given temperature, or whether additional stabilizing mechanisms are needed [15, 16, 17, 18]. This fundamental issue has been addressed in experimental studies on the stability of short L-alanine peptide chains[2] in water [15] as well as in the gas phase [16]. These experimental studies [15, 16] reveal stable helical conformations in water at 274 K and in the gas phase at 300 K. One could thus conclude that the helical motif is intrinsically stabilized by the hydrogen bonds at room temperature. However, to increase the solubility of the L-alanine peptides and to avoid aggregation, charged peptide units had to be attached to the alanine chains in these studies. The charged peptide units tend to mask the contribution of intra-helical hbs to the stability of the helices. Indeed, it has been suggested in Refs. [17, 18] that these charged peptide units attached to the peptides in the studies [15, 16] are responsible for the observed helix stability to a more pronounced degree than the intra-helical hydrogen bonds. Thus, a definite answer to the question, whether the hydrogen bonds alone are sufficient to stabilize the helical conformations at room temperature, has not been given yet.

II. Rates of occurrences of the different helix types — rarity of π-helices

As mentioned above, it is well known that the three experimentally observed helix types show rather different rates of occurrence in the protein structures. However, neither the origin of these differences, nor the relative importance of the protein environment and the intrinsic features of the peptide chain for the stability of the different conformations is understood at present.

In particular the rarity of the π-helix has given rise to various speculations in the literature:

1. The cavity in the center of the π-helix is larger than that in the α-helix and the 3_{10}-helix. It has thus been suggested that the van-der-Waals distances across the cavity are larger, which would result in a relative loss of stability. On the other hand the cavity would be still too small to allow water molecules to enter, which could in turn bridge the large van-der-Waals distances [20].

---

[2] L-Alanine is a simple amino acid (R=CH_3, Fig. 1.2b) with a strong propensity to form helices [19].

2. It has been suggested that the π-helix is energetically unfavorable, compared to the α-helix and the 3_{10}-helix, since it lies outside of the conformational flexibility of the peptide backbone, as has been determined with empirical analytical potentials for di-peptide model systems (e.g. [14, 21]).

3. The number of intra-helical hydrogen bonds in finite isomeric structures of helices are not equivalent. For a given finite chain length, the 3_{10}-helix forms one more hydrogen bond than the α-helix, whereas the π-helix forms one less hydrogen bond than the latter one. It has been suggested that this effect makes the π-helix energetically less favorable than the α-helix and the α-helix less favorable than the 3_{10}-helix (e.g. [22]).

4. It has been suggested that helix initiation is entropically unfavorable in the π-helix compared to the α-helix, since in the π-helix four peptide units must be oriented correctly before the first, (i, i+5)-hydrogen bond is formed, whereas for the α-helix only three peptide units must be oriented correctly [22].

The arguments 1) and 2) stem from the 50's and are speculative. In particular argument 2) is not necessarily valid (as we will show in Sec. 1.5). The arguments 3) and 4) are more feasible. These arguments are of energetic and kinetic character, respectively, and apply mainly for short helices. However, they do not apply for a residue in the middle of long peptides, i.e., a situation in which dangling hydrogen bonds are absent or properly capped. It is, however, known that also the bulk of extended helical motifs is predominantly adopting the α-type. Thus additional reasons must exist to explain the rarity of π-helices.

III. Helical tendencies of the amino acids

The tendency of a given protein segment to form helices depends on its amino acid sequence. This important issue has been extensively investigated experimentally and thermodynamic scales have been derived to quantify the helical tendencies of the amino acids [19, 23, 24, 25, 26, 27]. These studies are consistent in a qualitative manner, i.e., they largely agree in the order of the amino acids on the thermodynamic scale. For example, it is well accepted that proline and glycine (Gly, R = H, Fig. 1.2b) are the weakest helix formers, whereas L-alanine (Ala, R = CH_3) is the strongest helix former. However, the reported thermodynamic scales largely vary in a quantitative manner. Focusing on the two extrema, Ala and Gly, the reported differences for the helical propensities (definition will be given in Sec. 4.5.4) at room temperature are spread from 0.7 kcal/mol up to 2.0 kcal/mol. Furthermore, the *origin* of the differences in the helical propensities is not clarified yet. Several assumptions have been made to explain, for instance, the differences between Gly and Ala:

1. It has been suggested that the main chain (or backbone) conformational entropy[3] in the unfolded state is larger for Gly than for Ala, due to smaller excluded volume effects associated with steric interactions of adjacent peptide units. D'Aquino et al. have estimated the conformational entropy of a di-peptide model system by means of an empirical force field and

---

[3] The term "main chain conformational entropy" (or "backbone conformational entropy") denotes the entropy associated to the possible conformations the peptide chain may adopt in the given (folded or unfolded) state.

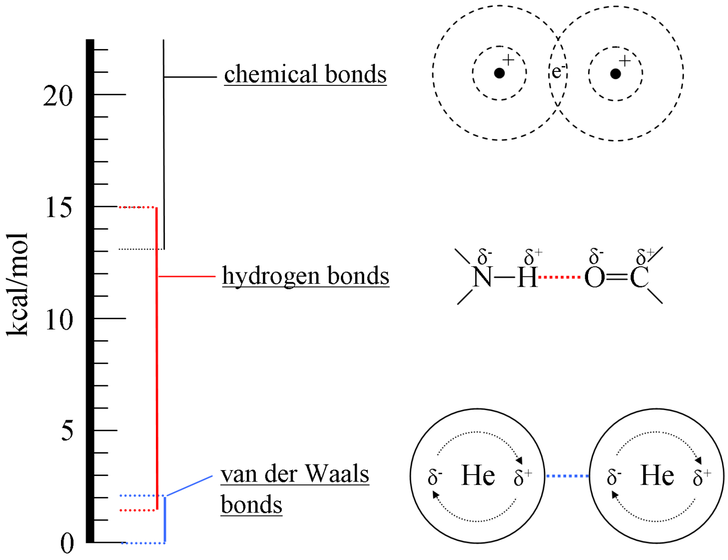

Figure 1.3: Energy scale of the electronic interactions relevant for the stability of biological systems (schematic).

found a difference of 0.7 kcal/mol between Ala and Gly [28] in good agreement with the early study of Nemethy et al. [29]. However, other force field studies have obtained a much smaller difference (< 0.2 kcal/mol) in the main chain conformational entropy [30, 31, 32].

2. It has been suggested that the helical state of Ala sequences could be energetically preferred. Scott et al. have drawn this conclusion, since they found the entropic differences between Ala and Gly to be small [32]. We will address this point in Sec. 1.5.

3. It has been suggested that the helix propensities of the different amino acids are influenced to some extend by the solvent [33, 34, 35]. The helical state of alanine sequences could be preferred relatively to that of glycine because of stronger hydrophobic interactions. However, recently Hudgins&Jarrold have analyzed the conformations of charged Ala- and Gly-based peptides in the gas phase, i.e., in the absence of a solvent, using ion-mobility measurements [36]. They found that the stability of Ala- and Gly-helices is (qualitatively) consistent with the helix propensity scales mentioned above.

Summarizing these speculations, both, experimental and theoretical investigation of the helical propensities have lead to partially contradictory interpretations. Thus the origin of the helical propensities still lacks a full understanding.

1.4 Intrinsic aspects of helix stability

Fundamental aspects of helix stability are thus not clarified yet. In particular the detailed balance of the various contributions to the stability is still a matter of controversy. To fully understand the helix formation process, it is required to develop a systematic and quantitative theory. A first step towards such a quantitative and systematic understanding must be the accurate acquisition of the *intrinsic aspects of helix stability*, i.e., the stability in the absence of any environmental effects, such as solvent, protein environment or helix endings. Only after these intrinsic aspects are quantitatively understood, the role of the various environmental effects, which are certainly important by themselves, can be adequately classified. The intrinsic aspects of stability are not directly accessible from experimental observation. Accurate theoretical studies of idealized model systems are therefore highly desirable.

For this kind of studies, however, the choice of the theoretical tools is of crucial importance. This is due to the fact that the requirements on accuracy are very high in these biological systems. We will at first briefly enumerate the basic requirements for an accurate description of the secondary structure. In the next section, we will then introduce an approach which meets these requirements.

- **Chemical bonding and Pauli repulsions:** A basic requirement on the theoretical approach in use is that it is able to accurately describe the covalent and ionic bonds which stabilize the peptide chain. Further, it must be able to correctly account for the steric hindrances and short range repulsions which may appear when the peptide chain folds to the secondary structure. Bond lengths, valence angles, and dihedral angles must be predicted correctly.

- **Hydrogen bonding:** The approach must be able to accurately describe hydrogen bonding. Hydrogen bonds are the key interactions, which drive the formation of the secondary structure of proteins. The origin for hydrogen bonding is thought to be predominantly of electrostatic nature and closely related to the charge distribution within the molecular structure [37]. In a simplified picture a hydrogen bond can be understood as a dipole-dipole interaction, involving the proton of an hydrogen atom as the positive pole and a strongly electronegative atom as the negative pole (Fig. 1.3). Of course, in reality the interaction is more sophisticated; it involves higher order multi-pole terms and depends in a complex manner on the relative orientation of the two interacting groups [38]. Furthermore, it has long been suggested [39] and recently confirmed by means of ab-initio calculations (Ref. [40] and references therein) that hydrogen bonds involve some covalent contribution.

- **Electronic polarizability:** The approach must adequately account for electronic polarizability. The electrostatic multi-pole terms as described above are not fixed, static quantities of the molecular geometry: An external electrical field may induce a charge density redistribution in the molecule, thereby altering the multi-poles. This process is called electronic polarizability and is crucial for the hydrogen bond formation in the secondary structure. It allows, e.g., the multi-poles associated with the hydrogen bonding network of the helix to interact with each other in a non-linear way, such that each hydrogen bond is much stronger in the network than

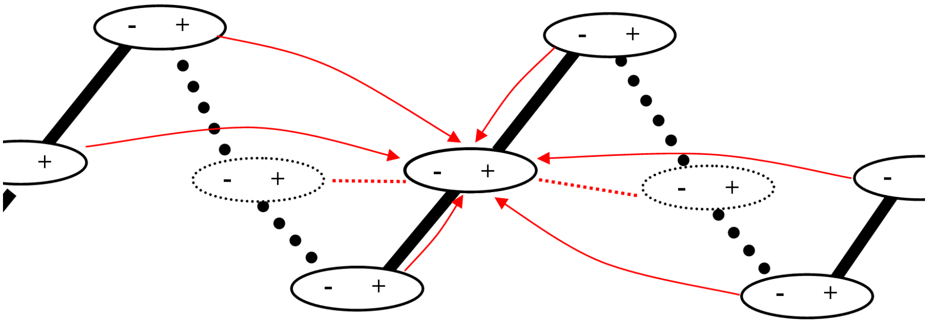

Figure 1.4: Schematic illustration of the cooperativity of hydrogen bonds in a helix.

it would be in the isolated case. This process is called hydrogen bond cooperativity (Fig. 1.4 and Sec. 1.5).

- **Van-der-Waals forces:** Van-der-Waals (or London-dispersion) forces are caused by the dynamically induced polarization effects connected to fluctuations in the electronic charge distribution, which arise from the oscillations of the electronic wavefunction. Due to these fluctuations a (spherical) atom has a transient dipole moment, which polarizes any neutral atom nearby and leads to an attraction between the atoms. Although the transient dipole changes constantly and rapidly, those of the other atoms tend to follow it and are correlated. These interactions are purely quantum mechanical in nature and exclusively attributed to electronic correlation (Sec. 2.4.3). The forces resulting from these interactions exist in any poly-atomic system, even in the absence of permanent multi-poles, and in electrostatically completely neutral objects. They are important for the stability of biological systems, in which other inter-molecular forces, like hydrogen bonds, are lacking. For predominantly hydrogen bonded systems, however, they play only a secondary role, since hydrogen bonds are in general an order of magnitude stronger than van-der-Waals bonds (Fig. 1.3). The question of whether the van-der-Waals bonds are important to describe the peptide chains analyzed in this project will be discussed in Sec. 2.4.3.

1.5 Density functional theory

Following the above considerations, explicitly taking into account the electronic structure is obviously inevitable to obtain an accurate description of the secondary structure. Density functional theory (DFT) [41, 42] is a powerful method to simulate molecular systems by fully taking into account their electronic structure. It is well known that DFT accurately predicts the structural and energetic properties related to chemical bonds (Sec. 2.4.3), and, recently, comparative studies to post-Hartree Fock approaches have also verified the high accuracy of this approach to describe hydrogen bonds (see Refs. [43, 44] and references therein).

a)

	ΔE^{el}
π	-2.2
α	-2.7
3_{10}	-2.3
2_7	-0.5

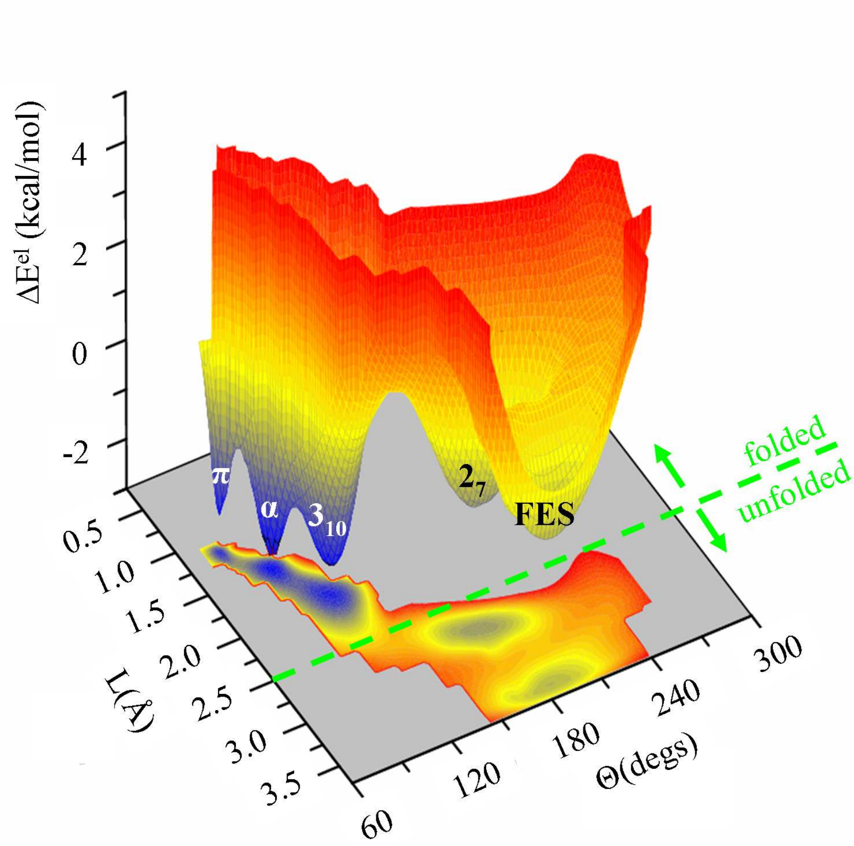

b)

	ΔE^{el}
π	-2.9
α	-2.9
3_{10}	-2.3
2_7	-0.5

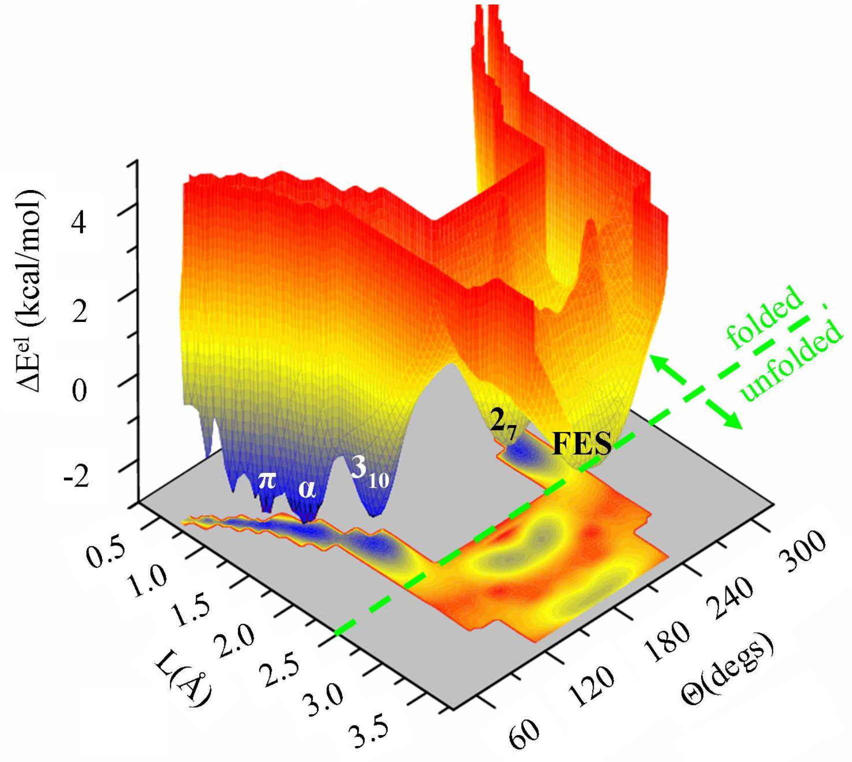

Figure 1.5: Potential energy surface for a) poly-L-alanine and b) poly-glycine. The tables on the left hand sides of the plots denote the static stability per peptide unit with respect to the FES (Eq. (1.1)). Courtesy of J. Ireta.

Indeed, DFT based studies of helices in vacuum have already been useful to unveil the role hydrogen bonds play in stabilizing these secondary structure motifs. For instance, DFT studies of finite and infinite peptide chains [45, 46, 47, 48, 49] have shown that cooperative effects in hydrogen bonding networks (Fig. 1.4) may lead to a dramatic increase in hydrogen bond strength and are crucial to stabilize helices with respect to hydrogen bond free conformations such as the fully extended structure (FES, Fig. 1.2). It has been shown that cooperativity strengthens the individual hydrogen bonds in the infinite poly-L-alanine α-helix by more than a factor of two [48].

Potential energy surface of infinite poly-L-alanine and poly-glycine chains

Recently, DFT has been employed to investigate the configurational space of infinite poly-L-alanine [50] and poly-glycine [51] chains. By sampling the configuration space spanned by the *helical parameters* L and Θ (Fig. 1.6) and fully relaxing the internal degrees of freedom of the peptide chain a 2-dimensional potential energy surface (PES) has been obtained.

This (L, Θ)-PES provides a valuable topographical representation of the configurational space of the helical motifs: As Fig. 1.5 shows, the PES exhibits several minima for both poly-L-alanine and poly-glycine. Three of these minima can be clearly identified with the three experimentally observed helix types, i.e., 3_{10}-, α- and π-helix. Besides these minima further minima exist for the unstrained chain in the fully extended structure (FES) and for the so called 2_7-structure (Figs. 1.5 and 1.2). Also, it has been found that the helical parameters are suitable reaction coordinates to describe the mechanical deformations of the peptide chain [50].

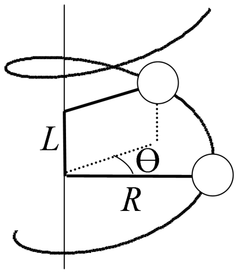

Figure 1.6: Helical parameters: pitch L, twist Θ and radius R.

Furthermore, the (L, Θ)-PES allows to determine the static stability of the helices, i.e., the stability at 0 K. To determine the static stability, let us set the energy zero as the total energy of the FES, because this reference system corresponds to the unstrained peptide chain which lacks hbs. The static stability is then given as:

$$\Delta E^{\mathrm{el}}(L, \Theta) = E^{\mathrm{el}}(L, \Theta) - E^{\mathrm{el}}(L_{\mathrm{FES}}, \Theta_{\mathrm{FES}}), \tag{1.1}$$

where $E^{\mathrm{el}}(L, \Theta)$ denotes the total energy per peptide unit for given L and Θ, and $E^{\mathrm{el}}(L_{\mathrm{FES}}, \Theta_{\mathrm{FES}})$ denotes that of the FES. As shown in Fig. 1.5, all three helical conformations are energetically preferred over the FES. The same applies to the 2_7-conformation, although the energetic preference is much smaller in this conformation. Hence, we may conclude that, in a static picture, the helical state is energetically preferred with respect to the unstrained, extended state by 2.3 to 2.9 kcal/mol per peptide unit, depending on the helix type and on the side chain. A more detailed discussion of the energetic differences between the helix types will be given later.

While the PES gives important insights into the *static* stability of the helical conformations and provides a valuable topographical representation of the configurational space, it is, however, not sufficient to find answers to the fundamental questions we have raised in Sec. 1.3. Namely, the peptide chain is not in rest, but is, even at the absolute temperature zero point, exposed to fluctuations (zero point vibrations). Even more important, the system performs strong thermal vibrations in the biologically relevant temperature range. The static stability of the helical motifs as induced by the hydrogen bonds is not particularly large. It is thus a basic question, whether or not the thermal vibrations are strong enough to break the helix structure.

Also, the information about the static stability as available from the PES does not explain the differences in helical propensities between Ala and Gly – the static stability of the Gly α-helix is even slightly larger than that of the Ala α-helix.

Furthermore, according to the static stability, the π-helix should be much more frequently observed than it actually is – the π-helix is only marginally destabilized with respect to the α-helix for Ala and degenerated to it for Gly. It is in this regard interesting to note that recent experimental studies suggest the presence of transient defect structures (,i.e., the content of π- and 3_{10}-helical segments) in solvated α-helices to be larger at low temperatures (e.g. at 0°C) than at high temperatures (e.g. at 30° C) [10, 11]. Based on these experimental findings it has been concluded that the melting temperature for π- and 3_{10}-helices is lower than the melting temperature for an α-helix [10, 11]. This implies that the relative thermodynamic stability (which is given by the difference in the free energy of formation) between the three helix-types is not a constant, but shows a strong temperature dependence.

To get a more realistic picture, it is therefore required to go beyond the static treatment and include the vibrational properties of the peptide chain in the stability analysis.

1.6 Temperature dependence

The theoretical treatment of dynamical properties of the secondary structure on an atomistic level has been traditionally reserved to molecular dynamics simulations based on empirical force fields. The force field approach treats chemical bonding by means of force constants and incorporates the weak bonding interactions, i.e., hydrogen bonding and van-der-Waals forces, by point charge models and Lennard-Jones potentials, respectively. The force constants are optimized to fit experimental and/or ab-initio data. The big advantage of force fields compared to ab-initio methods is that they are computationally inexpensive: Nowadays molecular dynamics simulations of systems containing hundred thousand atoms or more can be performed for time periods of several nanoseconds (see Ref. [52] and references therein). However, the approximate/parameterized nature of the force field approach reveals also deficiencies. For example it is not clear, whether or not the limited accuracy and predictive power of this approach allows to accurately reproduce the delicate differences between the individual stabilities of the different secondary structure types. Indeed, it has been shown that the relative stability of the helix types, i.e., 3_{10}-, α- and π-helix, strongly depends on the chosen force field parametrisation [53] and thus might be artificial for an individual force field.

The success of a force field in accurately describing a particular property of the system crucially depends on whether or not sufficient *relevant* input data for the optimization of the force constants is available. For the determination of the vibrations of the helix this limitation has serious consequences. To be more concrete, we quote as an example the vibrational spectrum of the poly-L-alanine α-helix, which has been the subject of various experimental and theoretical, force field based studies in the past [54, 55, 56]. The experimental spectra of this system are complete and accurate for the mid-to-high frequency range from 200 to 3500 cm^{-1}, however, they are incomplete for the low frequency range below 200 cm^{-1}. As a consequence, the force fields, which were optimized to fit these experimental spectra, revealed significant shortcomings in predicting the specific heat [55], indicating substantial errors in the low frequency vibrational branches. The low frequency branches in turn are fundamental for the thermodynamic stability, as they dominate the vibrational entropy and contain the mechanical deformations of the helix. To obtain an accurate description of the temperature dependence of the helix stability it is therefore required to fill this gap left behind by the existing experimental and force field studies and to determine the complete vibrational spectrum by explictly including the low frequency branches.

Density functional theory calculations applied on idealized model systems, such as infinite helices in vacuum are therefore highly desired, since they would allow to accurately determine the *complete* vibrational spectrum corresponding to the respective helical structure, in an unbiased, parameter free manner. Indeed, DFT based studies on vibrational properties of the secondary structure have already been published [57, 58]. These studies are, however, focussed on particular frequencies rather than the complete vibrational spectrum and are not treating thermodynamic properties such as the free energy. Recently, Wieczorek&Dannenberg have computed the contributions of vibrational *energy* to the stability of the poly-L-alanine α-helix at 0 K and at room temperature using DFT and finite chains up to the length of 18 peptides [59]. The corrections they found were rather small (0.2 kcal/mol per peptide unit) and an asymptotic limit for the formation enthalpy of the infinite α-helix of about -3.0 kcal/mol per peptide unit was predicted. While this study can be considered a first step towards a thorough thermodynamic description of these systems aspects, it is still incomplete in so far as not only the contributions of the vibrational *energy* but also those of the vibrational *entropy* should be included to accurately determine the free energy at elevated temperatures. As we will show in this thesis these entropic contributions are much more important for the helix stability at room temperature than the energetic vibrational contributions.

1.7 This project

In this project we have employed density functional theory to study the temperature dependence of the helix stability. To provide an unbiased view on the intrinsic helix stability, which is complementary to the experimental observation, we have focused on the bulk of the infinite structure, and excluded environmental effects, such as solvent or helix endings, from our investigation.

The concrete motivation for the project is given by the three fundamental issues discussed in Sec. 1.3. We focus at first on a poly-L-alanine chain to tackle the first two questions:

- Is the helical secondary structure motif intrinsically stable at room temperature?
- Why are π-helices rarely observed in proteins (compared to α- and $3_{10}-$helices)?

In order to determine the temperature dependence of their relative stability we have included the α-helix, π-helix, and 3_{10}-helix, in the stability analysis. Furthermore, we have investigated the 2_7-conformation to complete the study in terms of possible hb patterns (Fig. 1.2 a), and the fully extended structure (FES), which lacks hydrogen bonds, and serves as a reference point for the stability analysis.

The study is based on the concept of free energy, which is determined by solving the equations of motion in the harmonic approximation. This means we apply *Bloch's theorem,* i.e. we determine the phase dependent, symmetry reduced dynamical matrix, diagonalize it, and obtain the phonon dispersion relation. With the knowledge of the phonon dispersion relation we determine the partition function and with it the thermodynamic properties including the free energy. In order to achieve the high numerical accuracy required in this study for forces, vibrational frequencies and thermodynamic data, we have extended the established standard methodology by a novel method for calculating the dynamical matrix, i.e., a three-stages refinement (TSR) scheme.

To go beyond the harmonic approximation and to extend the study to anharmonic effects we apply the thermodynamic integration approach. The canonical thermodynamic averages as required along the thermodynamic integration path are determined by means of an efficient molecular dynamics approach (Langevin dynamics), which we have implemented together with an efficient extrapolation scheme for the electronic degrees of freedom.

The focus of this thesis is thus to accurately calculate the free energies of the *pure* phases corresponding to the possible equilibrium conformations of the peptide chain. Nevertheless, at finite temperatures the thermodynamic state of the peptide chain may be characterized by a coexistence of several phases rather than by a single phase. This is particularly true for the unfolded state, which is supposed to be occupied at high temperatures. An exact determination of the free energy of the unfolded state is beyond the scope of this project. However, we have *estimated* the free energy of the unfolded state by treating the unfolded state as an ideal solution of the bulk phases contributing to it.

For tackling the third issue:

- What is the origin of the difference in the helical propensities between L-alanine and glycine?

we have performed a comparative analysis for the infinite poly-glycine and poly-L-alanine chain. These amino acids, L-alanine and glycine, are most suitable for such a comparative study, since they are, on the one hand, the two amino acids with the simplest side chains ($R = CH_3$ for L-alanine and $R = H$ for glycine, Fig. 1.2 b) and, on the other hand, the two extrema of the (experimental) helix propensity scale.

Validating the accuracy of our approach is another important issue. While DFT would, in principle, allow to exactly determine the ground state properties of a given system, its practical implementation requires to introduce a fundamental approximation – in this study we use the generalized gradient approximation (GGA) – in form of the so called exchange-correlation functional. While comparative studies of DFT-GGA and the supposedly more accurate post-Hartree Fock methods have already verified the high reliability of DFT-GGA to describe the *static/energetic* contributions of the hydrogen bonds in the secondary structure, the performance of DFT-GGA to determine the *vibrational/thermodynamic* properties of the helix is essentially unknown. To validate its accuracy we have compared the calculated frequency spectra and thermodynamic data to available experimental data.

Furthermore, an analysis of the obtained results is presented with the aim of getting a deeper understanding of the underlying mechanisms that drive the differences between the various conformations of the peptide chain. For this purpose we have developed an analytical potential to model the vibrations of the peptide chain and to reproduce the thermodynamic trends.

2 Theoretical concepts

The purpose of this chapter is to provide the theoretical framework of the project. The chapter is arranged as follows: First, the model used to describe the secondary structure of the peptide chain is introduced and the basic terminology is clarified (Sec. 2.1). Then the theoretical approaches which have been employed in this work are presented. These include density functional theory (DFT) to determine the electronic groundstate (Sec. 2.4) and the quasi-harmonic approximation to solve the ionic equations of motion (Sec. 2.6) of the peptide chain. Furthermore, the basic thermodynamic tools to calculate the free energy and the temperature dependent stability of the various conformations of the peptide chain are developed. To estimate anharmonic contributions the thermodynamic integration method (Sec. 2.7) is introduced.

2.1 Model

For this project we model the secondary structure of the peptide chain as an isolated, infinitely long chain, assembled with a single peptide unit, which can be either glycine or L-alanine (Fig. 1.2b). In static equilibrium such a chain is completely periodic, with the peptide unit being the repeat unit. The repetition of the peptide units may be described by a lattice vector, $\mathbf{T}_n$, which is determined by a translation along the chain axis, i.e., a *pitch* L, and a rotation around the chain axis, i.e, a *twist* Θ (Fig. 1.6). In Cartesian coordinates $\mathbf{T}_n$ may be written as:

$$\mathbf{T}_n = (R \cdot \cos(n\Theta), R \cdot \sin(n\Theta), n \cdot L)\,, \tag{2.1}$$

where n indicates the peptide unit and R is the distance to the helix axis. Here we focus exclusively on single-stranded peptide chains, which include the most abundant secondary structure motif, the helix. Multi-stranded motifs, such as the β-sheet, are excluded from this study. Furthermore, we focus on isolated helices in vacuum and explicitly exclude effects of the helix-endings, of the protein environment, and of the solvent. Therefore, all properties of the peptide chain obtained in this study are *intrinsic* features of the respective chain conformations. As discussed in the introduction, it is the aim of this project to determine these intrinsic features as accurate as possible.

2.2 Many-body Schrödinger equation

We intend to analyze the behavior of the peptide chain by explicitly taking into account its N^{el} electronic degrees of freedom, denoted with $\mathbf{x}_i$, and its N^{ion} atomic degrees of freedom, denoted with $\mathbf{X}_I$. Thus, we have to solve the many-body Schrödinger equation (SE):

$$H(\mathbf{x},\mathbf{X})\Psi_\Upsilon(\mathbf{x},\mathbf{X}) = E_\Upsilon\Psi_\Upsilon(\mathbf{x},\mathbf{X}). \tag{2.2}$$

Here, $\Psi_\Upsilon(\mathbf{x},\mathbf{X})$ denotes the many-body wavefunction of the peptide chain corresponding to the total energy E_Υ, whereas Υ denotes the quantum number. The configurational vector of the electrons is given by $\mathbf{x} = (\mathbf{x}_1, \mathbf{x}_2, ..., \mathbf{x}_{N^{\mathrm{el}}})$, and $\mathbf{X} = (\mathbf{X}_1, \mathbf{X}_2, ..., \mathbf{X}_{N^{\mathrm{ion}}})$ denotes the configurational vector of the atomic cores, which are in the following denoted as "ions". $H(\mathbf{x},\mathbf{X})$ represents the many-body Hamiltonian which is, using atomic units, given by:

$$H(\mathbf{x},\mathbf{X}) = T^{\mathrm{el}}(\mathbf{x}) + T^{\mathrm{ion}}(\mathbf{X}) + V^{\mathrm{el-el}}(\mathbf{x}) + V^{\mathrm{el-ion}}(\mathbf{x},\mathbf{X}) + V^{\mathrm{ion-ion}}(\mathbf{X}), \tag{2.3}$$

where

$$T^{\mathrm{el}}(\mathbf{x}) = -\sum_{i=1}^{N^{\mathrm{el}}} \frac{\Delta_i}{2} \tag{2.4}$$

is the kinetic energy of the electrons. The term

$$V^{\mathrm{el}}(\mathbf{x}) = \frac{1}{2}\sum_{i\neq j}^{N^{\mathrm{el}}} \frac{1}{|\mathbf{r}_i - \mathbf{r}_j|} \tag{2.5}$$

describes the electrostatic interaction of the electrons,

$$T^{\mathrm{ion}}(\mathbf{X}) = -\sum_{J=1}^{N^{\mathrm{ion}}} \frac{\Delta_J}{2M_J}, \tag{2.6}$$

is the kinetic energy of the ions,

$$V^{\mathrm{ion-ion}}(\mathbf{X}) = \frac{1}{2}\sum_{I\neq J}^{N^{\mathrm{ion}}} \frac{Z_I Z_J}{|\mathbf{X}_I - \mathbf{X}_J|} \tag{2.7}$$

stands for the electrostatic interactions of the ions, and

$$V^{\mathrm{el-ion}}(\mathbf{x},\mathbf{X}) = -\sum_{J=1}^{N^{\mathrm{ion}}}\sum_{i=1}^{N^{\mathrm{el}}} \frac{Z_J}{|\mathbf{x}_i - \mathbf{X}_J|} \tag{2.8}$$

denotes the electrostatic electron-ion interaction. The terms M_J and Z_J stand for the ion masses and the ion charges, respectively.

2.3 Born-Oppenheimer approximation

Solving the SE of a poly-atomic system directly and exactly constitutes in general an intractable problem. A basic simplification for solving the SE, which we apply in this work, is contained in the Born-Oppenheimer approximation (BOA). The BOA employs the fact that the electrons move, due to their significantly lower mass ($\frac{M^{\mathrm{el}}}{M^{\mathrm{ion}}} < 0.005$), much faster than the ions. The idea behind the BOA is thus to assume the ions to be fixed on the electronic timescale. As a consequence, the electronic movement is decoupled from the ionic movement, in a sense that it does not depend on the velocities of the ion cores, but only on their positions. On the other side, the ions explore a conservative potential arising from the electronic state at the given ionic positions, the so called Born-Oppenheimer surface.

To realize the Born-Oppenheimer approximation, a separation ansatz is used for representing the many-body wavefunction:

$$\Psi_{\Upsilon}(\mathbf{x}, \mathbf{X}) = \Psi^{\mathrm{ion}}_{\nu\mu}(\mathbf{X}) \Psi^{\mathrm{el}}_{\nu}(\mathbf{x}; \mathbf{X}). \tag{2.9}$$

Here $\Psi^{\mathrm{el}}_{\nu}(\mathbf{x}; \mathbf{X})$ denotes the wavefunction for the electronic degrees of freedom, $\mathbf{x}$, and describes the solution for the electronic Schrödinger equation:

$$H^{\mathrm{el}}(\mathbf{x}; \mathbf{X}) \Psi^{\mathrm{el}}_{\nu}(\mathbf{x}; \mathbf{X}) = E^{\mathrm{el}}_{\nu}(\mathbf{X}) \Psi^{\mathrm{el}}_{\nu}(\mathbf{x}; \mathbf{X}), \tag{2.10}$$

where

$$H^{\mathrm{el}}(\mathbf{x}; \mathbf{X}) = T^{\mathrm{el}}(\mathbf{x}) + V^{\mathrm{el-el}}(\mathbf{x}) + V^{\mathrm{el-ion}}(\mathbf{x}; \mathbf{X}) + V^{\mathrm{ion-ion}}(\mathbf{X}) \tag{2.11}$$

is the electronic Hamiltonian. $E^{\mathrm{el}}_{\nu}(\mathbf{X})$ denotes the Born-Oppenheimer surface corresponding to the electronic quantum number ν and stands for the eigenvalues of the electronic Hamiltonian.

$\Psi^{\mathrm{ion}}_{\nu\mu}(\mathbf{X})$ describes the wavefunction for the ions and is the solution of the ionic Schrödinger equation:

$$H^{\mathrm{ion}}_{\nu}(\mathbf{X}) \Psi^{\mathrm{ion}}_{\nu\mu}(\mathbf{X}) = E^{\mathrm{tot}}_{\nu\mu} \Psi^{\mathrm{ion}}_{\nu\mu}(\mathbf{X}), \tag{2.12}$$

where

$$H^{\mathrm{ion}}_{\nu}(\mathbf{X}) \equiv T^{\mathrm{ion}}(\mathbf{X}) + E^{\mathrm{el}}_{\nu}(\mathbf{X}) \tag{2.13}$$

is the ionic Hamiltonian and $E^{\mathrm{tot}}_{\nu\mu}$ stands for the total energy corresponding to the electronic quantum number ν and the ionic quantum number μ.

We now substitute the separation ansatz Eq. (2.9) into the many-body Schrödinger equation:

$$\begin{aligned} H(\mathbf{x}, \mathbf{X}) \Psi^{\mathrm{ion}}_{\nu\mu}(\mathbf{X}) \Psi^{\mathrm{el}}_{\nu}(\mathbf{x}; \mathbf{X}) &= E^{\mathrm{tot}}_{\upsilon\mu} \Psi^{\mathrm{ion}}_{\nu\mu}(\mathbf{X}) \Psi^{\mathrm{el}}_{\nu}(\mathbf{x}; \mathbf{X}) \\ &- \left(\sum_{I=1}^{N^{\mathrm{ion}}} \frac{1}{2M_I} (2 \frac{\partial \Psi^{\mathrm{ion}}_{\nu\mu}}{\partial \mathbf{X}_I} \frac{\partial \Psi^{\mathrm{el}}_{\nu}}{\partial \mathbf{X}_I} + \Psi^{\mathrm{ion}}_{\nu\mu} \frac{\partial^2 \Psi^{\mathrm{el}}_{\nu}}{\partial \mathbf{X}_I^2}) =: E^{\mathrm{ph-el}} \right) \\ &\approx E^{\mathrm{tot}}_{\upsilon\mu} \Psi^{\mathrm{ion}}_{\nu\mu}(\mathbf{X}) \Psi^{\mathrm{el}}_{\nu}(\mathbf{x}; \mathbf{X}). \end{aligned} \tag{2.14}$$

Eq. (2.14) shows that the separation ansatz is valid, if the so called *electron-phonon interaction* term $E^{\mathrm{ph-el}}$ is neglected (details e.g. in Ref. [60]). The BOA thus neglects the possibility that electronic transitions could occur as consequence of ionic displacements (first part of $E^{\mathrm{ph-el}}$) and it neglects the part of the kinetic energy of the electrons, which arises from their movement along the ionic trajectory (second part of $E^{\mathrm{ph-el}}$). As mentioned above, the BOA is justified by the fact that the atomic masses are much larger than the electron mass and hence both terms of $E^{\mathrm{ph-el}}$ are small compared to the kinetic energy of the electrons.

There are important physical mechanisms, in which electron-phonon interactions play a crucial role. Examples are the electrical resistivity in metals, the broadening of spectral lines in optical luminescence measurements, and the primary steps of photosynthesis in green plants, where optically excited electronic states couple to specific low frequency vibrations of the so-called light-harvesting protein complex.

The peptide chains we are dealing with in the present work are, however, characterized by a huge HOMO-LUMO gap of

$$\epsilon^{\mathrm{HOMO-LUMO}} > 4.5\,\mathrm{eV}, \tag{2.15}$$

which is more than two orders of magnitude higher than the thermal energy $k_B T$ at room temperature [51]. Thus, in the relevant temperature range, the excited electronic states of the peptide chain are not contributing to the thermodynamic properties. Hence, we focus exclusively on the electronic ground state in this study, which implies that we may rely on the BOA.

2.4 Density functional theory

The electronic ground state of the peptide chain for a given set of ionic positions $\mathbf{X}$ is characterized by its ground state wavefunction $\Psi_g^{\mathrm{el}}(\mathbf{X})$ and the corresponding eigenvalue $E_g^{\mathrm{el}}(\mathbf{X})$, which can be obtained by solving the electronic Schrödinger equation (SE) (Eq. (2.10)). Solving Eq. (2.10) exactly is possible via the *full configuration interaction* (full CI) approach, but numerically extremely expensive and therefore not practicable for extended poly-atomic systems. Nevertheless, nowadays several *ab-initio* methods exist, which allow to solve the electronic SE in an approximate but highly accurate way. Typically *post-Hartree-Fock* methods, such as the *(truncated) configuration interaction* (CI), the *(truncated) coupled cluster* (CC), the *Quantum Monte Carlo* (QMC) and the *Möller-Plesset perturbation* (MP) theory are the ab-initio methods, which offer the highest accuracy. However, the computational effort connected to these methods is still particularly high and shows high order polynomial scaling with system size: Second order MP scales with $\left(N^{\mathrm{el}}\right)^5$[61]. CC, if truncated after single, doublet and triplet interactions, scales with $\left(N^{\mathrm{el}}\right)^8$[62]. QMC and CI scale even exponentially with the system size (both in timing and storage). Thus the post-Hartree-Fock methods are limited to systems with a small total number of chemically active electrons $N^{\mathrm{el}} \leq O(100)$ [1]. The number of valence electrons in the peptide chains studied here exceeds this limit by an order of magnitude. Hence, an alternative to the post-Hartree-Fock methods is required for this project. *Density functional theory* (DFT) is such an alternative approach. It focuses on the electron density distribution $n(\mathbf{r})$ in 3-dimensional real space rather than on the

---

[1] We remark that approximated forms of the post-Hartree-Fock methods exist, which improve the scaling behavior: e.g. local approximations for the correlation interaction for MP (e.g. [61]) and CC (e.g. [62]) or the fixed node approximation for QMC (e.g. [63]). The first two references report even linear scaling with system size. However, it has not been sufficiently tested how these approximations limit the accuracy in describing the systems we are interested in.

many-body wavefunction in $3 \cdot N^{\mathrm{el}}$-dimensional electronic configuration space. Consequently, its computational effort scales better than the post-Hartree Fock methods – DFT scales with $\left(N^{\mathrm{el}}\right)^{\alpha}$, where $\alpha \approx 2-3$ (depending on the basis set).[2] DFT can definitely handle systems consisting of 1000 to 10000 electrons, thus it can also handle the peptide chain. In principle the *Kohn-Sham formalism*, which implies an efficient method of calculation for the ground state electron density and energy, accounts for all many-body effects on the basis of the exchange-correlation (XC) density functional $E^{\mathrm{xc}}[n]$. In order to make DFT applicable in real calculations, this XC functional has, however, to be approximated.

In this section, key concepts of DFT are presented, including the Hohenberg-Kohn theorem and the Kohn-Sham formalism. Furthermore, a justification for the employment of the specific XC functional which has been used in this project, the generalized gradient approximation in the Perdew-Burke-Ernzerhoff formulation (GGA-PBE) [65], is given.

For simplicity, we will in the remaining part of this section suppress the explicit coordinate dependence of the respective operators constituting the electronic Hamiltonian. The coulombic interaction of the electrons with the ions will be expressed through a fixed, external potential

$$V^{\mathrm{el-ion}}(\mathbf{x};\mathbf{X}) \rightarrow V^{\mathrm{ext}}(\mathbf{r}). \tag{2.16}$$

Furthermore, the ion-ion interaction term $V^{\mathrm{ion-ion}}$ will be suppressed, since it enters in the electronic Hamiltonian only as a constant. We will write the energy eigenvalue of the electronic Hamiltonian without $V^{\mathrm{ion-ion}}$ as E_g^{e}. The relation between the Born-Oppenheimer surface and this eigenvalue is

$$E_g^{\mathrm{el}}(\mathbf{X}) = E_g^{\mathrm{e}}(\mathbf{X}) + V^{\mathrm{ion-ion}}(\mathbf{X}). \tag{2.17}$$

2.4.1 Hohenberg-Kohn theorem

The Hohenberg-Kohn theorem (HKT) [41] constitutes the theoretical basis of the density functional theory. It consist of two lemmas. The first lemma (HKT I) states:

- The ground state density $n_g(\mathbf{r})$ of a bound system of interacting electrons in some external potential $V^{\mathrm{ext}}(\mathbf{r})$ determines this potential uniquely (up to an additive constant).

In other words, there are no two systems with a different external potential leading to the same ground state electron density. Therefore, $n_g(\mathbf{r})$ also uniquely determines the electronic Hamiltonian H^{e}, and with it the ground state energy E_g^{e} and the wavefunction Ψ_g^{el}. The second lemma (HKT II) states that:

- For a given external potential $V^{\mathrm{ext}}(\mathbf{r})$ the ground state electron density and energy may be determined from a variational principle:

$$E_g^{\mathrm{e}} \quad = \quad \langle \Psi_g | H^{\mathrm{e}} | \Psi_g \rangle \tag{2.18}$$

---

[2] A Wannier-like formulation even allows to obtain linear scaling [64].

$$\begin{aligned} &= \min_{\Psi} \left(\langle \Psi \left| H^{\mathrm{e}} \right| \Psi \rangle \right) && (2.19) \\ &= \min_{n} \left(\langle \Psi_g[n] \left| H^{\mathrm{e}} \right| \Psi_g[n] \rangle \right) && (2.20) \\ &= \min_{n} \left(E^{\mathrm{e}}[n] \right). && (2.21) \end{aligned}$$

This means that, for a particular external potential $V^{\mathrm{ext}}(\mathbf{r})$, the ground state electron density minimizes the functional $E^{\mathrm{e}}[n]$ with:

$$E^{\mathrm{e}}[n] \quad = \quad \langle \Psi_g[n] \left| H^{\mathrm{e}} \right| \Psi_g[n] \rangle . \tag{2.22}$$

Eqs. (2.18-2.20) perform, under consideration of the HKT I (in Eq. (2.19)), a change from the *Ritz-variational principle* (in Eq. (2.18)), which deals with the $3 \cdot N^{\mathrm{el}}$-dimensional wavefunction, to a corresponding more trivial variational principle for the 3-dimensional electron density (in Eq. (2.20)). As mentioned above, this transition leads to the fact that the computational effort of DFT is usually much lower than that of the wavefunction based post Hartree-Fock methods.

The energy functional in Eq. (2.21) may be written in the form:

$$E^{\mathrm{e}}[n] = \int d^3r V^{\mathrm{ext}}(\mathbf{r}) n(\mathbf{r}) + F[n]. \tag{2.23}$$

In this decomposition, the first term contains the interaction of the electrons with the external potential $V^{\mathrm{ext}}(\mathbf{r})$ and the second term, i.e.,

$$F[n] = \langle \Psi_g[n] \right| T^{\mathrm{el}} + V^{\mathrm{el-el}} \left| \Psi_g[n] \rangle \tag{2.24}$$

contains the kinetic energy and the electron-electron interaction. The functional $F[n]$ is *universal*, i.e., it does not depend on the external potential. Once it is known, it can be applied to all kinds of systems, to exactly determine their ground state properties. Nonetheless, although the HKT proves that $F[n]$ exists and also gives a clear definition of $F[n]$, it does not give any information about the form of $F[n]$. Consequently, for the application of DFT on realistic poly-atomic systems, $F[n]$ must be approximated.

We remark that the Hohenberg-Kohn theorem only addresses the electronic ground state and does not tackle excited electronic states. This is however, not limiting our project, since we are exclusively interested in the electronic ground state of the peptide chain, as already discussed in Sec. 2.3.

2.4.2 Kohn-Sham equations

While the Hohenberg-Kohn theorem constitutes the formal basis of DFT, the Kohn-Sham equations provide a practical and effective method to determine the ground state electron density and energy [42]. The explicit derivation of the Kohn-Sham equations is presented elsewhere (e.g. in Refs. [42, 60, 66]). Here we focus on introducing the essential equations. The Kohn-Sham equations are effective one-particle equations:

$$H^{\mathrm{KS}}\phi_\nu^{\mathrm{KS}}(\mathbf{r}) = \epsilon_\nu^{\mathrm{KS}}\phi_\nu^{\mathrm{KS}}(\mathbf{r}), \tag{2.25}$$

where H^{KS} denotes the Kohn-Sham operator, and $\epsilon_\nu^{\mathrm{KS}}$ and $\phi_\nu^{\mathrm{KS}}(\mathbf{r})$ denote the Kohn-Sham eigenvalues and eigenstates, respectively. The latter form an orthonormal system of one-particle orbitals:

$$\langle\phi_\nu^{\mathrm{KS}} \mid \phi_\mu^{\mathrm{KS}}\rangle = \delta_{\nu\mu}, \tag{2.26}$$

that describe a set of non-interacting pseudo-particles, the Kohn-Sham electrons.

The Kohn-Sham operator is given by:

$$H^{\mathrm{KS}} \;=\; -\frac{1}{2}\Delta + V^{\mathrm{ext}}(\mathbf{r}) + V^{\mathrm{H}}[n](\mathbf{r}) + V^{\mathrm{xc}}[n](\mathbf{r}). \tag{2.27}$$

It consists of the kinetic energy corresponding to the Kohn-Sham electrons and three potential terms, $V^{\mathrm{ext}}(\mathbf{r})$, $V^{\mathrm{H}}[n](\mathbf{r})$ and $V^{\mathrm{xc}}[n](\mathbf{r})$. The first potential term, $V^{\mathrm{ext}}(\mathbf{r})$, is the external potential due to interaction with the ion cores (Eq. (2.15)). The second potential term, $V^{\mathrm{H}}[n](\mathbf{r})$, is the *Hartree potential* and is defined as:

$$V^{\mathrm{H}}[n](\mathbf{r}) = \int d^3\mathbf{r}' \frac{n(\mathbf{r})}{\mid \mathbf{r}' - \mathbf{r} \mid}. \tag{2.28}$$

It is just the electrostatic potential due to the ground state electron density $n(\mathbf{r})$. The latter is determined by filling the Kohn-Sham orbitals with occupation numbers, f_i^{occ}, according to the Pauli-principle:

$$n(\mathbf{r}) = \sum_i f_i^{\mathrm{occ}} \mid \phi_i(\mathbf{r}) \mid^2 . \tag{2.29}$$

The third potential term in Eq. (2.26), the *exchange-correlation (XC) potential*, is defined as the functional derivative of the *exchange-correlation energy*:

$$V^{\mathrm{xc}}[n](r) := \frac{\delta E^{\mathrm{xc}}[n]}{\delta n}. \tag{2.30}$$

The XC energy itself is defined as the difference between the exact universal functional $F[n]$ and the sum of the kinetic energy $T^s[n]$ of the Kohn-Sham electrons and their Hartree energy $E^{\mathrm{H}}[n]$:

$$E^{\mathrm{xc}}[n] := F[n] - (T^{\mathrm{s}}[n] + E^{\mathrm{H}}[n]), \tag{2.31}$$

where

$$T^{\mathrm{s}}[n] = -\frac{1}{2}\sum_i f_i^{\mathrm{occ}} \int d^3\mathbf{r}\phi_i^{\mathrm{KS}*}(\mathbf{r})\Delta\phi_i^{\mathrm{KS}}(\mathbf{r}), \tag{2.32}$$

and

$$E^{\mathrm{H}}[n] = \frac{1}{2}\int d^3r n(\mathbf{r}) V^{\mathrm{H}}(\mathbf{r}). \tag{2.33}$$

Thus, the XC energy contains all quantum mechanical many-body corrections to the two quantities $T^{\mathrm{s}}[n]$ and $E^{\mathrm{H}}[n]$, and makes, by definition, the Kohn-Sham equations exact. Eq. (2.24) has to be solved self-consistently, since both the Hartree- and the XC-potential depend on the ground state electron density. Once $n(\mathbf{r})$ is obtained, the ground state energy can be calculated. Substituting Eq. (2.30) into Eq. (2.22) reveals:

$$E^{\mathrm{e}}[n] = T^{\mathrm{s}}[n] + \int d^3r V(\mathbf{r}) n(\mathbf{r}) + E^{\mathrm{H}}[n] + E^{\mathrm{xc}}[n]. \tag{2.34}$$

The XC energy gives, according to its absolute value, the smallest contribution to the total energy. However, its inclusion is mandatory for a correct treatment of the electronic system. The exact form of the XC functional is unknown, in the same way that the exact form of $F[n]$ (Eq. (2.23)) is unknown. According to Kohn, the practicality of DFT depends entirely on whether an approximation for $E^{\mathrm{xc}}[n]$ can be found, which is at the same time sufficiently simple and accurate [67]. Possibilities for such an approximation are discussed in the next section.

2.4.3 Exchange-correlation functional

To explain the terms *exchange* and *correlation* let us turn briefly to the *Hartree-Fock theory*, since the definitions of exchange and correlation stem from this theory. Hartree-Fock is based on an approximate ansatz for the many-body wavefunction Ψ^{el}. In this ansatz the wavefunction is considered to be a *Slater-determinant*, i.e., a product of one-particle orbitals, which is antisymmetric with respect to an exchange of any two electrons. Inserting this ansatz into the electronic SE results, similarly to the Kohn-Sham formalism, in a set of effective one-particle equations, the *Hartree-Fock equations* (see e.g. [60]).

Exchange energy

The *Hartree-Fock equations* can be understood as a (quantum-mechanical) correction to the *Hartree equations,* which by themselves arise from a separation ansatz for the many-body wavefunction and describe the electron-electron interaction exclusively by the Hartree potential. The according correction term is contained in a non-local operator, the so called *Fock-operator,* which contributes the *exchange energy* E^{x} to the ground state energy. Together with the contributions of the kinetic energy E^{T}, the external potential E^{V}, and of the Hartree potential E^{H}, the Hartree-Fock ground state energy may be written as:

$$E_g^{\mathrm{HF}}[\phi_1 ... \phi_{N^{\mathrm{el}}}] = E^{\mathrm{T}}[\phi_1 ... \phi_{N^{\mathrm{el}}}] + E^{\mathrm{V}}[\phi_1 ... \phi_{N^{\mathrm{el}}}] + E^{\mathrm{H}}[\phi_1 ... \phi_{N^{\mathrm{el}}}] + E^{\mathrm{x}}[\phi_1 ... \phi_{N^{\mathrm{el}}}]. \tag{2.35}$$

The exchange energy, $E^{\mathrm{x}}[\phi_1 ... \phi_{N^{\mathrm{el}}}]$, arises from the electrons with the same spin and is negative; it thus counteracts the positive Hartree energy that is due to the electrostatic repulsion of the electrons. It corrects for the *self interaction*, i.e., the electrostatic interaction of an electron with itself, which is (spuriously) contained in the Hartree energy. Furthermore, the exchange energy is largely responsible for chemical bonding, since it leads to the splitting of atomic valence orbitals into bonding and anti-bonding orbitals in chemical compounds.

Correlation energy

The Hartree-Fock equations are, by construction, exact as long as the many-body wavefunction can be described by a single Slater determinant. However, when the system contains more than one electron, a single Slater determinant is in general insufficient for describing the wavefunction. Instead, the true ground state has to be described by a linear combination of Slater determinants, which contain excited one-electron states ϕ_i. The difference between the Hartree-Fock ground state energy and the true ground state energy is defined as the *correlation energy* E^{c}:

$$E^{\mathrm{c}} := E_g^{\mathrm{HF}} - E_g^{\mathrm{exact}}. \tag{2.36}$$

Electronic correlation is a pure quantum mechanical effect and arises due to the spatial position of electrons with opposite spin. The electronic system may lower the Coulomb repulsion of these electrons by optimizing the phase correlation of these electrons as contained within the many-body wavefunction. Post Hartree-Fock methods aim to improve the Hartree-Fock method by including electronic correlation effects. Usually these methods give very accurate results, but for the price of a very high computational effort, as has been already mentioned in the introduction of this chapter.

Treatment of exchange and correlation in DFT

In the Kohn-Sham equations the exchange and correlation interactions enter via a *local* potential, the exchange-correlation potential:

$$V^{\mathrm{xc}}[n](\mathbf{r}) = V^{\mathrm{x}}[n](\mathbf{r}) + V^{\mathrm{c}}[n](\mathbf{r}). \tag{2.37}$$

This is fundamentally different from Hartree-Fock and post-Hartree-Fock methods, in which both, exchange and correlation, are treated as *non-local*, integrated quantities of the wavefunction. A further important difference between the two approaches is that, in its “traditional” form, DFT contains an approximation for both, correlation and exchange, whereas post-Hartree Fock methods are based on an exact treatment of exchange and approximate only the correlation. Recently, DFT methods have also been developed, which include the exact exchange as a local potential that can be combined with approximations for the correlation either from “traditional” DFT or from even more accurate methods, such as the GW approach (see Ref. [68] and references therein). However, these methods are still computationally too demanding to be applicable to systems containing hundreds of electrons, as a peptide chain. Therefore the “traditional” DFT has been applied in this project.

Quasi-local expansion

A very effective approximation for the XC functional results from the so-called quasi-local expansion of the XC hole. The quasi-local expansion is formally based on the following exact expression for the XC functional:

$$E^{\mathrm{xc}} = -\frac{1}{2}\int d^3r \frac{n(\mathbf{r})}{R^{\mathrm{xc}}[n](\mathbf{r})}, \tag{2.38}$$

where $R^{\mathrm{xc}}[n](\mathbf{r})$ is the *effective reach of the average*[3] *XC hole* $\overline{n}^{\mathrm{xc}}[n](\mathbf{r},\mathbf{r}')$:

$$[R^{\mathrm{xc}}[n](\mathbf{r})]^{-1} = -\int d^3r' \frac{\overline{n}^{\mathrm{xc}}[n](\mathbf{r},\mathbf{r}')}{\mid \mathbf{r}-\mathbf{r}' \mid}. \tag{2.39}$$

Within the quasi-local expansion it is assumed that $[R^{\mathrm{xc}}[n](\mathbf{r})]^{-1}$ is a “short-sighted” functional of $n(\mathbf{r})$. This means that the effective reach at a certain point in space, $\mathbf{r}$, depends on the electron densities at $\mathbf{r}$ and in the neighborhood of $\mathbf{r}$, but not on the densities far away from $\mathbf{r}$. In other words, $[R^{\mathrm{xc}}[n](\mathbf{r})]^{-1}$ may be approximated by performing respective Taylor expansions of the electron density at $\mathbf{r}$ and expressing $[R^{\mathrm{xc}}[n](\mathbf{r})]^{-1}$ as a function, f^{xc}, of the according expansion coefficients:

$$[R^{\mathrm{xc}}[n](\mathbf{r})]^{-1} = f^{\mathrm{xc}}\left(n(\mathbf{r}') \mid_{\mathbf{r}'=\mathbf{r}}, \frac{\partial}{\partial r_i'} n(\mathbf{r}') \mid_{\mathbf{r}'=\mathbf{r}}, \frac{\partial^2}{\partial r_i \partial r_j} n(\mathbf{r}') \mid_{\mathbf{r}'=\mathbf{r}}, \ldots \right). \tag{2.40}$$

Through ordering of these coefficients and consideration of the scalar nature of both, XC hole and effective reach, one obtains the quasi-local expansion of the XC functional. Truncating after the zeroth-order Taylor coefficient for the charge density gives the local density approximation (LDA) [63, 69]:

$$E^{\mathrm{xc}}_{\mathrm{LDA}} = E^{\mathrm{xc}}_0 = \int d^3r\, f^{\mathrm{xc}}_{\mathrm{LDA}}\left(n(\mathbf{r})\right) n(\mathbf{r}). \tag{2.41}$$

LDA is the most simple and rudimentary approximation for the XC functional. Nevertheless, it has been shown in many studies that LDA performs surprisingly well in predicting the ground state properties related to chemical bonds: Ionization energies, dissociation energies of molecules and cohesive energies of solids are predicted with an error which is usually 10-20 % and bond lengths are even accurate within an error of $\approx 1\%$ [67]. For applications in the field of biological physics, however, the LDA functional is not adequate, since these systems demand a higher accuracy than can be guaranteed by LDA. In particular for the description of hydrogen bonds the LDA functional is improper, as it strongly overestimates hydrogen bond strengths [70, 71]. Therefore, we have to drive the quasi-local expansion to a higher order.

Truncating after first order is called *generalized gradient approximation* (GGA):

$$E^{\mathrm{xc}}_{\mathrm{GGA}} = E^{\mathrm{xc}}_1 = \int d^3r\, f^{\mathrm{xc}}_{\mathrm{GGA}}\left(n(\mathbf{r}), \mid \nabla n(\mathbf{r}) \mid\right) n(\mathbf{r}). \tag{2.42}$$

Functionals in which the quasi-local expansion include the second order are called *meta*-GGA’s. According to Ref. [72], however, meta-GGA’s also contain, in addition to the Laplacian of the charge density $\nabla^2 n(\mathbf{r})$, orbital dependence information in the form of the kinetic energy density

---

[3] The average XC hole is the average over the physical XC holes, which stem from an interpolation between the physical Hamiltonian and the XC Hamiltonian, see e.g. Ref. [67].

$\tau(\mathbf{r}) = \frac{1}{2}\sum_i^{occ} |\nabla\varphi_i(\mathbf{r})|^2$ (which stems from a fourth order expansion in the exchange):

$$E^{\mathrm{xc}}_{\mathrm{MGGA}} = \int d^3r\, f^{\mathrm{xc}}_{\mathrm{MGGA}}\left(n(\mathbf{r}), \mid \nabla n(\mathbf{r}) \mid, \nabla^2 n(\mathbf{r}), \tau(\mathbf{r})\right) n(\mathbf{r}). \tag{2.43}$$

Both, GGA and meta-GGA, are not unique, but represent, due to the freedom in the parametrization of f^{xc}, a whole class of functionals. Each of these two classes can be (roughly) decomposed into two sub-classes, which correspond to two different (partially contradictory) philosophies or "flavors" of DFT: on the one hand the so called "ab-initio" functionals and on the other hand the "empirical" and "semi-empirical" functionals.

The parameters of semi-empirical and empirical functionals are determined from fitting procedures to either exact data available for simple systems like the rare gas atoms in the case of semi-empirical functionals or even by fitting to a large set of experimental chemical data in the case of empirical functionals. Examples are the Becke-Lee-Yang-Parr (BLYP) functional [73, 74], the empirical-density-functional-1 (EDF1) [75] and the empirical-density-functional-2 (EDF2) [76] for GGA and VSXC [77] for MGGA.

In contrast, ab-initio functionals are constructed to satisfy a set of key properties of the exact exchange-correlation hole rather than to fit molecular target data. Through this disengagement from any specific system one attempts to obtain a maximum possible transferability/universality of the XC functionals. Examples of ab-initio functionals are the Perdew-Wang 91 (PW91) [78, 79] and the Perdew-Burke-Ernzerhoff (PBE) [65] functional for GGA and the PKZB [80] and the KCIS [81] functional for meta-GGA.

GGA/MGGA performance in predicting chemical bonding and hydrogen bonding

In general GGA and meta-GGA's achieve, albeit if they are of the ab-initio or the empirical type, a significant improvement in the description of molecular properties with respect to LDA: The error for molecular atomization energies is typically three to five times smaller [67, 82, 83], and also energy barriers and structural energy differences are improved [84, 85]. Further, it is known that GGA's predict too large bond lengths and too soft bonds, an effect that sometimes corrects and sometimes over-corrects the LDA prediction [65].

The description of hydrogen bonding is also improved with respect to LDA by using GGA [70, 71] and meta-GGA (see Ref. [86] and references therein). However, the accuracy is still not perfect and depends on the type of hydrogen bonds to be described, as will be discussed in more detail further below. There exists also a considerably large difference in the accuracy between the various functionals. For example, the BLYP functional and the B3LYP hybrid functional, both functionals of the semi-empirical type, are known to underestimate hydrogen bond strengths by 10%-50% [87]. The pure ab-initio GGA functionals PW91 and PBE perform much better with errors typically in the range of 5%-20% [44, 87].[4]

---

[4] The percentages reported here might not solely be due to the functionals, since also the basis set is an issue for the accurate estimation of hydrogen bond strengths. However, we remark that great care has been taken in the two studies cited above to reduce the basis set error.

Choice for this project: the PBE functional

To perform our calculations on the peptide chain we have decided to not use a meta-GGA functional, since they are computationally too demanding for the purposes of this project. Instead we have implemented the Perdew-Burke-Ernzerhof (PBE) functional [65] and employed it exclusively throughout the entire project. PBE is a widespread functional of the pure "ab-initio" GGA-type: All of its parameters have been obtained by fitting to properties of the exchange-correlation hole, none by fitting to experimental data. It is a derivate of the PW91 functional [78, 79]. Both, PW91 and PBE give very similar results and are similarly well performing in describing hydrogen bonds (as mentioned above), but PBE has a much simpler functional form. Indeed it has been designed as a simplification of the PW91 functional: In contrast to the PW91 functional, which is designed to satisfy as many exact conditions as possible, PBE satisfies only those which are energetically significant.

The explicit formulas for the PBE functional are presented in the Appendix (Sec. 6.2.1).

GGA performance in predicting van-der-Waals bonding

One of the main deficiencies of the standard DFT and thus also of the PBE functional is that it does not properly take into account for van-der-Waals (vdW) interactions. This becomes clear when considering the quasi-local form of the functional on the one side (Eq. (2.41)) and the non-local character of the vdW interaction on the other side (Sec. 1.4). In order to properly take into account the vdW interaction, a XC functional must be able to correlate the electron densities at two different points $\mathbf{r}$ and $\mathbf{r}'$ with each other, where $\mathbf{r}$ and $\mathbf{r}'$ can be separated by several Angstroms. This cannot be achieved by any GGA functionals. None of them is therefore suitable to deal with systems which are predominantly stabilized by van-der-Waals interactions.

How accurately does DFT-GGA describe the secondary structure?

The accuracy of DFT-GGA in describing the secondary structure of proteins is still a matter of debate in the literature. The question is connected to another question, namely: How important are van-der-Waals interactions and other interactions which are not correctly treated within DFT-GGA, for the stability of the secondary structure?

To answer this question, Wu&Yang have examined the DFT functionals BLYP, B3LYP, PW91 and BPW91 to study the stability of finite poly-L-alanine helices [88]. They found that, compared with the α-helix, the 3_{10}-helix is spuriously favored in these peptides by the DFT functionals compared to the (assumed) more accurate MP2[5] results. A similar "preference" of the 3_{10}-helix was found in an earlier work by Improta et al., in which DFT-GGA calculations on an infinite poly-glycine chain were performed [89]. Wu&Yang report that the employment of an empirical vdW correction improves the agreement of DFT-GGA with the MP2 calculations. They interpret these findings as an indication for stronger vdW interactions in the closer packed α-helix. These stronger vdW interactions favor, according to their interpretation, the α-helix conformation in long-chain peptides. These calculations were performed with a relatively small localized basis set. However, it is known

---

[5] Abbreviation for 2^{nd}-order Möller-Plesset perturbation theory.

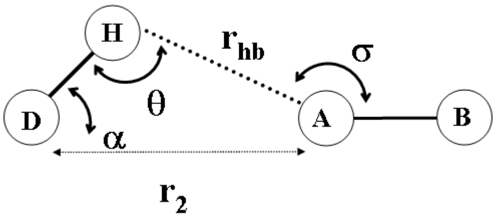

Figure 2.1: Parameters for describing the hydrogen bond geometry according to Ref. [44].

that hydrogen bond energetics are strongly basis set dependent [87]. It is interesting to note in this context that a calculation on the corresponding system in a *converged* plane wave basis reveals that the poly-glycine α-helix is actually lower in energy than the 3_{10}-helix (Sec. 1.5). It is thus possible that the results and interpretations of Refs. [88, 89] might be biased by the basis set, in the sense that the spurious over-stabilization of the 3_{10}-helix with respect to the α-helix, as has been reported in these studies, is mainly an effect of the basis set rather than of a sizable contribution from vdW forces, which are not properly treated within DFT-GGA, specifically within DFT-PBE. Consequently, the importance of van-der-Waals interactions may be smaller than reported in these studies.

The employment of a plane waves basis allows to completely rule out any error arising from the basis set (as will be discussed more in detail in Chap. 3) and to separate the error which is solely due to the XC functional. Recently, Ireta et al. have employed the plane waves approach to investigate the error "purely" due to the XC functional [44]. They compared hydrogen bond strengths and geometry parameters for a set of representative hydrogen bonded dimers as calculated within DFT-PBE, with those results of the most accurate MP2 and CC values reported in literature and uncovered an important correlation between the accuracy of DFT for describing hydrogen bonds and the directionality of the hydrogen bonds: They found that, the more the hydrogen bond geometry deviates from linearity, the larger is the DFT error. More precisely, the error of DFT-PBE in predicting hydrogen bond strengths is smaller than 1 kcal/mol as long as the bending angle Θ (Fig. 2.1) is smaller than 130°, but can be as much as 1.5 kcal/mol for strongly bent hydrogen bonds. This trend is assumed to be related to the fact that for highly bent hydrogen bonds the permanent electrostatic interactions, such as charge-dipole and dipole-dipole interactions, are less prominent than in a linear conformation. This effect reduces the total hb strength and makes the van-der-Waals interaction a more relevant contribution [44].

The hydrogen bonds in the helical conformations of the peptide chains are, however, almost linear [50], thus we expect the DFT-PBE error in predicting the hydrogen bond strengths in these systems to be smaller than 1 kcal/mol per peptide unit.

2.5 Free energy surface

The density functional theory allows to determine the electronic ground state energy for a given atomic configuration. In other words, it allows to determine the potential which the atoms (ions) of the peptide chain experience, i.e., the Born-Oppenheimer surface. By means of a suitable geometry optimization algorithm (Sec. 3.3) it is, furthermore, possible to identify the equilibrium conformations of the peptide chain, which correspond to the local minima of the Born-Oppenheimer surface. The potential energy at these local minima may be used as basis for a *static* stability analysis of the peptide chain. Such static stability analysis has has been discussed in Sec. 1.5.

The next crucial step is to analyze the *dynamical properties* of the peptide chain and to perform the transition from a static stability analysis to a *thermodynamic stability analysis,* which invokes also distortions from the equilibrium structures, i.e., to investigate the Born-Oppenheimer surface in the vicinity of the local minima. In the following we briefly introduce the basic concepts of thermodynamics and then apply these concepts to calculate the corresponding free energy surface. Based on the free energy surface we will then derive expressions to define the thermodynamic phase stability of the various conformations of the peptide chain.

2.5.1 Energy and entropy

We now consider the ions of the peptide chain to be not at rest but rather undergoing vibrations and movements. To model a realistic situation we consider the system to be in thermal contact with a large heat reservoir of temperature T. Under these macroscopic conditions the microscopic state of the system is not well defined, but is, due to the heat exchange with the reservoir, subject to certain thermal fluctuations. Indeed the thermodynamic state of the system is given by a whole ensemble of microscopic states $\{|n\rangle\}$, each weighted with a certain probability, given by its Boltzmann-factor*:*

$$P_n = \frac{1}{Z}\exp(-\beta E_n), \tag{2.44}$$

where $\beta = (k_{\mathrm{B}}T)^{-1}$ is the reciprocal temperature, k_{B} is the Boltzmann constant, E_n denotes the energy of the state $\mid n\rangle$, and

$$Z = \sum_n \exp(-\beta E_n) \tag{2.45}$$

is called the canonical partition function. The impact of pressure may be neglected for this project, since we are rather interested on the stability at normal conditions (atmospheric pressure) than in the high pressure regime. Thus we may set the pressure $p = 0$. The thermodynamic state of the system is then characterized by its Helmholtz free energy:

$$F := -k_{\mathrm{B}}T\ln Z = U - TS. \tag{2.46}$$

The laws of thermodynamics state that the system is in thermal equilibrium when F is minimal:

$$F \to min. \tag{2.47}$$

This implies that any spontaneous change in the thermodynamic state of the system is accompanied by a reduction of F, i.e.,

$$dF \leqslant 0. \tag{2.48}$$

All thermodynamic equilibrium properties are connected to that thermodynamic state, which fulfills Eq. (2.46). Further, all thermodynamic equilibrium properties may be expressed through the corresponding partition function Z. The partition function is the central quantity, which connects the quantum mechanical eigenspectrum E_n to the thermodynamic (macroscopic) state.

In Eq. (2.45), U denotes the internal energy and S denotes the entropy. The internal energy is the thermodynamic ensemble average of the total energy:

$$U = \langle E_n \rangle = \sum_n P_n E_n = k_{\mathrm{B}} T^2 \frac{\partial \ln Z}{\partial T} = -\frac{\partial \ln Z}{\partial \beta}. \tag{2.49}$$

The entropy represents the number of possible eigenstates of the motif commensurable with its thermodynamic state:

$$S = -\sum_n P_n \ln P_n = -\left(\frac{\partial F}{\partial T}\right)_{V,N} = k_{\mathrm{B}} \frac{\partial}{\partial T} (T \ln Z) \tag{2.50}$$

and it is thus a measure of the disorder in the microscopic state. The broader the probability distribution P_n is, the larger is the entropy.

2.5.2 Helical parameters as reaction coordinates

To exactly determine the thermodynamic state of the peptide chain, we would have to sample the full phase space corresponding to an infinite number of degrees of freedom, which is in practice not possible. Thus, to reduce the dimensionality of the problem and to perform a physically meaningful partitioning of the configurational space, we introduce a set of reaction coordinates as external constraints to the thermodynamic analysis. We choose here the helical parameters L and Θ as reaction coordinates, since these two parameters are most relevant for a characterization of the various conformations and the mechanical deformations of the peptide chain (Secs. 1.5 and 4.4).

In other words, we introduce the two helical parameters L and Θ as additional *macroscopic* thermodynamic observables, such that

$$F(T) \rightarrow F(T, L, \Theta). \tag{2.51}$$

The right hand side of expression (2.50) denotes the *free energy surface* of the peptide chain spanned by the helical parameters. By introducing the helical parameters as *macroscopic* thermodynamic observables, we put a constraint on them. This does *not* mean that the *microscopic* parameters Θ_i and L_i corresponding to the individual peptide units are fixed. Only the corresponding average values over the entire chain are fixed – the microscopic parameters may fluctuate about these average values. In this terms $F(T, L, \Theta)$ is defined as the free energy of the part of the complete thermodynamic ensemble commensurable with the average values L and Θ at a given temperature:

$$F(T, L, \Theta) \quad = \quad -k_{\mathrm{B}}T \, \ln Z(T, L, \Theta), \tag{2.52}$$

where

$$Z(T, L, \Theta) \quad = \quad \sum_n \exp\left\{-\beta E_n(L, \Theta)\right\}. \tag{2.53}$$

In order to fulfill Eq. (2.46) a necessary condition is:

$$dF = 0. \tag{2.54}$$

In terms of L and Θ, the total differential of Eq. (2.53) may be written as:

$$dF \quad = \quad \frac{\partial F}{\partial L} dL + \frac{\partial F}{\partial \Theta} d\Theta = 0, \tag{2.55}$$

and we obtain by a comparison of the coefficients the two equations of state:

$$0 = \frac{\partial F}{\partial \Theta} \text{ and } 0 = \frac{\partial F}{\partial L}. \tag{2.56}$$

In general, Eq. (2.55) does not uniquely define the thermodynamic state of the system, since the free energy surface contains several minima. We identify the ensembles corresponding to the various minima of the free energy surface with the possible *thermodynamic phases* that the system may adopt.

To determine, whether a phase A of the peptide chain is *stable* with respect to another phase B, we calculate the *Helmholtz free energy of formation* per peptide unit of the phase A out of the phase B:

$$\Delta F^{\mathrm{f}}{}_{\mathrm{A}\to\mathrm{B}}(T) := \frac{F(T, L_A, \Theta_A)}{N_A} - \frac{F(T, L_B, \Theta_B)}{N_B}. \tag{2.57}$$

Here, L_X and Θ_X denote the minimum of the free energy surface corresponding to the conformation X and N_X denotes the number of peptides. In thermodynamic equilibrium the phase A is *stable* with respect to a phase B, if $\Delta F^{\mathrm{f}}{}_{\mathrm{A}\to\mathrm{B}}$ is negative. The term “stable” does, however, not necessarily imply that the whole peptide chain consists of a single phase. In fact, at elevated temperatures it is possible that several phases may coexist. This possibility has important consequences for the thermodynamic equilibrium of the peptide chain. We will discuss this issue in Sec. 2.8. However, before that, we will in the next two sections explain, how the free energy corresponding to the pure phases is determined.

2.6 Vibrational dynamics

In order to determine the free energy of the thermodynamic phase corresponding to a given conformation X of the peptide chain, we have to calculate the partition function $Z(T, L_X, \Theta_X)$ determined in Eq. (2.52). In this section we derive this quantity by applying the harmonic approximation (Secs. 2.6.2-2.6.5). After that we evaluate corrections to the harmonic approximation: At first by means of the quasi-harmonic approximation, which allows already to account for some basic anharmonic effects, such as the thermal expansion (Sec. 2.6.6). Then by means of the thermodynamic integration method, which allows to fully take into account the complete anharmonicity (Sec. 2.7).[6]

2.6.1 Partition function of a thermodynamic phase

The partition function of the thermodynamic phase corresponding to a conformation X of the peptide chain is determined by the energy eigenspectrum $E_n(L_X, \Theta_X)$. If we apply the Born-Oppenheimer approximation and if the system is always in its electronic groundstate (both these approximations are well justified, as has been discussed in Sec. 2.3) the eigenspectrum of the peptide chain is confined to the vibrational levels corresponding to the electronic ground state:

$$E_n(L_X, \Theta_X) = E_g^{\mathrm{el}}(L_X, \Theta_X) + E_{g\mu}^{\mathrm{ion}}(L_X, \Theta_X) \qquad n \to g\mu, \quad \mu = 1 \ldots \infty. \tag{2.58}$$

Here, g denotes the electronic ground state; for convenience we will suppress this index in the following. The quantum number μ labels the vibrational eigenstates of the peptide chain. Using the above expression we obtain for the partition function:

$$\begin{aligned} Z(T, L_X, \Theta_X) &= \sum_\mu \exp\left\{-\beta\left(E^{\mathrm{el}}(L_X, \Theta_X) + E_\mu^{\mathrm{ion}}(L_X, \Theta_X)\right)\right\} && (2.59) \\ &= \exp\left\{-\beta E^{\mathrm{el}}(L_X, \Theta_X)\right\} \sum_\mu \exp\left\{-\beta E_\mu^{\mathrm{ion}}(L_X, \Theta_X)\right\} && (2.60) \\ &= Z^{\mathrm{el}}(L_X, \Theta_X) Z^{\mathrm{vib}}(T, L_X, \Theta_X). && (2.61) \end{aligned}$$

The partition function thus factorizes into the electronic partition function $Z^{\mathrm{el}}(L_X, \Theta_X)$ and the vibrational partition function $Z^{\mathrm{vib}}(T, L_X, \Theta_X)$. Substituting Eq. (2.60) into Eq. (2.45) reveals the corresponding separation of the free energy:

$$\begin{aligned} F(T, L_X, \Theta_X) &= -k_{\mathrm{B}} T \ln\left(Z^{\mathrm{el}}(T, L_X, \Theta_X) Z^{\mathrm{vib}}(T, L_X, \Theta_X)\right) && (2.62) \\ &= E^{\mathrm{el}}(L_X, \Theta_X) + F^{\mathrm{vib}}(T, L_X, \Theta_X), && (2.63) \end{aligned}$$

where $F^{\mathrm{vib}}(T, L_X, \Theta_X)$ denotes the free energy corresponding to the vibrational degrees of freedom. Since the peptide chain remains in its electronic groundstate (Sec. 2.3), the electronic entropy is

---

[6] We remark, however, that the thermodynamic integration avoids a direct evaluation of the partition function, as will be discussed in Sec. 2.7.

zero and the electronic free energy is temperature independent:

$$F^{\mathrm{el}}(T, L_X, \Theta_X) = E^{\mathrm{el}}(L_X, \Theta_X). \tag{2.64}$$

In the following, we will describe, how the temperature dependence, i.e., the vibrational part of the free energy can be obtained.

2.6.2 Harmonic approximation

In the harmonic approximation the ions are assumed to perform small oscillations around their static equilibrium positions. Hence, they experience a strictly harmonic potential, like a perfect mathematical pendulum. To derive the harmonic approximation, we introduce mass-weighted, relative coordinates $\mathbf{Y}$ with:

$$Y_i = (X_i - X_{0i})/\sqrt{M_i}, \tag{2.65}$$

where the X_{0i} are the equilibrium coordinates of the peptide chain corresponding to the helical equilibrium parameters L_X^0 and Θ_X^0, and the M_i are the ionic masses. We then write the Born-Oppenheimer surface, which is the potential of the ionic Hamiltonian (Eq. (2.13)), as a Taylor expansion:

$$\begin{aligned} E^{\mathrm{el}}(\mathbf{Y}) &= E^{\mathrm{el}}(L_X^0, \Theta_X^0) \\ &+ \sum_i \frac{\partial}{\partial Y_i} E^{\mathrm{el}} \bigg|_{L_X^0, \Theta_X^0} Y_i \ (\equiv 0) \\ &+ \frac{1}{2} \sum_{i,j} \frac{\partial^2}{\partial Y_i \partial Y_j} E^{\mathrm{el}} \bigg|_{L_X^0, \Theta_X^0} Y_i Y_j \\ &+ \ldots. \end{aligned} \tag{2.66}$$

Breaking this expansion after the third, i.e., the *harmonic,* term yields

$$E^{\mathrm{el}}(Y) \approx E^{\mathrm{el}}(L_X^0, \Theta_X^0) + \frac{1}{2} \sum_{i,j} \frac{\partial^2}{\partial Y_i \partial Y_j} E^{\mathrm{el}} \bigg|_{L_X^0, \Theta_X^0} Y_i Y_j. \tag{2.67}$$

Substituting this into Eq. (2.13) yields[7]

$$H^{\mathrm{ion}} \approx E^{\mathrm{el}}(L_X^0, \Theta_X^0) + H^{\mathrm{vib}}. \tag{2.68}$$

Here $E^{\mathrm{el}}(L_X^0, \Theta_X^0)$ is a constant value, which shifts the eigenvalues of the ionic Hamiltonian, but does not explicitly enter the solution of the ionic SE. It corresponds to the (free) energy of the electronic system (Eq. (2.63)) , or, in other words, denotes the static contributions to the free energy (Eq. (1.1)). H^{vib} is the *vibrational Hamiltonian in harmonic approximation* and is given by:

$$H^{\mathrm{vib}} = \frac{1}{2} \dot{\mathbf{Y}}^{\mathrm{T}} \dot{\mathbf{Y}} + U^{\mathrm{harm}}. \tag{2.69}$$

---

[7] For convenience the explicit dependence of H^{vib} and H^{ion} on L_X and Θ_X will be suppressed in the following.

Here U^{harm} is the *harmonic potential*

$$U^{\mathrm{harm}} = \frac{1}{2}\mathbf{Y}^{\mathrm{T}} \cdot \mathbf{D} \cdot \mathbf{Y}, \tag{2.70}$$

$\mathbf{D}$ is the *dynamical matrix*

$$\mathbf{D} = \left.\frac{\partial^2 E^{\mathrm{el}}}{\partial Y_i \partial Y_j}\right|_{L_X^0, \Theta_X^0}, \tag{2.71}$$

and $\dot{\mathbf{Y}}$ contains the ionic momenta.

Eq. (2.68) describes coupled harmonic oscillations of the $3N^{\mathrm{ion}}$ ionic degrees of freedom. To decouple these oscillations and to solve the ionic SE, we have to diagonalize the dynamical matrix by solving the eigenvalue equation:

$$\mathbf{D} \cdot \mathbf{L} = \mathbf{\Lambda} \cdot \mathbf{L} \qquad \mathbf{\Lambda}_{ij} = \omega_i^2 \delta_{ij}. \tag{2.72}$$

Here, the ω_i^2 are the eigenvalues of $\mathbf{D}$, where ω_i are the eigenfrequencies, and $\mathbf{L}$ is a $(3N^{\mathrm{ion}} \times 3N^{\mathrm{ion}})$-dimensional matrix containing the eigenvectors of $\mathbf{D}$ as columns. Applying the unitary transformation $\mathbf{L}^{-1} = \mathbf{L}^{\top}$ on coordinates and momenta leads to so called *normal coordinates* $\mathbf{Q}$:

$$\mathbf{Q} = \mathbf{L}^{-1} \cdot \mathbf{Y} \tag{2.73}$$

with the conjugated momenta:

$$\mathbf{P}_q = \mathbf{L}^{-1} \cdot \dot{\mathbf{Y}}. \tag{2.74}$$

In terms of these new coordinates, the vibrational Hamiltonian is:

$$H^{\mathrm{vib}} = \frac{1}{2}\mathbf{P}_q^T \cdot \mathbf{P}_q + \frac{1}{2}\mathbf{Q}^T \cdot \mathbf{\Lambda} \cdot \mathbf{Q} \tag{2.75}$$

and may, since Λ is a diagonal matrix, be understood as a sum of 3N decoupled, independent Hamiltonians:

$$H^{\mathrm{vib}} = \sum_{i=1}^{3N^{\mathrm{ion}}} H_i^{\mathrm{vib}}, \tag{2.76}$$

where

$$H_i^{\mathrm{vib}} = \frac{1}{2}\left(\frac{\partial}{\partial q_i}\right)^2 + \frac{1}{2}\omega_i^2 q_i^2, \tag{2.77}$$

Each of these $3N^{\mathrm{ion}}$ Eqs. (2.76) can be solved independently from the others, with the well known harmonic oscillator approach:

$$H_i^{\mathrm{vib}} \phi_{ij}^{\mathrm{vib}} = E_{ij}^{\mathrm{vib}} \phi_{ij}^{\mathrm{vib}}, \tag{2.78}$$

where the eigenvalues are given by[8]:

$$E_{ij}^{\text{vib}} = \omega_i (j + \frac{1}{2}) \quad j = 0 \ldots \infty. \tag{2.81}$$

2.6.3 Bloch formalism

To solve the equations of motion we do *not* directly diagonalize that dynamical matrix as denoted in Eq. (2.70), since this is impracticable with respect to the infinite number of ionic degrees of freedom of the peptide chain (Sec. 2.1). Instead, we employ the fact that the peptide chain is a periodic repetition of identical peptide units and apply *Bloch's theorem* to map the dynamical matrix from the real space to the reciprocal space, as will be shown below. Then we obtain the corresponding symmetry reduced, phase dependent dynamical matrix $\mathbf{D}(\varphi)$, which is of finite dimensions ($3N^{\text{APP}} \times 3N^{\text{APP}}$), where N^{APP} denotes the number of atoms per peptide unit. Before performing this mapping we have to transform the ionic Hamiltonian from the Cartesian coordinate system to a set of suitable helix symmetry coordinates. We choose cylindrical coordinates as our helix symmetry coordinates and rewrite the vibrational Hamiltonian:

$$H^{\text{vib}} = \frac{1}{2} \mathbf{P}^{cT} \cdot \mathbf{P}^{c} + \frac{1}{2} \mathbf{Y}^{c\text{T}} \cdot \mathbf{F}^{\text{c}} \cdot \mathbf{Y}^{c}, \tag{2.82}$$

where

$$\mathbf{Y} = \{ ..., (x_I, y_I, z_I), ... \} \rightarrow \mathbf{Y}^c = \{ ..., (r_I, \Theta_I, z_I), ... \}, \tag{2.83}$$

$$\mathbf{P} = \left\{ ..., \left(\frac{\partial}{\partial x_I}, \frac{\partial}{\partial y_I}, \frac{\partial}{\partial z_I} \right), ... \right\} \rightarrow \mathbf{P}^c = \left\{ ..., \left(\frac{\partial}{\partial r_I}, r_I \frac{\partial}{\partial \Theta_I}, \frac{\partial}{\partial z_I} \right), ... \right\}, \tag{2.84}$$

and $\mathbf{F}^{\text{c}}$ is the mass-weighted force constant matrix in cylindrical coordinates

$$\mathbf{F}_{IJ}^{\text{c}} = \begin{pmatrix} \frac{\partial^2 E}{\partial r_I \partial r_J} & \frac{\partial^2 E}{\partial \Theta_I \partial r_J} & \frac{\partial^2 E}{\partial z_I \partial r_J} \\ \frac{\partial^2 E}{\partial r_I \partial \Theta_J} & \frac{\partial^2 E}{\partial \Theta_I \partial \Theta_J} & \frac{\partial^2 E}{\partial z_I \partial \Theta_J} \\ \frac{\partial^2 E}{\partial r_I \partial z_J} & \frac{\partial^2 E}{\partial \Theta_I \partial z_J} & \frac{\partial^2 E}{\partial z_I \partial z_J} \end{pmatrix}. \tag{2.85}$$

Eq. (2.81) can, like Eq. (2.71), be solved by diagonalizing the *dynamical matrix in cylindrical coordinates*:

$$\mathbf{D}^{\text{c}} = \mathbf{G}^{c} \mathbf{F}^{c} \mathbf{G}^{c}, \tag{2.86}$$

---

[8] The corresponding eigenfunctions are given by:

$$\phi_j^{\text{vib}}(y_i) = \left(\frac{\omega_i}{\pi} \right)^{1/4} \frac{1}{\sqrt{n! 2^n}} \exp \left(-\frac{1}{2} \xi_i^2 \right) H_j(\xi_i), \tag{2.79}$$

where $\xi_j = \sqrt{\omega_j} y_j$ and the H_j are the *Hermite Polynomials*:

$$H_j(\xi_i) = (-1)^{æ} \exp(\xi_i^2) \frac{\mathrm{d}^n}{\mathrm{d}\xi^n} \exp(-\xi_i^2). \tag{2.80}$$

where $\mathbf{G}^{\mathrm{c}}$ is a diagonal matrix[9] with

$$\mathbf{G}^{\mathrm{c}}_{IJ} = \delta_{IJ} \begin{pmatrix} 1 & 0 & 0 \\ 0 & r_I & 0 \\ 0 & 0 & 1 \end{pmatrix}, \tag{2.87}$$

and the eigenvalue equation 2.71 can be rewritten:

$$\mathbf{D}^{\mathrm{c}}\mathbf{L}^{\mathrm{c}} = \Lambda\mathbf{L}^{\mathrm{c}}. \tag{2.88}$$

The matrix $\mathbf{D}^{\mathrm{c}}$ exhibits, in contrast to $\mathbf{D}$, a translational symmetry with respect to the screw symmetry operation (Eq. (2.1)) and can be written in the following form:

$$\mathbf{D}^{\mathrm{c}} = \begin{pmatrix} \mathbf{D}^{\mathrm{c}}(0) & \mathbf{D}^{\mathrm{c}}(1) & \mathbf{D}^{\mathrm{c}}(2) & \cdots \\ \mathbf{D}^{\mathrm{c}}(-1) & \mathbf{D}^{\mathrm{c}}(0) & & \\ \mathbf{D}^{\mathrm{c}}(-2) & & \mathbf{D}^{\mathrm{c}}(0) & \\ \vdots & & & \ddots \end{pmatrix}, \tag{2.89}$$

where $\mathbf{D}^{\mathrm{c}}(n)$ are $(3N^{\mathrm{APP}} \times 3N^{\mathrm{APP}})$-dimensional matrices and correspond to the interaction of a given peptide unit with its n^{th} nearest neighbor:

$$\mathbf{D}^{\mathrm{c}}_{ij}(n) = \mathbf{D}^{\mathrm{c}}_{i,n\cdot 3N^{\mathrm{APP}}+j}. \tag{2.90}$$

As an ansatz to solve Eq. (2.87), we consider the eigenvectors of $\mathbf{D}^{\mathrm{c}}$ as *Bloch-functions*:

$$\mathbf{l}^{\mathrm{c}}_i(m) = \exp\left(\mathrm{i}\varphi(m-n)\right)\mathbf{l}^{\mathrm{c}}_i(n). \tag{2.91}$$

Here, $\mathbf{l}^{\mathrm{c}}_i(n)$ and $\mathbf{l}^{\mathrm{c}}_i(m)$ are $3 * N^{\mathrm{APP}}$-dimensional vectors and determine the vibrational amplitude of the peptide units with indices n and m, respectively. Eq. (2.90) states that, for a given eigenvector with index i, the vibrational amplitudes of the individual peptide units are differing only by a phase factor. The latter is determined by the product of the phase difference in between adjacent peptide units, φ, and the in-chain distance $m - n$. Substituting this ansatz into Eq. (2.87) gives:

$$\sum_n \mathbf{D}^{\mathrm{c}}(n-m)\exp\left(-\mathrm{i}\varphi(n-m)\right)\mathbf{L}^{\mathrm{c}}(m) = \Lambda(m)\mathbf{L}^{\mathrm{c}}(m) \qquad \forall m, \varphi. \tag{2.92}$$

These expressions are independent of the value of m. We may therefore set $m = 0$ and suppress this index in the following. We further introduce the *symmetry reduced dynamical matrix* $\mathbf{D}^{\mathrm{c}}(\varphi)$:

$$\mathbf{D}^{\mathrm{c}}(\varphi) = \sum_n \mathbf{D}^{\mathrm{c}}(n)\exp(-\mathrm{i}\varphi n) \qquad \forall\varphi, \tag{2.93}$$

---

[9] $\mathbf{G}^{\mathrm{c}}$ performs the transformation of the angular part of the variation in the cylindrical coordinate $d\phi_I$ to a metric length $r_I d\phi_I$ by rescaling it with the radial part r_I.

and obtain for the eigenvalue equation:

$$\mathbf{D}^{\mathrm{c}}(\varphi)\mathbf{L}^{\mathrm{c}}(\varphi) = \Lambda(\varphi)\mathbf{L}^{\mathrm{c}}(\varphi) \qquad \forall\varphi, \tag{2.94}$$

or equivalently, by breaking down to the individual eigenvectors $\mathbf{l}_i^{\mathrm{c}}(\varphi)$, i.e., the i^{th} columns of the matrix $\mathbf{L}^{\mathrm{c}}(\varphi)$:

$$\mathbf{D}^{\mathrm{c}}(\varphi)\mathbf{l}_i^{\mathrm{c}}(\varphi) = \omega_i^2(\varphi)\mathbf{l}_i^{\mathrm{c}}(\varphi) \qquad \forall\varphi, i = 1, ..., 3N^{\mathrm{APP}}. \tag{2.95}$$

Eqs. (2.93) and (2.94) denote the secular equations for the symmetry reduced dynamical matrix. They satisfy the Eq. (2.71) if and only if they are fulfilled for any phase angle φ. Thus, to determine the complete eigenspectrum of the peptide chain, we have to diagonalize the matrix $\mathbf{D}^{\mathrm{c}}(\varphi)$ for all possible phase angles φ. It is important to note that, just as $\mathbf{D}^{\mathrm{c}}(\varphi)$, the eigenvectors and eigenvalues are also functions of φ, which has been accounted for in Eq. (2.93).

2.6.4 Phonon dispersion relation

Following Eq. (2.94), the vibrational frequencies of the peptide chain are arranged in $3N^{\mathrm{APP}}$ *vibrational branches* $\omega_i(\varphi)$, which are continuous functions of the phase angle φ and labeled with i. This depiction of the vibrational eigenfrequencies of a periodic system is referred to as *phonon dispersion relation.* The term *phonon* stems from solid state theory and designates the harmonic eigenvibrations of a crystalline system. The phonons of a 3-dimensional crystal are understood as quantum mechanical *quasi-particles,* with energies $E = \hbar\omega_i(\mathbf{k})$ and *quasi-momentum* $\mathbf{p} = \hbar\mathbf{k}$. Thus, the phonon dispersion relation of a 3-dimensional crystal describes the relation between the quasi-momentum and the energy of the individual phonon with branch index i and wavevector $\mathbf{k}$. This quasi-particle picture is also transferable to the helix. It is, however, interesting to note that the phase-angle φ plays here a slightly different role than the *wavevector* $\mathbf{k}$ plays in 3-dimensional crystals. This difference can be understood when considering the *group velocity* v. While the group velocity in crystals,

$$\mathbf{v}_i(\mathbf{k}) = \frac{\partial\omega_i}{\partial\mathbf{k}}, \tag{2.96}$$

can be directly related to the phonon velocity along the direction given by $\mathbf{k}$, the corresponding expression for the peptide chain,

$$v_i(\varphi) = \frac{\partial\omega_i}{\partial\varphi}, \tag{2.97}$$

denotes the number of peptides passed by the phonon per time unit and does not correspond to a velocity in the physical sense. Nevertheless, the projection $v_i^{\mathrm{g}}(\varphi)$ on the structural parameters of the peptide chain, i.e., the helix pitch L and the helix twist Θ are related to physical velocities. Thus, the phonons in the peptide chain are quasi-particles traveling with the velocity

$$v_i^z = L\frac{\partial\omega_i}{\partial\varphi} \tag{2.98}$$

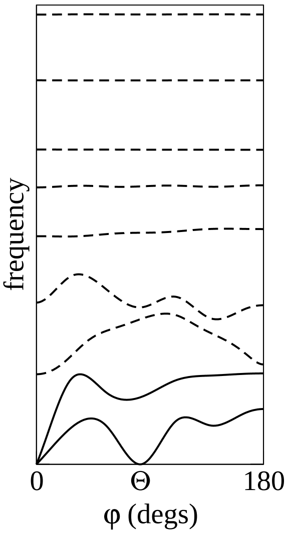

Figure 2.2: Sketch of a phonon dispersion relation of a helix characterised by a twist angle Θ: Shown are the acoustical branches (solid lines) and the optical branches (dashed lines).

along the helix axis and the angular velocity

$$v_i^{\Theta} = \Theta \frac{\partial \omega_i}{\partial \varphi} \tag{2.99}$$

around the helix axis.

The phonon dispersion relation of the peptide chain is symmetric with respect to a full period of the phase angle φ:

$$\omega_i(\varphi) = \omega_i(\varphi + 360^\circ), \tag{2.100}$$

since $\mathbf{D}^{\mathrm{c}}(\varphi) = \mathbf{D}^{\mathrm{c}}(\varphi + 360^\circ)$ (Eq. (2.92)) and from the time inversion invariance it follows that:

$$\omega_i(\varphi) = \omega_i(-\varphi). \tag{2.101}$$

Thus, it is sufficient to display the phonon dispersion relation in the first half of the first Brillouin zone, i.e., for $0 \leq \varphi \leq 180^\circ$.

Acoustical and optical branches

A schematic illustration of the phonon dispersion relation is shown in Fig. 2.2. The two lowest branches of the helix are zero at the Γ-point ($\varphi = 0$). These two branches are called *acoustical branches*, whereas the remaining $3N^{\mathrm{APP}} - 2$ branches are called *optical branches* (where N^{APP} denotes the number of atoms per peptide unit). Phonons from the *long-wavelength-limit* $\varphi \to 0$ of the acoustical branches are called acoustical, because they perform a mechanical deformation of the helix and may thus be excited by external sound waves. Phonons of the optical branches are called optical, since they deform the internal structure of the peptide units and couple to their dipole moments and polarizabilities, and hence may interact with electromagnetic waves (light).

Geometrical sum rules

There are four degrees of freedom of the infinite helix, i.e., the three translational degrees of freedom and the rotation around the helix axis, for which the corresponding vibrational frequency must be zero. Two of these degrees of freedom, the translation along and the rotation around the helix, force the two acoustical branches to be zero at the Γ-point:

$$\mathbf{D}^{\mathrm{c}}(\varphi=0)\mathbf{l}_1^{\mathrm{c}}(\varphi=0)=0 \quad \text{and} \quad \mathbf{D}^{\mathrm{c}}(\varphi=0)\mathbf{l}_2^{\mathrm{c}}(\varphi=0)=0, \tag{2.102}$$

where

$$\mathbf{l}_1^{\mathrm{c}}(\varphi=0)=(0,1,0,0,1,0,\ldots,0,1,0) \tag{2.103}$$

and

$$\mathbf{l}_2^{\mathrm{c}}(\varphi=0)=(0,0,1,0,0,1,\ldots,0,0,1)\,. \tag{2.104}$$

The remaining two correspond to the translations in the plane perpendicular to the helix axis and force the first acoustical branch to be zero at $\varphi=-\Theta$ and $\varphi=+\Theta$:

$$\mathbf{D}^{\mathrm{c}}(\varphi=\Theta)\mathbf{l}_1^{\mathrm{c}}(\varphi=\Theta)=0 \quad \text{and} \quad \mathbf{D}^{\mathrm{c}}(\varphi=-\Theta)\mathbf{l}_1^{\mathrm{c}}(\varphi=-\Theta)=0, \tag{2.105}$$

where

$$\mathbf{l}_1^{\mathrm{c}}(\varphi=\pm\Theta)=(0,1,0,0,1,0,\ldots,0,1,0)\,. \tag{2.106}$$

Eqs. (2.101) and (2.104) we denote as the *geometrical sum rules* of the peptide chain.

2.6.5 Thermodynamic properties

With the knowledge of the phonon dispersion relation we determine the partition function and with it the thermodynamic properties (in the harmonic approximation). To deduce an appropriate expression for the partition function, we consider the $3N^{\mathrm{ion}}$ decoupled oscillators which reveal the vibrational spectrum of the helix. As a consequence of the decoupling of these oscillators (Sec. 2.6.2) the partition function is written as the product sum of the partition function of each individual oscillator:

$$Z^{\mathrm{vib}}=\prod_{i=1}^{3N^{\mathrm{ion}}} Z_i^{\mathrm{vib}}, \tag{2.107}$$

where the individual partition functions are, according to Eq. (2.80), given (save a meaningless pre-factor) by:

$$Z_i^{\mathrm{vib}}=\sum_j \exp(-\beta j\omega_i). \tag{2.108}$$

These expressions may be simplified by applying a sum rule:

$$Z_i^{\mathrm{vib}}=\left(1-\exp(-\beta\omega_i)\right)^{-1}, \tag{2.109}$$

and the partition function of the system may be written as:

$$Z = \prod_{i=1}^{3N} \left(1 - \exp(-\beta\omega_i)\right)^{-1}. \tag{2.110}$$

Hence, the free energy of the system is:

$$\begin{aligned} \widetilde{F}^{\mathrm{vib}} &= -k_{\mathrm{B}} T \ln Z^{\mathrm{vib}} \\ &= \sum_{i=1}^{3N^{\mathrm{ion}}} \left(\frac{\hbar\omega_i}{2} + \frac{1}{\beta} \ln\left(1 - \exp(-\beta\hbar\omega_i)\right) \right) \end{aligned} \tag{2.111}$$

the entropy of the system is:

$$\begin{aligned} \widetilde{S}^{\mathrm{vib}} &= \frac{\partial}{\partial T}\left(T \ln Z^{\mathrm{vib}}\right) \\ &= \sum_{i=1}^{3N^{\mathrm{ion}}} \left(\frac{1}{T} \frac{\hbar\omega_i}{\exp(\beta\hbar\omega_i) - 1} - k_{\mathrm{B}} \ln\left(1 - \exp(-\beta\hbar\omega_i)\right) \right) \end{aligned} \tag{2.112}$$

and the internal energy of the system is:

$$\begin{aligned} \widetilde{U}^{\mathrm{vib}} &= -\frac{\partial \ln Z^{\mathrm{vib}}}{\partial \beta} \\ &= \sum_{i=1}^{3N^{\mathrm{ion}}} \left(\frac{\hbar\omega_i}{2} + \frac{\hbar\omega_i}{\exp\left[\beta\hbar\omega_i\right] - 1} \right). \end{aligned} \tag{2.113}$$

The summations in the equations above run over the infinite number of degrees of freedom of the system. Next we want to express the thermodynamic properties per irreducible unit of the structure, i.e., per peptide unit:

$$F^{\mathrm{vib}} = \frac{1}{N^P}\widetilde{F}^{\mathrm{vib}}, S^{\mathrm{vib}} = \frac{1}{N^P}\widetilde{S}^{\mathrm{vib}},\ U^{\mathrm{vib}} = \frac{1}{N^P}\widetilde{U}^{\mathrm{vib}}, \tag{2.114}$$

where N^{P} denotes the number of peptide units of the chain. The infinite summation in these equations can be replaced by an integration over the BZ:

$$\sum_{i=1}^{3N^{\mathrm{ion}}} \rightarrow \frac{1}{\pi} \sum_{i=1}^{3N^{\mathrm{APP}}} \int_{-180^\circ}^{+180^\circ} d\varphi. \tag{2.115}$$

Thus, for the vibrational entropy, vibrational energy and vibrational free energy we have, respectively:

$$S^{\mathrm{vib}} = \frac{1}{N^{\mathrm{P}}\pi} \sum_{i=1}^{3N^{\mathrm{APP}}} \int_{-180^\circ}^{+180^\circ} d\varphi \left(\frac{1}{T} \frac{\hbar\omega_i(\varphi)}{\exp\left(\beta\hbar\omega_i(\varphi)\right) - 1} - k_{\mathrm{B}} \ln\left(1 - \exp\left(-\beta\hbar\omega_i(\varphi)\right)\right) \right) \tag{2.116}$$

$$U^{\mathrm{vib}} = \frac{1}{N^{\mathrm{P}}\pi} \sum_{i=1}^{3N^{APP}} \int_{-180°}^{+180°} d\varphi \left(\frac{\hbar\omega_i(\varphi)}{\exp\left(\beta\hbar\omega_i(\varphi)\right) - 1} \right), \tag{2.117}$$

and

$$F^{\mathrm{vib}} = \frac{1}{N^{\mathrm{P}}\pi} \sum_{i=1}^{3N^{APP}} \int_{-180°}^{+180°} d\varphi \left(\frac{\hbar\omega_i(\varphi)}{2} + \frac{1}{\beta} \ln\left(1 - \exp\left[-\beta\hbar\omega_i(\varphi)\right]\right) \right). \tag{2.118}$$

2.6.6 Quasi-harmonic approximation and Grüneisen parameters

The harmonic approximation is strictly valid only for small displacements of the atoms from their static equilibrium positions. A first step to effectively include anharmonic corrections in the statistical averages is to consider the dependence of the harmonic vibrations on the macroscopic state variables. In complete analogy to the formulation developed for 3D crystals (e.g. [90]) we write for the peptide chain:

$$\omega_i = \omega_i(T, L(T), \Theta(T)). \tag{2.119}$$

For sufficiently low temperatures one can assume that the frequencies do not depend on temperature explicitly, but only implicitly via the helical parameters:

$$\omega_i \approx \omega_i(L(T), \Theta(T)). \tag{2.120}$$

Eq. (2.118) denotes the *quasi-harmonic approximation*[10]. It allows us to study the softenings and hardenings in the vibrational spectrum of the peptide chains upon mechanical deformations along the most relevant reaction coordinates, i.e., the helical parameters Θ and L. Furthermore, we may determine corresponding corrections to the free energy. Substitution of Eq. (2.118) into Eq. (2.45) reveals:

$$\begin{aligned} F(T, L, \Theta) &= E^{\mathrm{el}}(L, \Theta) + F^{\mathrm{vib}}(L, \Theta) \\ &= E^{\mathrm{el}}(L, \Theta) + \\ &+ \frac{1}{N^{\mathrm{P}}} \sum_i \int_{-180°}^{+180°} d\varphi \left(\frac{\hbar\omega_i(\varphi, L, \Theta)}{2} + \frac{1}{\beta} \ln\left(1 - \exp\left[-\beta\hbar\omega_i(\varphi, L, \Theta)\right]\right) \right) \end{aligned} \tag{2.121}$$

We now write the functional dependence in Eq. (2.118) as a Taylor-expansion:

$$\omega_i(L, \Theta) = \omega_i(L_0, \Theta_0) + \begin{pmatrix} \Delta L & \Delta\Theta \end{pmatrix} \begin{pmatrix} \frac{\partial\omega_i}{\partial L} \\ \frac{\partial\omega_i}{\partial\Theta} \end{pmatrix}_{L_0, \Theta_0} + \begin{pmatrix} \Delta L & \Delta\Theta \end{pmatrix} \begin{pmatrix} \frac{\partial^2\omega_i}{\partial L^2} & \frac{\partial^2\omega_i}{\partial\Theta\partial L} \\ \frac{\partial^2\omega_i}{\partial\Theta\partial L} & \frac{\partial^2\omega_i}{\partial\Theta^2} \end{pmatrix} \begin{pmatrix} \Delta L \\ \Delta\Theta \end{pmatrix} + \ldots., \tag{2.122}$$

---

[10] Note that we here address the dependence of the frequencies within the basin of the (Θ, L)-free-energy-surface corresponding to *one* given conformation, rather than the fact that different conformations of the peptide chain exhibit different vibrational spectra.

where $\Delta L = L - L_0$ and $\Delta\Theta = \Theta - \Theta_0$. Considering the Taylor-expansion up to the linear term results in an approximation that is known as *Grüneisen approximation [91]*:

$$\omega_i(L,\Theta) \approx \omega_i(L_0,\Theta_0) + \Delta L \frac{\partial \omega_i}{\partial L} + \Delta\Theta \frac{\partial \omega_i}{\partial \Theta}. \tag{2.123}$$

Substituting Eq. (2.121) into Eq. (2.55) reveals the two *Grüneisen-Mie-equations-of-state* [92] for the peptide chain:

$$0 = -\frac{\partial E}{\partial a} + \frac{1}{a}\frac{1}{N^{\mathrm{P}}} \sum_{i=1}^{3N^{\mathrm{APP}}} \int_{-180^\circ}^{+180^\circ} d\varphi \gamma_i^a(\varphi) \left(\frac{\omega_i(\varphi)}{\exp\left(\beta\omega_i(\varphi)\right) - 1} \right) \tag{2.124}$$

where a can be either L or Θ and the $\gamma_i(\varphi)$ denote the Grüneisen parameters, and are defined as:

$$\gamma_i^a(\varphi) = -\frac{\partial \omega_i(\varphi)}{\partial a} \frac{a}{\omega_i(\varphi)}. \tag{2.125}$$

In passing from the harmonic to the quasi-harmonic approximation, the equilibrium helical parameters of the peptide chain are no longer fixed quantities with respect to temperature. In fact, the peptide chain undergoes a *thermal expansion*, which is defined as:

$$\alpha_a = \frac{1}{a} \frac{\partial a}{\partial T}\bigg|_{p=0}. \tag{2.126}$$

In order to evaluate the thermal expansion, the equation of state has to be solved iteratively.

2.7 Thermodynamic integration

The quasi-harmonic approximation is valid as long as the vibrations of the peptide chain experience a harmonic potential for given helical parameters L and Θ. Raising the temperature, however, makes the vibrational modes exploring more extended regions of the phase space and exhibiting larger displacements from the equilibrium conformation. In particular, for the soft, low frequency modes of the peptide chain we therefore expect significant anharmonic contributions which may lead to significant deviations from the free energy calculated within the quasi-harmonic approach. To account for these deviations, a more powerful and general approach is required. A technique which basically allows to take into account the full anharmonicity is the thermodynamic integration. In the following the basic ideas behind this method are introduced, whereas its implementation is discussed in Sec. 3.5.

2.7.1 Concept of thermodynamic integration

When extending the study to anharmonic effects, a direct evaluation of the partition function — as is the basis for the harmonic thermodynamic study — is not possible anymore, since a general analytical expression for the partition function does not exist, and a direct numeric evaluation would be computationally too demanding.

Thermodynamic integration is a concept that allows to determine the free energy F^{tgt} of a thermodynamic state of interest (target state), by *eluding* a direct numeric evaluation of its partition function. Instead the target state is linked to a reference state with known free energy F^{ref} and only the differences to the reference state are addressed. A basic prerequisite for the applicability of this concept is that a thermodynamic path exists that links the target state to the reference state, such that we may write:

$$\underbrace{F^{\text{ref}} =: F(\lambda = 0)}_{\text{reference state}} \quad \longrightarrow \quad \underbrace{F(\lambda)}_{\text{integration path}} \quad \longrightarrow \quad \underbrace{F(\lambda = 1) := F^{\text{tgt}}}_{\text{target state}}. \tag{2.127}$$

Here, λ is a thermodynamic variable (coupling parameter) that parametrizes the thermodynamic integration path and $F(\lambda)$ is the free energy of the intermediate states along the path. A further prerequisite is that the thermodynamic path must be reversible. This means that the thermodynamic states visited on the forward and backward path in going from F^{tgt} to F^{ref} are identical along the λ-coordinate.

If these prerequisites are matched, the free energy of the target state may be calculated by the following integration:

$$F^{\text{tgt}} = F^{\text{ref}} + \int_{\lambda=0}^{\lambda=1} d\lambda \left(\frac{\partial F(\lambda)}{\partial \lambda}\right)_{N,V,T}. \tag{2.128}$$

The basic strategy behind thermodynamic integration is to employ prior knowledge about the system, and to define the reference system to mimic the target system as close as possible. If we successfully construct such a reference state, the thermodynamic integration will be effective, i.e., we may determine the anharmonic free energy of the system with a low computational effort. At this point of the analysis we already have determined the dynamical matrix and thus have the complete knowledge about the system in the harmonic approximation (Sec. 2.6.2). The idea (e.g. [93]) is thus to identify the reference potential with the harmonic potential $U^{\text{harm}} = \mathbf{Y}^{\text{T}}\mathbf{D}\mathbf{Y}$ (Eq. (2.69)). As the thermodynamic integration path (Eq. (2.125)) we choose a linear interpolation between reference and target potential:

$$U(\lambda) = (1 - \lambda)U^{\text{harm}} + \lambda U^{\text{DFT}}. \tag{2.129}$$

It can be shown (e.g. [94]) that the integrand in the Eq. (2.126) can be replaced by the canonical ensemble average of the potential energy $U(\lambda)$:

$$\left(\frac{\partial F(\lambda)}{\partial \lambda}\right)_{N,V,T} = \left\langle \frac{\partial U(\lambda)}{\partial \lambda} \right\rangle_{\lambda}. \tag{2.130}$$

The quantity $\left\langle \frac{\partial U(\lambda)}{\partial \lambda} \right\rangle_{\lambda}$ corresponds to an ensemble average which is evaluated from the trajectory corresponding to a proper canonical sampling of the potential $U(\lambda)$, as will be discussed in Sec.

3.5[11].

Substituting Eq. (2.127) into Eq. (2.128) makes the advantages of the thermodynamic approach particularly clear:

$$\left(\frac{\partial F(\lambda)}{\partial \lambda}\right)_{N,V,T} = \left\langle \frac{\partial U(\lambda)}{\partial \lambda} \right\rangle_{\lambda} = \left\langle U^{\mathrm{DFT}} - U^{\mathrm{harm}} \right\rangle_{\lambda} \tag{2.131}$$

The thermodynamic integration method thus us to determine the anharmonic free energy as a *correction* to the harmonic free energy. For a given λ value we only have to determine (statistically converge) the *difference* to the harmonic approximation, i.e., the explicit anharmonicity. This is obviously much more effective than directly evaluating the anharmonic free energy, including both harmonic and anharmonic contributions.

2.8 Phase coexistence

In the previous sections we have described, how the free energy of a thermodynamic phase corresponding to a given conformation X of the peptide chain may be determined. However, at finite temperatures the thermodynamic state of the peptide chain does not necessarily consist of a single phase. In fact, it is possible that several thermodynamic phases may coexist. This possibility has important consequences for the thermodynamic equilibrium of the peptide chain: Phases with a low energetic cost to form an interface between each other may coexist in a solution (liquid), inducing a high degree of disorder in the chain. In contrast, phases with a high interface energy tend to form ordered bulk-like (solid) states, i.e, the are composed of a single phase. The higher degree of disorder in the solution-like states is reflected in a gain of configurational entropy, which stabilizes them with respect to the bulk-like states at increasing temperatures.

A likely candidate for a solution-like state is the unfolded state of the peptide chain, since it is mainly stabilized by short-ranged, nearest-neighbor peptide-peptide interactions and thus adjacent peptide units in the chain may adopt their individual conformations independently from each other. In contrast, the helical conformations are more bulk-like in this sense, since they are stabilized by specific long-ranged hydrogen bonding patterns, which require a proper alignment of a certain number of consecutive peptide units in one and the same helical conformation.

As already mentioned, this project is mainly dedicated to the free energy of the pure bulk phases, which implies the accurate determination of the *vibrational* entropy of the structural conformation, which characterize the respective phases. The *exact* inclusion of interface energies and *configurational* entropy is beyond the scope of this thesis. Nevertheless, to *approximately* account for the differences in the conformational segregation characteristics between unfolded and helical states, we introduce some basic approximations below. These approximations may help us later to estimate the stability of the helix against unfolding at a given temperature.

---

[11] The integration in Eq. (2.126) is discretized, i.e., $\left\langle \frac{\partial U(\lambda)}{\partial \lambda} \right\rangle_{\lambda}$ is evaluated for a finite set of varying λ's, and the integral is calculated with an efficient integration scheme (as will be also discussed in Sec. 3.5).

2.8.1 Chemical potential

To treat the chemical equilibrium between the thermodynamic phases, i.e., a coexistence of phases, we introduce the chemical potential:

$$\mu_{\mathrm{X}}(T, N_{\mathrm{X}}) = \frac{\partial F(T, L_X, \Theta_X)}{\partial N_{\mathrm{X}}}. \tag{2.132}$$

Here, X indicates one of the phases and N_{X} is the number of peptide units corresponding to this phase. The phase A is in chemical equilibrium with another phase B if:

$$\mu_{\mathrm{A}}(T, N_{\mathrm{A}}) = \mu_{\mathrm{B}}(T, N_{\mathrm{B}}). \tag{2.133}$$

We define now the "bulk" chemical potential to be the free energy F_{X} per peptide unit of the system in the "pure" phase X:

$$\mu_{\mathrm{X}}^{\mathrm{bulk}}(T) := \frac{F_{\mathrm{X}}(T, L_X, \Theta_X)}{N_{\mathrm{X}}}. \tag{2.134}$$

Further, we neglect, in a first step, any effects at the interface of the two phases A and B in the mixture state. For this "ideal solution" one can show that:

$$\mu_{\mathrm{X}}(T, N_{\mathrm{X}}) = \mu_{\mathrm{X}}^{\mathrm{bulk}}(T) + k_{\mathrm{B}} T \ln \frac{N_X}{N}. \tag{2.135}$$

Inserting Eq. (2.133) into Eq. (2.131) gives the following rate equation:

$$\frac{N_{\mathrm{A}}}{N_{\mathrm{B}}}(T) = \exp\left(-\beta\left(\mu_{\mathrm{A}}^{\mathrm{bulk}}(T) - \mu_{\mathrm{B}}^{\mathrm{bulk}}(T)\right)\right). \tag{2.136}$$

We remark that the right hand side of Eq. (2.134) is determined just by the free energy of formation (Eq. (2.56)) of the phase A out of the phase B:

$$\mu_{\mathrm{A}}^{\mathrm{bulk}}(T) - \mu_{\mathrm{B}}^{\mathrm{bulk}}(T) = \Delta F^{\mathrm{f}}{}_{\mathrm{A}\to\mathrm{B}}(T). \tag{2.137}$$

In other words, provided that the states A and B may form an *ideal solution*, $\Delta F^{\mathrm{f}}_{\mathrm{A}\to B}$ determines the relative number of peptide units (concentration) of the chain which can be found in phase A with respect to the number of peptide units which can be found in phase B via Eq. (2.134).

2.8.2 Flory's hypothesis

It is convenient and also widely accepted to separate the configurational space of the peptide chain into two domains, which we call the helical/folded domain and the non-helical/unfolded domain. The helical domain is defined here as the configurational space occupied by the three basins corresponding to the helical conformations and the unfolded domain as the remaining configurational space (Fig. 1.5). This definition of the two domains is arbitrary, nevertheless it corresponds to the common understanding of the folded, helical state on the one hand and of the unfolded state on the other hand. Furthermore, it is justified by the fact that changing between the two domains requires to cross a comparatively huge energy barrier and hence the two domains are topographically well separated (Fig. 1.5).

We now introduce two assumptions. The first assumption addresses the unfolded state and is commonly referred to as the *Flory's hypothesis*:

- In the unfolded state each pair of peptide units may adopt its conformation independently of the adjoining pairs of peptide units [95].

This assumption implies that we may treat the unfolded state as an ideal solution of the non-helical bulk phases of the peptide chain. Following Eq. (2.134) we may thus write for the chemical potential of the unfolded state:

$$\begin{aligned}
\mu^{\text{unfolded}} &\approx \mu_A^{\text{bulk}} - k_{\text{B}}T \ln\left(\frac{N_{\text{unfolded}}}{N_A}\right) \\
&= \mu_A^{\text{bulk}} - k_{\text{B}}T \ln\left(1 + \sum_{X\neq A}^{\text{non-helical}} \frac{N_X}{N_A}\right) \\
&= \mu_A^{\text{bulk}} - k_{\text{B}}T \ln\left(1 + \sum_{X\neq A}^{\text{non-helical}} \exp(-\beta\Delta F^f_{A\to X})\right) \\
&= \mu_A^{\text{bulk}} - k_{\text{B}}T \ln R^{\text{conf}},
\end{aligned} \tag{2.138}$$

where

$$R^{\text{conf}} = 1 + \sum_{X\neq A}^{\text{non-helical}} \exp(-\beta\Delta F^f_{A\to X}). \tag{2.139}$$

Here, A corresponds to either one of the various phases $\{X\}$ which may occur in the unfolded state. For convenience we will define it in the following as the phase with the lowest bulk chemical potential. The term $-T \ln R^{\text{conf}}$ denotes the additional stabilization of the unfolded state, due to the fact that bulk phases other than A contribute to it. In the special case, in which all the phases contributing to the unfolded state have the same free energy, it would simplify to a pure entropy term, the so called configurational entropy. Then $R^{\text{conf}} = S^{\text{conf}} = \ln s$, where s denotes the number of phases which may occur in the unfolded state.

Our second assumption is:

- The helical phases are, in contrast to the unfolded conformations, not able to form interfaces at all.

This implies that the chain can be either completely unfolded or completely helical and that the helical state is exclusively assembled from the phase corresponding to the lowest bulk free energy:

$$\mu^{\text{helix}} \approx \min_{X \text{ is helix}} \mu_X^{\text{bulk}}. \tag{2.140}$$

Using these two approximations we may estimate the stability of the helical state against unfolding:

$$\Delta F^{\mathrm{f}}_{\mathrm{helix}\rightarrow\mathrm{unfolded}} \approx \mu^{\mathrm{helix}} - \mu^{\mathrm{unfolded}}, \tag{2.141}$$

where μ^{unfolded} and μ^{helix} are defined in Eqs. (2.136) and (2.138), respectively.

3 Implementation

The purpose of this chapter is to explain the implementation of the theoretical concepts, which have been introduced in the previous chapter. All implementations for this project have been undertaken with the S/PHI/nX package. S/PHI/nX is an *ab-initio based multi-scale library* written in C++. For more details about S/PHI/nX check the webpage www.sxlib.de.

The chapter starts with an introduction to the standard methodology of the plane waves pseudopotential approach (Sec. 3.1), which is employed in this study to determine the electronic ground-state properties of the peptide chain.

We remark, however, that the numerical accuracy of the interatomic forces as provided by the standard methodology is insufficient to accomplish an adequate description of the low frequency vibrations of the peptide chain, which have a fundamental meaning for the thermodynamic stability. Therefore, in order to achieve the high numerical accuracy required for forces, vibrational frequencies and thermodynamic data, several extensions to the standard methodology have been implemented into the S/PHI/nX code. In particular, the elimination (smoothing) of the exchange-correlation wiggles (which have been identified as the main source of numerical errors) and the refinement techniques for the calculation of the dynamical matrix were major implementations to achieve an accurate determination of the vibrational spectra and free energies (Sec. 3.4).

Furthermore, the implementation of the anharmonic corrections to the free energy is explained (Sec. 3.5). Particularly, we describe the implementation of the Langevin stochastic equations of motion and we explain the necessary practical steps to determine the anharmonic corrections.

We remark that this chapter provides an extensive documentation of the implementational aspects, which may be used as a reference guide. However, it is not required for the understanding of the results chapter and may therefore be skipped by a reader, who is exclusively interested in the physical aspects of the study.

3.1 Periodic boundary conditions

To investigate the vibrational and thermodynamic properties of the system, we first have to determine its electronic ground state for a given atomic configuration. The latter is achieved by solving the Kohn-Sham equations (KSE) (Eq. (2.24)). Solving directly the KSE for our system is impossible, since the Kohn-Sham Hamiltonian for an infinite peptide chain (Eq. (2.1)) contains the interaction of an infinite number of particles. However, such infinite number of particles can be reduced to a finite number by exploiting the symmetry of the peptide chain.

In principle, the Kohn-Sham Hamiltonian for this particular system exhibits a screw symmetry

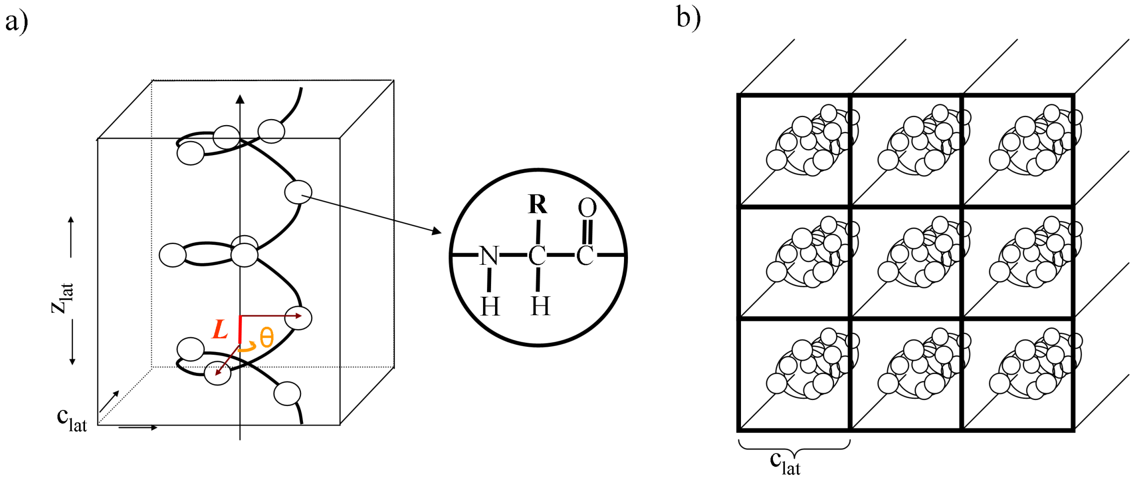

Figure 3.1: Schematic view of the α-helix, as modeled in an orthorhombic supercell: a) Side-view on the helix. b) Top-view on the 3-dimensional, artificial crystal of helices, which is imposed by the periodic boundary conditions.

according to Eq. (2.1):

$$H^{\mathrm{KS}}(\mathbf{r}+\mathbf{T}_n) = H^{\mathrm{KS}}(\mathbf{r}). \tag{3.1}$$

Therefore, if the Kohn-Sham Hamiltonian is described in a proper set of helix symmetry coordinates (for example cylindrical coordinates), its electronic eigenstates can, in close analogy to the eigenstates of the ionic Hamiltonian, be written as Bloch-functions:

$$\phi_\nu^{\mathrm{KS}}(\varphi, \mathbf{r}) = \exp(in\varphi) u_\nu(\varphi, \mathbf{r}). \tag{3.2}$$

Here $u_\nu(\varphi, \mathbf{r}) = u_\nu(\varphi, \mathbf{r} + \mathbf{T}_n)$ denotes a function, which is periodic with the lattice vector $\mathbf{T}_n$ (Eq. (2.1)) and is modulated by a phase factor $\exp(in\varphi)$. The variable φ denotes the phase difference in the wavefunction between adjacent peptide units and n indicates the peptide unit.

Using such cylindrical symmetric representation to solve the KSE would, however, require to expand the Hamiltonian and the electronic wavefunction in the corresponding symmetry adapted basis functions (cylindrical plane waves). Instead of implementing such elaborated method we rather model the peptide chain by means of a 3-dimensional *supercell* spanned by the vectors:

$$\mathbf{a}_1 = \mathrm{c}_{\mathrm{lat}}\mathbf{e}_1, \mathbf{a}_2 = \mathrm{c}_{\mathrm{lat}}\mathbf{e}_2, \mathbf{a}_3 = \mathrm{z}_{\mathrm{lat}}\mathbf{e}_3, \tag{3.3}$$

where the $\mathbf{e}_i$ are the Cartesian basis vectors, z_{lat} denotes the extension of the supercell along the z-axis, which is chosen to be parallel to the axis of the peptide chain, and c_{lat} denotes the lateral extension of the supercell (Fig. 3.1; details in Appendix, Sec. 6.6.1).

The KSE are thus solved by applying the symmetry of the lattice corresponding to the 3-dimensional periodicity of these lattice vectors:

$$H^{\mathrm{KS}}(\mathbf{r}+\mathbf{a}_n) = H^{\mathrm{KS}}(\mathbf{r}) \tag{3.4}$$

The artificial interactions of the individual peptide chain with its periodic images in the crystal directions lateral to the helix axis (Fig. 3.1b) are minimized by choosing a sufficiently large lateral supercell parameter c_{lat}. The latter implies an increase in the computational resources needed (both memory and computation time), but is still feasible and we intend to benefit from the methodological advantages that come with the employment of the plane wave basis set (see below).

3.1.1 Plane wave basis

Plane waves are functions of the form:

$$u(\mathbf{r}) = A \exp(\mathrm{i}\mathbf{k}\mathbf{r} + B), \tag{3.5}$$

where A denotes the amplitude (or plane wave coefficient), B denotes the phase and $\mathbf{k}$ denotes the wavevector. The plane waves are constant on the orthogonal planes to the wavevector and periodic, sinus-shaped along it, with a wavelength given by $|\mathbf{k}|^{-1}$.

Plane waves are “natural” to describe periodic systems, although other basis sets are also possible and efficient. The use of Gaussian orbitals in electronic structure calculations with periodic boundary conditions, for example, has a long history for both, Hartree-Fock [96, 97] and DFT calculations [98, 99, 100]. Recently, Scuseria et al. have also applied this methodology to perform a DFT-GGA study on infinite poly-glycine and poly-L-alanine chains [45]. According to [45, 100], the advantage of this approach compared to plane waves is its better suitability to model covalently bonded systems and hence a better scaling behavior is reported for large supercells. Furthermore, Gaussians allow to selectively exploit the periodicity along one axis in Cartesian space, i.e., the helix axis, while the periodicity along the other two axes can be “switched off”, which is not possible if the plane wave basis is used.

Still, there are basically three reasons for employing plane waves. First, an adequate description of hydrogen bonds demands a high accuracy of the basis set, which can be only achieved using a very large Gaussian basis set or plane waves. A practical advantage of the plane wave basis is hereby that its quality (size, completeness) can be controlled by a single parameter (the so-called cutoff energy; Sec. 3.1.3), whereas, such a control is not straightforward for localized basis sets. Second, the use of a localized basis implies an unphysical effect, the so called basis set superposition error[1] (BSSE), which can lead to a significant spurious overestimation of hydrogen bond strengths (e.g. [101]). The BSSE can be partially corrected a posteriori by the counterpoise method [102]. However, the plane wave basis does not cause a BSSE at all. Third, the plane waves basis does not depend on the atomic positions. This allows for a straightforward evaluation of the inter-atomic forces by using the Hellmann-Feynman theorem (Sec. 3.2), which is important also for this project, i.e., for determining the vibrational and thermodynamic properties of a system.

Thus in this study the electronic states are expanded in terms of plane waves. We recall that the

---

[1] The origin of the BSSE is the non-orthogonality of a localized basis set: If the atom centered orbitals of the two molecular fragments corresponding to a given hydrogen bond overlap, an improvement in the description of the individual fragments is achieved. This improvement is inconsistent with the non-bonded case, where the molecular fragments are spatially more separated.

Kohn-Sham orbitals with periodicity of Eqs. (3.3) and (3.4) may be written as Bloch waves:

$$\phi_\nu^{\mathrm{KS}}(\mathbf{k},\mathbf{r}) = \exp(\mathrm{i}\mathbf{k}\mathbf{r})u_\nu(\mathbf{k},\mathbf{r}). \tag{3.6}$$

Here $u_\nu(\mathbf{k},\mathbf{r}) = u_\nu(\mathbf{k},\mathbf{r}+\mathbf{R}_n)$ denotes a function, which is periodic with the supercell and is the amplitude of the corresponding Bloch wave. The wavevector $\mathbf{k}$ determines the phase of the Bloch wave. It is confined to the first Brillouin zone, which is spanned by the reciprocal lattice vectors:

$$\mathbf{b}_1 = \frac{2\pi}{c_{\mathrm{lat}}}\mathbf{e}_1,\ \mathbf{b}_2 = \frac{2\pi}{c_{\mathrm{lat}}}\mathbf{e}_2,\ \mathbf{b}_3 = \frac{2\pi}{z_{\mathrm{lat}}}\mathbf{e}_3. \tag{3.7}$$

Following Bloch's theorem we may expand the electronic eigenstates in terms of a discretized plane wave basis:

$$\phi_\nu^{\mathrm{KS}}(\mathbf{k},\mathbf{r}) = \frac{1}{\Omega}\sum_{\mathbf{G}} c_\nu(\mathbf{k}+\mathbf{G})\exp\left(\mathrm{i}(\mathbf{k}+\mathbf{G})\mathbf{r}\right), \tag{3.8}$$

where the wave vectors are given by the reciprocal lattice vectors $\mathbf{G}$:

$$\mathbf{G} = m_1\mathbf{b}_1 + m_2\mathbf{b}_2 + m_3\mathbf{b}_3, \quad m_i\epsilon\mathbb{Z}. \tag{3.9}$$

3.1.2 Hamiltonian matrix

Substituting the plane wave (Eq. (3.8)) into the Kohn-Sham equation (Eq. (2.24)) and integrating over $\mathbf{r}$ gives the secular equation of the Hamiltonian matrix in a plane wave expansion:

$$\sum_{\mathbf{G}'} H^{\mathrm{KS}}_{\mathbf{k}+\mathbf{G},\mathbf{k}+\mathbf{G}'} c_\nu(\mathbf{k}+\mathbf{G}') = \epsilon_\nu^{\mathrm{KS}} c_\nu(\mathbf{k}+\mathbf{G}), \tag{3.10}$$

where the matrix elements are given by:

$$H^{\mathrm{KS}}_{\mathbf{k}+\mathbf{G},\mathbf{k}+\mathbf{G}'}[n] = \frac{1}{2}|\mathbf{k}+\mathbf{G}|^2\delta_{\mathbf{G}\mathbf{G}'} + V^{\mathrm{ext}}(\mathbf{G}-\mathbf{G}') + V^{\mathrm{H}}[n](\mathbf{G}-\mathbf{G}') + V^{\mathrm{xc}}[n](\mathbf{G}-\mathbf{G}'). \tag{3.11}$$

Eq. (3.10) has to be solved self-consistently (see Sec. 3.1.5), since the Hamiltonian matrix depends on the electron density, which in turn depends on the plane wave coefficients $c_\nu(\mathbf{k}+\mathbf{G})$.

3.1.3 Cutoff energy and k-point sampling

The basis set as introduced in Eq. (3.8) contains an infinite number of plane waves. Consequently, the secular equation denoted by Eq. (3.10) implies a matrix of infinite dimensions for each given $\mathbf{k}$. Further, in principle, Eq. (3.10) demands to be solved for each individual $\mathbf{k}$-point of the electronic Brillouin zone. Hence, an *exact and complete* treatment of the electronic system would require to solve an infinite number of infinitely large matrices. Such a complete treatment is, however, not necessary, since both, plane wave basis as well as $\mathbf{k}$-point sampling, can be effectively reduced to finite sizes.

To introduce a finite number of basis functions we take advantage of the fact that the Kohn-Sham orbitals of the valence electrons (, i.e., the electrons, which are responsible for the chemical bonding) become smoothly varying at small scales[2] – meaning that plane waves with large **G**-vectors do not contribute significantly to the electronic eigenfunctions. Therefore the plane wave basis set can be effectively truncated by introducing a *cutoff sphere* in the reciprocal space, i.e., by excluding the plane waves from the basis set, whose kinetic energy exceeds a certain threshold called *cutoff energy* E^{cut}:

$$\begin{aligned} \frac{\mathbf{G}^2}{2} &\leqslant E^{\mathrm{cut}} && (3.12)\\ \Leftrightarrow \quad G^{\max} &= \sqrt{2E^{\mathrm{cut}}}, && (3.13) \end{aligned}$$

where $G^{\max}$ denotes the radius of the cutoff sphere[3]. Increasing the cutoff energy always leads to a lowering of the total energy according to Ritz principle. The quality of the plane wave basis set may therefore be systematically controlled by one single parameter E^{cut}. As mentioned before, this is one of the major advantages of the plane wave basis compared to other basis sets (e.g. Gaussian orbitals), where no systematic scheme is available to check the convergence with respect to the basis set size.

Similarly, the sampling of the Brillouin zone is performed on a finite mesh of **k**-points. For the peptide chain, it turns out that in practice one single **k**-point is sufficient, since the supercell already contains a sufficiently extended part of the peptide chain to account for the electronic dispersion along the helix axis. Along the two orthogonal directions to the helix axis electronic dispersion is absent by construction, since a sufficiently large vacuum region is chosen to separate the periodic images of the peptide chain (convergence checks are discussed in the Appendix, Sec. 6.1.1).

3.1.4 Pseudo-potentials

Although in principle possible, it is not practical to *directly* describe the Kohn-Sham orbitals in a plane wave basis: In the region close to the atomic cores the orbitals oscillate heavily and exhibit various nodes. High Fourier coefficients $c_\nu(\mathbf{k}+\mathbf{G})$ are required to describe such oscillating behavior and thus a very large number of plane waves is needed, i.e., a very high cutoff energy, to achieve convergence in the total energy. However, an explicit treatment of the Kohn-Sham orbitals inside the core region may not be necessary anyway. This fact is employed by the concept of pseudo-potentials to fundamentally improve the efficiency of the plane wave basis set.

A prerequisite for the introduction of pseudo-potentials is the frozen core approximation. It exploits the fact that the chemical activity of a given atomic species is almost completely determined by the valence electrons. In the frozen core approximation the Kohn-Sham equations are exclusively solved for the valence electrons while the core electrons are considered as frozen. This implies a simplification over the all-electron calculation, since the number of degrees of freedom (electrons) to be treated is reduced. Furthermore, the numerical error of the calculation is reduced, since the energy terms corresponding to the core states, which are orders of magnitude higher than the

---

[2] Provided the ion cores are properly treated, e.g. by pseudo-potentials, as described in Sec. 3.1.4.

[3] The cutoff energy is usually treated in Rydberg, and not in Hartree (atomic unit), which makes the factor 1/2 redundant.

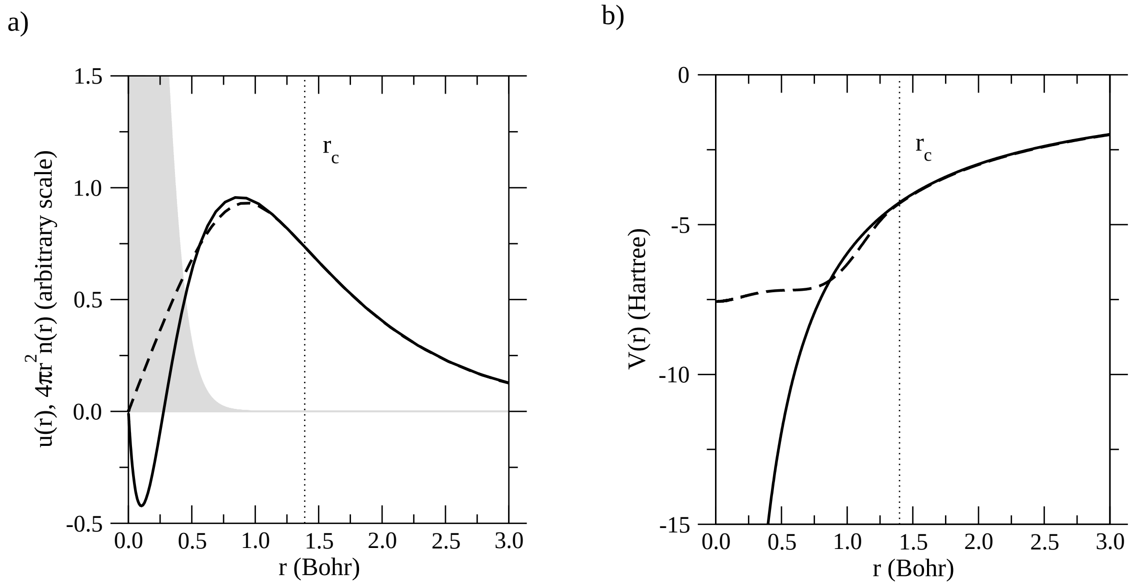

Figure 3.2: Pseudo-potential concept demonstrated exemplary for the oxygen 2s-Orbital: a) true valence-orbital (solid line), pseudo-orbital (dashed line) and core electron density (gray region). b) effective core potential (schematic, solid line) and pseudo-potential (dashed line). The radius r_c defines the atomic core region.

energies of the valence electrons, are excluded from the calculation.

For the expansion in a plane wave basis, however, the main problem is that the valence orbitals by themselves exhibit strong oscillations in the core region. These oscillations ultimately occur, since the core potential contains a singularity for $r \to 0$ and the valence orbitals have to be orthogonal to the core orbitals. In the pseudo-potential concept these oscillations are removed by replacing the core-potential with the pseudo-potential, which is smooth and soft in the core region (Fig. 3.2b). As a consequence of the replacement of the core potentials also the valence orbitals are changed to the so called pseudo-valence orbitals. However, providing that the pseudo-potential is adequately chosen, the pseudo-valence orbitals correspond exactly to the true valence orbitals *outside* the core region (core region will be defined below) and hence conserve their chemical properties. On the other hand the pseudo-potentials can be tuned to make the pseudo-valence orbitals smooth and node-less *inside* the core region, as is shown for the example of the oxygen atom in Fig. 3.2a. Hence the pseudo-valence orbitals may be expanded with a small plane waves basis set.

For generating a pseudo-potential two basic requisites are considered and balanced against each other. The first requisite is *transferability* – that is determined by the ability to reproduce accurately the behavior of the valence electrons in diverse chemical environments. The second requisite is *efficiency* – that is determined by the size of the plane wave basis required to expand the pseudo-potentials and -orbitals. Both, transferability and efficiency can be controlled during the generation of the pseudo-potential by defining the atomic core region through the cutoff radius r_c^l (l denotes the angular momentum quantum number). Generally, an increase of r_c^l leads to softer pseudo-potentials and a better efficiency, but it also lowers accuracy and transferability.

Typically, pseudo-potentials are generated by considering the isolated atomic species (details on the pseudo-potential generation can be found in Ref. [103]). Different schemes exist to construct pseudo-potentials. For this project we have used norm-conserving pseudo-potentials [104, 105] generated with the Troullier-Martins scheme [106]. Usually norm-conserving pseudo-potentials are set up and derived in terms of an angular momentum dependent, *semi-local* operator,

$$V^{\mathrm{ps-SL}} = V^{\mathrm{loc,ps}}(r) + \sum_{l=0}^{l_{\mathrm{max}}} \sum_{m=-l}^{l} \mid Y_{lm}\rangle \delta V_l^{\mathrm{ps}}(r) \langle Y_{lm} \mid, \tag{3.14}$$

written in terms of the local, long-ranged pseudo-potential, $V^{\mathrm{ps,loc}}(r)$, the l-dependent components $\delta V_l^{\mathrm{ps}}(r) = V_l^{\mathrm{ps}}(r) - V^{\mathrm{ps,loc}}(r)$, which are confined to the core region, and the spherical harmonics $\mid Y_{\mathrm{lm}}\rangle$ [103]. The summation of the semi-local part can be truncated beyond some l_{max}. For reasons of computational efficiency the semi-local form is transformed into a *fully non-local* form as suggested by Kleinmann and Bylander [107]:

$$V^{\mathrm{ps-NL}} \quad = \quad V^{\mathrm{loc,ps}}(r) + V^{\mathrm{nloc,ps}}. \tag{3.15}$$

where:

$$V^{\mathrm{nloc,ps}} \quad = \quad \sum_{l=0}^{l_{\mathrm{max}}} \sum_{m=-l}^{l} \frac{\delta V_l^{\mathrm{ps}}(r) \mid \phi_{lm}\rangle\langle\phi_{lm} \mid \delta V_l^{\mathrm{ps}}(r)}{\langle\phi_{lm} \mid \delta V_l^{\mathrm{ps}}(r) \mid \phi_{lm}\rangle}. \tag{3.16}$$

Here, the semi-local spherical harmonics Y_{lm} are replaced by the fully non-local projectors ϕ_{lm}, which are simply the atomic pseudo-orbitals. Due to their separability with respect to the atomic pseudo-orbitals the Kleinmann-Bylander form scales linearly with the number of plane waves, and is thus more efficient than the original semi-local form, which scales quadratically with the number of plane waves.

Employed pseudo-potentials and the estimation of their transferability

The pseudo-potentials for oxygen, nitrogen and carbon have been constructed with the tool fhi98PP [103]. For the hydrogen atom we have used the bare $1/r$-potential instead of a pseudo-potential. The reason is that an effective pseudoisation of hydrogen is hardly possible without introducing significant deviations of the results with respect to the results arising from the “true” non-pseudoised hydrogen [43].

The pseudo-potentials used here have been found to accurately reproduce the geometries, i.e., bond lengths and angles, of a set of small molecules [51]. To directly estimate the error in the description of the peptide chain introduced by the pseudo-potentials one would have to compare to a corresponding all-electron reference calculation for this system. Such calculations have (to the knowledge of the author) not been published yet. However, as mentioned in the Sec. 2.4.3, the overall error of the DFT-PBE pseudo-potential plane waves approach in predicting hydrogen bond energetics has been extensively investigated and found to be less than 1 kcal/mol [44], which corresponds to about 10 % of the strength of an intermediate hydrogen bond. The main contribution to this error is believed to be due to the PBE functional. Thus, we conclude that the error due to the pseudo-potentials is significantly smaller than 1.0 kcal/mol.

3.1.5 Solving the Kohn-Sham equations

In the pseudo-potential approximation the Kohn-Sham matrix (Eq. (3.11)) is written as[4]:

$$\begin{aligned} H^{\mathrm{KS}}_{\mathbf{G}'+\mathbf{k},\mathbf{G}+\mathbf{k}}[n] &= \frac{1}{2}|\mathbf{k}+\mathbf{G}|^2\delta_{\mathbf{G}\mathbf{G}'} + V^{\mathrm{nloc,ps}}_{\mathbf{G}'+\mathbf{k},\mathbf{G}+\mathbf{k}} \\ &+ \widetilde{V}^{\mathrm{loc,ps}}(\mathbf{G}-\mathbf{G}')+\widetilde{V}^{\mathrm{H}}[n](\mathbf{G}-\mathbf{G}') + V^{\mathrm{xc}}[n](\mathbf{G}-\mathbf{G}') \end{aligned} \tag{3.17}$$

and the electronic ground state energy is given by:

$$E^{\mathrm{el}}[n] = T^{\mathrm{s}}[n] + \widetilde{E}^{\mathrm{loc,ps}}[n] + E^{\mathrm{nloc,ps}}[n] + \widetilde{E}^{\mathrm{H}}[n] + E^{\mathrm{xc}}[n] + E^{\mathrm{ion}} - E^{\mathrm{self}}. \tag{3.18}$$

The formulas for the individual contributions to the Hamiltonian matrix and to the electronic ground state energy are, except for the XC contributions, standard and details are described elsewhere (e.g. in Refs. [108, 109]). Here we focus on the XC contributions, since the demands coming with our project requires to go beyond the standard treatment. The corresponding discussion is given in Sec. 3.4.2.

The secular equation of $H^{\mathrm{KS}}_{\mathbf{G}'+\mathbf{k},\mathbf{G}+\mathbf{k}}[n]$ has to be solved self-consistently in an iterative cycle, since the Hamiltonian depends on the electron density $n(\mathbf{r})$, which is not known from the beginning. This task amounts to finding the minimum on an energy surface $E^{\mathrm{el}}\left(\{c_i(\mathbf{G},\mathbf{k})\}\right)$, which is spanned by the $N^{\mathrm{el}} \cdot N^{\mathrm{pw}}$ plane wave basis functions and is defined by:

$$E^{\mathrm{el}}\left(\{c_i(\mathbf{G},\mathbf{k})\}\right) := E^{\mathrm{el}}\left[n\left(\{c_i(\mathbf{G},\mathbf{k})\}\right)\right]. \tag{3.19}$$

Here, $n\left(\{c_i(\mathbf{G},\mathbf{k})\}\right)$ is the electron density for a given set (guess) of plane wave coefficients (Eq. (3.24)), and $E^{\mathrm{el}}[n]$ is defined by Eq. (2.33). Several iterative schemes exist to find the minimum of $E^{\mathrm{el}}\left(\{c_i(\mathbf{G},\mathbf{k})\}\right)$. Most of these schemes require, at each iteration step m, the knowledge of the

---

[4] For the sake of completeness it shall be here remarked that the attractive local pseudo-potential $V^{\mathrm{loc,ps}}(\mathbf{r})$, as well as the repulsive Hartree potential $V^{\mathrm{H}}(\mathbf{r})$ are divergent, infinite quantities within an infinite crystal, since the potentials arising from the single ions show a $1/r$ behavior for large r values. However, the sum of the two potentials is a convergent, finite quantity. To be able to treat Hartree potential and local pseudo-potential separately, a "constructive zero" in the form of two Gaussian charges is added, which results in the modified potentials:

$$\widetilde{V}^{\mathrm{loc},ps}(\mathbf{r}) = V^{\mathrm{loc}}(\mathbf{r}) + \int d^3\mathbf{r}' \frac{n^{\mathrm{gauss}}(\mathbf{r}')}{|\mathbf{r}-\mathbf{r}'|}$$

$$\widetilde{V}^{\mathrm{H}}(\mathbf{r}) = V^{\mathrm{H}}(\mathbf{r}) - \int d^3\mathbf{r}' \frac{n^{\mathrm{gauss}}(\mathbf{r}')}{|\mathbf{r}-\mathbf{r}'|},$$

As a consequence, an additional term, E^{self}, appears in the expression for the electronic ground-state energy (Eq. (3.18)), which accounts for the electrostatic self interaction of the Gaussian charges.

local energy $E^{\mathrm{el}}\left(\{c_i^m(\mathbf{G},\mathbf{k})\}\right)$ and also the gradient:

$$\mid \zeta_{i,\mathbf{k}}\left(\{c_i^m(\mathbf{G},\mathbf{k})\}\right)\rangle := \frac{\delta E^{\mathrm{el}}\left(\{\varphi_i^m\}\right)}{\delta \varphi_i^m} \text{ with } \langle \varphi_i^m \mid \varphi_j^m \rangle = \delta_{ij}. \tag{3.20}$$

It can be shown (e.g. [110]) that the gradient is given by:

$$\mid \zeta_{i,\mathbf{k}}^m \rangle = -(H^{\mathrm{KS}^m} - \Lambda_{i,\mathbf{k}}^m) \mid \varphi_{i,\mathbf{k}}^m \rangle, \tag{3.21}$$

where

$$\Lambda_{i,\mathbf{k}}^m = \langle \varphi_{i,\mathbf{k}}^m \mid H^{\mathrm{KS}^m} \mid \varphi_{i,\mathbf{k}}^m \rangle. \tag{3.22}$$

The essential arithmetic operation to evaluate the gradient is thus to apply the Kohn-Sham matrix $H^{\mathrm{KS}^m}_{\mathbf{G}'+\mathbf{k},\mathbf{G}+\mathbf{k}}$ on the wavefunction $\varphi^m_{i,\mathbf{G}+\mathbf{k}}$.

Based on the knowledge of the local energy $E^{\mathrm{el}}\left(\{c_i^m(\mathbf{G},\mathbf{k})\}\right)$ and the gradient $\mid \zeta_{i,\mathbf{k}}^m\left(\{c_i^m(\mathbf{G},\mathbf{k})\}\right)\rangle$ for a given guess of the plane wave coefficients a local minimization scheme may find the minimum of the energy surface $E^{\mathrm{el}}\left(\{c_i^m(\mathbf{G},\mathbf{k})\}\right)$ to thus solve the KS equations.

In this project we use the *preconditioned all-state conjugate gradient scheme* to fulfill this task (details e.g. in Refs. [43, 111]). Using this scheme, usually 10-20 steps are sufficient to converge to the electronic ground state of the peptide chain up to the edge of numerical precision (10^{-9} kcal/mol).

3.1.6 The FFT mesh

The *Fast Fourier Transformation* (FFT) is an essential tool employed by the plane wave formalism. It allows to efficiently transform between the *real space expansion* and the *reciprocal space expansion* of the operators during the solving of the Kohn-Sham equations. Hence, one may calculate specific quantities, such as the kinetic energy, very efficiently in the reciprocal space and other quantities, such as the electron density in the real space. The operators may then be very easily merged in the reciprocal space to form the plane-wave Hamiltonian (Eq. (3.10)).

To use the FFT, the charge density and the potentials are described on (three-dimensional) so called FFT meshes — the *reciprocal space mesh*, or **G**-mesh, and the *real space mesh*, or **R**-mesh. The **G**-mesh is spanned by the reciprocal lattice vectors with:

$$\mathbf{G} = m_1\mathbf{b}_1 + m_2\mathbf{b}_2 + m_3\mathbf{b}_3, \text{ where } m_i \in \mathbb{Z} \ \mid m_i\mathbf{b}_i \mid \leq 2G^{\max}. \tag{3.23}$$

The FFT mesh to describe the charge density in the reciprocal space has to be twice the diameter of the cutoff sphere along each reciprocal space direction. This can be understood if the plane wave expansion is substituted in the Kohn-Sham-orbitals (Eq. (3.8)) for a given cutoff E^{cut} into the expression for the charge density (Eq. (2.28)):

$$n(\mathbf{r}) = \sum_{\mathbf{k},\nu} f^{occ}_{\nu,\mathbf{k}} \sum_{\mathbf{G}:\ |\mathbf{G}+\mathbf{k}|<G^{\max}} \ \sum_{\mathbf{G}':\ |\mathbf{G}'+\mathbf{k}|<G^{\max}} c_{\mathbf{k},\nu}(\mathbf{G}) c^*_{\mathbf{k},\nu}(\mathbf{G}') \exp\left(\mathrm{i}(\mathbf{G}-\mathbf{G}')\mathbf{r}\right). \tag{3.24}$$

This Fourier expansion contains components corresponding to wave vectors $\mathbf{G}-\mathbf{G}'$, which are up to twice as long as the longest wave vector of the plane wave basis. Hence, to exactly describe the charge density the minimum FFT $\mathbf{G}$-mesh must contain all wave vectors $\mathbf{G}$ up to a length of $2G^{\max}$ (Eq. (3.23)).

According to the sampling theorem [112] a minimum $\mathbf{R}$-mesh contains the same number of sampling points as the $\mathbf{G}$-mesh and the distance ΔR between two adjacent points in the $\mathbf{R}$-mesh (real space resolution) is given by:

$$\Delta R = \frac{\pi}{G^{\max}}. \tag{3.25}$$

The minimum FFT mesh to describe the charge density is also sufficient to describe the operators contributing to the plane wave Hamiltonian (Eq. (3.17)), as long as these operators are linear functionals of the charge density. This is the case for all operators contributing to the Hamiltonian, except for the XC potential. Treating the XC potential on the minimum FFT mesh introduces numerical errors in the calculations. This issue is discussed in Sec. 3.4.2.

3.2 Hellmann-Feynman forces

The previous section 3.1 has provided us with all necessary tools to determine the ground state properties, i.e., Born-Oppenheimer surface (ground-state energy) and electron distribution for given ionic positions. The main scope of this project, however, involves the determination of the ionic dynamics, i.e., the vibrations of the peptide chain.

To solve the ionic equations of motion it is necessary to determine the *derivatives* of the Born-Oppenheimer surface (BOS) with respect to the ionic positions, i.e., the inter-atomic forces. Hereby the *Hellmann-Feynman theorem* is very helpful. It states that the derivative of the ground-state energy is given as the expectation value of the first derivative of the electronic Hamiltonian:

$$\begin{aligned}
\frac{dE_g(\mathbf{X})}{d\mathbf{R}_I} &= \frac{d}{d\mathbf{R}_I}\langle\Psi_g(\mathbf{X}) \mid H^{\mathrm{el}}(\mathbf{X}) \mid \Psi_g(\mathbf{X})\rangle \\
&= \Bigg(\langle\frac{d}{d\mathbf{R}_I}\Psi_g(\mathbf{X}) \mid H^{\mathrm{el}}(\mathbf{X}) \mid \Psi_g(\mathbf{X})\rangle + \\
&+ \langle\Psi_g(\mathbf{X}) \mid H^{\mathrm{el}}(\mathbf{X}) \mid \frac{d}{d\mathbf{R}_I}\Psi_g(\mathbf{X})\rangle + \\
&+ \langle\Psi_g(\mathbf{X}) \mid \frac{d}{d\mathbf{R}_I}H^{\mathrm{el}}(\mathbf{X}) \mid \Psi_g(\mathbf{X})\rangle\Bigg) \qquad (3.26) \\
&= \langle\Psi_g(\mathbf{X}) \mid \frac{d}{d\mathbf{R}_I}H^{\mathrm{el}}(\mathbf{X}) \mid \Psi_g(\mathbf{X})\rangle. \qquad (3.27)
\end{aligned}$$

The first two terms of Eq. (3.26) vanish, since:

$$\begin{aligned}
&\langle\tfrac{d}{d\mathbf{R}_I}\Psi_g(\mathbf{X}) \mid H^{\mathrm{el}}(\mathbf{X}) \mid \Psi_g(\mathbf{X})\rangle + \langle\Psi_g(\mathbf{X}) \mid H^{\mathrm{el}}(\mathbf{X}) \mid \tfrac{d}{d\mathbf{R}_I}\Psi_g(\mathbf{X})\rangle \qquad (3.28) \\
&= 2E^{\mathrm{el}}\tfrac{d}{d\mathbf{R}_I}\langle\Psi_g(\mathbf{X}) \mid \Psi_g(\mathbf{X})\rangle = 0. \qquad (3.29)
\end{aligned}$$

Thus to determine the inter-atomic forces only the expectation value of Eq. (3.27) and the derivative of the ion-ion potential have to be evaluated:

$$\mathbf{F}_I(\mathbf{X}) := -\frac{dE_g^{\mathrm{el}}(\mathbf{X})}{d\mathbf{R}_I} = -\frac{dE_g^{\mathrm{e}}(\mathbf{X})}{d\mathbf{R}_I} - \frac{dV^{\mathrm{ion-ion}}}{d\mathbf{R}_I}. \tag{3.30}$$

These contributions can be calculated straightforwardly, once the ground state electron density has been found by solving the Kohn-Sham equations[5]. The explicit terms of the Hellmann-Feynman forces have been discussed in detail in Ref. [108].

Eq. (3.27) is in general, however, not exact when a *localized* basis set is applied to expand the electronic system. If this basis set is incomplete (and this is usually the case in a calculation) in general additional, artificial terms occur, which arise from the explicit dependence of the basis set on the atomic coordinates. These forces are called *Pulay forces*. The treatment of Pulay forces significantly complicates the calculation of the ionic forces. Fortunately, the plane wave basis does not depend on the atomic coordinates. Therefore, the Pulay forces are always zero in a plane wave basis. This is a (further) important advantage over a localized basis set.

The computational cost for calculating the Hellmann-Feynman forces in the plane wave basis is approximately the same as that for one iterative step in the self consistent cycle. This high efficiency provides an important support for all the following steps of the dynamical analysis: Regardless if we determine the equilibrium structures, the harmonic vibrational spectra, or the anharmonic contributions – all these procedures heavily involve the calculation of the forces.

3.3 Geometry optimization

Before we can determine the vibrational spectrum of a given conformation of the peptide chain, we have to determine the corresponding equilibrium structure. To perform geometry optimizations we have implemented a *quasi-Newton* scheme into S/PHI/nX. The quasi-Newton scheme is a parameter free second order optimization scheme. A detailed discussion of this scheme is given in Ref. [43], here we restrict ourselves to write down only the essential formulas. In each optimization step the geometry is updated by:

$$\Delta\mathbf{X}^{\mathrm{n}+1} = (\mathbf{K}^n)^{-1}\mathbf{F}^n, \tag{3.31}$$

where $\mathbf{K}$ corresponds to the Hessian matrix:

$$\mathbf{K}_{ij} = \frac{\partial^2 E^{\mathrm{el}}}{\partial X_i \partial X_j}. \tag{3.32}$$

The Hessian matrix is not known from the beginning, therefore it is *on-the-fly* updated after each structure step according to the Broyden-Fletcher-Goldfarb-Shanno (BFGS) [113, 114, 115, 116]

---

[5] The Hellmann-Feynman theorem can be generalized to the so called $(2n+1)$-theorem, which states that the knowledge of the derivatives up to order n allows to calculate the derivatives of the energy up to order $2n+1$.

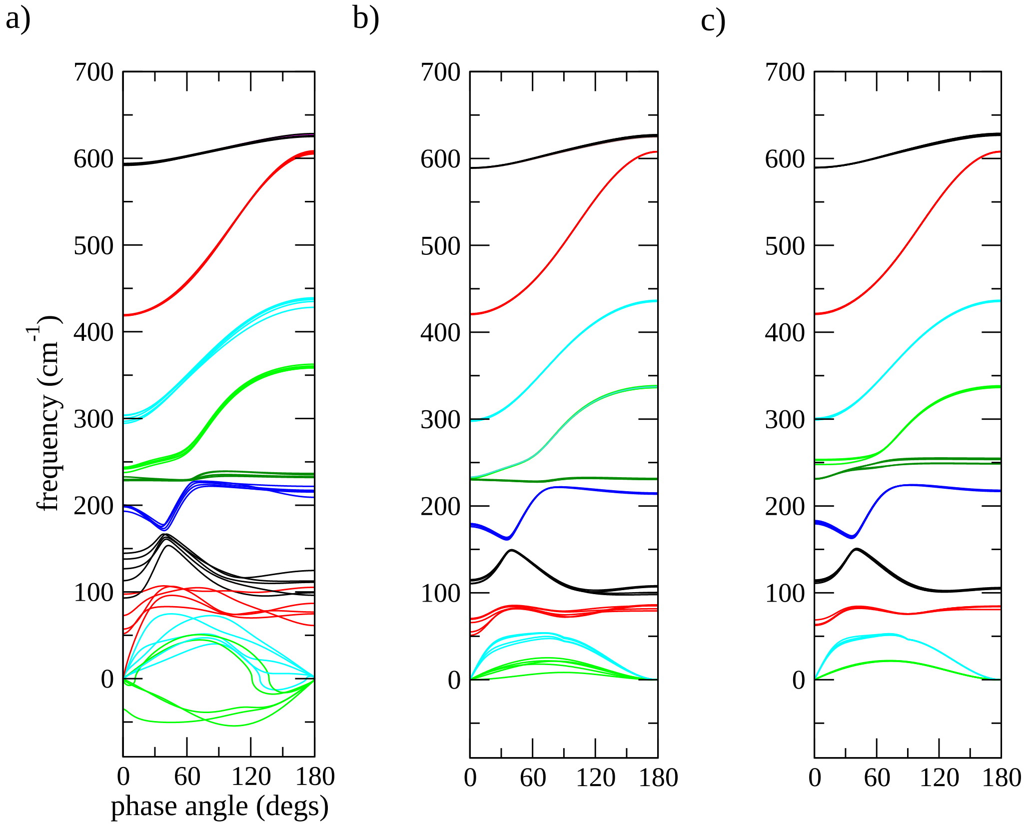

Figure 3.3: Numerical noise in the low frequency branches of the fully extended structure (FES) of the poly-L-alanine chain: a) Determined with the standard finite differences scheme as described in Sec. 3.4.1 and without smoothing the XC contributions. b) Determined with the standard finite differences scheme and with a (2-fold) smoothing of the XC contributions as described in Sec. 3.4.2, c) Determined with the TSR scheme as described in Sec. 3.4.3. The numerical noise is determined by performing the calculation of the dynamical matrix for (five) different, arbitrarily chosen positions of the FES in the supercell. In the absence of numerical noise these calculations are equivalent and would yield exactly the same vibrational spectra.

scheme:

$$\Delta\mathbf{K}^{n+1} = \frac{\Delta\mathbf{F}^n(\Delta\mathbf{F}^{n+1})^\dagger}{(\Delta\mathbf{X}^n)^\dagger\Delta\mathbf{F}^n} - \frac{\mathbf{K}^n\Delta\mathbf{X}^n(\Delta\mathbf{X}^n)^\dagger\mathbf{K}^n}{(\Delta\mathbf{X}^n)^\dagger\mathbf{K}^n\Delta\mathbf{X}^n}. \tag{3.33}$$

After each step of the geometry optimization, geometry and forces are symmetrized according to the helical symmetry. The geometries are optimized up to a certain maximum value for the remaining force of $2.5 * 10^{-5}$ Hartree/Bohr, since a convergence test revealed that this accuracy is needed to obtain an accurate vibrational spectrum (details in Appendix, Sec. 6.1.1). Starting geometries were obtained from previous projects [50, 51].

3.4 Phonon spectra and thermodynamic properties

Having obtained the equilibrium structures we may determine the vibrational frequencies of the peptide chain. These are given by the square-roots of the mass-scaled curvatures at the local minima of the Born-Oppenheimer surface (Sec. 2.6.2). To determine the curvatures, we employ a finite differences scheme, i.e., we compute them from the force responses to small displacements of individual ions from the equilibrium structure. The corresponding standard procedure, in which the ionic displacements along the Cartesian basis vectors are taken, is implemented nowadays in numerous available DFT codes or software packages for phonon calculations. However, we found that such a procedure is inadequate to perform the necessary calculations for this project. The main problem is numerical noise. Its influence on the calculated frequency spectra is severe, particularly for determining the low frequency branches with $\omega < 300\text{cm}^{-1}$ and the thermodynamic properties of the peptide chain, as is shown for the example of the fully extended structure (FES) of the poly-L-alanine chain in Fig. 3.3a. It is therefore required to go beyond the standard procedure.

To reduce the impact of numerical noise, we combine two strategies: First, the main source of numerical noise, which is located in the exchange-correlation potential, is directly reduced by developing a smoothing scheme (Sec. 3.4.2). Second, the standard procedure is extended by employing an adapted basis to expand the finite differences (Sec. 3.4.3). This allows us to use larger finite differences as it is possible in the standard scheme and, hence, to increase the fraction of the "physical" part of the Hellmann-Feynman forces[6]. It is important to mention that only the combination of these two strategies allowed us to achieve the required numerical accuracy. The resulting method for calculating the dynamical matrix is a three-stages refinement (TSR) scheme, where subsequent stages constitute an improvement in accuracy over the previous ones. By means of the TSR scheme it is possible to reduce the numerical error in the frequencies by more than an order of magnitude (Fig. 3.3c). We remark that this high accuracy is crucial for all the results derived for the project. For a detailed analysis of the considered sources of error and an estimation of the remaining numerical uncertainty see appendix, Sec. (6.1.1).

Below, first the finite differences approach is introduced. Then the smoothing scheme for the XC contributions is explained and finally the TSR scheme is described in detail.

3.4.1 Finite differences approach

Following Sec. 2.6.4, a basic requirement to obtain the phonon dispersion relation of the peptide chain is the knowledge of the dynamical matrix $\mathbf{D}^{\mathrm{c}}(\varphi)$. To determine the dynamical matrix within the supercell approach we replace the exact expression of Eq. (2.92) by a finite summation:

$$\mathbf{D}^{\mathrm{c}}(\varphi) = \sum_{n=-n^{\max}}^{n^{\max}} \mathbf{D}^{\mathrm{c}}(n) \exp(-\mathrm{i}\varphi n). \tag{3.34}$$

Here, n labels the peptide units of the chain, and the bound $n^{\max}$ for the summation in Eq. (3.34) is a cutoff and limits intra-chain vibrational coupling up to the $n^{\max}$th nearest neighbor. The cutoff is inherently dictated by the chosen size of the supercell, i.e., it corresponds to half the number of peptides contained in the supercell. The accuracy of Eq. (3.34) depends on whether or not significant long-ranged interactions exist beyond the cutoff distance $n^{\max}$. This has been tested by

---

[6] "Physical" means here the part of the forces that would remain in the absence of any numerical noise.

performing convergence checks with respect to $n^{\max}$ (Sec. 6.1.1).

Once an appropriate cutoff radius $n^{\max}$ has been determined by choosing an appropriate supercell size, the remaining task is the evaluation of the dynamical matrices $\mathbf{D}^{\mathrm{c}}(n)$ for $|n| \leq n^{\max}$, which correspond to the interaction of a given peptide (where $n = 0$) with its n^{th} nearest neighbor.

Standard procedure

When following the standard way of calculating phonons, the dynamical matrix $\mathbf{D}^{\mathrm{c}}(n)$ is determined in a basis spanned by the displacements of the atoms along the Cartesian coordinate axes. More precisely, we choose an arbitrary peptide unit from the peptide chain, which we label with the index $n = 0$. In this peptide unit each atom is displaced by a small distance Δs along each Cartesian direction, once parallel to it and once anti-parallel. This results in a total number of $2 \cdot 3 \cdot N^{\mathrm{APP}}$ displaced geometries:

$$\mathbf{X}^{i+/-} : \;=\; \mathbf{X} \pm \Delta s \cdot \mathbf{e}^{i} \tag{3.35}$$

where $\mathbf{X}$ is the equilibrium geometry, i labels the Cartesian degrees of freedom in the peptide unit with $n = 0$, $\mathbf{e}^{\mathrm{i}}$ is the unity vector corresponding to the i^{th} of these degrees of freedom, and $+/-$ symbolizes, whether the corresponding atom is displaced parallel ($'+'$) or anti-parallel ($'-'$) to the unity vector. We then evaluate, for each of these geometries, the respective electronic ground state and the Hellmann-Feynman forces $\mathbf{F}^{i+/-} := \mathbf{F}|_{\mathbf{X}^{i+/-}}$. From these forces we may construct the Hessian matrix in Cartesian coordinates, since:

$$\begin{aligned}
\mathbf{K}^{\mathrm{cart}}_{ij}(n) &= \frac{\partial^2 E^{\mathrm{el}}}{\partial X_i(0) \partial X_j(n)} && (3.36)\\
&= \frac{\partial F_j(n)}{\partial X_i(0)} \\
&= \lim_{\Delta s \to 0} \frac{F_j^{i+} - F_j^{i-}}{2\Delta s} && (3.37)\\
&\approx \frac{F_j^{i+} - F_j^{i-}}{2\Delta s}. && (3.38)
\end{aligned}$$

The Hessian matrices $\mathbf{K}^{\mathrm{cart}}(n)$ are then transformed to the dynamical matrices $\mathbf{D}^{\mathrm{c}}(n)$ and the phonon dispersion may be calculated.

Fig. 3.3a shows, however, that following this standard procedure leads to, in terms of an accurate vibrational and thermodynamic analysis, useless results. In particular the obtained low frequency branches, where $\omega < 300$ cm^{-1}, strongly depend on the position of the structure in the coordinate frame of the supercell. This dependence is completely artificial and therefore indicates a strong impact of numerical noise. The example of the poly-L-alanine FES reveals a scattering of up to 100 cm^{-1} for the lowest vibrational branch, which roughly corresponds to three times the absolute value of this branch.

We remark that the numerical error has been found to be resistant to changes of any of the "standard" convergence parameters of the plane wave methodology, such as the cutoff energy, the

FFT mesh size, and the accuracy of the electronic loop. Consequently, to uncover the origin of the numerical noise, it is required to have a closer look at the implementation.

3.4.2 Exchange-correlation wiggles

A valuable indication regarding the origin of the numerical noise was obtained, by performing calculations using LDA instead of PBE-GGA to describe the exchange-correlation (XC) interaction: Then the numerical noise largely disappeared. The LDA functional is not a viable option to perform the calculations for this project, since it does not adequately describe the hydrogen bonds in the helical conformations of the peptide chain (Sec. 2.4.3). However, the comparison between LDA and PBE-GGA shows that the numerical noise is due to the basic difference between the two functionals, i.e., the gradient correction in the PBE functional.

In order to understand this problem, we have a closer look at the implementation of the XC functional in the plane wave formalism. Here the local XC energy is discretized on the minimum FFT mesh and the continuous, analytical real space integration defining the XC energy (Eq. (2.41)) is replaced by the respective discretized summation over the FFT mesh [117]:

$$\widetilde{E}^{\mathrm{xc}}[n] := \frac{\Omega}{N} \sum_{\mathbf{r}_{ijk}} f^{\mathrm{xc}}\left(n(\mathbf{r}_{ijk}), \nabla n(\mathbf{r}_{ijk})\right) n(\mathbf{r}_{ijk}). \tag{3.39}$$

In this representation all Fourier components of f^{xc} with $\mid \mathbf{G} \mid^2 > 2E^{\mathrm{cut}}$ are set equal to zero and the XC-energy is treated as a *function* of the electron densities only at the mesh points $\mathbf{r}_{ijk}$, rather than as a *functional* of the (continuous) electron density [117].

We, however, recall that the XC functional is, in contrast to the remaining contributions to the ground state energy, i.e., Hartree energy, electron-ion interaction and kinetic energy, a *non-linear* functional of the charge density. Hence it is not exactly described on the minimum FFT mesh corresponding to the charge density, and, in contrast to the former contributions, gives rise to Fourier components for $\mid \mathbf{G} \mid^2 > 2E^{\mathrm{cut}}$. The deviations from the linearity are numerically negligible, as long as the local XC energy is a *slowly* varying function of $\mathbf{r}$, as is the case for the LDA XC functional. However, in contrast to LDA, the gradient corrected functionals (Eq. (2.41)), like the PBE functional, contain terms of the form:

$$\mid \nabla n \mid, \nabla^2 n, \text{ or } \nabla n \nabla \mid \nabla n \mid . \tag{3.40}$$

These terms may rapidly vary with $\mathbf{r}$ and therefore give rise to larger Fourier components for $\mid \mathbf{G} \mid^2 > 2E^{\mathrm{cut}}$. Therefore, the gradient correction could indeed be the origin of the observed numerical fluctuations in the calculation.

To investigate this possibility by means of a simple example, we show in Fig. 3.4a the total energy of an isolated carbon atom that is moved across the real space (supercell). In the absence of numerical noise the energy should be constant. This is almost perfectly accomplished when the LDA functional is employed (Fig. 3.4a, green line). However, it is *not* the case, when PBE-GGA is used (Fig. 3.4a, black line). Hence, a *spurious* dependence of the total energy on the *relative*

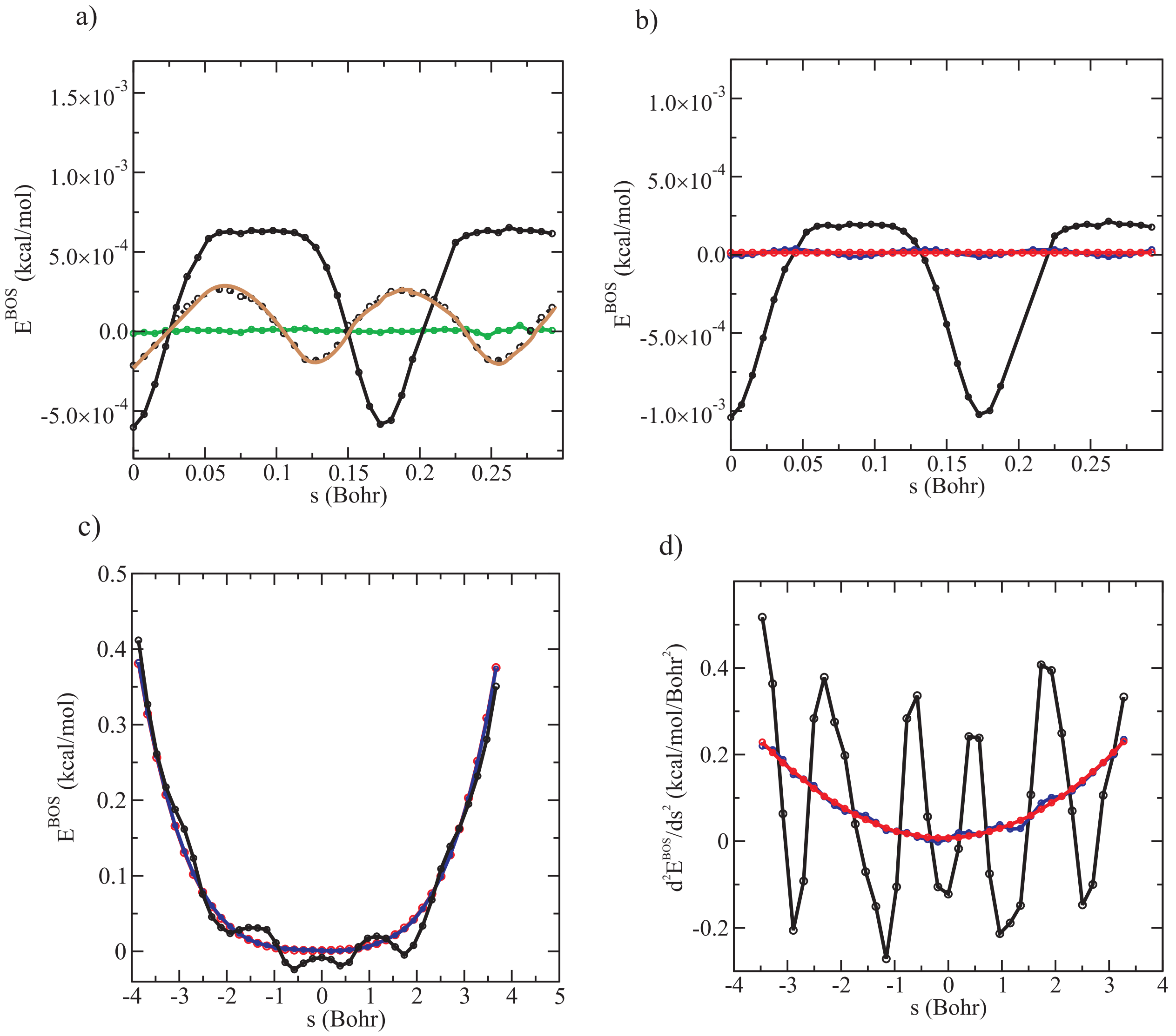

Figure 3.4: a) “XC wiggles”: Born-Oppenheimer energy for a carbon atom that is moved along the diagonal of the supercell (, i.e., along the (111) direction in the FFT mesh), calculated by employing the PBE functional and a cutoff energy of 70 Ry (black line) and 140 Ry (brown line). Further shown is the corresponding curve for the LDA functional at 70 Ry (green line). b) “XC wiggles” for the carbon atom without any smoothing (black line, same quantity as in a)), for a 2-fold smoothing of the XC wiggles (blue line) and for a 4-fold smoothing (red line). The smoothing is explained in Eqs. (3.41-3.48) c) Born-Oppenheimer energy along the eigenmode corresponding to the lowest frequency branch of the poly-L-alanine FES at $\varphi = 90°$ without smoothing the XC wiggles (black line), for a 2-fold smoothing (blue line) and a 4-fold smoothing (red line). d) Corresponding second derivatives along that eigenmode.

position of the atoms with respect to the FFT mesh exists, which is caused by the discretization of the gradient corrections of the PBE-GGA functional. This problem has been recognized earlier by White&Bird, who introduced the connotation "wiggles" for it [117].

For studies solely related to total energies these XC wiggles are harmless, since their magnitudes are very small. However, for the calculation of the first and in particular the second derivatives of the Born-Oppenheimer surface, i.e., the forces and the vibrational frequencies, the impact of the XC wiggles can reach a magnitude, which is as large as or even larger than the "physical" forces/frequencies. In fact the XC wiggles heavily modify the low frequency branches of the peptide chain. This is demonstrated for the example of the lowest frequency (acoustical) branch of the poly-L-alanine FES: In Fig. 3.4c and 3.4d the total energy and, respectively, the curvature along the eigenmode representing this branch is plotted. As can be seen, the XC wiggles have a strong impact on the energy curve. Consequently, the curvature, which determines the vibrational frequency, is heavily oscillating, making an accurate determination of the vibrational frequency impossible.

Removing the XC wiggles

The XC wiggles have thus been identified as the main source of numerical errors in the calculation. Note again that the problem with the XC wiggles may not be solved by just increasing the cutoff energy or simply increasing the FFT mesh size[7]. Fig. 3.4a shows that even using twice the cutoff as required for convergence of the total energy for the "physical" aspects of the calculation, the XC wiggles are not removed. A similar behavior has been found when doubling the FFT mesh size.

In order to solve the problem with the XC wiggles we introduce a "smoothing" strategy. For this purpose, we rewrite the Born-Oppenheimer surface:

$$E^{\mathrm{el}'}(\mathbf{X}) = \frac{1}{\Omega^{\mathrm{vx}}} \int_{\Omega^{\mathrm{vx}}} d^3r' E^{\mathrm{el}} \left(\mathbf{X}_1 + \mathbf{r}', \mathbf{X}_2 + \mathbf{r}', ..., \mathbf{X}_{N^{\mathrm{ion}}} + \mathbf{r}'\right), \tag{3.41}$$

where $\mathbf{X} = (\mathbf{X}_1, \mathbf{X}_2, ...\mathbf{X}_{N^{\mathrm{ion}}})$ denotes the configurational vector of the ions (Sec. 2.2) and $\mathbf{r}'$ denotes an *uniform* translation of the structure (with respect to the FFT mesh). The integration in Eq. (3.41) performs an average (smoothing) over the *voxels* of the FFT mesh. The voxels are defined as the volume Ω^{vx} spanned by the vectors, which connect a point of the $\mathbf{R}$-mesh (real space FFT mesh) with its next nearest neighbors lying in the three lattice directions. This definition of the Born-Oppenheimer energy is "wiggle-free":

$$E^{\mathrm{el}'}(\mathbf{X}) = E^{\mathrm{el}'} \left(\mathbf{X}_1 + \mathbf{r}, \mathbf{X}_2 + \mathbf{r}, ..., \mathbf{X}_N + \mathbf{r}\right), \tag{3.42}$$

since the wiggles are periodic with the voxels of the FFT mesh. Therefore, we may remove the XC wiggles from the calculation by computing the Born-Oppenheimer energy (and accordingly all its derivatives) corresponding to this new definition.

To explain the method of determining $E^{\mathrm{el}'}(\mathbf{X})$, it is recalled that the XC wiggles are exclusively

---

[7] Increasing the cutoff energy or the FFT mesh size is actually often spuriously assumed to be a proper solution for the XC wiggles problem. We remark that, in principle, an extremely high cutoff energy of several thousands of Ry would indeed allow to effectively reduce the wiggles. However such high cutoff energy is not a viable option for reasons of computational efficiency.

caused by the XC part of the Kohn-Sham Hamiltonian, since all remaining contributions to the Kohn-Sham Hamiltonian are linear in the electron density and therefore invariant with respect to the position of the FFT mesh. Therefore, the correction has to be performed only for the XC contributions, i.e., XC potential and the XC energy:

$$V^{\mathrm{xc}'}(\mathbf{R}) = \frac{1}{\Omega^{\mathrm{vx}}} \int_{\Omega^{\mathrm{vx}}} d^3r' V^{\mathrm{xc}}(\mathbf{R};\mathbf{r}'), \text{ and} \tag{3.43}$$

$$\epsilon^{\mathrm{xc}'}(\mathbf{R}) = \frac{1}{\Omega^{\mathrm{vx}}} \int_{\Omega^{\mathrm{vx}}} d^3r' \epsilon^{\mathrm{xc}}(\mathbf{R};\mathbf{r}'). \tag{3.44}$$

Here, $V^{\mathrm{xc}'}(\mathbf{R})$ and $\epsilon^{\mathrm{xc}'}(\mathbf{R})$ denote the "wiggle-free" XC potential and energy at mesh point $\mathbf{R}$, respectively, and $V^{\mathrm{xc}}(\mathbf{R};\mathbf{r}')$ and $\epsilon^{\mathrm{xc}}(\mathbf{R};\mathbf{r}')$ denote the "wiggled" quantities, which arise from a shift $\mathbf{r}'$ of the atomic geometry with respect to the FFT mesh. To evaluate the quantities $V^{\mathrm{xc}}(\mathbf{R};\mathbf{r}')$ and $\epsilon^{\mathrm{xc}}(\mathbf{R};\mathbf{r}')$ at first the electron density is shifted on the $\mathbf{R}$-mesh:

$$n^{\mathrm{shift}}(\mathbf{R}) = \sum_{\mathbf{G}} \left(\exp(\mathrm{i}\mathbf{G}(\mathbf{R}+\mathbf{r}')n(\mathbf{G})\right). \tag{3.45}$$

Then the XC energy and potential are calculated for the shifted charge density:

$$\epsilon^{\mathrm{xc,shift}}(\mathbf{R}), V^{\mathrm{xc,shift}}(\mathbf{R}) \tag{3.46}$$

and finally these quantities are "shifted back", by performing a translation along $-\mathbf{r}$' , to obtain the needed integrands of Eq. (3.43):

$$V^{\mathrm{xc}}(\mathbf{R};\mathbf{r}') = \sum_{\mathbf{G}} \left(\exp(\mathrm{i}\mathbf{G}(\mathbf{R}-\mathbf{r}'))V^{\mathrm{xc,shift}}(\mathbf{G})\right), \quad \text{and} \tag{3.47}$$

$$\epsilon^{\mathrm{xc}}(\mathbf{R};\mathbf{r}') = \sum_{\mathbf{G}} \left(\exp(\mathrm{i}\mathbf{G}(\mathbf{R}-\mathbf{r}'))\epsilon^{\mathrm{xc,shift}}(\mathbf{G})\right). \tag{3.48}$$

Here, $V^{\mathrm{xc,shift}}(\mathbf{G})$ and $\epsilon^{\mathrm{xc,shift}}(\mathbf{G})$ are the $\mathbf{G}$-mesh expansions corresponding to $V^{\mathrm{xc,shift}}(\mathbf{R})$ and $\epsilon^{\mathrm{xc,shift}}(\mathbf{R})$, respectively. To sample the volume Ω^{vx} we have tested a couple of simple schemes. The scheme, which has been found to be most systematic, is to generate the points $\mathbf{r}'$ on a sub-mesh, in which the sampling points are separated by a n^{th} fractional of the voxel dimensions.[8] Thus for $n = 2$ the voxel is sampled by 8 points, for $n = 3$ it is sampled by 27 points etc. In the following this scheme will be denoted as *n-fold averaging of the XC wiggles.*

The smoothing scheme has to be applied self-consistently for each step of the electronic minimization scheme. However, it is most effective to first fully converge to the "wiggled" BOS, and then, perform 3-5 steps applying the smoothing scheme, to obtain the "un-wiggled" BOS. The smoothing scheme increases the required computation time by a factor of approximately 1.5 for the 2-fold smoothing and a factor of approximately 4 for the 4-fold smoothing.

---

[8] This particular scheme is equivalent to representing the XC-contributions on a n-fold larger mesh with respect to the minimum FFT mesh. The averaging corresponds then to skipping the high Fourier coefficients in reciprocal space. The advantage of the smoothing scheme developed here in this regard is that it requires less memory.

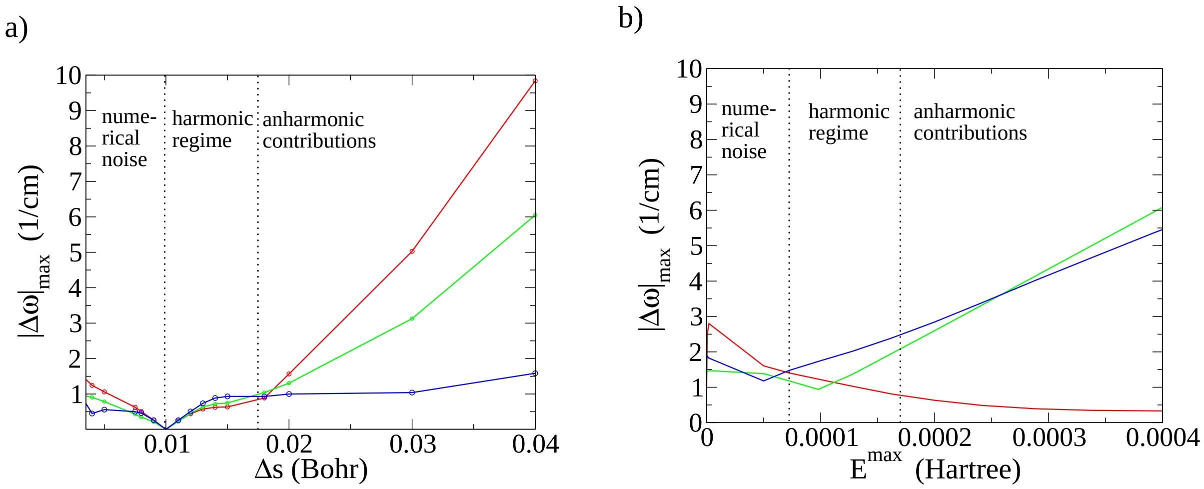

Figure 3.5: a) Maximum error in the harmonic frequencies, $|\Delta\omega|_{\mathrm{max}}$, for the poly-glycine 3_{10}-helix , if the dynamical matrix is determined in a Cartesian basis, i.e., by means of the standard finite difference scheme (Eq. (3.36)), plotted with respect to the atomic displacement, Δs. The plot shows $|\Delta\omega|_{\mathrm{max}}$ for the high frequency vibrations with $\omega > 3000$ cm^{-1} (red line), for the mid frequency interval with 200 cm^{-1} $< \omega <$ 3000 cm^{-1} (green line) and for the low frequency vibrations $\omega < 200$ cm^{-1} (blue line). The reference values to determine the error are taken from the calculation with $\Delta s = 0.01$ Bohr. b) Corresponding error, if the dynamical matrix is determined in the eigenbasis of the matrix $\mathbf{K}^{\mathrm{c}}(\varphi = 0)$ (Eq. (3.55)), plotted with respect to the convergence parameter E^{max}, as defined in Eq. (3.51). The calculations for both a) and b) have been performed by means of the SCCDFTB approach (Sec. 6.2.2) since they are computationally rather demanding.

The application of the smoothing scheme significantly reduces the impact of the XC wiggles. Already the 2-fold smoothing reduces the amplitude of the wiggles in the total energy of the carbon atom by several orders of magnitude (Fig. 3.4b). Consequentially, also the wiggles along the acoustical eigenmode of the peptide chain are reduced (Figs. 3.4c and d). Hence, we expect in general a significant improvement for the calculation of the vibrational spectrum of the peptide chain.

3.4.3 The TSR scheme

As expected, a significant reduction of the numerical noise is observed if the dynamical matrix is calculated by using a 2-fold smoothing of the XC wiggles (Fig. 3.3b). For the vibrational branches with $\omega > 200$ cm^{-1} the numerical error largely disappears. For the vibrational branches with $\omega < 200$ cm^{-1} the error is reduced by an order of magnitude. Nevertheless, the remaining error is still too large in terms of an accurate thermodynamic analysis.

Performing equivalent calculations with a 4-fold smoothing of the XC wiggles does not improve sufficiently the accuracy and using an even denser smoothing mesh than 4-fold makes the computational effort too high. Therefore, an alternative approach to further increase the accuracy is required.

Refined calculation of the dynamical matrix in its eigenbasis

An option to reduce the numerical noise in the calculation of the dynamical matrix is to use large finite displacements Δs for the evaluation of the finite differences quotients (Eq. (3.38)). Following this strategy does increase the ratio of the "physical" force response with respect to the "noise" part and consequently leads to numerically stable results. However, large displacements also introduce uncontrollable, artificial anharmonic contributions (Fig. 3.5a) since the equality of the Eqs. (3.37) and (3.38) is violated. In other words, in the Cartesian basis the necessary limitation to the harmonic regime does not allow to efficiently follow this option.

However, let us define Δs^{max} as the maximum displacement, which still maintains the equality of the Eqs. (3.38) and (3.37). In Fig. 3.5a we show that Δs^{max} is significantly larger for the low frequency region (Fig. 3.5a, blue line) of the vibrational spectrum, than it is for the high frequency region (Fig. 3.5a, red line):

$$\omega_1 > \omega_2 \quad \Rightarrow \quad \Delta s^{\mathrm{max}}(\omega_1) < \Delta s^{\mathrm{max}}(\omega_2). \tag{3.49}$$

To understand this dependence, we introduce, as a very simple model, an infinitely long, one-dimensional chain of atoms, which is linked together exclusively by nearest neighbor bonds. Two deformations of the chain segment are considered: i) a deformation s^{s}, which exclusively stretches a single bond of the chain and ii) a collective deformation s^{l}, which stretches all the bonds of a finite, N-atomic segment of the chain by the same value. Let $\Delta s^{\mathrm{max,s}}$ be the maximum possible displacement for the single-bond deformation. Then the maximum displacement $\Delta s^{\mathrm{max,l}}$ for the collective bond deformation is:

$$\Delta s^{\mathrm{max,l}} = \sqrt{\sum_{i=1}^{N} \left(\Delta s^{\mathrm{max,s}}\right)^2} = \sqrt{N} \Delta s^{\mathrm{max,s}}. \tag{3.50}$$

It follows that the energy E^{max} arising to the maximal displacement is the same for both displacements:

$$E^{\mathrm{max}} = \frac{1}{2} k^{\mathrm{l}} \left(\Delta s^{\mathrm{max,l}}\right)^2 = \frac{1}{2} k^{\mathrm{s}} \left(\Delta s^{\mathrm{max,s}}\right)^2, \tag{3.51}$$

where k^{l} and k^{s} are the harmonic force constants corresponding to the collective deformation and the single bond deformation, respectively:

$$k^{\mathrm{l}} = \frac{\partial^2 E}{\partial (s^{\mathrm{l}})^2} \text{ and } k^{\mathrm{s}} = \frac{\partial^2 E}{\partial (s^{\mathrm{s}})^2} = N k^{\mathrm{l}}. \tag{3.52}$$

Thus we have

$$\frac{\Delta s^{\mathrm{max,l}}}{\Delta s^{\mathrm{max,s}}} = \sqrt{\frac{k^{\mathrm{s}}}{k^{\mathrm{l}}}}, \tag{3.53}$$

and hence we may explain, by considering $k^{\mathrm{l}} > k^{\mathrm{s}}$ and $\omega(k) \approx \mathrm{const} \cdot \sqrt{k}$, the observation formulated in Eq. (3.49), i.e., that Δs^{max} is larger for the low frequency branches of the peptide chain than it is for the high frequency branches[9].

Even more important, we may employ these findings to improve the accuracy of the vibrational analysis: The idea is to take the displacements of the peptide chain not from the Cartesian basis but rather from an adapted basis, in which the collective (low frequency) deformations are decoupled from the single-bond (high frequency) deformations. Then we use a constant *energy* ΔE, instead of a constant displacement Δs, for displacing each degree of freedom to re-calculate the dynamical matrix. As a consequence we may use larger displacements for the low frequency branches as for the high frequency branches – and hence reduce the impact of the numerical noise.

To apply this idea, we at first rewrite Eq. (3.51) to derive an explicit expression for the choice of a proper adapted displacement $\Delta s^{\max}$:

$$\Delta s^{\max}(k) = \sqrt{\frac{2E^{\max}}{k}}. \tag{3.54}$$

Here k is a force constant, i.e., the second derivative of the energy with respect to a given (and properly chosen) displacement, and $\Delta s^{\max}(k)$ is the maximum displacement along that direction.

Then we derive a new set of displacement vectors. These have to be taken from an orthonormal basis, which on the one hand effectively decouples the collective deformations of the peptide chain from the single-bond deformations and on the other hand can be obtained from the Cartesian displacement basis by a unitary transformation. A basis, which meets these two requirements, is given by the eigenvectors of the symmetry reduced Hessian matrix at the Γ-point

$$\mathbf{K}^{\mathrm{c}}(\varphi = 0) = \sum_{n=-n^{\max}}^{n^{\max}} \mathbf{K}^{\mathrm{c}}(n), \tag{3.55}$$

Since a first guess for the Hessian matrix is required to apply this scheme, we have to perform a preceding calculation in the Cartesian basis (details below) for getting such guess. Provided we have performed this preceding calculation, a new Hessian is calculated by displacing the atoms according to the eigenvectors $\widetilde{\mathbf{X}}$ of $\mathbf{K}^{\mathrm{c}}(\varphi = 0)$ of the guessed Hessian matrix, thus:

$$\begin{aligned}
\widetilde{\mathbf{K}}^{\mathrm{c}}_{ij}(n) &= \frac{\partial^2 E^{\mathrm{el}}}{\partial \widetilde{X}_i(0) \partial \widetilde{X}_j(n)} && (3.56)\\
&= \frac{\partial \widetilde{F}_j(n)}{\partial \widetilde{X}_i(0)} && (3.57)\\
&\approx \frac{\widetilde{F}^{i+}_j - \widetilde{F}^{i-}_j}{2\Delta \widetilde{s}(k_i)}. && (3.58)
\end{aligned}$$

Here k_i denotes the eigenvalue of $\mathbf{K}^{\mathrm{c}}(\varphi = 0)$ corresponding to the i^{th} eigenvector and the finite displacement $\Delta \widetilde{s}(k_i)$ is obtained from Eq. (3.54). This matrix can be transformed to the refined

---

[9] To be exact: The frequency does also depend on the reduced mass corresponding to the vibrational eigenmode. This dependence plays, however, a minor role in this context.

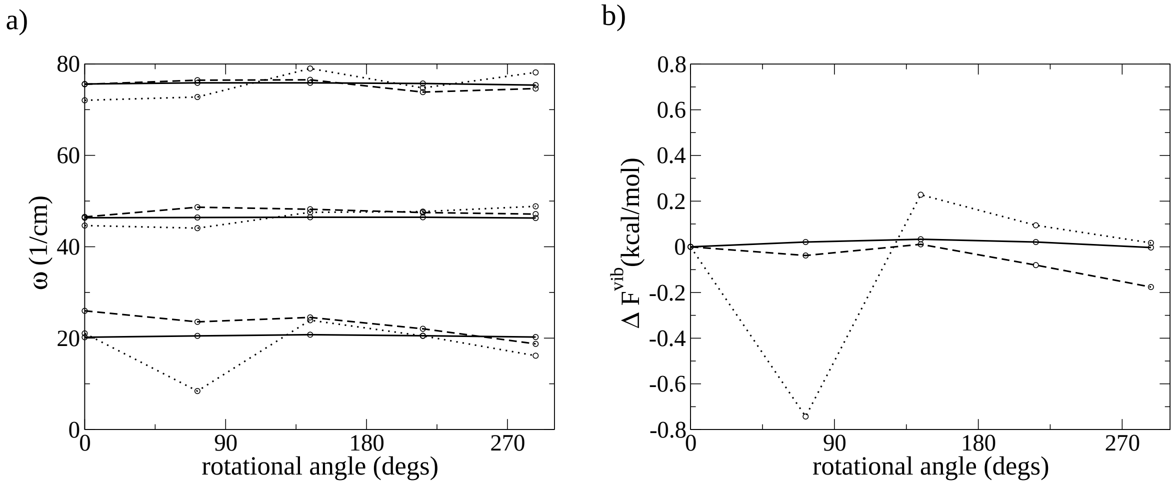

Figure 3.6: a) Vibrational frequency for the three lowest branches of the poly-L-alanine FES at $\varphi = 90^o$, and, b) vibrational free energy per peptide unit at 300 K, for five different rotational alignments of the structure relative to the FFT mesh. Shown are the values after the first (dotted lines), the second (dashed lines), and the third refinement stage (solid lines) of the TSR scheme. The (arbitrary) reference value for the free energies is here the free energy for the first structure.

dynamical matrix:

$$\mathbf{D}^{\mathrm{c}}(n) = \mathbf{M}^{-1/2}\mathbf{U}^{\dagger}\widetilde{\mathbf{K}}^{\mathrm{c}}(n)\mathbf{U}\mathbf{M}^{-1/2}, \tag{3.59}$$

where $\mathbf{U}$ is a unitary transformation and contains the eigenvectors of $\widetilde{\mathbf{K}}^{\mathrm{c}}$ as columns and $\mathbf{M}$ is a diagonal matrix containing the ionic masses. The parameter $E^{\max}$ in Eq. (3.54) has to be taken as large as possible to facilitate the maximum possible stability of the obtained vibrational spectrum against numerical noise and as small as necessary to prevent the influence of uncontrollable, artificial anharmonic contributions. An exemplary convergence check for $E^{\max}$ is shown in Fig. 3.5b. The ratio $\sqrt{k^{\mathrm{l}}/k^{\mathrm{s}}}$ is typically about 5-10 for the peptide chain. Thus a 5-10 times larger displacement can be used for the low frequency branches if displacements in the eigenbasis of $\mathbf{K}^{\mathrm{cyl}}(\varphi = 0)$ are employed instead of the displacements in the Cartesian basis.

The three stages of the refinement scheme

In order to effectively decouple the low frequency modes from the high frequency modes, prior knowledge about the system is required, i.e., a first guess for the dynamical matrix. For this reason the refinement calculation is embedded in a three stages scheme.

In the *first stage* the dynamical matrix is calculated by means of the standard finite differences procedure as described in Eqs. (3.36-3.38). Here a 2-fold smoothing is used to reduce the XC wiggles. The remaining numerical error in the frequencies after the first stage has been estimated to be about 15 cm^{-1} (Fig. 3.6a, dotted lines). The corresponding error in the vibrational free energies is 0.8 kcal/mol (per peptide unit) at 300 K (Fig. 3.6b, dotted lines).

In the *second stage* the dynamical matrix is (re-)calculated by means of the refinement procedure as described in Eqs. (3.55-3.59). It is usually sufficient to perform the second refinement stage only for eigenvectors corresponding to the 5-10 lowest eigenvalues of $\mathbf{D}^{\mathrm{c}}(\varphi = 0)$, which corresponds to the vibrational frequencies with $\omega < 300$ cm^{-1}. Thus the computational effort of the second refinement stage reduces to about 30 percent of the computational effort of the first stage. The accuracy after the second stage is significantly improved compared to the first stage: For the vibrational frequencies the maximal error is about 10 cm^{-1}(Fig. 3.6a, dashed lines), the error in the corresponding vibrational free energies at 300 K is reduced to about 0.2 kcal/mol per peptide unit (Fig. 3.6b, dashed lines). However, for some specific applications, for example for a comparison of the relative thermodynamic stability between the helical conformations the accuracy is still not sufficient.

The remaining error is exclusively located in the low frequency branches with $\omega < 100$ cm^{-1}. To further improve the accuracy, it is therefore sufficient to focus on this part of the vibrational spectrum. In the *third stage* of the TSR scheme such low frequencies are re-calculated by directly sampling the Born-Oppenheimer surface (BOS) along the corresponding vibrational eigenmodes $\mathbf{L}_i^{\mathrm{cell}}$ of the dynamical matrix $\mathbf{D}^{\mathrm{cell}}$:

$$\mathbf{D}^{\mathrm{cell}}\mathbf{L}_i^{\mathrm{cell}} = \omega_i^2\mathbf{L}_i^{\mathrm{cell}}. \tag{3.60}$$

Here, the superscript “cell” refers to the dynamical matrix and eigenvectors in the real-space notation corresponding to the supercell (see Appendix, Sec. 6.6.2).

To sample the BOS we use here a 4-fold smoothing of the XC wiggles, in contrast to the stages one and two, where a 2-fold smoothing has been used. The BOS is sampled along the eigenmodes at five equidistant points and the frequencies are obtained by means of a harmonic fit through these five points. The maximum error in the vibrational frequencies after the final stage of the TSR scheme is about 3 cm^{-1} (Fig. 3.6a dotted lines, and Fig. 3.3c). The error in the corresponding vibrational free energies at 300 K is about 0.03 kcal/mol per peptide unit (Fig.3.6b, dotted lines). This numerical accuracy is sufficient, but also necessary to perform a meaningful thermodynamic stability analysis of the peptide chain.

3.4.4 Sum rules and long-wavelength limits

The symmetry reduced dynamical matrix $\mathbf{D}^{\mathrm{c}}(\varphi)$ (Eq. (3.34)) and the phonon dispersion relation are thus determined using the dynamical matrix $\mathbf{D}^{\mathrm{c}}(n)$ that was obtained by means of the TSR scheme. Despite the effort that has been paid to reduce the numerical noise in the dynamical matrix, still a problem remains, which appears for the acoustical branches at the long-wavelength limits $\varphi \to 0$ and $\varphi \to \pm\Theta$. These branches are not exactly zero at the long-wavelength limits, as they should be according to the geometrical sum rules (Sec. 2.6.4). Further, the asymptotic behavior is rather discontinuous and “unphysical” (Fig. 3.7a, dotted lines).

To solve this problem, first the noise is eliminated *directly at* the long-wavelength limits by applying the sum rules, as is explained in the Appendix (Sec. 6.6.3), which, by construction, makes the long-wavelength limits equal to zero. However, the problem still remains for the asymptotic behavior of the acoustical branches in the proximate surrounding of the long-wavelength limit. In

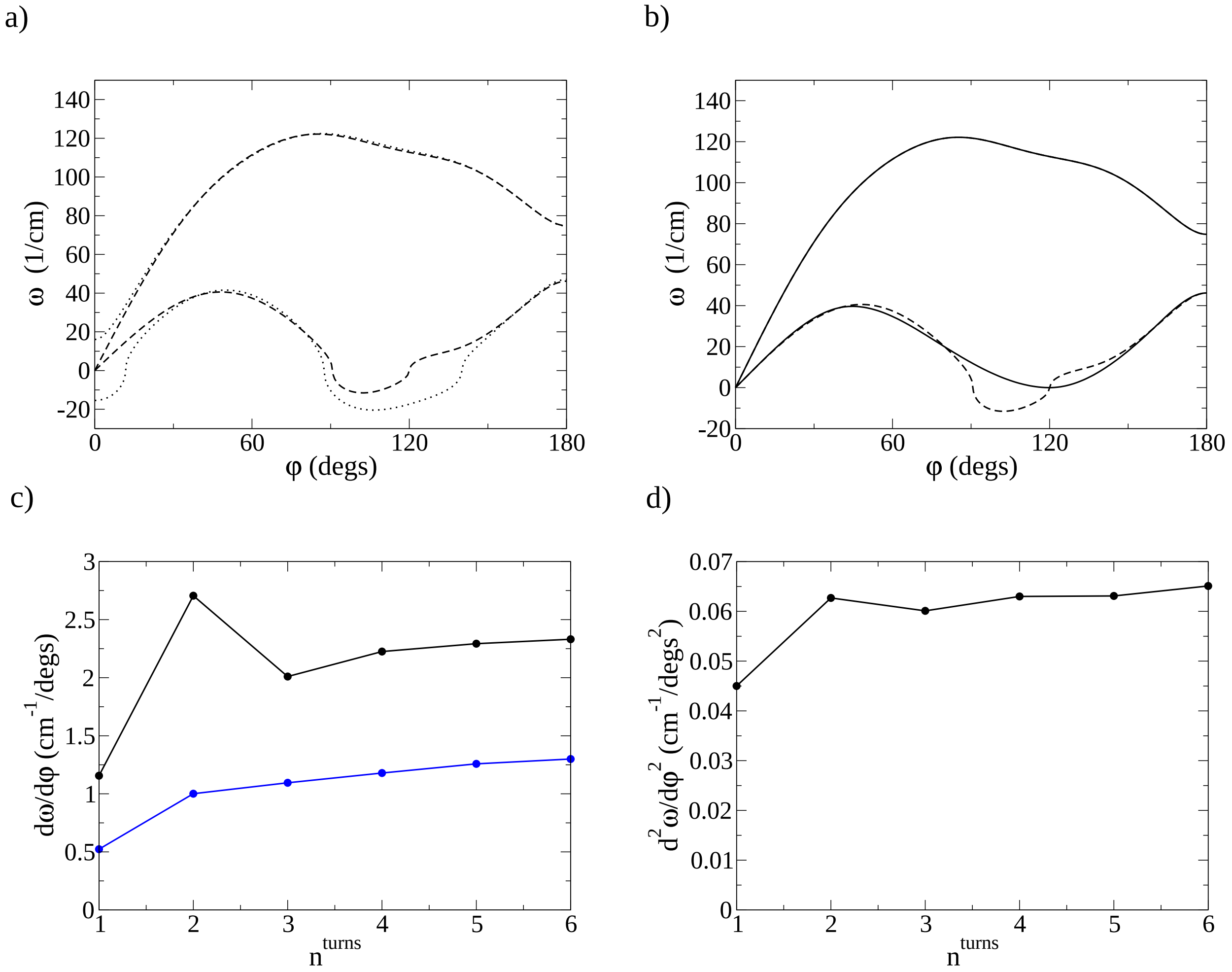

Figure 3.7: a) Acoustical branches, as calculated for the poly-glycine 3_{10}-helix: with (dashed lines) and without (dotted lines) applying the geometrical acoustical sum rules (Eq. (6.69)). b) Acoustical branches after Eq. (3.34) has been replaced by a spline interpolation for the long-wavelength region of the acoustical branches (solid lines). The negative frequency axis in the plot has been chosen to plot the imaginary frequencies. c) Slopes of the first (blue line) and second (black line) acoustical branch at the long-wavelength limit $\varphi \rightarrow 0$ plotted against the number of helix turns, n^{turns}, included in the supercell. d) Corresponding plot for the curvature of the first acoustical branch at the long-wavelength limit $\varphi \rightarrow \Theta$.

particular the first vibrational branch is problematic in the region close to Θ (Fig. 3.7a and b, dashed lines). To solve this problem the acoustical branches as given by Eq. (3.34) are replaced by a *cubic spline interpolation* in the proximate surroundings of the long wavelength limits (Fig. 3.7b, solid lines). The boundary values of the spline interpolation are chosen to smoothly migrate into the interpolation of Eq. (3.34) on the one side and to meet the long-wavelength conditions on the other side.

To verify the validity of the interpolation scheme, we have performed respective convergence tests for the long-wavelength limits of the acoustical branches using the SCCDFTB approach (Sec. 6.2.2). As a test system we chose the poly-glycine 3_{10}-helix. Figs. 3.7c and d show the long-wavelength limits plotted against the number of helical turns, n^{turns}, included in the supercell[10]. A smooth and monotonous behavior is observed for $n^{\mathrm{turns}} \geq 3$, which verifies the reliability of the used interpolation scheme. We remark that the long wavelength limits are not completely converged even for $n^{\mathrm{turns}} = 6$, which is supposed to be due to long-ranged (cooperative) effects accompanying the acoustical branches. However, it was found to be sufficient to include only three helical turns in the supercell to achieve convergence in the thermodynamic properties (details in the Appendix, Sec. 6.1.1).

3.4.5 Grüneisen-Mie equation of state

To investigate the thermal expansion of the peptide chain with respect to the helical parameters L and Θ and the corresponding corrections in the free energy, the Grüneisen-Mie equation of state (Eq. (2.122)) is solved for a given temperature T (and pressure $p = 0$). To solve Eq. (2.122) the quasi harmonic free energy surface (Eq. (2.119)) is completely parametrized. The Eq. (2.122) can then be solved in a post-processing stage without the need to perform any further DFT calculation. In a previous project it has been found that the coupling of the two lattice parameters in the BOS is negligible [50]. Thus it is a valid approximation to parametrize the BOS as follows:

$$E^{\mathrm{el}}(L,\Theta) = E^{\mathrm{el}}(L_0,\Theta_0) + E^{\mathrm{murn}}(L) + E^{\mathrm{murn}}(\Theta), \tag{3.61}$$

Here L_0 and Θ_0 are the helical parameters corresponding to the local minimum of the PES and E^{murn} are Murnaghan functions:

$$E^{\mathrm{murn}}(x) = \frac{k^x x}{k^{x\prime}(k^{x\prime}-1)}\left[k^{x\prime}(1-\frac{x_0}{x}) - (\frac{x_0}{x})^{k^{x\prime}} - 1\right], \tag{3.62}$$

with x being either L or Θ and:

$$k^x := x\frac{d^2E^{\mathrm{el}}(L,\Theta)}{dx^2}; \quad k^{x\prime} := \frac{dk^x}{dx}. \tag{3.63}$$

---

[10] We expect n^{turns} to be a suitable control parameter to monitor the quality of the interpolation scheme at the long wavelength limits, since the extend of the interpolated region of the long-wavelength limit can be systematically reduced by increasing this parameter (n^{max} in Eq. (3.34) is proportional to n^{turns}).

The free parameters of the Murnaghan equation are optimized to fit the (L, Θ)-PES in the vicinity of the local minima corresponding to the various equilibrium conformations of the peptide chain. The Murnaghan function has been found to accurately reproduce the BOS in the region, in which the thermal expansion takes place.

The vibrational free energy $F^{\mathrm{vib}}(L, \Theta)$ is parametrized within the framework of the Grüneisen theory, i.e., by means of linear Grüneisen parameters (Eq. (2.121)). The linear Grüneisen parameters for the L-dependence and the Θ-dependence are determined for each phase angle φ by a finite differences approach:

$$\gamma_i^x(\varphi) = -\frac{\partial \omega_i(\varphi)}{\partial x} \frac{x}{\omega_i(\varphi)} \approx \frac{\omega_i(x + \Delta x) - \omega_i(x - \Delta x)}{2\Delta x} \frac{x}{\omega_i(\varphi)}, \tag{3.64}$$

where x can be either L or Θ.

3.5 Thermodynamic integration

In the previous sections we have described how the electronic groundstate and the vibrational properties of the peptide chain in the (quasi-)harmonic approximation have been obtained. Going now beyond the harmonic approximation to include also anharmonic effects constitutes a further significant extension of the methodology applied in this study, since it enters the field of molecular dynamics simulations, as will be described in this section. Following Eqs. (2.126-2.127) the free energy including all anharmonic effects is given by:

$$F^{\mathrm{ah}}(T, L, \Theta) = F^{\mathrm{harm}}(T, L, \Theta) + \int_{\lambda=0}^{\lambda=1} d\lambda \left\langle \frac{\partial U(\lambda)}{\partial \lambda} \right\rangle_{\lambda,\Theta,L,T}, \tag{3.65}$$

where:

$$U(\lambda, \mathbf{X}) = \lambda E_g^{\mathrm{el}}(\mathbf{X}) + (1 - \lambda)\, \mathbf{X} \cdot \mathbf{K} \cdot \mathbf{X}^\dagger. \tag{3.66}$$

Here, $F^{\mathrm{harm}}(T, L, \Theta)$ is the free energy in harmonic approximation, $\mathbf{X}$ denotes the atomic configuration, $E_g^{\mathrm{el}}(\mathbf{X})$ denotes the Born-Oppenheimer surface, and $\mathbf{K}$ is the Hessian matrix (,i.e., the Born-Oppenheimer approximation in harmonic approximation).

To determine the anharmonic correction several steps have to be performed: Most important, the acquisition of the statistical average

$$\left\langle \frac{\partial U(\lambda)}{\partial \lambda} \right\rangle_{\lambda} \tag{3.67}$$

is required for a (sufficiently large) number of λ values. Having a proper scheme to determine them is of crucial importance for the efficiency of the thermodynamic integration, as is discussed in Secs. 3.5.1 - 3.5.3. In Sec. 3.5.4 we present the scheme we implemented for this purpose, i.e., the Langevin dynamics (LD). A crucial point for the efficiency of the LD simulation is the choice of the friction parameter – in Sec. 3.5.6 it is discussed how the optimum friction parameter has been found.

The schemes to determine the correlation time from a Langevin dynamics run and to parallelize a Langevin dynamics run are described in the appendix (Secs. 6.3.2 and 6.3.3, respectively).

3.5.1 Thermodynamic averages

For performing a thermodynamic integration the main computational task is to calculate the thermodynamic averages $\left\langle \frac{\partial U(\lambda)}{\partial \lambda} \right\rangle_\lambda$ for a given coupling parameter λ. In the field of computer simulations thermodynamic averages are commonly calculated from a finite series of data points:

$$\overline{A} = \frac{\sum_{n=1}^{N} A_n}{N}. \tag{3.68}$$

Here, the index n counts a total number of N microscopic states X_n of the system and $A_n = A(X_n)$ is the observable of interest.

We assume that the series $\{X_n\}$ has been extracted from the *canonical ensemble* corresponding to the system of interest. Canonical means here that the simulation scheme would, in the infinite limit, generate the canonical ensemble corresponding to the system. Then we may write:

$$\langle A \rangle = \mathrm{lim}_{\mathrm{N}\to\infty} \overline{A}, \tag{3.69}$$

i.e., in the *infinite* limit the geometric average of the observable over the series $\{X_n\}$ corresponds to the true thermodynamic average $\langle A \rangle$. In any case of a *finite* series $\{X_n\}$ the corresponding geometric average deviates from the true thermodynamic average within a certain statistical error bar. More precisely $\langle A \rangle$ falls within the range of values

$$\langle A \rangle = \overline{A} \pm a_N \frac{s}{\sqrt{N}}, \tag{3.70}$$

with a probability that depends on a_N, where a_N is a parameter of the Student's distribution for $N-1$ random variables[11] and s^2 is the variance:

$$s^2 = \frac{\sum_{n=1}^{N} \left(A_n - \overline{A}\right)^2}{N-1}. \tag{3.71}$$

We remark, however, that in practice, for many simulation schemes a properly long *equilibration time* is required to approach the thermal equilibrium. This ensures that the measured thermodynamic average is independent of the initial conditions of the simulation.

Besides the thermal equilibration, a further fundamental prerequisite for the Eqs. (3.67) and (3.69) is the statistical independence of the individual quantities A_n. This demand is not at all trivial. In most applications the data points stored in the series $\{X_n\}$ are highly correlated with each other and consequently only a small portion of the output may be used for "production", while a major part must be "thrown away". It is in fact one of the main challenges on an efficient simulation scheme to, if possible, reduce the *correlation length* of the output data set. The correlation length is defined as the distance from a data point in the series $\{X_n\}$ beyond which there is no further correlation of the physical observable associated with that point.

---

[11] A complete table for the $a_N^{\prime}s$ ranging from $N = 1...\infty$ and confidence intervals of 75% to 99.95% can be found for instance on http://en.wikipedia.org/wiki/Student's_t-distribution.

3.5.2 Choice of the simulation scheme

To generate a finite series $\{X_n\}$ of configurations representing the thermodynamic ensemble various different schemes have been developed in the past. These schemes can be roughly divided into two classes: the first class is given by the *Monte Carlo* (MC) schemes (MC) and the second class is given by the *molecular dynamics* (MD) schemes. A strict division is not possible, since, in many cases, schemes of the one class are extended by elements characterizing the other class. However, a brief introduction of the most rudimentary forms of MC and MD, respectively, is helpful to explain the main challenges towards an efficient simulation scheme to determine thermodynamic ensemble averages.

Monte Carlo schemes emphasize the importance of randomness for the canonical ensemble. Here, the series $\{X_n\}$ is generated exclusively through random numbers. A pure Monte Carlo scheme has the advantage that the generated series of microstates is (by definition) completely de-correlated. However, it has the disadvantage that it neglects any prior knowledge of the system in form of the potential energy function. The majority of systems generated by MC thus have an energy very different from the average value, therefore a major part of the computational time is wasted in calculating these microstates. This is expressed in a very large variance (Eq. (3.70)) on the calculated thermodynamic averages. MC schemes are therefore usually connected with *importance sampling methods,* as e.g. the Metropolis-Hastings algorithm [118].

In contrast to Monte Carlo schemes, Molecular dynamics schemes emphasize the importance of the potential energy function, i.e., the physical coherences characterizing the system. The series $\{X_n\}$ is generated based on solving the Newtonian equations of motion. Thermal fluctuations are generated either, in the case of *deterministic dynamics* by connecting a thermostat or a chain of thermostats, [119, 120, 121], or, in the case of *stochastic (Langevin) dynamics* by introducing a random force (more details in Sec. 3.5.4). Molecular dynamics schemes usually generate highly correlated data series, in contrast to Monte Carlo schemes. Thus, a major part of the computational time is wasted in de-correlating the time series. However, they have the advantage to implicitly contain importance sampling, i.e., the MD trajectory is automatically biased towards conformations that are significantly populated at equilibrium. Another advantage is that in case of self-consistent field approaches (like DFT) the strong correlation of the successive elements in $\{X_n\}$ enables the application of efficient extrapolation schemes for the electronic wavefunction and/or electron density, which significantly reduces the effort in the electronic loop (Sec. 3.5.5).

We have therefore decided to implement a MD type algorithm to determine the thermodynamic averages.

3.5.3 Comparison of Nose-Hoover dynamics and Langevin dynamics

We have implemented two different MD schemes and compared with one another: the Nose-Hoover dynamics [119, 120, 121] and the Langevin dynamics. The Nose-Hoover scheme corresponds to a standard deterministic molecular dynamics schemes, in which the canonical ensemble is realized by means of (thermal) oscillations of the total energy, as triggered by a thermostat (see Ref. [111] for more details). In contrast, the Langevin scheme corresponds to a stochastic molecular dynamics

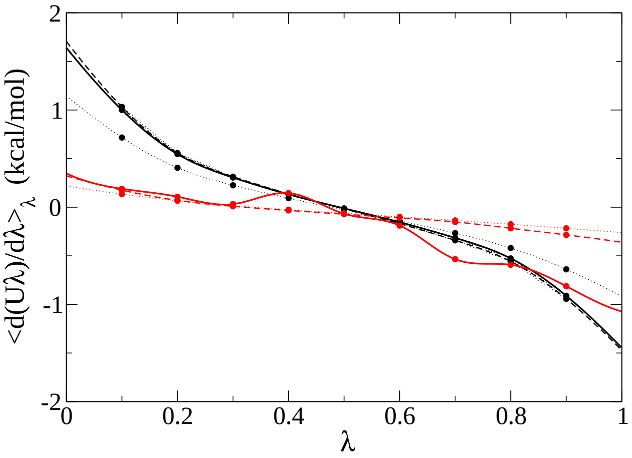

Figure 3.8: The statistical averages $\langle \frac{\partial U}{\partial \lambda} \rangle_\lambda$ along the thermodynamic integration path determined with Langevin dynamics (black lines) and Nose Hoover dynamics (red lines). As test system a poly-glycine FES and the SCCDFTB potential was used. Shown are the statistical averages after simulation times of 1 ps (dotted lines), 2.5 ps (dashed lines), and 50 ps (solid lines).

scheme, i.e., the canonical ensemble is here realized by means of a stochastic random force. We remark that the latter approach shows a dramatic increase in the computational efficiency as compared to the former scheme. This is demonstrated in Fig 3.8 for an exemplary test system, i.e., the poly-glycine FES (as potential we used the SCCDFTB approach , see Sec. 6.2.2): The statistical averages are much more rapidly converging for the Langevin dynamics than for the Nose-Hoover dynamics. In particular, for potentials $U(\lambda)$ with strong harmonic contributions, i.e., where $\lambda < 0.3$ we could not equilibrate the system at all, when using Nose-Hoover dynamics[12]. The equilibration and correlation times we obtained with the Langevin dynamics were, in contrast, largely independent of λ and for any λ much shorter as the correlation times found for Nose-Hoover dynamics. We thus decided to use the Langevin dynamics.

3.5.4 Langevin dynamics

The Langevin equations of motion are stochastic equations of motion:

$$m_I \ddot{\mathbf{X}}_I(t) = \mathbf{F}_I(t) - \gamma \dot{\mathbf{X}}_I(t) + \mathbf{R}_I(t), \tag{3.72}$$

i.e., they correspond to the Newtonian equations of motion, extended by a stochastic force term $-\gamma\dot{\mathbf{X}}_I + \mathbf{R}_I$, where $\mathbf{R}_I$ is a random force, generated by a Gaussian distribution, and γ is the so called friction parameter and will be discussed further below. One can show by means of the *fluctuation dissipation theorem* that the phase space trajectory of the Langevin equations of motion corresponds

---

[12] This problem is related to a well known deficiency of the Nose-Hoover scheme: it is not ergodic for harmonic oscillators [120]. The problem can be solved by using so called Nose-Hoover chains [122]. However, this scheme has not been implemented for this project, since satisfying results were already obtained by the Langevin dynamics.

to the classical canonical ensemble, provided the random force satisfies at any time the relations:

$$\langle \mathbf{R}_I \rangle = 0 \text{ and } \left\langle \mathbf{R}_I^2 \right\rangle = 6Nk_BT\gamma. \tag{3.73}$$

Here, $\langle \mathbf{R}_I \rangle$ and $\left\langle \mathbf{R}_I^2 \right\rangle$ denote the mean value and the variance of the time evolution of the random force, respectively, and N denotes the number of atoms.

The Langevin dynamics may thus be used to evaluate the canonical thermodynamic averages $\left\langle \frac{\partial U}{\partial \lambda} \right\rangle_\lambda$ (see Eq. (3.67)). However, the Langevin equations of motion are based on a classical picture of the motion of the ion cores. Thus quantum mechanical effects (like zero point vibrations) are completely excluded. The approach is therefore invalid for low temperatures and it has to be (and will be) verified that the temperature at which it is applied falls into the classical regime.

3.5.5 The BBK scheme

To integrate the Langevin equations of motion the van-Gunsteren-and-Berendsen (vGB) -scheme [123] has been implemented. This algorithm is, like any other molecular dynamics integration scheme, based on a discretized treatment of the time evolution, i.e., a finite time step Δt. The integration of the physical forces in this algorithm is equivalent to the integration of the forces in the Verlet algorithm, which is a widely used and efficient integration algorithm for deterministic MD. This implies that the (vGB)-scheme is symplectic and thus stable for long simulation times. Further, the size of the finite time step Δt applied to integrate the equations of motion is only limited by the fastest oscillation of the system, but not by the stochastic fluctuations. For our simulations we have used a timestep of $\Delta t = 1.8$ fs, which corresponds to about a fifth of the oscillation period of the Hydrogen stretching modes, which are the fastest oscillations in the peptide chain.

The explicit formulas of the vGB-scheme can be found elsewhere [123]. Instead, we restrict on outlining the integration algorithm as described in Ref. [123]. A single iteration in the integration cycle is divided into five steps:

1. Assume that, for the actual time step t_n, the atomic positions $\mathbf{X}(t_n)$, and $\mathbf{X}(t_{n-1})$, the random variables $\mathbf{X}^{\text{rnd}}_{n-1}(t_{n-1}, \Delta t)$ [13] and the Hellmann-Feynman forces $\mathbf{F}(t_{n-1})$ are known (from the previous time step). In the first step of the iteration use $\mathbf{X}^{\text{rnd}}_{n-1}(0, \Delta t) = 0$.

2. Evaluate the Hellmann-Feynman forces $\mathbf{F}(t_n) = \mathbf{F}(\mathbf{X}(t_n))$.

3. Compute the derivative of the Hellmann-feynman forces from:

$$\dot{\mathbf{F}}(t_n) = [\mathbf{F}(t_n) - \mathbf{F}(t_{n-1})]/\Delta t. \tag{3.74}$$

4. Sample the random variable $\mathbf{Y}$ from a Gaussian with zero mean and a width according to Eq.

---

[13] In order to be consistent with the previous chapters the notation used here slightly deviates from the notation used in Ref. [123]. We use capital $\mathbf{X}$'s to describe atomic positions, whereas Ref. [123] uses small $\mathbf{x}$'s. Further we mark the random variables with a super-scripted 'rnd', whereas Ref. [123] uses capital $\mathbf{X}$'s to describe the random variables.

(2.15) in Ref. [123] and calculate the random variable:

$$\mathbf{X}_n^{\mathrm{rnd}}(t_n,-\Delta t)=\mathbf{X}_{n-1}^{\mathrm{rnd}}(t_n,\Delta t)\frac{G(\gamma\Delta t)}{C(\gamma\Delta t)}+\mathbf{Y}, \tag{3.75}$$

with the quantities $G(\gamma\Delta t)$ and $C(\gamma\Delta t)$ from the Eqs. (2.17) and (2.18) in Ref. [123], respectively. Sample $\mathbf{X}_n^{\mathrm{rnd}}(t_n,\Delta t)$ from a Gaussian with zero mean and a width according to Eq. (2.12) in Ref. [123]. Note that the widths of the Gaussian distributions generating the above random variables are functions of the temperature T, the friction parameter γ and the time step Δt. Calculate the new ionic positions

$$\begin{aligned}\mathbf{X}(t_{n+1}) &= \mathbf{X}(t_n)\left(1+\exp(-\gamma\Delta t)\right)-\mathbf{X}(t_{n-1})\exp(-\gamma\Delta t)\\ &+ \mathbf{M}^{-1}\mathbf{F}(t_n)(\Delta t)^2(\gamma\Delta t)^{-1}\left(1-\exp(-\gamma t)\right)\\ &+ \mathbf{M}^{-1}\dot{\mathbf{F}}(t_n)(\Delta t)^3(\gamma\Delta t)^{-2}\left(\frac{1}{2}\gamma\Delta t\left(1+\exp(-\gamma t)\right)-\left(1-\exp(-\gamma t)\right)\right)\\ &+ \mathbf{X}^{\mathrm{rnd}}(t_n,\Delta t)+\exp(-\gamma\Delta t)\mathbf{X}(t_n,-\Delta t).\end{aligned} \tag{3.76}$$

5. Calculate the velocities $\dot{\mathbf{X}}(t_n)$ according to Eq. (2.22) in Ref. [123] .

Note that in step (2) the ionic forces have to be calculated, which denotes (in case of DFT calculations) by far the most time consuming step of the iteration, since, in principle, a complete electronic self-consistent loop has to be performed. A proper choice of the initial guess for the wavefunction and the charge density is thus crucial. To improve the initial guess, a linear extrapolation scheme for the wavefunction has been implemented [110]:

$$\Psi'_{n,\mathbf{k}}(\mathbf{X}(t_{n+1}))=\Psi_{n,\mathbf{k}}(\mathbf{X}(t_n))+\alpha(\Psi_{n,\mathbf{k}}(\mathbf{X}(t_n))-\Psi_{n,\mathbf{k}}(\mathbf{X}(t_{n-1})), \tag{3.77}$$

where α is a fitted parameter that is optimized to minimize the quantity:

$$|\mathbf{X}(t_{n+1})-\mathbf{X}'(t_{n+1})|=|\mathbf{X}(t_{n+1})-(1+\alpha)\mathbf{X}(t_n)+\alpha\mathbf{X}(t_{n-1})|. \tag{3.78}$$

By employing this extrapolation the computational effort is reduced by approximately a factor of two compared to the case in which the initial guess is taken to be the converged wavefunction of the preceding step in the LD simulation.

3.5.6 Choice of the friction parameter

The choice of the friction parameter γ (Eq. 3.71) is crucial for the LD simulation. The value for the anharmonic corrections to the vibrational free energy, ΔF^{ah}, may converge to a wrong value if γ is chosen from an unfavorable interval[14]. Moreover, the computational effort strongly depends on γ. Thus the value of γ should be adequate, to save computational resources, but such that the LD simulation converges to correct values.

---

[14] In principle, the value of ΔF^{ah} should converge to the same, correct value for any choice of λ. However the calculation shows that this is not the case in practice, as is discussed below.

Determination of a validity region of the friction parameter

To determine the validity region for γ, we have performed two LD simulations for the poly-glycine FES as a representative test system. In both simulations the reference thermodynamic state corresponds to the harmonic potential as calculated within the SCCDFTB approach (Sec. 6.2.2), whereas the target thermodynamic state is chosen to be different in the two simulations: For the first simulation (Fig. 3.9a) the harmonic potential rescaled with a factor of 0.8 is used as target potential, whereas for the second simulation (Fig. 3.9b) the "real" SCCDFTB potential is used.

We start with the discussion of the first simulation. Here, the free energy difference ΔF^{ah} can be calculated exactly, since both, reference and target potential are harmonic. Further, we may, of course, determine ΔF^{ah} with the thermodynamic integration. Fig. 3.9a shows, however, that only for a friction parameter with

$$\gamma < 1 \tag{3.79}$$

the value for ΔF^{ah} converges to the expected value: When γ is not taken from this interval, the simulation does not converge to the expected value even after 10^6 simulation steps (Fig. 3.9a, black line). This behavior can be understood in terms of the 'collision frequency' ζ :

$$\zeta = \gamma / M^{\mathrm{eff}}. \tag{3.80}$$

Here M^{eff} is an effective mass and may be identified with the reduced masses associated to the eigenmodes of the peptide chain. For the high frequency (hydrogen stretching) vibrations it holds that $M^{\mathrm{eff}} \approx 1$. To transform the upper bound for the friction parameter $\gamma^{\mathrm{max}} = 1$ to a respective upper bound for the collision frequency, we substitute $\gamma^{\mathrm{max}} = 1$ and $M^{\mathrm{eff}} = 1$ into Eq. (3.78) and obtain (after unit conversion) an upper bound for the collision frequency of $\zeta^{\mathrm{max}} = 3000\ \mathrm{cm}^{-1}$. Hence the upper bound for the collision frequency (approximately) corresponds to the value for the highest frequency vibrations of the peptide chain. We conclude that the validity region for γ is determined by the vibrational spectrum of the peptide chain. In other words, the collision frequency triggering the random force in Eq. (3.71) must be in resonance with the vibrations of the system. One may argue that the behavior for $\gamma > 1$ in the first simulation could be an artifact due to the fact that both, the target and the reference potential, are harmonic. However, qualitatively the same behavior is observed also for the second simulation with the "real" anharmonic SCCDFTB energy surface as target potential (Fig. 3.9b). Thus to obtain reliable results for the anharmonic corrections to the free energy of the peptide chain, the friction parameter γ has to be chosen such that the collision frequency lies within the vibrational spectrum of the peptide chain.

Determination of the most efficient friction parameter

To determine the optimum γ *within* the validity interval, first the total number of time steps of the Langevin dynamics, τ^{sim}, required to reach convergence within a desired statistical error bar ΔF^{err} is estimated. According to Eq. (3.69) ΔF^{err} is given by:

$$\Delta F^{\mathrm{err}} = \frac{a_n^2 s}{\tau^{\mathrm{ind}}}. \tag{3.81}$$

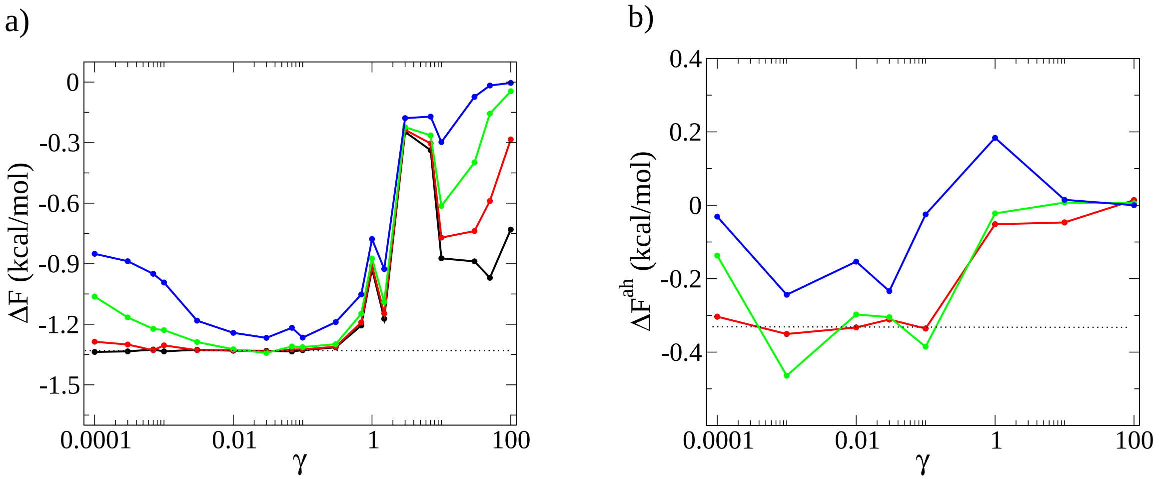

Figure 3.9: Anharmonic free energy contributions $\Delta F^{\mathrm{ah}} = F^{\mathrm{ah}} - F^{\mathrm{harm}}$ at room temperature, as evaluated by thermodynamic integration for different friction parameters γ in the Langevin equations of motion (Eq. (3.71)) and for different simulation lengths: 10^3 steps (blue lines), 10^4 steps (green lines), 10^5 steps (red lines) and 10^6 steps (black lines). The reference potential is, in both a) and b) given by the harmonic potential as evaluated within the SCCDFTB approach for a poly-glycine FES in a supercell containing four peptide units. The target potential is different between a) and b): In a) the target potential corresponds to a harmonic toy potential resulting from a rescaling (softening) of the dynamical matrix with a factor of 0.8. In b) it is the “real” SCCDFTB potential energy surface. The dotted lines denote reference values: In a) it is the expected free energy difference in between the target and the reference potential as calculated from the difference of the two harmonic potentials. In b) it is the best guess for the free energy difference as determined after 10^5 simulation steps with $\gamma = 0.01$.

Here, a_n is the Student's parameter, s is the variance as defined in Eq. (3.70), and τ^{ind} is the number of statistically independent data points contained in a Langevin dynamics trajectory $\{X_n\}$. Substituting $\tau^{\mathrm{ind}} = (\tau^{\mathrm{sim}}\Delta t^{\mathrm{max}}/t^{\mathrm{cor}})$ into Eq. (3.79), where τ^{sim} is the number of required simulation steps, Δt^{max} is the maximum time step, and t^{cor} is the correlation time (see below), reveals:

$$\tau^{\mathrm{sim}}(\gamma) = \frac{a_n}{\Delta\Delta F} \cdot \frac{s t^{\mathrm{cor}}}{\Delta t^{\mathrm{max}}} \propto \frac{s(\gamma) t^{\mathrm{cor}}(\gamma)}{\Delta t^{\mathrm{max}}(\gamma)}. \tag{3.82}$$

The amount of computational time is proportional to τ^{sim}, hence we define the efficiency, $\upsilon(\gamma)$, as:

$$\upsilon(\gamma) = \left(\frac{s(\gamma) t^{\mathrm{cor}}(\gamma)}{\Delta t^{\mathrm{max}}(\gamma)} \right)^{-1}. \tag{3.83}$$

The efficiency $\upsilon(\gamma)$ reaches its maximum for the optimum friction parameter. To determine this point we have determined the three quantities $t^{\mathrm{cor}}(\gamma)$ (Fig. 3.10a), $s(\gamma)$ (Fig. 3.10b) and $t^{\mathrm{max}}(\gamma)$ (Fig. 3.10c) for various γ values inside the validity region (Fig. 3.10). The variance $s(\gamma)$ and the correlation time $t^{\mathrm{cor}}(\gamma)$ have been obtained by means of the method of minimum statistical inefficiency [124] (see Appendix, Sec. 6.3.2). The quantity $t^{\mathrm{max}}(\gamma)$ is taken as the maximum time step at which the LD simulation is generating a stable trajectory.

For both simulations we found an optimum friction parameter of $\gamma \approx 1 \cdot 10^{-2}$ (Fig. 3.10d). The corresponding collision frequency is located in the low frequency part of the vibrational spectrum of the peptide chain. We conclude that, in order to obtain an efficient sampling of the part of the phase space relevant for estimating the free energy, the random force must be in resonance with the low frequency modes of the peptide chain. For all LD simulations of this project we have in the following used the friction value $\gamma = 1 \cdot 10^{-2}$.

3.5.7 Generalized Simpson's rule

Once the quantity $\langle \frac{\partial U}{\partial \lambda} \rangle_\lambda$ has been obtained for a sufficiently large number of λ-values the free energy difference between the reference (harmonic) and target potential is determined from Eq. (2.126). To perform an efficient interpolation between the sample points of the integral in Eq. (2.126), it is important to employ a scheme that incorporates the non-linear progress of the quantity $\langle \frac{\partial U}{\partial \lambda} \rangle_\lambda$. Therefore, we employ the generalized Simpson's rule [125] to integrate Eq. (2.126), which uses quadratic polynomials for the interpolation. Using the Simpson's rule, sampling $\langle \frac{\partial U}{\partial \lambda} \rangle_\lambda$ with only five points is sufficient to reduce the error arising from the discretization of the integration to less than 0.05 kcal/mol per peptide unit (at room temperature).

To distribute the sampling points for the integration in an efficient way, first a SCCDFTB calculation (Sec. 6.2.2) is performed for the system of interest using a very dense sampling mesh containing more than twenty points. From this mesh the five most representative points are chosen[15]. The DFT calculations are then performed on the mesh containing these five most representative sampling

---

[15] The importance of a given sample point is determined by evaluating the absolute difference between the thermodynamic integral calculated for the mesh without this sample point and the thermodynamic integral calculated for the full mesh.

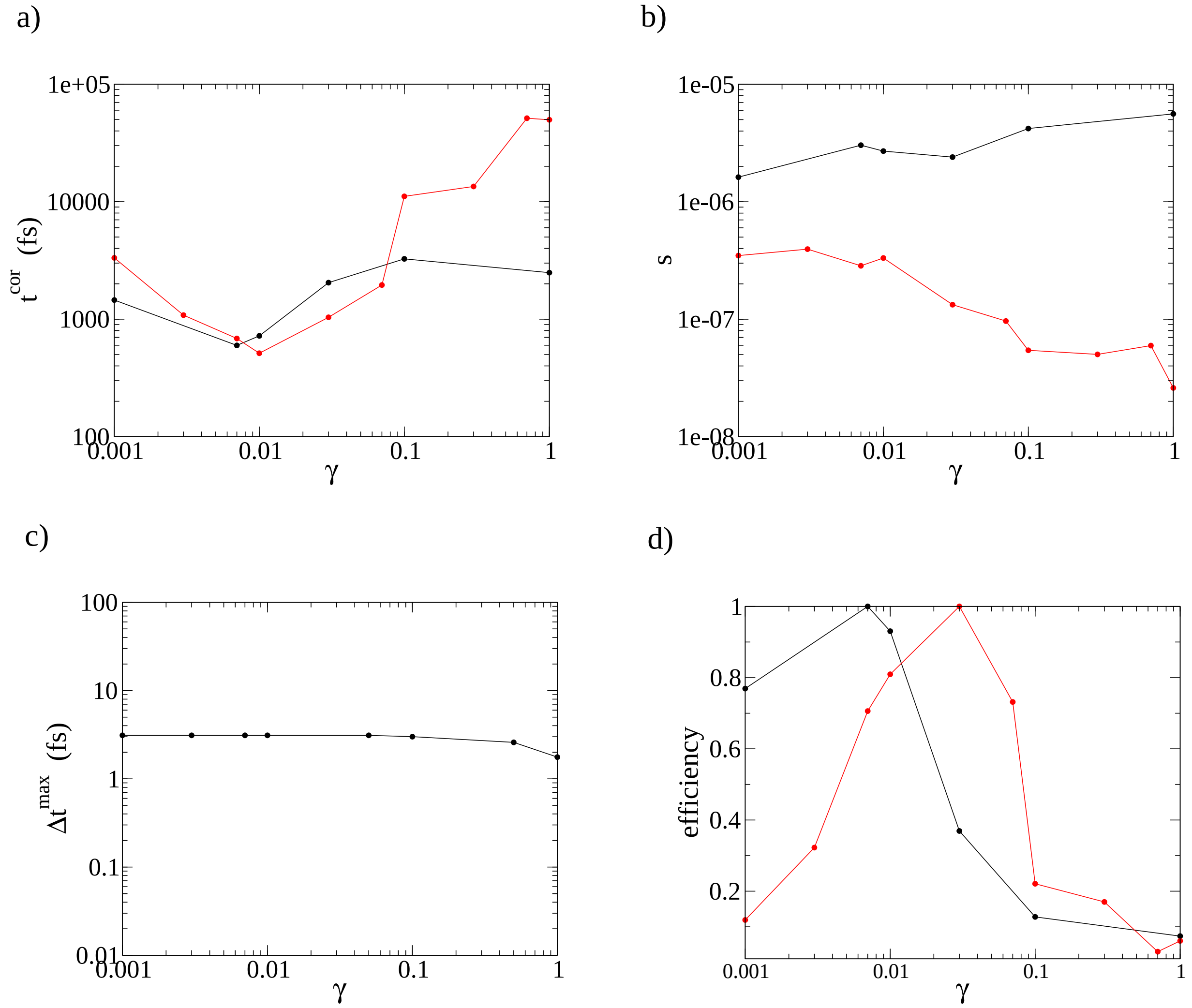

Figure 3.10: Parameters and quantities with relevance for the efficiency of the Langevin Dynamics simulation as a function of the friction parameter γ: a) Correlation time t^{cor}, b) variance s, c) maximal time-step Δt^{max}, and d) the efficiency as defined in Eq. (3.81). These quantities have been determined for a poly-glycine FES in a supercell containing four peptide units for the SCCDFTB potential (black lines) and for the corresponding harmonic potential (red lines). In c) the red and black lines are superimposed.

points.

4 Results

Having discussed the relevant theoretical concepts underlying this study and their implementation, we now focus on the presentation and interpretation of the results.

First, to validate the accuracy of our approach, we determine the phonon dispersion relation of a prototypical system, the poly-L-alanine α-helix, and compare it to experimental literature data (Sec. 4.1). Furthermore, the results for the α-helix are also compared to previous theoretical studies, which were based on the force field approach.

The study is then extended to include the other two experimentally observed helix types, i.e, the π- and the 3_{10}-helix, and the unfolded conformations, i.e., the FES and the 2_7-structure. By calculating the free energies in the harmonic approximation, thermodynamic trends for these conformations are identified and key aspects of the stability – whether a helix is stable at room temperature, and, how the relative stability of the three helix types depends on temperature – are examined (in Sec. 4.2).

In Secs. 4.3 and 4.4 the thermodynamic trends are investigated in detail. An analytical ball-and-spring model is introduced to analyze the three lowest vibrational branches of the peptide chain, which determine the main part of the thermodynamic trends. By deriving explicit spring constants for this model, the effect of the formation of the hydrogen bonding network on these vibrational branches is evaluated and is compared with the effect due to the changes in the backbone stiffness of the peptide chain. Moreover, analytical formulae are derived to describe the long-wavelength limit of the acoustical branches. This description allows for a straightforward interpretation of the thermodynamic trends and elastic properties of the helices.

In Sec. 4.5 the effect of the side chain is analyzed by studying the glycine peptide chains and comparing the results with respect to L-alanine. According to the experimental results, glycine is, in contrast to L-alanine, a weak helix former. To check whether these differences are due to differences in the vibrational properties, a detailed comparative analysis between L-alanine and glycine is performed.

Finally, in Sec. 4.6 the effect of anharmonicity is investigated. The thermal expansion for various conformations is determined by applying the quasi-harmonic approximation. Moreover, anharmonic corrections to the free energy are determined by means of the thermodynamic integration approach.

4.1 Phonons and specific heat of the α-helix

In Chapters 2 and 3, two basic approximations have been introduced to facilitate an effective description of the electronic structure of the peptide chain. These are the PBE functional to approximate the exchange-correlation interaction and the pseudo-potential approach to approximate the interaction of and with the ionic cores. To correctly evaluate the results of this project, an estimation of the error in the description of the vibrational frequencies and thermodynamic properties of the peptide chains due to these two approximations is inevitable. Therefore, we have computed in this section the phonon dispersion and specific heat of the poly-L-alanine α-helix and compared it to experimental values from literature[1]. We have chosen the poly-L-alanine α-helix for this comparison, since L-alanine has a high propensity to form helices (e.g. [27]) and thus offers the possibility to synthesize long, regular helices (e.g. [56, 126]). Therefore, the according experimental results are adequate for the comparison with the theoretical values for the infinitely long helix[2].

Our study is not the first theoretical work on the poly-L-alanine α-helix. As mentioned in the introduction (Sec. 1.6) previous theoretical approaches based on empirical force fields reveal significant shortcomings in predicting the specific heat [55] of this system, implying substantial errors in the low frequency vibrational branches. We therefore also compare our results to these previous theoretical works to validate whether or not our approach gives rise to new insights.

4.1.1 Comparison to experimental frequency spectra

Both, vibrational and thermodynamic properties of the poly-L-alanine α-helix have been experimentally determined in the past [55, 56, 126, 127, 128, 129]. We compare here to the results from Lee&Krimm [56] who obtained their experimental data points from polarized infrared (IR) and Raman spectra. They prepared oriented films of poly-L-alanine helices, either on a AgCl plate (for the measurements from 500-4000 cm^{-1}) or on a glass slide (for the measurements with $\omega < 500$ cm^{-1}). The residual solvent (dichloroacetic acid) was removed from the film by extraction with diethyl ether or pure water followed by drying in a vacuum oven at 40^{o}C. However, indications exist that the drying was incomplete in the sense that residual solvent or water remained. This issue is discussed below.

The comparison between our calculated phonon dispersion relation and the experimental results of Lee&Krimm is shown in Fig. 4.1. Further, we have investigated the eigenmodes corresponding to the vibrational branches. A classification of the corresponding eigenmodes is given in Tab. 4.2, for a graphical illustration see appendix, Fig. 6.8.

Concerning the agreement of experimental and theoretical results for the frequency spectra we have to differentiate between the 28 optical branches and the two acoustical branches of the helix.

Comparison for the optical branches

For the optical branches we find an excellent agreement of DFT with experiment, except for a small, systematic red-shift of the DFT values (Fig. 4.1). We remark that such small systematic discrepancies between ab-initio and experimental vibrational spectra are well known and have been extensively discussed in the literature [130, 131, 132]. It is thus a common practice in the field of quantum chemistry to rescale the theoretical values with a single, universal scaling factor f^{cor},

---

[1] A more direct way to validate the accuracy of the employed approach would be to compare our results with more accurate theoretical approaches, e.g. coupled cluster, configuration interaction or quantum Monte Carlo at the basis set limit. Taking this way is, however, not possible due to the lack of reliable benchmark data.

[2] According to Xie et al. the average molecular weight of poly-L-alanine samples used in experiment is 18 kD per peptide chain, which corresponds to an average of 253 peptide units per peptide chain [126].

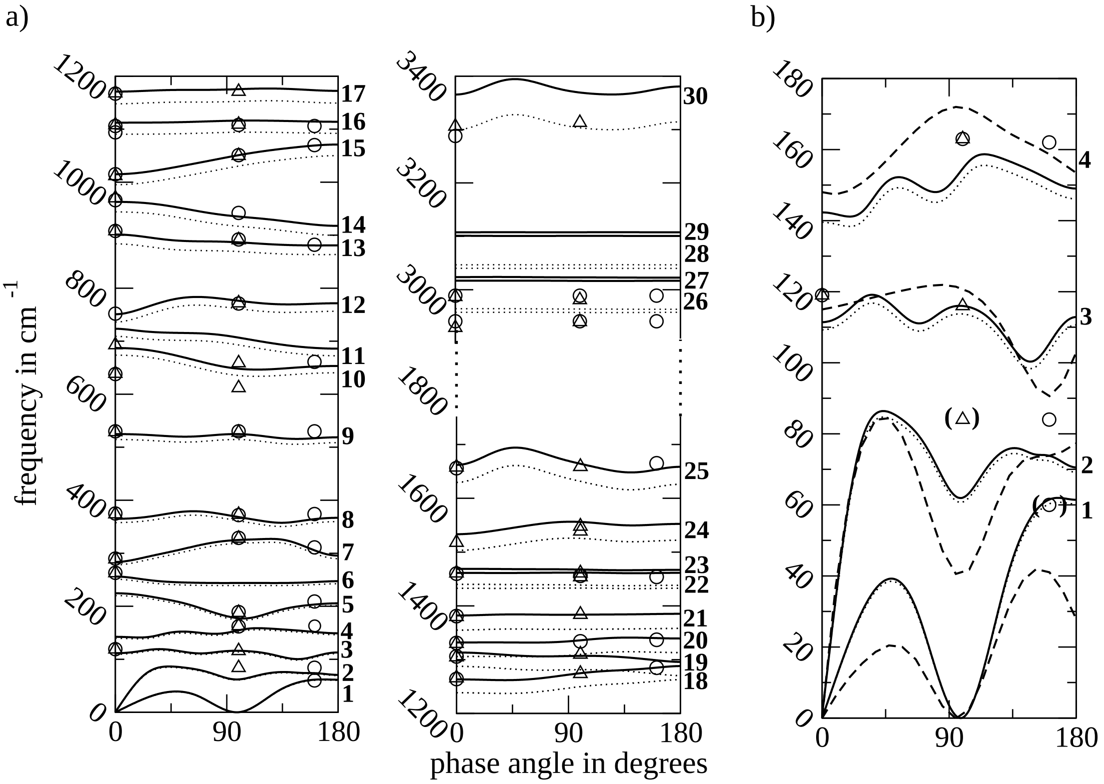

Figure 4.1: a) Comparison of the phonon dispersion relation of the poly-L-alanine α-helix (solid line for scaled frequencies, dotted line for un-scaled frequencies) to experimental data of Ref. [56] from polarized IR (triangles) and Raman measurements (circles). The bold numbers on the right hand side denote the labels for the vibrational branches as used in the text and in Tab. 4.2. b) Comparison for the 4 lowest vibrational branches to the results of Ref. [56]. Force field results from Ref. [56] are also shown (dashed line, from Fig. 3 in [56]).

label	type	nomenclature
1-2	acoustical branches	-
3-9	backbone vs side group r or tr	-
10	backbone t, N-H b	Amide 5
11-13,17	backbone t or b	-
14-16	backbone or $\mathrm{C}_\alpha - \mathrm{C}_\beta s$, $\mathrm{C}_\alpha - \mathrm{H}b$	-
18,19	backbone s, N-H b	Amide 3
20-23	$\mathrm{C}_\beta - \mathrm{H}b$	-
24	N-C s, N-H b	Amide 2
25	C-O s	Amide 1
26-29	$\mathrm{C}_\beta - \mathrm{H}s$,$\mathrm{C}_\alpha - \mathrm{H}\ s$	Amide B
30	N-H s	Amide A

Table 4.2: Qualitative classification of the vibrational branches based on an analysis of the corresponding eigenvectors. Notation: s = stretch, b = bend, t = torsion, r = rotation, tr = translation. The amide nomenclature is according to Ref. [133]. A graphical illustration of the vibrational eigenmodes is presented in the Appendix, Fig. 6.8.

which usually significantly improves the agreement between theory and experiment [132]. The scaling factor depends on the employed ab-initio methodology, in particular the exchange-correlation approximation and the employed basis set. Further, it depends on the degree of anharmoncity in the respective vibrational modes. It usually falls into the interval:

$$0.95 < f^{\mathrm{cor}} < 1.05. \tag{4.1}$$

For the PBE functional we have found an optimal scaling factor of $f^{\mathrm{cor}} = 1.02$ by fitting f^{cor} to optimize the agreement between theoretical and experimental values. Rescaling the vibrational spectrum with this factor (change from dotted to solid lines in Fig. 4.1a) makes the deviations between experiment and DFT largely disappearing – the remaining error is smaller than 15 cm^{-1} for the entire optical spectrum of the helix, in most cases the error is even smaller than 10 cm^{-1}. Nevertheless, exceptions are found for the branches 10 and 11 with $\omega \sim 700$ cm^{-1}, here the deviations are about ~ 50 cm^{-1} and for the high frequency branches 26 to 30 with $\omega \approx 3000$ cm^{-1} (Figs. 4.1a and 6.8).

Let us first discuss the deviations for the branches 10 and 11: A possible explanation for the large deviation of these branches is the existence of residual water in the experimental species investigated by Lee&Krimm. In particular the L_2 libration of liquid water at 686 cm^{-1} [134] is in resonance with these branches and is a candidate for perturbations of the corresponding helical vibrations.[3]

We now discuss the deviations for the branches 26 to 30 at $\omega \approx 3000$ cm^{-1}. These branches exclusively correspond to the hydrogen stretching vibrations in the peptide chain, i.e., the N-H

---

[3] This explanation is rather speculative, since the amount of residual water attached to the experimental species is unknown. Nonetheless the explanation is feasible, since on the one hand no other resonances except that for the L_2 libration are found between the frequency spectrum of liquid water and the mid frequency spectrum of the α-helix, and, on the other hand, no other branch from the mid frequency region except the branches 10 and 11 shows such a huge discrepancy between experiment and DFT.

stretching branch (with id = 30) and C-H stretching branches (with ids = 26-29 in Figs. 4.1a and 6.8). In the following we call these five branches “high frequency branches”, while the remaining optical branches with id 3 to 25 we call “mid frequency branches”. In contrast to the mid frequency branches, the (un-scaled) theoretical values for the high frequency branches are not red-shifted but blue-shifted by up to ~ 60 cm^{-1} with respect to experimental data. Consequently, a rescaling of the theoretical values with the factor $f^{\mathrm{cor}} = 1.02$, as has been derived above to optimize the agreement for the mid frequency branches, leads to an “over”-correction for the high frequency branches. To provide an understanding of this different scaling behavior, we recall that differences between experimental and theoretical values are not only arising from the ab-initio error, i.e., the approximated treatment of the electronic system, but also from anharmonic contributions, which are not included in our calculations. The fact that a *single* factor accurately describes the scaling for the mid frequency branches indicates that these vibrations are dominated by the ab-initio error, since the ab-initio error is expected to behave rather systematically. In contrast, the high frequency hydrogen stretching vibrations are expected to contain an “over-proportional” strong degree of anharmonicity, which compensates or even exceeds the impact of the ab-initio error. Indeed it is well known that stretching vibrations involving hydrogen atoms contain strong anharmonic contributions, which are typically in the range of $100 - 200$ cm^{-1} (Ref. [135]) and most likely, due to the small hydrogen mass, much larger than the anharmonic corrections in the mid frequency region.

To check for this possibility we have estimated the anharmonic corrections for the lowest lying C-H stretching branch (with id=26) by means of a simple Morse oscillator model (see appendix, Sec. 6.5). Indeed a strong anharmonic correction of $\Delta\omega^{\mathrm{ah}} = -115$ cm^{-1} has been found. Based on this shift we determine a correction factor *exclusively* due to the anharmonicity:

$$f^{\mathrm{cor,ah}} = \frac{\omega^{\mathrm{ah}}}{\omega^{\mathrm{harm}}} = 0.96. \tag{4.2}$$

Further, we determine a correction factor *exclusively* due to the ab-initio error:

$$f^{\mathrm{cor,ab-initio}} = \frac{\omega^{\mathrm{ah}}}{\omega^{\mathrm{exp}}} = 1.03. \tag{4.3}$$

Thus, for the high frequency hydrogen stretching branches the correction factor f^{cor} is dominated by the anharmonicity rather than by the methodology to treat the electronic degrees of freedom, verifying the above explanation.

The factor $f^{\mathrm{cor,DFT-PBE}} = 1.03$ is very close to the factor $f^{\mathrm{cor}} = 1.02$ we found for the rescaling of the mid frequency branches. This shows that the degree of anharmonicity is smaller for these branches than for the high frequency branches and that the ab-initio error can be corrected by a single, universal scaling factor.

Comparison for the acoustical branches

For the two acoustical branches the information available from the experiment of Ref. [56] is rather limited. This is mainly due to a principal deficiency of the spectroscopic methods: In the IR- and Raman spectroscopy only vibrational modes at special high symmetry points of the Brillouin zone

(BZ) are optically active. In case of the α-helix the A-point at $\varphi = 0°$ and the E_1-point at $\varphi = \Theta$ are both IR and Raman active; the E_2-point at $\varphi = 2\Theta$, which is degenerated with $\varphi = 360° - 2\Theta$, is only Raman active[4]. Thus, the first acoustical branch is completely "invisible" to IR spectroscopy, since it is zero at the two IR-active points A and E_1. And Raman spectroscopy only marginally resolves this branch at E_2. The complex, strongly dispersive shape for $\varphi \neq E_2$ remains completely in the "darkness". For the second acoustical branch the situation is slightly improved, since, at least in principle, IR and Raman spectroscopy could give information about its value at E_1 and E_2. According to the remarks in Ref. [56], however, even these few data points are in practice only partially accessible, since the IR bands in this frequency region are very weak and only the Raman bands are well determined. Thus Ref. [56] does not report any reliable experimental results below the Raman active $\omega(E_2) = 84$ cm^{-1} . With respect to this (only) available experimental data point for the acoustical branches the DFT value is red-shifted by about 15 cm^{-1}.

In principle the problems connected with the spectroscopic methods could be partially overcome employing inelastic neutron scattering measurements (INS), since this method (approximately) delivers the phonon density of states, i.e., the complete phonon dispersion relation integrated over the reciprocal space. Nevertheless, we do not compare our results to any experimental results from INS, since these studies [136, 137, 138] were not found to give any quantitative information exceeding that given in the study of Lee&Krimm, neither with respect to accuracy nor with respect to completeness.

Comparison to results from force field calculations

As mentioned in the introduction (Sec. 1.6), previous theoretical approaches based on empirical force fields revealed significant shortcomings in predicting the specific heat [55] of the α-helix, indicating substantial errors in the description of the low frequency vibrational branches. We now compare our results to these data to check, whether our approach may help to gain new insights.

We note that the overall agreement of the empirical force field models [54, 55, 56] with experiment is, for most of the optical active points of the vibrational Brillouin zone, similar to what we have achieved with DFT. However, in contrast to the force field calculations, which by construction reproduce the vibrational spectra at available experimental data points (since they are fitted to reproduce these points), DFT calculations are free of any experimental input parameter. Therefore, it is more interesting to check the accuracy of the force field models in the region *not* accessible in experiment, i.e., away from the high-symmetry (optical active) points in the Brillouin zone. The part of the vibrational spectrum in which deviations are most likely to occur are branches exhibiting large dispersion and/or a complex shape of the $\omega(\varphi)$ dependence. Indeed, we find significant deviations between DFT and force field results for two types of such branches.

The first type is given by the vibrational modes most directly involved in the hydrogen bonds of the helix, i.e., the Amide A, 1, and 2 branches (Tab. 4.2, Figs. 4.5 and 6.8, with index 30, 25, and 24, respectively). Particularly the dispersive splitting of the Amide A branch, which we find to be

---

[4] Here, Θ denotes the helical twist angle (see Sec 2.1).

of the order of 32 cm^{-1}, is completely absent in the force field calculations.

The second class is given by the two lowest branches, the acoustical branches, for which we find significant shifts with respect to the force field calculations: Compared to the latter our data are blue shifted by up to 25 cm^{-1}, as shown for the force field results of Ref. [56] in Fig. 4.1b. Similar differences we find, when comparing our results to the force field results published in Refs. [54, 55]: Also the acoustical branches reported in these studies are strongly red-shifted with respect to the DFT results.

4.1.2 Specific heat

As we will show in Sec. 4.3, the two acoustical branches primarily determine the temperature dependence of the thermodynamic stability of the helix. Unfortunately, a *direct* validation of the accuracy of the theoretical approaches (DFT and force fields) in predicting the dispersion of these branches cannot be given due to the limited amount of experimental data (see above).

However, experimental data exist for a quantity that is determined predominantly by the low frequency branches, i.e., the specific heat at low temperatures [139]. A comparison to these experimental data allows for an *indirect* validation of the accuracy of the theoretical approaches in predicting the acoustical branches. Furthermore, it allows to check, whether the deviations between force fields and DFT for the acoustical branches give rise to changes in the thermodynamic properties.

We have therefore calculated the heat capacity:

$$C_V = \left(\frac{\partial U^{\mathrm{vib}}}{\partial T}\right)_V , \tag{4.4}$$

and compared this quantity to experimental data: Fig. 4.2 shows the calculated heat capacity as function of temperature as obtained with DFT-PBE, together with experimental data [139] for crystalline α-helical poly-L-alanine and results from force field calculations [54, 55]. We have calculated the specific heat at constant volume, whereas the experimental values are reported for constant pressure. However, the difference between these quantities is small for low temperatures [55] and has thus been neglected.

For the following discussion we consider only the heat capacity for temperatures below 150 K. For larger temperatures the experimental values show a drastic increase in the specific heat, which has been reported to be an artifact of the experimental conditions, i.e., this increase is most likely due to residual water molecules in the poly-L-alanine sample rather than due to the internal motion of the poly-L-alanine chains [55]. A comparison for $T > 150$ K is therefore not meaningful.

As can be seen in Fig. 4.2, the agreement with experiment is significantly improved for our DFT results in comparison to the force field results. This implies that an improved description in the acoustical branches has been achieved. It is, furthermore, interesting to note that DFT and force fields exhibit not only a quantitative but also a qualitative difference in the behavior of the specific heat: Force field models predict in the low temperature region up to $\approx 50\ K$ a linear behavior ($C_V \sim T$). Following the Debye law, this dependence is characteristic for a one-dimensional

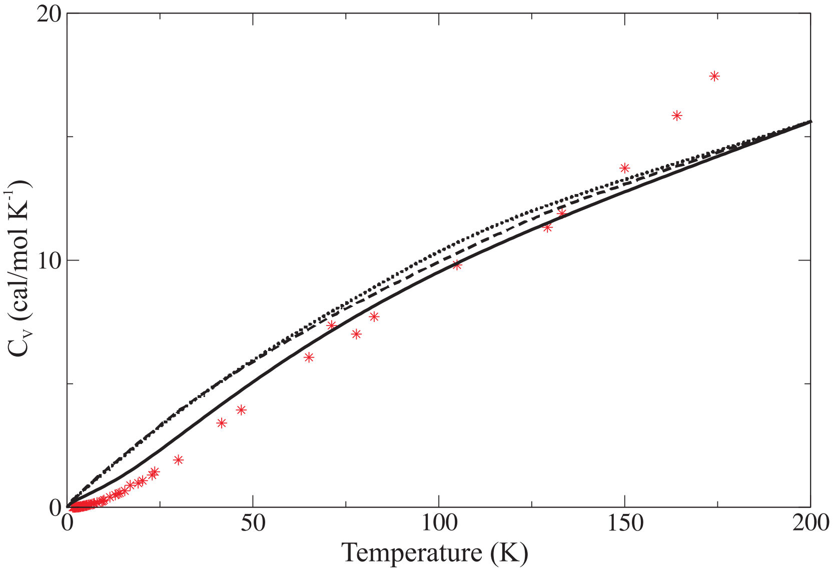

Figure 4.2: Specific heat of the poly-L-alanine α-helix: DFT values (solid line) compared to experimental values (stars, [139]) and to force field calculations (dotted line, [54] and dashed line, [55])

periodic crystal at low temperatures, whereas for two/three dimensional crystals a T^2/T^3 behavior is predicted, respectively. The deviation of the experimental data from the linear behavior has been thus interpreted by inter-helix couplings [55] in the crystal of poly-L-alanine, which were expected to become important at low temperatures. However, our results clearly demonstrate that the deviation from linearity is not due to inter-helix couplings, but an intrinsic property of the isolated α-helix and results from the strong dispersion of the low frequency branches.

We conclude that a fundamental difference exists between the empirical force field studies [54, 55, 56] and our DFT approach regarding the treatment of the interactions that determine the low temperature specific heat and the two acoustical branches. Later on in this chapter it becomes clear that these shortcomings of the force fields are ultimately due to an insufficient characterization of hydrogen bonding interactions. To fully understand the discrepancies between force field and DFT results, it is, however, first necessary to understand, which interactions influence the low frequency vibrations. The corresponding analysis and interpretations are given in Secs. 4.3-4.4 and in chapter 5, respectively.

4.1.3 Conclusions

To summarize this section, the calculated phonon dispersion relation for the poly-L-alanine shows excellent agreement with the experimental data: A constant scaling factor close to 1 is sufficient to obtain an agreement better than 10 cm^{-1} for the main part of the vibrational spectrum. For the high frequency hydrogen stretching branches the deviations between experiment and theory are larger, mainly due to strong anharmonic contributions in the stretching modes involving hydrogen atoms. Nevertheless, these contributions are negligible for the thermodynamic analysis in Secs. 4.3

and 4.5, since they largely cancel out in the evaluation of quantities like differences in vibrational free energies.

The comparison for the low frequency region is incomplete due to the lack of experimental data. For the only available experimental data point the DFT value is red-shifted by 15 cm^{-1}. A discussion of this discrepancy between DFT-GGA and experiment remains speculative. Possible sources are van-der-Waals attractions, which are not properly described by current exchange-correlation functionals (Sec. 2.4.3) and could lead to a hardening of the low frequency force constants. Further inter-helix interactions may occur in the experimental species, but are absent in our study.

However, the comparison to experimental data shows that first principles calculations, as performed in this project, are crucial and allow an insight which has not been possible by previous experimental and theoretical approaches. The comparison to previous empirical force field calculations, which are optimized by means of available experimental frequency data, shows that DFT significantly improves the description of the low temperature specific heat. This implies that a significant improvement has been achieved in predicting the acoustical branches, which in turn describe the mechanical/elastic properties of the system and dominate the vibrational contributions to the free energy, as will be shown in Sec. 4.3. Furthermore, since the resolution of the phonon-dispersion relation of our approach exceeds experimental data (where only the high symmetry points A, E_1 and E_2 are accessible) the calculated data may be used to fit a new generation of force fields/model potentials, which in turn will then contain an improved description of the thermodynamic properties (free energy) of the peptide chain. An example for such a model potential will be presented in Sec. 4.4.

4.2 Stability analysis for poly-L-alanine

In the previous section we have shown that our approach accurately describes the thermodynamic properties of the helix. We now intend to address the basic questions on the helix stability as raised in the introduction (Sec. 1.3). First we focus on the poly-L-alanine chain and determine the free energies of the thermodynamic phases corresponding to the three experimentally observed helix types, i.e., the α-helix, the π-helix, and the 3_{10}-helix. Further included is the 2_7-structure, which completes the study in terms of possible hb patterns and the FES which lacks hydrogen bonds and serves as a reference system.

By evaluating the phase stability for these conformations we aim to answer the following fundamental questions:

1. Is the helical secondary structure motif intrinsically stable at room temperature?
2. How is the temperature dependence of the relative stability of the different helix types?

4.2.1 The fully extended structure as reference phase

A definition of the relative phase stability between two conformations is given in Eq. (2.56). For convenience we define here the phase stability of the various conformations with respect to the

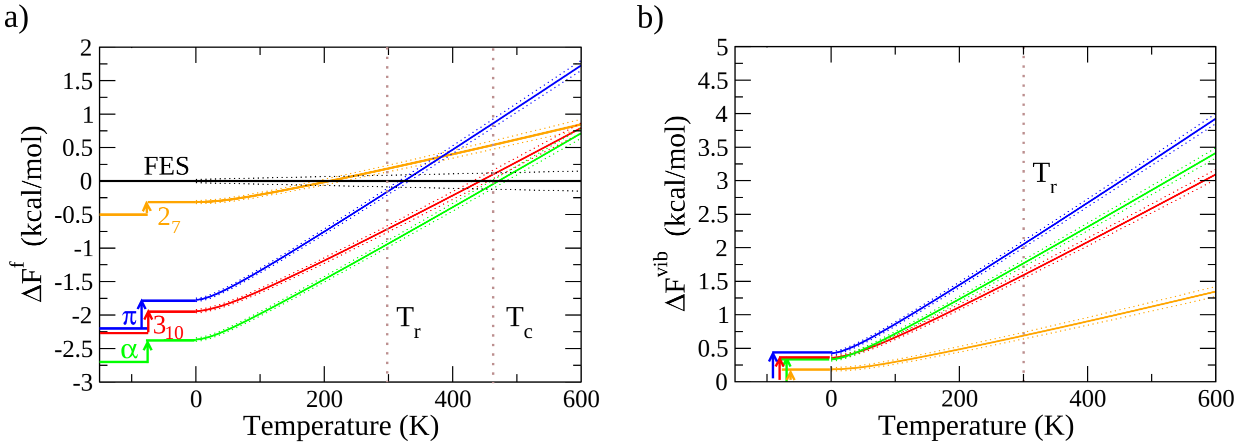

Figure 4.3: a) Stability of the poly-L-alanine conformations with respect to FES as the temperature increases (Eq. (4.5)). The dotted lines denote the numerical uncertainty (see also Sec. 6.1.1). The horizontal bars and the arrows at the left hand side of the curves denote the static stability at 0 K and the zero-point vibrational corrections, respectively. T_r is the room temperature and T_c is the critical temperature, at which the FES becomes more stable than the helices. b) Differences in the vibrational free energy with respect to the FES.

unstrained, fully extended structure (FES):

$$\Delta F^{\mathrm{f}}_S(T) = F_S(T) - F_{\mathrm{FES}}(T). \tag{4.5}$$

Here, $F_S(T) = F(T, L_S, \Theta_S)$ stands for the free energy per peptide unit of either one of the five analyzed conformations (which are indicated with a subscripted 'S') and $F_{\mathrm{FES}}(T)$ is the free energy of the FES. Following the Born-Oppenheimer approximation (Sec. 2.3, 2.6.1) and the harmonic approximation (Secs. 2.6.2) $\Delta F^{\mathrm{f}}_S(T)$ is given by:

$$\Delta F^{\mathrm{f}}_S(T) \quad = \quad \Delta U^{\mathrm{el}}_S + \Delta F^{\mathrm{vib}}_S(T), \tag{4.6}$$

where

$$\Delta F^{\mathrm{vib}}_S \quad = \quad \Delta U^{\mathrm{vib}}_S(T) - T * \Delta S^{\mathrm{vib}}_S(T). \tag{4.7}$$

Here, ΔU^{el}_S is the difference in total energy per peptide unit, $\Delta F^{\mathrm{vib}}_S(T)$ is the difference in vibrational free energy per peptide unit, and $\Delta S^{\mathrm{vib}}_S(T)$ and $\Delta U^{\mathrm{vib}}_S(T)$ denote the differences in entropic and enthalpic vibrational contributions to the free energy all with respect to the FES.[5]

4.2.2 Phase stability at elevated temperatures

We start the stability analysis recalling the results for the static stability of the bulk phases at 0 K (Sec. 1.5[6]). According to these static contributions to the stability, ΔU_S^{el}, (Fig. 4.3a, Fig. 1.5) all three helical conformations are energetically preferred over the FES, owing to the formation of hydrogen bonds. The same applies to the 2_7-structure, although the energetic preference is much smaller for this conformation than for the helices (Fig. 4.3a). The α-helix is the global minimum of the potential energy surface, thus it is the preferred conformation at 0 K with $\Delta U_\alpha^{\text{el}} = -2.7$ kcal/mol per peptide unit. The π- and the 3_{10}-helix are almost degenerate to each other and higher in energy than the α-helix by about 0.5 kcal/mol per peptide unit.

The zero-point vibrational corrections ΔU_S^{vib} (arrows in Fig. 4.3) make the helical conformations slightly less stable with respect to the FES by ≈ 0.35 kcal/mol and the 2_7-structure by 0.2 kcal/mol. However, the energetic ordering of the conformations remains. This result is consistent with the findings reported for the α-helix in Ref. [59] (see also Sec. 1.6).

At finite temperatures, a significant change in the stability is observed: A pronounced stabilization by vibrational free energy contributions of the FES with respect to the other chain conformations makes it the thermodynamically most stable phase at temperatures above $T_c = 470$ K (Fig. 4.3a). The 2_7-conformation is higher in free energy than the FES already for $T > 200$ K. Despite the small differences in the stabilization energies, the trends shown in Fig. 4.3b clearly reveal that the finite temperature effects make the π-helix the least favored of the three helical conformations. At room temperature it is nearly degenerated to the FES and will be unstable for $T > 300$ K. In contrast, the α- and 3_{10}- helix are still stable at room temperature by 1.0 kcal/mol and 0.7 kcal/mol per peptide unit, respectively. A small relative stabilization of the 3_{10}-helix with respect to the α-helix is observed. However, the α-helix remains the lowest free energy minimum at room temperature, owing to its lower energy at $T = 0$ K.

The poly-proline-II structure

The thermodynamic analysis presented above is complete in a sense that it includes all the structural conformations corresponding to (known) local minima of the (L, Θ) potential energy surface (Sec. 1.5). However, we decided, in a late stage of the project, to include a further structural conformation, the so called poly-proline-II (PPII) structure. The PPII-structure is characterized by a pitch $L =$ 5.92 Bohr and a twist $\Theta = 240°$ and is located in the domain corresponding to the unfolded state of the peptide chain. Recent studies, which are based on a statistical analysis of random coil segments as extracted from the protein data base, report a significant population of this structure [140, 141, 142] and it has been proposed that the PPII-structure might be characteristic for unfolded proteins [143, 144, 145].

We remark that the PPII-structure does, in contrast to the other structures analyzed in this study, not correspond to a minimum with respect to the helical parameters L and Θ. Moreover, we find that

---

[5] In Eq. (4.6) electronic entropy contributions are neglected, which is well justified since the electronic band gap is huge (Secs. 2.3 and 2.6.1).

[6] With a different notation for the total energy: Note that $E^{\text{el}}(L_S, \Theta_S) = U_S^{\text{el}}$.

it is strongly unstable with respect to the other conformations, since it is higher in potential energy than the FES by $\Delta U^{\mathrm{el}}_{\mathrm{PPII}} = 2.70$ kcal/mol per peptide unit. Nonetheless, we have investigated this structure, to check whether it could be stabilized by vibrational contributions. Indeed, we find that this structure has the lowest vibrational free energy of all analyzed conformations with $\Delta F^{\mathrm{vib}}_{\mathrm{PPII}} = -0.74$ kcal/mol. However, owing to its high potential energy, it remains a less stable conformation also at room temperature. This result lets us presume that the significant population of the PPII-structure as reported in the experimental studies is due to the protein environment, e.g., the solvent. Furthermore the results clearly show that the PPII-structure is irrelevant for the thermodynamic state of the isolated, infinite peptide chain, i.e., is *not* intrinsically stable at the relevant temperature range. We will therefore largely exclude this structure from the further analysis.

4.2.3 Stability of the helix against unfolding

Based on the knowledge of the phase stability of the various conformations we may also estimate the stability of the helix against unfolding. According to Eq. (2.139) the stability of the helical state against unfolding is given by:

$$\Delta F^{\mathrm{f}}_{\mathrm{helix}\to\mathrm{unfolded}} \approx \mu^{\mathrm{helix}} - \mu^{\mathrm{unfolded}}, \tag{4.8}$$

where μ^{helix} is the chemical potential of the helical state (Eq. (2.138)) and μ^{unfolded} is the chemical potential of the unfolded state (Eq. (2.136)). Following Sec. 2.8.2 the unfolded state is approximately an ideal solution of the bulk phases corresponding to the unfolded domain of the (Θ, L)-PES. These are the FES, and the PPII- and 2_7-structure. Thus, we obtain for the chemical potential of the unfolded state at room temperature:

$$\begin{aligned}
\mu^{\mathrm{unfolded}} &\approx \mu^{\mathrm{bulk}}_{\mathrm{FES}} - (k_{\mathrm{B}}T)_{300K} \ln\left(1 + \sum_{X\neq A}^{\mathrm{non-helical}} \exp(-\beta\Delta F^{f}_{\mathrm{FES}\to X})\right) \\
&= \mu^{\mathrm{bulk}}_{\mathrm{FES}} - (k_{\mathrm{B}}T)_{300K} \ln\left(1 + \exp(-\beta\Delta F^{f}_{\mathrm{FES}\to 2_7}) + \exp(-\beta\Delta F^{f}_{\mathrm{FES}\to\mathrm{PPII}})\right) \\
&= \mu^{\mathrm{bulk}}_{\mathrm{FES}} - 0.60\frac{\mathrm{kcal}}{\mathrm{mol}} \ln(1 + 0.73 + 0.04) \\
&= \mu^{\mathrm{bulk}}_{\mathrm{FES}} - 0.35\frac{\mathrm{kcal}}{\mathrm{mol}}.
\end{aligned} \tag{4.9}$$

Eq. (4.34) shows that the chemical potential of the unfolded state is ≈ 0.35 kcal/mol lower than the chemical potential of the FES. Hence "adding" the 2_7-structure and PPII-structure to the unfolded state does not substantially lower the chemical potential of the unfolded state with respect to the that of the FES.

According to Eq. (2.138) the chemical potential of the helical state is approximately given by the helical bulk phase with the lowest free energy. At room temperature this is the α-helix:

$$\mu^{\mathrm{helix}} = \mu^{\mathrm{bulk}}_{\alpha-\mathrm{helix}} \tag{4.10}$$

Hence, the stability of the helical state against unfolding at room temperature amounts to:

$$\begin{aligned}\Delta F^{\mathrm{f}}_{\mathrm{helix}\rightarrow\mathrm{unfolded}} &\approx \mu^{\mathrm{helix}} - \mu^{\mathrm{unfolded}} \\ &= \mu^{\mathrm{bulk}}_{\alpha-\mathrm{helix}} - \mu^{\mathrm{bulk}}_{\mathrm{FES}} + 0.35\frac{\mathrm{kcal}}{\mathrm{mol}} \\ &= \Delta F^{f}_{\alpha-\mathrm{helix}\rightarrow\mathrm{FES}} + 0.35\frac{\mathrm{kcal}}{\mathrm{mol}} \\ &= -0.65\frac{\mathrm{kcal}}{\mathrm{mol}}. \qquad (4.11)\end{aligned}$$

We conclude that the helical state will be stable at room temperature.

4.2.4 Conclusions

Our results on poly-L-alanine verify that vibrational contributions to the free energy play a key role for the stability of the helix in the biologically relevant temperature range, as they strongly reduce the phase stability of the folded, helical conformations with respect to the fully extended structure of the peptide chain – they thus counteract the enthalpic stability of the helices due to the formation of hydrogen bonds.

Nevertheless, the hydrogen bonds are still sufficiently strong to make the α-helix the most stable bulk phase at room temperature. We thus conclude that a long, single-stranded and isolated poly-L-alanine chain will fold to an α-helix at room temperature. This conclusion remains also valid, when we replace the FES by a more realistic reference for the unfolded state. We found that the 2_7-structure and the poly-II-proline structure are significantly higher in free energy than the FES at room temperature. The unfolded state of the peptide chain is thus strongly dominated by the FES. Therefore the chemical potential of the unfolded state is not substantially lower than that of the FES.

Furthermore, our results clearly reveal a significant temperature dependence of the *relative* stability between the three helix types. The π-helix exhibits the strongest temperature dependence amongst the three helix types. In contrast to the 3_{10}- and the α-helix it is, with respect to the free energy, almost degenerate to the FES at room temperature (and higher than the unfolded state). Hence, our results may be used to rationalize why the population of π- and 3_{10}-helices varies with temperature as well as to explain why the π-helical motif is the least common of the helical conformations in proteins. What is still missing, however, is an identification of the mechanisms which drive these thermodynamic trends.

4.3 Origin of the thermodynamic trends

In order to identify the origin of the thermodynamic trends we have analyzed the vibrational contributions to the free energy in detail. In this section at first the particular vibrational branches, which most prominently contribute to the free energy differences between the various conformations are identified. Then we unveil the mechanisms, which drive the differences observed for these particular branches by investigating the dynamical matrix corresponding to the relevant conformations.

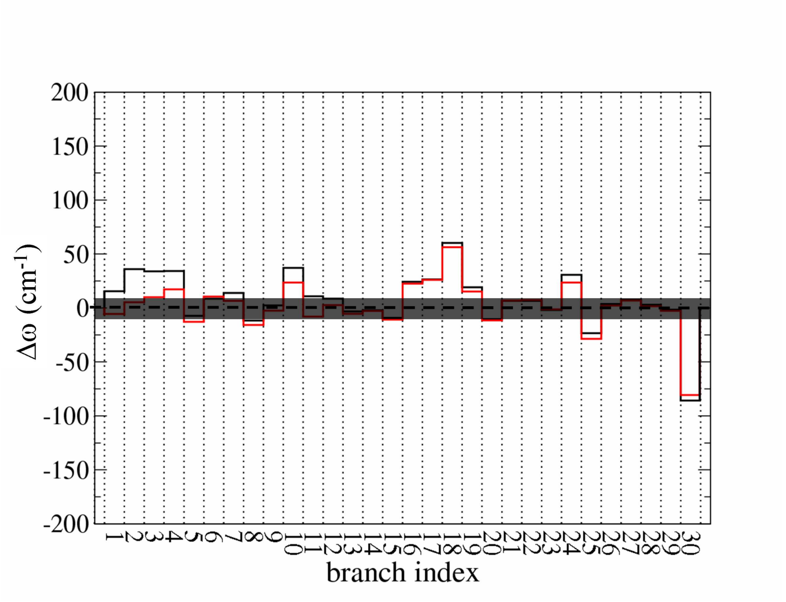

Figure 4.4: Band center shifts in the α-helical conformation compared to the FES. The band center shifts are defined by $\Delta\omega_i = \frac{1}{\pi}\int_0^\pi \omega_i^\alpha(\varphi)d\varphi - \frac{1}{\pi}\int_0^\pi \omega_i^{\text{FES}}(\varphi)d\varphi$, where i denotes the branch index as explained in Fig. 4.5. The black line denotes the shifts for the un-manipulated dynamical matrix, whereas the red line shows the shift, if the long-ranged interactions are removed from the dynamical matrix (Sec. (4.3.2)). The dark, semi-transparent bar denotes an (arbitrarily defined) region of insignificance, where $\Delta\omega_i < 10\text{cm}^{-1}$.

Hereby we focus on the α-helix and the FES, since these two structures are representative for the helical and the unfolded state, respectively.

4.3.1 Decomposition of the vibrational free energy

A complete overview of the vibrational spectra of the investigated conformations of the poly-L-alanine chain is given in the appendix (Fig. 6.6). Furthermore, we have performed a detailed comparison of the phonon dispersion relations between the α-helix and the FES, which is also presented in the appendix (Sec. 6.1.3). From the latter comparison we obtain “fingerprints” of the helix formation on the vibrational spectrum of the peptide chain, which may be characterized as follows: The internal vibrations of the side-chain (methyl group) remain largely unaffected by the helix formation. In contrast, significant changes are found for the vibrational branches which correspond to a deformation of the backbone of the peptide chain. Most importantly we determined significant shifts for the four lowest vibrational branches, i.e., the two acoustical and the first two optical branches. We found that the helix formation is connected to a significant hardening (blue-shift) in these branches (Fig. 4.4).

type of contribution →	$-T\Delta S^{\mathrm{vib}}$					ΔU^{vib}
included branches →	1	1,2	1,2,3	1,2,3,4	5-30	1-30
$\alpha \rightarrow FES$	22	67	79	88	3	9
$\alpha \rightarrow \pi$	48	64	59	65	13	22

Table 4.3: Individual contributions of the vibrational branches (Eq. (4.12)) to the vibrational free energy differences at room temperature in percent for the L-alanine chain. The second column contains the contributions of entropy associated with the lowest lying vibrational branch (first sub-column), the two lowest lying vibrational branches (second sub-column), the three lowest lying vibrational branches (third sub-column) and the four lowest lying vibrational branches (fourth sub-column) and the entropy associated with the branches 5-30, respectively. The third column contains the energetic vibrational contributions originating from the entire vibrational spectrum.

This hardening is of fundamental importance for the thermodynamic properties, which becomes clear, when decomposing the vibrational free energy differences into the contributions arising from the individual vibrational branches:

$$\Delta F^{\mathrm{vib}}_{A \rightarrow B,i} = \Delta U^{\mathrm{vib}}_{A \rightarrow B,i} - T\Delta S^{\mathrm{vib}}_{A \rightarrow B,i}, \tag{4.12}$$

where i runs over the individual branches as labeled in Fig. 4.1. We have evaluated how large the contributions of the individual branches are to the integrated, total free energy difference, i.e:

$$\Delta F^{\mathrm{vib}}_{A \rightarrow B} = \textstyle\sum_{i=1}^{30} \Delta F^{\mathrm{vib}}_{A \rightarrow B,i}. \tag{4.13}$$

Indeed, we found that the vibrational free energy is strongly dominated by vibrational entropy differences associated with the lowest frequency branches. More precisely, 88 % of the free energy difference between the FES and the helical conformations is already contained in vibrational entropy differences associated with the four lowest vibrational branches (Tab. 4.3, first row). The 3 lowest vibrational branches contribute with 79% of the vibrational free energy differences and the two acoustical still with 67 %. The contributions of vibrational energy (zero point vibrations) are less important and amount to 9 % of the vibrational free energy differences at room temperature. When coming to the differences between helices, the picture is similar, although the relative contribution of the zero-point vibrations is slightly larger here (Tab. 4.3, second column).

According to this decomposition of the vibrational free energy, we conclude that it is sufficient to focus on the three or four lowest frequency branches in order to understand the thermodynamic trends. Indeed, it is the hardening of the two acoustical branches, which is mainly responsible for the free energy differences.

4.3.2 Analysis of the dynamical matrix

The vibrational spectra are derived from the dynamical matrix. Therefore, to gain further understanding of the changes the helix formation induces in the low frequency branches, we have compared the dynamical matrix of the α-helix with that of the FES (Fig. 4.5b).

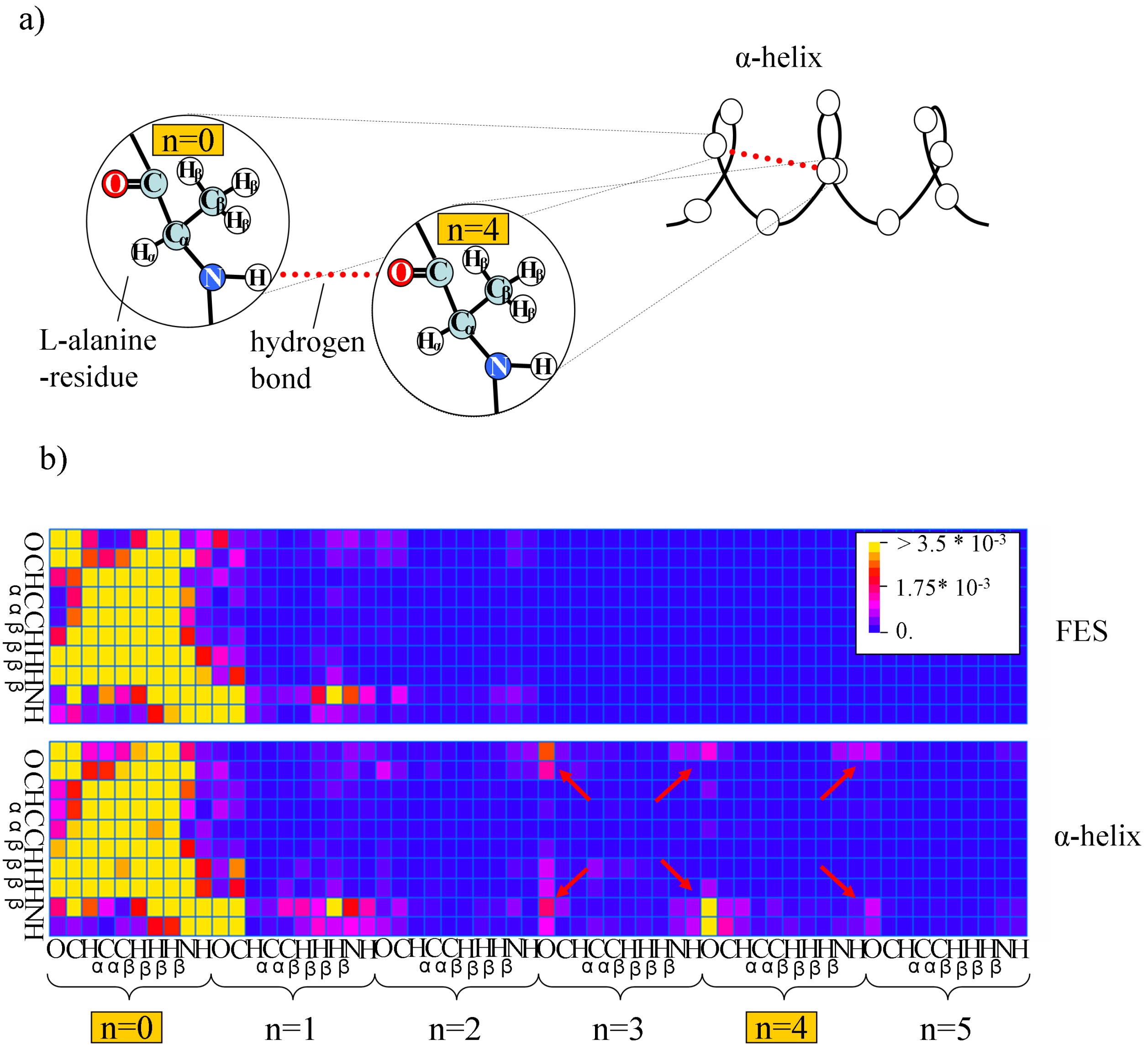

Figure 4.5: a) Schematic illustration of a hydrogen bond in the poly-L-alanine α-helix. The index n labels the peptide units. b) Dynamical matrix of the α-helix and the FES. Shown is the *atom-atom coupling*, as defined in Eq. (4.16), normalized to the maximum value. For convenience of visualization it is only plotted in the range from 0 to 0.0035; several atom-atom couplings for n=0 are exceeding the plot range. The arrows point at C-O$\cdots$H-N atom-atom couplings which correspond to the hydrogen bonds [see also a), dotted red lines].

We have hereby focused on the the atom-atom interaction, as contained in the dynamical matrix:

$$\mathbf{D}_{IJ} = \begin{pmatrix} \frac{\partial^2 E^{\text{el}}}{\partial X_I^{(1)} \partial X_J^{(1)}} & \frac{\partial^2 E^{\text{el}}}{\partial X_I^{(2)} \partial X_J^{(1)}} & \frac{\partial^2 E^{\text{el}}}{\partial X_I^{(3)} \partial X_J^{(1)}} \\ \frac{\partial^2 E^{\text{el}}}{\partial X_I^{(1)} \partial X_J^{(2)}} & \frac{\partial^2 E^{\text{el}}}{\partial X_I^{(2)} \partial X_J^{(2)}} & \frac{\partial^2 E^{\text{el}}}{\partial X_I^{(3)} \partial X_J^{(2)}} \\ \frac{\partial^2 E^{\text{el}}}{\partial X_I^{(1)} \partial X_J^{(3)}} & \frac{\partial^2 E^{\text{el}}}{\partial X_I^{(2)} \partial X_J^{(3)}} & \frac{\partial^2 E^{\text{el}}}{\partial X_I^{(3)} \partial X_J^{(3)}} \end{pmatrix}. \tag{4.14}$$

Here I and J label the atoms of the peptide chain, and the superscribted numbers $(1, 2, 3)$ denote the three Cartesian degrees of freedom of each atom.

To obtain a meaningful comparison between the α-helix and the FES, we have not directly plotted the dynamical matrix (Eq. (4.14)). The reason is that the dynamical matrix depends not only on the strength of the atom-atom interaction, but also on the relative rotational position of the atoms in the coordinate frame, i.e., on the respective structural conformations. We are, however, exclusively interested in the strength of the interaction. Therefore we have performed the comparison in the following way: For each pair of atoms I and J the three *moments of interaction,* $d_{IJ}^{(1,2,3)}$, are determined, which we define by

$$\mathbf{D}_{IJ}\mathbf{v}^{(i)} = d_{IJ}^{(i)}\mathbf{v}^{(i)} \qquad i = 1, 2, 3. \tag{4.15}$$

Here, the $\mathbf{v}^{(i)}$ are the 3 dimensional eigenvectors corresponding to the eigenvalue $d_{IJ}^{(i)}$. The absolute values of the moments of interactions are summed up to obtain a quantity, which we here define as *atom-atom coupling* $D_{IJ}^{\text{atom}-\text{atom}}$:

$$D_{IJ}^{\text{atom}-\text{atom}} = \sum_{i=1}^{3} |d_{IJ}^{(i)}|. \tag{4.16}$$

Although the atom-atom coupling has no direct physical meaning, it is particularly helpful to visualize the dynamical matrix and to identify the atom-atom interactions specific for the various conformations. The reason for the latter is that the atom-atom couplings are rotational invariant, i.e., they do not depend on structural properties of the conformation, but only on the atom-atom interaction strength.

We find in this analysis (Fig. 4.5b) that the dynamical matrix contains a strong "core" of short-ranged atom-atom couplings close to the diagonal (Fig. 4.5b, n=0), which we suppose to be related to the chemical bonds stabilizing the backbone of the peptide chain. Aside from that we find a significant amount of smaller long-ranged atom-atom couplings (Fig. 4.5b, n>0). Outstanding of these long-ranged atom-atom couplings we find a characteristic pattern corresponding to the interaction of the C=O and N-H groups which constitute the hydrogen bonds in the helix (Fig. 4.5a). These atom-atom couplings are found for the α-helix (Fig. 4.5b, n>3,4) but not for the FES.

To analyze the importance of these specific hydrogen bonding atom-atom couplings more in detail, we have determined the change in the vibrational branches, if these specific atom-atom couplings are eliminated from the dynamical matrix. We find that this elimination results in a significant red shift of the low frequency branches, which indicates a strong influence of the hydrogen bonds on these branches. Moreover, Fig. 4.4 shows that the band-center shifts with respect the FES (black

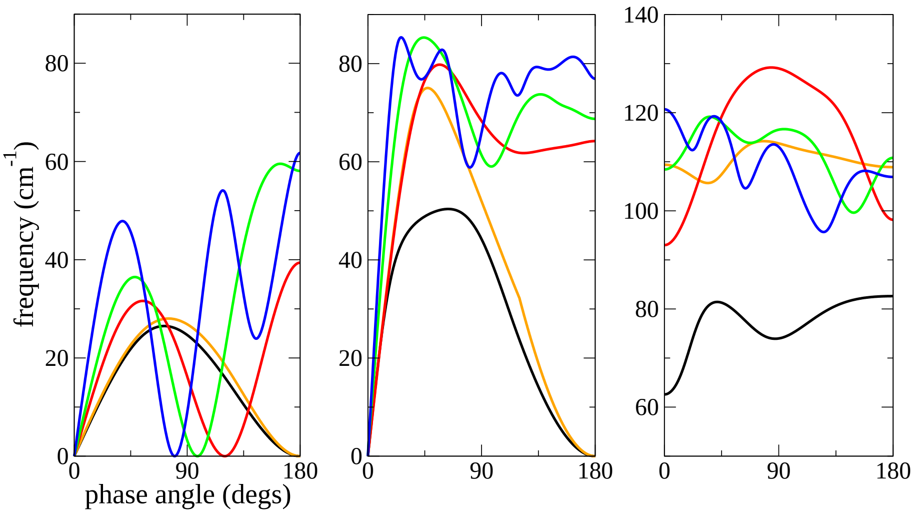

Figure 4.6: Lowest frequency branches of π- (blue lines), α- (green lines) and 3_{10}-helix (red lines), 2_7-conformation (orange lines) and FES (black lines).

lines in Fig.4.4) almost disappear (red lines in Fig.4.4). Thus we conclude that a major part of the observed thermodynamic trends is a direct effect of the formation of the hydrogen bonding network in the helical structures. We analyze this issue in more detail in the following section.

4.4 Development of an analytical model

In the previous section we have shown that a strong direct correlation exists between the formation of the hydrogen bonds in the helix and its temperature dependent stability: The hydrogen bonds cause a hardening of the low frequency branches, which is then reflected in a loss of vibrational entropy with respect to the FES, in which hydrogen bonds are absent. This effect has been suggested in the literature since long – Fanconi et al. realized already in the early 70s that the acoustical branches of the helix are not only determined by the backbone of the helix, i.e., nearest neighbor peptide-peptide interactions (Fig. 4.7a), but also depend sensitively on the hydrogen bonds [54]. Nevertheless, the employment of empirical force fields in that and subsequent studies [55, 56, 146] made it impossible to accurately quantify the influence of the hydrogen bonds as, e.g., compared to the influence of nearest neighbor peptide-peptide interactions in the backbone of the helix.

In this section we therefore intend to obtain a more quantitative understanding of the interplay of nearest neighbor backbone interactions and hydrogen bonds for the low frequency branches. Furthermore, we would like to understand how this interplay ultimately drives the observed thermodynamic trends — for instance why the π-helix has a lower vibrational entropy than the other two helices.

4.4.1 Ball-and-spring model

The fact that the three lowest branches (Fig. 4.6) almost entirely (by 79 %, Sec. 4.3.1) determine the thermodynamic behavior allows to map the problem on a simple ball-and-spring model. Here,

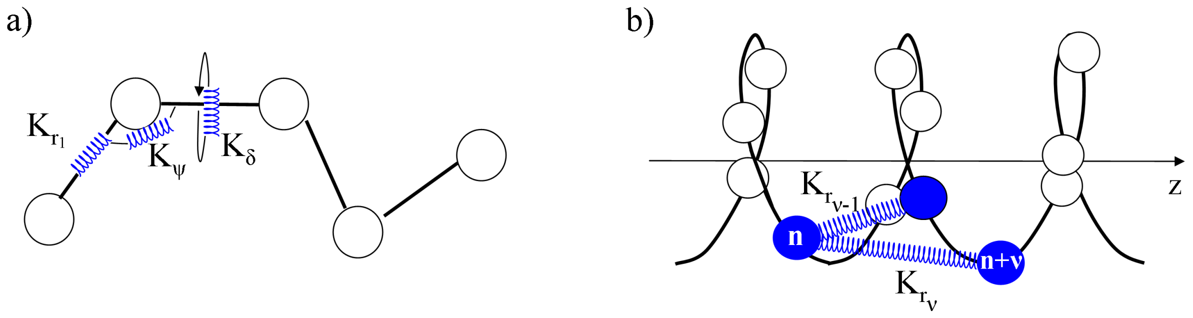

Figure 4.7: Illustration of the ball-and-spring model: a) Backbone contributions corresponding to U^{bb} (Eq. (4.19)). b) Hydrogen bonding contributions corresponding to U^{hb} (Eq. (4.20)).

the peptide units are considered as rigid units (balls), connected with each other by harmonic springs. In order to obtain a straightforward decomposition of the hydrogen bonds and the backbone interactions, we have developed such a ball-and-spring model and derived explicit spring constants for these contributions.

Within this model the potential energy of the peptide chain is decomposed into contributions arising from the deformation of the backbone U^{bb} and of the hydrogen bonds U^{hb}. Together with the kinetic energy, T, the model Hamiltonian can be expressed as:

$$H = T + U \tag{4.17}$$

$$U = U^{\mathrm{bb}} + U^{\mathrm{hb}} \tag{4.18}$$

$$U^{\mathrm{bb}} = \frac{1}{2}\sum_{n}\left\{K_{r_1} \mid \Delta r_{n_1} \mid^2 + K_{\Psi} \mid \Delta\Psi_n \mid^2 + K_{\delta} \mid \Delta\delta_n \mid^2\right\} \tag{4.19}$$

$$U^{\mathrm{hb}} = \frac{1}{2}\sum_{n}\left\{K_{r_\nu} \mid \Delta r_{n_\nu} \mid^2 + K_{r_{\nu-1}} \mid \Delta r_{n_{\nu-1}} \mid^2\right\}. \tag{4.20}$$

An illustration of the model is given in Fig. 4.7. The backbone contributions, U^{bb}, are modeled in terms of displacements in the bond distances Δr_{n_1}, the valence angles $\Delta\Psi_n$, and the dihedral angles $\Delta\delta_n$ at peptide unit n. The backbone stiffness is contained in the spring constants K_{r_1}, K_{Ψ} and K_{δ}. The hydrogen bonds, U^{hb}, are modeled in terms of the distances Δr_{n_ν} between the peptide units n and $n+\nu$ and the distances $\Delta r_{n_{\nu-1}}$ between the peptide units n and $n+\nu-1$. The corresponding spring constants are K_{r_ν} and $K_{r_{\nu-1}}$.

Similar model Hamiltonians have recently been applied to study the propagation of solitons along helical polymers [147, 148]. However, we found that several extensions to these models are required to obtain an accurate reproduction of the vibrational spectra as derived with DFT. A detailed discussion of the model of Ref. [147] is given in the Appendix (Sec. 6.4.1). Here we describe the main improvements over this model. Whereas in Ref. [147] the hydrogen bonds have been described

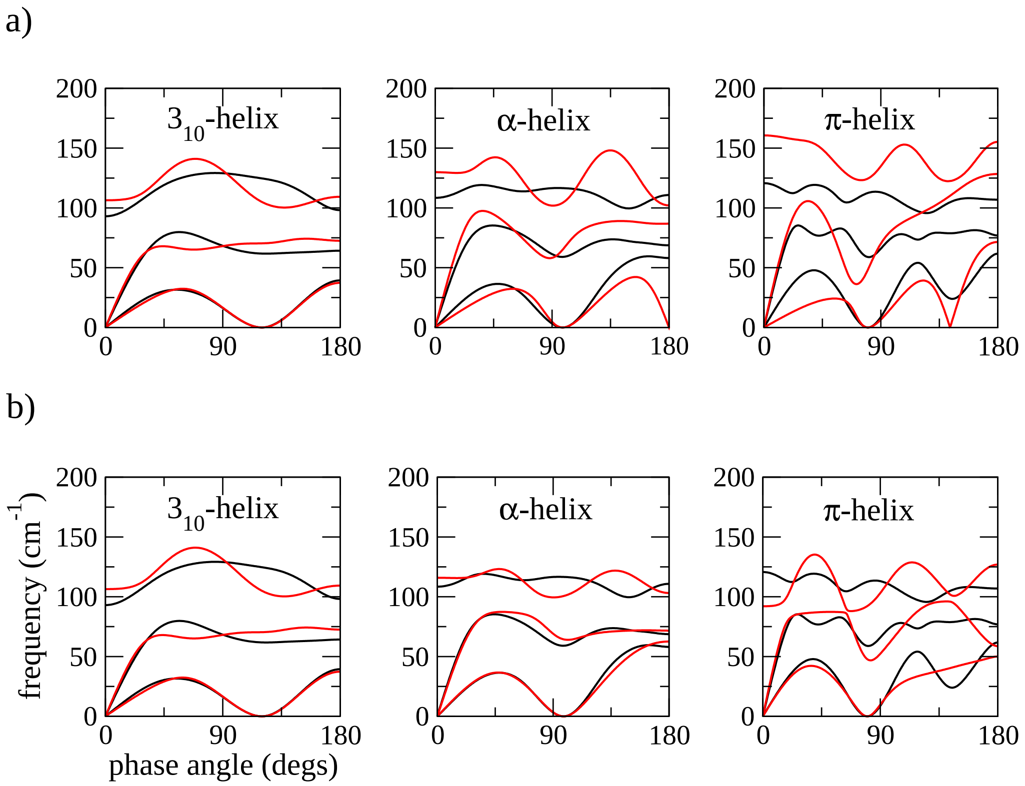

Figure 4.8: Comparison of the 3 lowest vibrational branches as obtained with the analytical spring model (red lines) to the DFT values (black lines). a) For the model proposed in Ref. [147], which models the hydrogen bonds by means of a single spring (Eq. (6.27)). b) For the extended model developed for this project (Eq. (4.17)).

backbone	K_{r_1}	K_δ	K_Ψ
$2_7, 3_{10}, \alpha, \pi$	21.6	0.79	3.02
FES	21.6	0.17	3.02

hydrogen bonds	$K_{r_{\nu-1}}$	K_{r_ν}
$3_{10}, \alpha, \pi$	21.6	12.3
2_7	8.60	12.3

Table 4.4: Optimized parameter-set for the ball-and-spring model (Eq. (4.17)). The spring constants are expressed in $\mathrm{cm}^{-1} \cdot 10^4$.

by a single force constant, we found that an effective 3-body treatment of the hydrogen bonding, i.e., the introduction of two independent spring constants, is essential to get an accurate fit to the low frequency branches of the helices, as calculated within the DFT approach. In particular for an accurate reproduction of the α- and the π-helix this effective 3-body treatment is essential, as is shown in Fig. 4.8. The nature of the three-body interaction is likely due to the large cooperativity (Sec. 1.4, Ref. [48]) and/or directionality [44] of the hbs. We point out that the accurate calculations of the acoustical branches with DFT were fundamental to obtain this improved parametrization of the hydrogen bonds – which again highlights the importance of the DFT calculations. Besides the improvement of the description of the hydrogen bonding we found it also necessary to extend the treatment of the backbone interactions as described above in Eq. (4.20). To be able to reproduce the vibrational branches of the FES and the 2_7-conformations we have included also force constants for the dihedral angle and for the valence angle in the model.

The parameters for the model, i.e., the spring constants, have been optimized to fit the three lowest vibrational branches for each individual chain conformation as calculated with DFT (details in the appendix, Sec. 6.4.1). Great care has been taken to avoid over-parametrization and to ensure the maximum transferability by determining the parameters in the following way: In a minimal model we assumed the spring constants to be the same in the different chain conformations. An exception was made for the FES, where hydrogen bonding is absent and the corresponding force constants are set equal to zero. The minimal model is then successively extended by introducing independent force constants for the conformation with the worst reproduction of the DFT frequencies. A good agreement, for all five conformations, is already achieved by introducing only two additional force constants to the minimal model – one for the dihedral angle of the FES and one for the hydrogen bonding in the 2_7-conformation. Thus, we need only seven spring constants to describe the vibrational properties of all five conformations (Tab. 4.4). As Fig. 4.9 shows, this model excellently reproduces the thermodynamic trends associated with the three lowest vibrational branches of the L-alanine chain.

Results of the ball-and-spring model

Based on the obtained spring constants we now apply the ball-and-spring model to analyze the impact of the hydrogen bonds and the backbone interactions on the lowest frequency branches and the vibrational entropy in detail.

By setting the corresponding force constants to zero, the model allows to quantify, which bonds (hydrogen bonds or backbone) determine the entropic character of the various conformations. By setting all hydrogen bonds to zero (dots in Fig. 4.9) the entropic differences between the conforma-

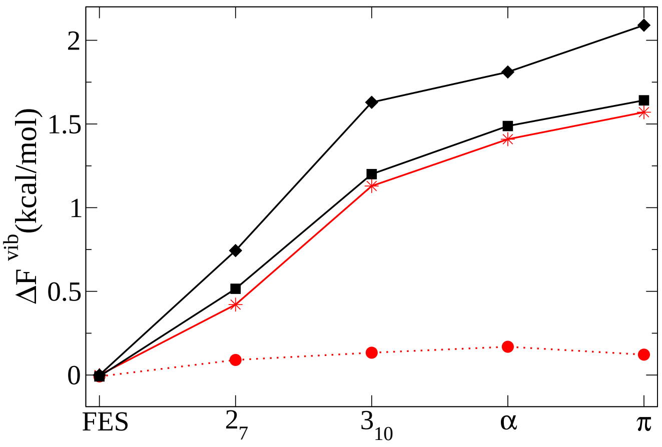

Figure 4.9: Vibrational free energy contributions to the stability with respect to the FES (Eq. (4.7)) at room temperature for the different conformations of the poly-L-alanine chain: Shown are the DFT results for the contributions from the full vibrational spectrum (solid black line, diamonds) and the contributions arising from exclusively the 3 lowest vibrational branches (solid black line, squares). Further shown are the results from the ball-and-spring model with the spring constants listed in Tab. 4.4 (solid red line, stars) and the corresponding vibrational free energy contributions, if the spring constants corresponding to the hydrogen bonds are removed from the model (dotted red line, circles).

tions almost completely disappear. We therefore conclude that the temperature effects, which make helices unstable at higher temperatures, are almost exclusively determined by the hydrogen bonds. The impact of the stiffness of the helix backbone on the thermodynamic differences is negligible.

Another important result obtained with the ball-and-spring model is that the obtained spring constants are *the same* for all three helix conformations. Hence, we conclude that the entropic differences between the helix conformations should *not* be explained by differences in the *strength* of the peptide-peptide interactions.

4.4.2 Elastical moduli, speed of sound and long-wavelength limits

We now like to go one step further and to uncover the mechanism, which drives the thermodynamic differences between the helical conformations. In particular, we aim to understand, why the π-helix presents a lower vibrational entropy than the other two helix types, i.e., α-helix and 3_{10}-helix. As mentioned above, the obtained spring constants for the ball-and-spring model are the same for the three helix types. Hence, since no alternative mechanisms are possible, it is tempting to conclude that the entropic differences between the helices are dictated exclusively by the geometrical differences between the helix types.

To investigate the impact of the helix geometry on the vibrational entropy, we focus on the asymptotic behavior at the long-wavelength limits of the acoustical branches. The reason is that the asymptotic behavior dominates the shape of the acoustical branches (Fig. 4.10) and consequentially the entropic differences between the helices. Indeed, the relative loss of vibrational entropy in the π-helix correlates to a relative increment of the asymptotic slopes/curvatures at the long wavelength

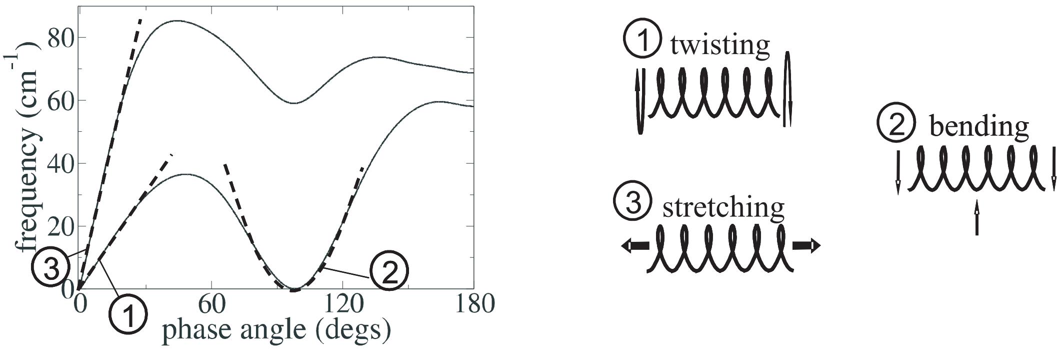

Figure 4.10: Long-wavelength limits of the α-helix and the corresponding mechanical deformations. The dotted lines denote the asymptotic behavior. The dotted line for the bending deformation describes a parabola, the dotted lines for stretching and twisting describe straight lines.

limits. More precisely, we observe the following behavior:

1. The asymptotic behavior of the acoustical branches is characterized by a linear dispersion law of $\omega_1(\varphi)$ and $\omega_2(\varphi)$ for $\varphi \to 0$ (Fig. 4.10a, labels '1' and '3', respectively) and by a quadratic dispersion law of $\omega_1(\varphi)$ for $\varphi \to \pm\Theta$ (Fig. 4.10a, label '2').

2. The corresponding curvatures and slopes are largest for the π-helix, followed by the α- the 3_{10}-helix, the 2_7-structure and the FES (Fig. 4.11a and b).

The eigenmodes at the long-wavelength limits are the *mechanical* deformations of the helix. We identified them with the torsional, the bending and the longitudinal deformation, respectively (Fig. 4.10). For convenience, we will in the following not directly discuss the slopes at the long-wavelength limits but instead a closely related quantity, the speed of sound. The corresponding velocities are, following Eq. (2.97), given by:

$$v_T = v_1^z(\varphi \to 0) = L \left(\frac{\partial \omega_1(\varphi)}{\partial \varphi} \right)_{\varphi \to 0}, \quad v_L = v_2^z(\varphi \to 0) = L \left(\frac{\partial \omega_2(\varphi)}{\partial \varphi} \right)_{\varphi \to 0}$$

$$\text{and} \quad v_B = v_2^z(\varphi \to \Theta) = L \left(\frac{\partial \omega_2(\varphi)}{\partial \varphi} \right)_{\varphi \to \Theta} . \tag{4.21}$$

Here v_T, v_L, and v_B denote the speed of the torsional, longitudinal and bending sound waves, respectively. Fig. 4.11 shows the slopes as well as the speed of sound. It is interesting to note that for the longitudinal waves and the torsional waves the speed of sound is roughly constant amongst the helices and about 900 m/s (upper lines in Fig.4.11c) and 300 m/s (lower lines in Fig.4.11c), respectively. The speed of the bending waves is increasing in going from 3_{10}-helix over α-helix to π-helix (Fig.4.11d) .

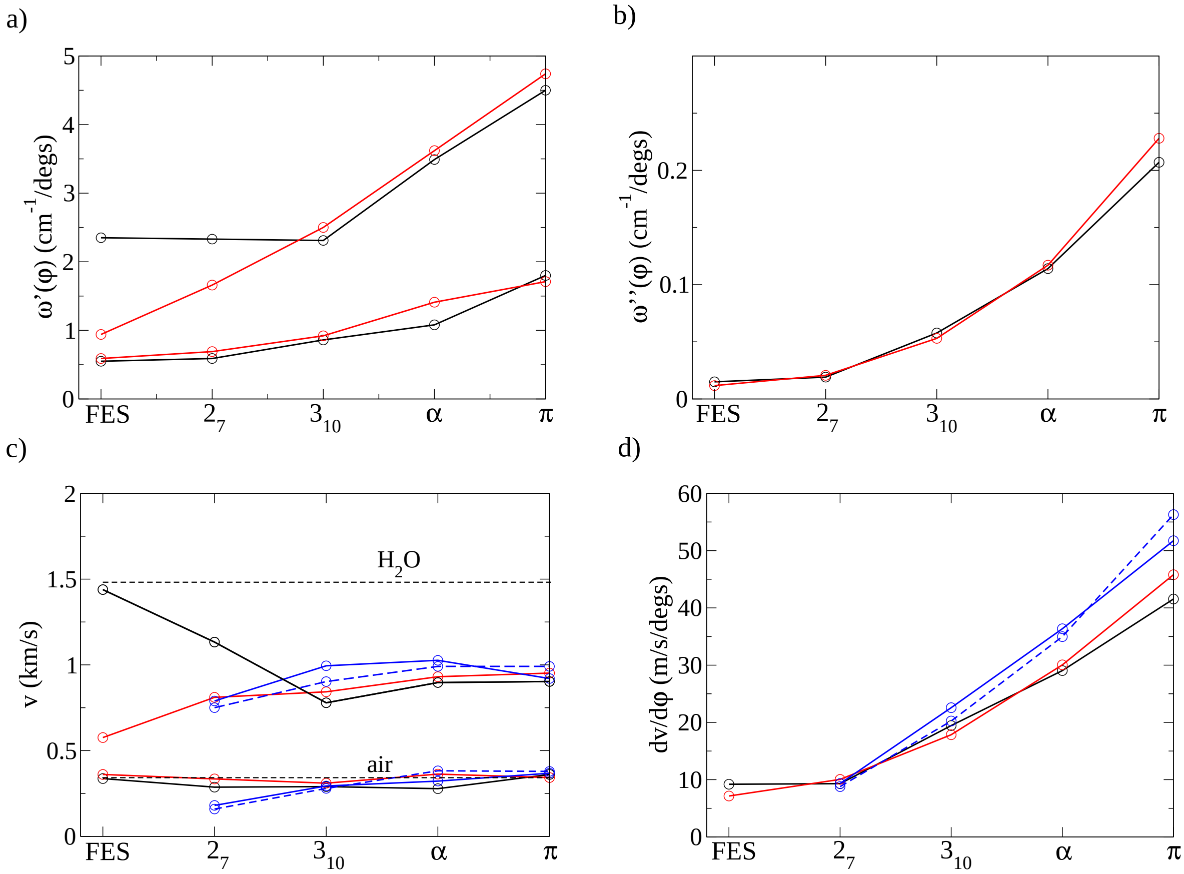

Figure 4.11: a) Slopes at the long-wavelength limits of the acoustical branches corresponding to the longitudinal (upper lines) and the torsional deformation (lower lines) for the DFT calculations (black lines) and the ball-and-spring model (red lines). b) Curvatures at the long-wavelength limit corresponding to the bending deformation. c) Speed of sound for the longitudinal and the torsional waves (Eq. (4.21)) for the DFT calculations (black lines), the ball-and-spring model (red lines), the thin rod approximation (dashed blue lines, see Appendix, Sec. 6.4.3, Eqs. (6.48-6.53)) and the geometrical formulas denoted in Eqs. (4.27) and (4.29). For comparison also the speeds of sound in water [149] and air are shown (dashed lines). d) Corresponding values for the speed of sound per phase angle for the bending waves.

Thin rod approximation

To understand the thermodynamic trends it is essential to understand these trends for the long wavelength limits and the speeds of sound formulated above. Therefore we will investigate the speeds of sound by means of a simple model stemming from elasticity theory, the thin rod approximation [150]. This approximation, combined with the analytical ball-and-spring model (Eq. (4.17)), will allow us, to derive very simple analytical formulas for the speeds of sound, and hence through Eq. (4.21) also for the long-wavelength limits. Based on these expressions we will arrive to an interpretation of the thermodynamic trends.

As described in Ref. [150], the thin rod approximation may be applied to describe the mechanical deformations/waves in a system, provided the system fulfills the following conditions:

1. The lateral dimensions of the system are much smaller than its longitudinal dimensions.
2. The system is isotropic, i.e., the stress tensor is diagonal in the basis of longitudinal and lateral coordinates.
3. The system is homogeneous, i.e., the microscopic stress, which would occur as a response on a macroscopic deformation (i.e. by applying macroscopic strain) is evenly distributed throughout the entire system.

The helical conformations fulfill these conditions, since they are much longer than thick, contain a homogeneous distribution of the amino acids, and the three helical parameters L, Θ and R are approximately decoupled [50]. The 2_7-conformations and in particular the FES violate condition ii), since the pitch and the twist are significantly coupled here, giving rise to the existence of non-diagonal elements in the stress tensor. We will therefore focus on the three helical conformations in the following.

By considering the thin rod approximation, the mechanical waves of the helix may be described by three separated homogeneous wave-equations (for details see appendix, Sec. 6.4.2, Eqs. (6.30) and (6.35)). Solving these wave-equations yields three different kinds of mechanical waves in the peptide chain: longitudinal waves, torsional waves and bending waves. For the longitudinal and the torsional waves the following *linear* dispersion laws are obtained:

$$\omega_L(k) = v_L k \quad \text{and} \quad \omega_T(k) = v_T k. \tag{4.22}$$

Here, $k = \frac{2\pi}{\lambda}$ is the reciprocal wavelength and ω is the frequency of the wave. The quantities v_L and v_T denote the longitudinal and the torsional velocities of sound, respectively, and are given by:

$$v_L = \sqrt{\frac{Y}{\rho}} \quad \text{and} \quad v_T = \sqrt{\frac{T}{\rho}}. \tag{4.23}$$

Here, ρ is the density, and Y and T are the Young's and the torsional modulus[7], respectively, and

---

[7] We remark that the density ρ and the elastical moduli depend on the volume and on the cross-sectional area, respectively, which are *not* well defined quantities for the peptide chain. However, the sound velocities and the long-wavelength limits in turn only depend on the ratio of volume and cross-sectional area, which is a well defined physical quantity.

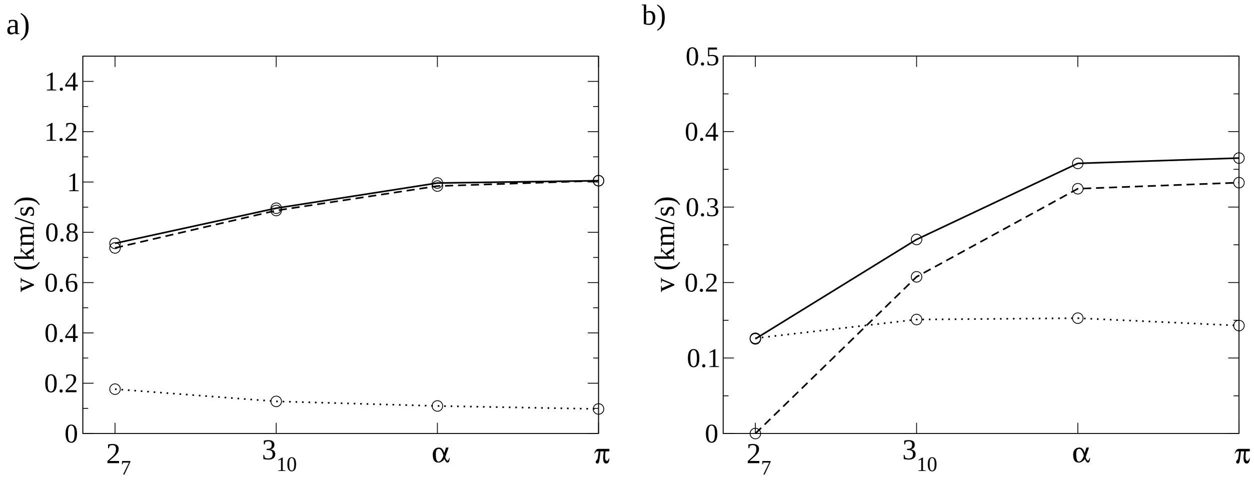

Figure 4.12: Decomposition of the speed of sound with respect to hydrogen bonding contributions (dashed black lines) and backbone contributions (dotted black lines) in the framework of the thin rod approximation, for a) the longitudinal waves and b) the torsional waves. The hydrogen contributions estimated with from Eq. (4.26) by setting the backbone contributions to zero. The backbone contributions are estimated with Eq. (4.26) by setting the hydrogen bonding contributions to zero. For comparison purposes the "full" speeds of sound in thin rod approximation (solid black lines) are also shown.

are defined as:

$$Y = \frac{\sigma_{zz}}{\epsilon_{zz}} \quad \text{and} \qquad T = \frac{\sigma_{\Theta\Theta}}{\epsilon_{\Theta\Theta}}. \tag{4.24}$$

In Eq. (4.24) σ_{zz} and $\sigma_{\Theta\Theta}$ denote the longitudinal and the torsional stress, and ϵ_{zz} and $\epsilon_{\Theta\Theta}$ denote the longitudinal and the torsional strain, respectively.

For the bending waves the thin rod approximation predicts a *quadratic* dispersion law, in nice agreement with the observations formulated above for the long-wavelength limits:

$$\omega = \frac{1}{2} a_B k^2 \quad \text{where} \quad a_B = R\sqrt{\frac{Y}{\rho}} = R v_L. \tag{4.25}$$

Analytical expressions for the speed of sound

By combining the thin rod approximation with the ball-and-spring-model, we were able to derive analytical expressions for the Young's and the torsional modulus. This derivation is described in detail in the Appendix (Sec. 6.4.3, Eqs. (6.48-6.53)). By substituting these formulas into the Eqs. (4.23) and (4.25) an excellent reproduction of the speeds of sound of the acoustical waves is achieved (dashed blue lines in Fig. 4.11c and d). Therefore these formulas constitute the key to the analytical understanding of the acoustical branches and of the thermodynamic trends. For a deeper discussion, however, it is more convenient to further simplify these formulas by introducing some approximations:

1. We find that the longitudinal speed of sound (Fig. 4.12a, solid black lines) is almost completely determined by the hydrogen bonds (Fig. 4.12a, dashed black lines). The contribution of the

	Θ	L	R	Ψ	δ	D_1	$D_{\nu-1}$	D_ν	ν	$L\nu$
FES	180.00	6.74	0.961	148.16	180	7.01	-	-	-	
2_7	180.00	5.35	2.608	91.5	180	7.47	7.47	10.7	2	10.7
3_{10}	120.00	3.71	3.48	85.04	84.56	7.07	9.56	11.13	3	11.1
α	98.18	2.83	4.1	93.16	51.26	6.82	9.59	11.54	4	11.3
π	80.00	2.21	5.03	105.9	30.4	6.83	9.48	11.57	5	11.1

Table 4.5: Geometrical parameters for poly-L-alanine: twist Θ, pitch L, radius R, valence angle Ψ, dihedral angle δ and equilibrium distances to the D_1, D_ν and $D_{\nu-1}$ first, ν^{th} and $(\nu-1)^{\text{th}}$ nearest neighbor, respectively, number of peptides ν to form a hydrogen bond and the quantity $L\nu$.

backbone is rather small (Fig.4.12a, dotted black lines). Hence we may write:

$$v_L = \sqrt{\frac{Y}{\rho}} = \sqrt{\frac{Y^{\text{bb}} + Y^{\text{hb}}}{\rho}} \approx \sqrt{\frac{Y^{\text{hb}}}{\rho}}. \tag{4.26}$$

Here Y^{bb} denotes the backbone contributions and Y^{hb} denotes the hydrogen bonding contributions to the Young's modulus (see Appendix, Eq. (6.48), (6.51), and (6.50), respectively). We remark that the description of torsional waves is more complicated, since both, hydrogen bonds and backbone are contributing (Fig. 4.12b): In the 3_{10}-helix the backbone contributions are almost as large as the contributions of the hydrogen bonds. However, for the α-helix and in particular for the π-helix the contributions of the hydrogen bonds are strongly dominating the speed of sound, as will become more clear below.

2. We find hydrogen bonding geometries, e.g., the distances to the ν^{th} and ν^{th}-1 nearest neighbor (Tab. 4.5), are largely the same in the three helical conformations .

Considering these approximations, the speeds of sound are still well reproduced (Fig. 4.11c and d, solid blue lines). Moreover, these approximations lead to simplified analytical formulas which enable a straightforward understanding. The longitudinal speed of sound simplifies to[8]

$$v_L \approx L\nu\sqrt{K^{\text{l,hb}}/M}, \tag{4.27}$$

where $K^{\text{l,hb}} = 0.34K_{r_{\nu-1}} + 0.98K_{r_\nu}$, M corresponds to the mass of the peptide unit, L denotes the helix pitch, and ν denotes the number of peptide units to form a hydrogen bond (see Fig. 1.2). We note that the quantity $L\nu$ is roughly a constant quantity amongst the helices (Tab. 4.5). Thus the approximations leading to Eq. (4.27) reveal an important result: The longitudinal speed of sound in the three helix types is (approximately) the same because the sound waves are traveling predominantly along the hydrogen bonds rather than along the backbone (Eq. 4.27), and both, the hydrogen bond strength (Tab. 4.4) and the hydrogen bond geometry (Tabs. 4.5 and 6.4), are the same in all three helical conformations. For the same reasons we may describe the increase per

---

[8] The explicit derivation of these simplified analytical formulas is presented in the Appendix, in the Eqs. (6.57) and (6.58- 6.59), respectively.

phase angle of the speed of sound of the bending waves velocity (Eq. (4.25)) with:

$$a_B = Rv_L = RL\nu\sqrt{\frac{K^{\mathrm{l,hb}}}{M}} \tag{4.28}$$

Here R denotes the radius of the helix. In contrast to the longitudinal speed of sound, the torsional speed of sound is determined by both, hydrogen bonding and backbone contributions:

$$v_T \quad = \quad LR\sqrt{\frac{K^{\mathrm{t,bb}} + \nu^2 K^{\mathrm{t,hb}}}{M}}, \tag{4.29}$$

where $K^{\mathrm{t,hb}} = 0.0029K_{r_{\nu-1}} + 0.0037K_{r_\nu}$ and $K^{\mathrm{t,bb}} = 0.021K_{r_1}$. We note, however, that also for the torsional waves the hydrogen bonds dominate, since $\nu^2 K^{\mathrm{t,hb}} > K^{\mathrm{t,bb}}$.

4.4.3 Conclusions

Our investigations with the ball-and-spring model revealed that the temperature dependence of the helical stability, i.e., the loss of vibrational entropy of the helices with respect to the extended structures, is almost entirely an effect of the formation of the hydrogen bonds, whereas the impact of the backbone stiffness is rather negligible. While this is already an important result on its own, a deeper understanding of the entropic differences *between* the three helix types has been only gained with the analysis in terms of the thin rod approximation. This analysis has revealed, in close correspondence to the findings with the ball-and-spring model, a strong dominance of the hydrogen bonds (compared to the backbone interactions) also for the elastical moduli of the helices, and correspondingly for the speeds of sound of longitudinal, torsional and bending waves. As a consequence of this fact we could derive very simple analytical formulas for the speeds of sound. We now substitute these Eqs. (4.27) to (4.29) into Eq. (4.21) and obtain for the long wavelength limits:

$$\left(\frac{\partial\omega^L}{\partial\varphi}\right)_{\varphi\to 0} = \nu\sqrt{\frac{K^{\mathrm{l,hb}}}{M}}, \tag{4.30}$$

$$\left(\frac{\partial\omega^B}{\partial\varphi}\right)_{\varphi\to\Theta} = \frac{R\nu}{L}\sqrt{\frac{K^{\mathrm{l,hb}}}{M}}(\varphi-\Theta), \tag{4.31}$$

$$\left(\frac{\partial\omega^T}{\partial\varphi}\right)_{\varphi\to 0} = R\sqrt{\frac{K^{\mathrm{t,bb}} + \nu^2 K^{\mathrm{t,hb}}}{M}}. \tag{4.32}$$

These formulas give a very direct relation between the geometrical parameters of the helical conformations and the long-wavelength limits. An interesting consequence is that the π-helix exhibits the hardest response on elastic deformations owing to its geometric peculiarities: the largest radius, the smallest pitch and the largest number of peptides forming the hydrogen bonds (Tab. 6.4a).

We may now also explain the loss of vibrational entropy of the π-helix with respect to the α-helix and the 3_{10}-helix in terms of these geometric scaling effects. We remark that the long-wavelength limits in Eqs. (4.30-4.32) cannot be directly converted to the vibrational entropy of the helices

– such a conversion would correspond to applying a Debye-model, which is not strictly valid at room temperature. In the parts of the acoustical branches away from the long-wavelength limits the analytical description of the geometrical scaling effects is more complex. However, the trends as contained in the Eqs. (4.30-4.32) are qualitatively still valid also in these parts of the vibrational spectrum. Hence we conclude that the geometric ratios of helix radius, pitch, and twist, are the main driving force for the entropic differences. The geometric ratios between the helical conformations are in turn largely independent of the amino acid conformation. Therefore, this trend as observed here for the poly-L-alanine chain is expected to be generic, i.e., independent of the amino acid sequence, and might be a reason why the π-helix is only seldom observed in proteins.

4.5 Exchanging the amino acid

So far we have exclusively dealt with the poly-L-alanine chain. L-alanine is known to be the amino acid with the strongest propensity to form helices. In order to study the impact of the side chain on the helix stability we will now switch to poly-glycine. Glycine is known to be a very weak helix former. The origin of this difference between L-alanine and glycine is basically not clarified yet as has been discussed in detail in the introduction (Sec. 1.3). By comparing the stability of *isolated, infinite* L-alanine and glycine chains we therefore aim to clarify, whether or not (and, if yes, to what extend) differences in the helical propensities are *intrinsic* features of the amino acids, i.e., exist in the absence of environmental effects (e.g. solvent).

We have already mentioned in Sec. 1.5 that the differences in the helix propensities cannot be explained by the *static* energetic contributions to the intrinsic stability – according to these the α- and π-helix are even slightly more stable with respect to the FES for glycine than for L-alanine (Figs. 1.5, 4.3a and 4.13a).

We now analyze, whether the origin of the differences may be explained by the *dynamic*, vibrational contributions to the free energy. By employing the same methodology for glycine as before for L-alanine (Secs. 4.2-4.4) we perform a comparative analysis for extracting the impact of the side chain on the thermodynamic stability and on the relative free energy differences of the helices.

4.5.1 Comparison between L-alanine and glycine

Comparing the temperature dependence of the phase stabilities for L-alanine and glycine we find a similar behavior. As for L-alanine, the stability of the helices with respect to the FES is significantly reduced also for glycine at elevated temperatures (Fig. 4.13a), predominantly due to vibrational entropy contributions associated with the lowest frequency branches (Tab. 4.6).

Two important thermodynamic trends, which have been found for poly-L-alanine, are also observed for poly-glycine. First, the π-helix is again the conformation with the lowest vibrational entropy (Fig. 4.13b). This underlines the dominance of the hydrogen bonding pattern and of the geometric scaling effects for the thermodynamic trends, as have been derived in Sec. 4.4. The study of the poly-glycine chain therefore clearly verifies the generic character of the low entropy of π-helices. Second, we find again that the α-helix is the conformation with the lowest free energy at

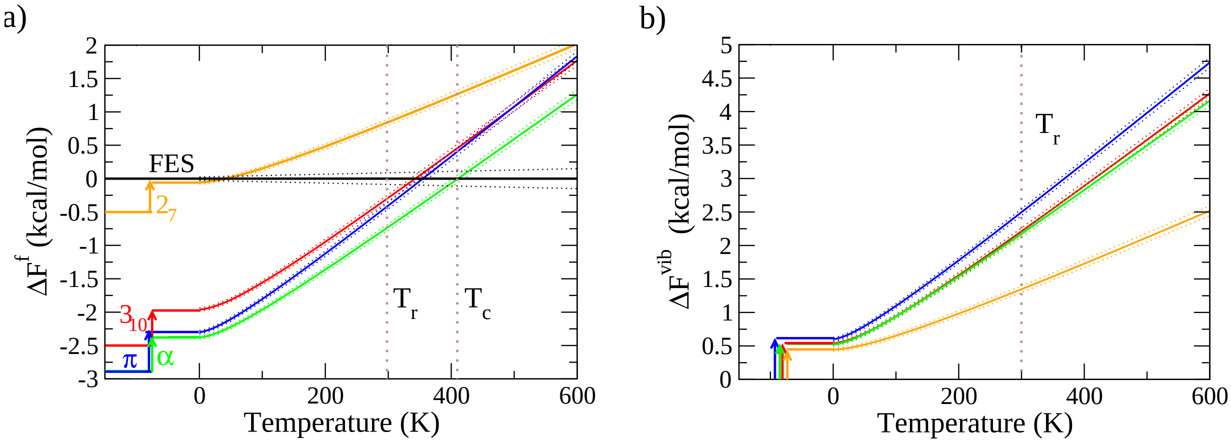

Figure 4.13: a) Stability of the poly-glycine conformations with respect to the FES as the temperature increases (Eq. (4.5)). The dotted lines denote the numerical uncertainty. The arrows represent zero-point vibrational corrections. T_r is the room temperature and T_c denotes the critical temperature at which the FES becomes more stable than the helices. b) Differences in vibrational free energy with respect to FES.

type of contribution→	$-T\Delta S^{\text{vib}}$					ΔU^{vib}
included branches→	1	1,2	1,2,3	1,2,3,4	5-21	21
$\alpha-$FES	24	59	73	80	9	11
$\alpha-\pi$	78	88	78	75	1	24

Table 4.6: Individual contributions of the vibrational branches (Eq. (4.12)) to the vibrational free energy differences at room temperature in percent for the glycine chain. The second column contains the contributions of entropy associated with the lowest lying vibrational branch (first sub-column), the two lowest lying vibrational branches (second sub-column), the three lowest lying vibrational branches (third sub-column) and the four lowest lying vibrational branches (fourth sub-column) and the entropy associated with the branches 5-21, respectively. The third column, which is titled with U^{vib}, contains the energetic vibrational contributions corresponding to the entire vibrational spectrum.

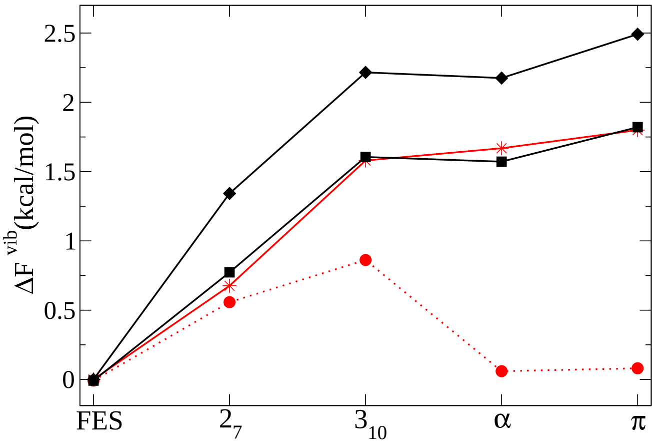

Figure 4.14: Vibrational free energy contributions to the stability with respect to the FES (Eq. (4.7)) at room temperature for the different conformations of the poly-glycine chain: Shown are the DFT results for the contributions from the full vibrational spectrum (solid black line, diamonds) and the contributions arising from exclusively the 3 lowest vibrational branches (solid black line, squares). Further shown are the results from the ball-and-spring model with spring constants of Tab. 4.7 (solid red line, stars) and the corresponding vibrational free energy contributions in the case, in which the hydrogen bonding spring constants are removed from the model (dotted red line, circles).

room temperature.

However, a closer look also reveals differences. Regarding the vibrational contributions we find that both zero point vibrational and entropic contributions to the phase stabilities are more pronounced for glycine (Fig. 4.13b) than for L-alanine (Fig. 4.3b). These two contributions, zero point vibrations and vibrational entropy, lead to an inversion of the stability for the α-helix: While the static contributions at 0 K make the poly-glycine α-helix more stable with respect to the FES than the poly-L-alanine α-helix, the vibrational free energy contributions cause the poly-L-alanine α-helix to be more stable than the poly-glycine α-helix at room temperature. Furthermore, these contributions cause the critical temperature[9] to be significantly lower in glycine ($T_c = 410$ K) than in alanine ($T_c = 470$ K). Thus, vibrational free energy contributions may partially explain the low helical propensity of glycine compared to L-alanine. However, since the determined differences are much too small, they cannot serve as a full explanation. We discuss this issue in more detail in the Sec. 4.5.4.

Before this, we have a look at the 3_{10}-helix and 2_7-structure, since for these two structures the differences between L-alanine and glycine are larger than for the α- and the π-helix.

4.5.2 Low entropy of the glycine 3_{10}-helix

For the glycine 3_{10}-helix and the 2_7-structure a rather unexpected strong loss of vibrational entropy is observed as compared to L-alanine (Fig. 4.13b and Fig. 4.3b). This extraordinary low entropy of the glycine 3_{10}-helix and 2_7-structure might be of importance for the kinetic aspects of the helix

---

[9] The critical temperature T_c is defined as the temperature, at which the FES becomes more stable than the helices (see Figs. 4.3a and 4.13a).

backbone	K_{r_1}	K_δ	K_Ψ
$2_7, \alpha, \pi$	21.1	0.17	4.01
dev to Ala in %	-2	-82	+33
3_{10}	21.1	2.16	6.15
dev to Ala in %	-2	+173	+104
FES	21.1	0.05	4.01
dev to Ala in %	-2	-71	+33

hydrogen bonds	$K_{r_{\nu-1}}$	K_{r_ν}
$3_{10}, \alpha, \pi$	26.3	11.4
dev to Ala in %	+22	-7
2_7	4.3	11.4
dev to Ala in %	-50	-7

Table 4.7: Parameter-set for the ball-and-spring model (Eq. (4.17)) as derived for the poly-glycine chain. The spring constants are expressed in $\mathrm{cm}^{-1} \cdot 10^4$. The numbers below the force constants denote the deviations to the respective force constants as derived for poly-L-alanine (Tab. 4.4) in percent.

folding process. Provided that this process follows the lowest energy pathway as suggested by the (Θ, L)-PES (Fig. 1.5), the 3_{10}-helix and the 2_7-structure might form a free energy barrier for poly-glycine, which is lower/absent for poly-L-alanine. Further, the low entropy of the 3_{10}-helix might be of importance for the free energy of short, finite helices — 3_{10}-helices are supposed to play an important interfacial role at the endings of helices. Both, kinetics as well as finite size aspects are beyond the scope of this thesis, but will be the topic of future projects. Here, we restrict ourselves to uncovering the origin of the low entropy.

The loss of vibrational entropy in the glycine 3_{10}-helix is associated with blue-shifts in the lowest frequency branches with respect to L-alanine (Fig. 4.15). We have therefore analyzed the three lowest vibrational branches of the poly-glycine chain by means of the ball-and-spring model as introduced in Sec. 4.4. Comparing L-alanine to glycine we found two differences. First, a larger number of independent parameters is required to describe poly-glycine: While in the L-alanine chain the backbone interactions were basically the same for all the helical conformations (Tab. 4.4), for the glycine chain the backbone interactions of the 3_{10}-helix had to be treated independently from those of the other two helices (Tab. 4.7). Second, the backbone interactions, i.e., valence angle and dihedral angle stiffness, are significantly hardened for poly-glycine, in particular in the 3_{10}-helix (Tab. 4.7, compare red dotted lines in Fig. 4.9 and Fig. 4.14).

In order to localize the atomistic origin of this hardening in the glycine 3_{10}-helix we have compared the dynamical matrix of this conformation to that of the α-helix. This comparison is based on the *atom-atom couplings* as defined in Eq. (4.16). As a reference we have taken the L-alanine chain. This means that we have compared the differences in the atom-atom couplings in the glycine helices with the respective atom-atom couplings in the L-alanine helices.

Fig. 4.16 shows strong differences between glycine and L-alanine for the force constants corresponding to the short-ranged interaction within the peptide unit (n=0 in Fig. 4.16), while the differences in the long-ranged interactions corresponding to the hydrogen bonds are rather small[10] (n>1 in Fig. 4.16). The strongest differences are found for interactions involving the C_α-atom, i.e., the atom which constitutes the chemical link between side chain and backbone. The comparison

---

[10] The fact that this finding is in close correspondence to the results obtained with the ball-and-spring model – although it has been obtained in an completely independent analysis – verifies (once more) the strength of the ball-and-spring model in analysing the low frequency branches of the peptide chain.

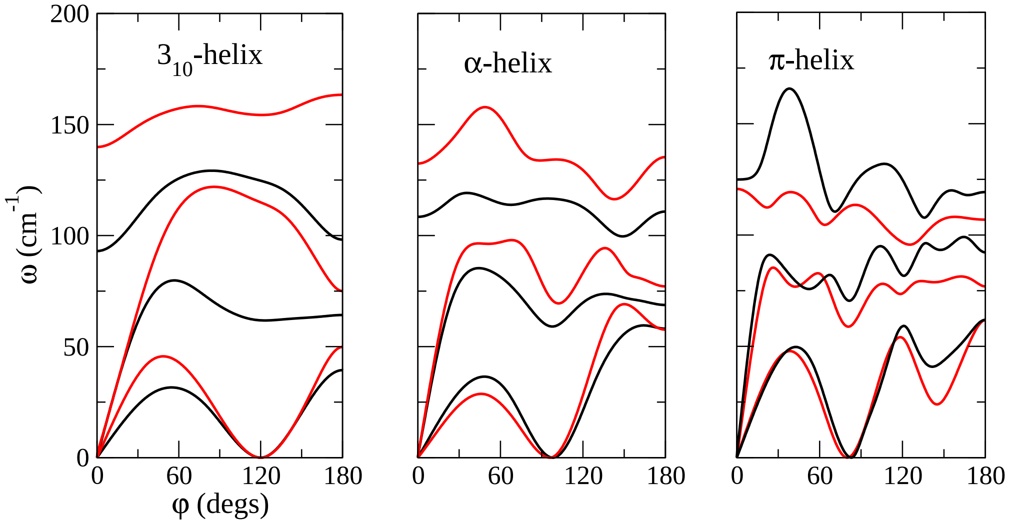

Figure 4.15: Comparison of the three lowest frequency branches between poly-glycine (red lines) and poly-L-alanine (black lines) for the three helical conformations.

between α- and 3_{10}-helix verifies that these differences are conformation dependent, i.e., for the 3_{10}-helix the differences are more pronounced than for the α-helix. This analysis clearly shows that the hardening in the low frequency branches of the glycine 3_{10}-helix short-ranged (backbone) interactions is induced by the side-chain and mainly involves the chemical bonding in the direct proximity of the C_α atom.

4.5.3 Stability of the helix against unfolding

We now investigate the stability of the poly-glycine helical state against unfolding. We obtain, in close analogy to the considerations already made for the poly-L-alanine chain in Sec. 4.2.3, for the free energy of the unfolded state at room temperature:

$$\begin{aligned}
\mu^{\text{unfolded}} &\approx \mu^{\text{bulk}}_{\text{FES}} - (k_{\text{B}}T)_{300K} \ln\left(1 + 2 \cdot \sum_{X \neq A}^{\text{non-helical}} \exp(-\beta \Delta F^{f}_{\text{FES} \to X})\right) \qquad (4.33)\\
&= \mu^{\text{bulk}}_{\text{FES}} - (k_{\text{B}}T)_{300K} \ln\left(1 + 2 \cdot \exp(-\beta \Delta F^{f}_{\text{FES} \to 2_7}) + 2 \cdot \exp(-\beta \Delta F^{f}_{\text{FES} \to \text{PPII}})\right)\\
&= \mu^{\text{bulk}}_{\text{FES}} - 0.60 \frac{\text{kcal}}{\text{mol}} \ln\left(1 + 0.6 + 0.08\right)\\
&= \mu^{\text{bulk}}_{\text{FES}} - 0.20 \frac{\text{kcal}}{\text{mol}}. \qquad (4.34)
\end{aligned}$$

Here the factor 2 in front of the summation over the non-helical states in Eq.(4.33) stands for the degeneracy of the phases, i.e., except for the FES, for each right handed conformation a corresponding left-handed conformation exists in the unfolded domain for the poly-glycine chain with identical free energy. This symmetric character of the glycine-PES is due to the fact that the glycine amino

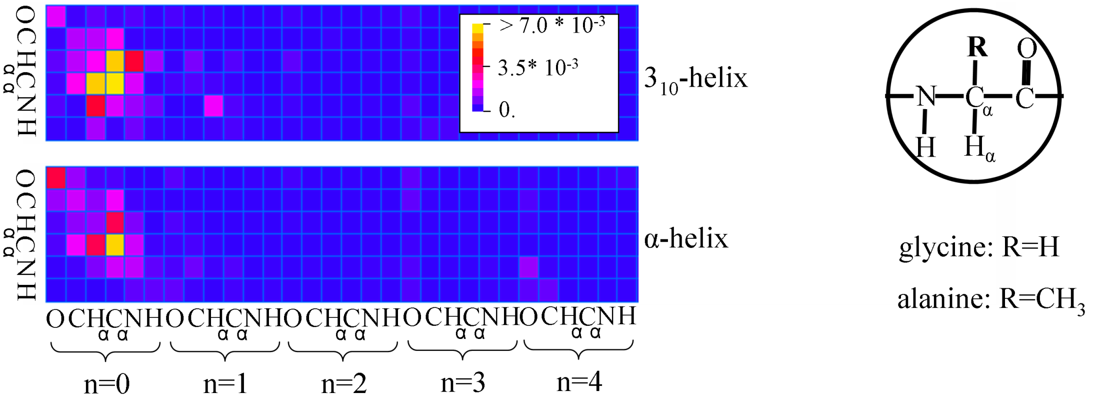

Figure 4.16: Differences of the atom-atom couplings (Eq. (4.16)) between poly-glycine and poly-L-alanine for the α-helix and the 3_{10}-helix for the backbone atoms (side chains are excluded). Plotted are absolute values in the range from 0 to 0.007.

acid is, in contrast to alanine, not chiral[11]. Eq. (4.34) shows that the chemical potential of the ideal solution formed by the FES, the 2_7-structures and the poly-proline-structures is lower than the chemical potential of the isolated FES by only ≈ 0.20 kcal/mol. Thus, similarly to the observations made for poly-L-alanine, “adding” the 2_7- and PPII-structures does not substantially lower the chemical potential of the unfolded state compared to the FES.

According to Eq. (2.138) the chemical potential of the helical state is approximately given by the helical bulk phase with the lowest chemical potential. At room temperature the α-helix is the helical conformation with the lowest bulk phase free energy also for poly-glycine. Hence the stability of the helical state against unfolding is given by:

$$\begin{aligned}\Delta F^{\mathrm{f}}_{\mathrm{helix}\rightarrow\mathrm{unfolded}} &\approx \mu^{\mathrm{helix}} - \mu^{\mathrm{unfolded}} \\ &= \mu^{\mathrm{bulk}}_{\alpha-\mathrm{helix}} - \mu^{\mathrm{bulk}}_{\mathrm{FES}} - 0.2\frac{\mathrm{kcal}}{\mathrm{mol}} \\ &= \Delta F^{f}_{\alpha-\mathrm{helix}\rightarrow\mathrm{FES}} + 0.2\frac{\mathrm{kcal}}{\mathrm{mol}} \\ &= -0.5\frac{\mathrm{kcal}}{\mathrm{mol}} \qquad (4.35)\end{aligned}$$

We conclude that, according to our results, also for poly-glycine the helical state will be stable at room temperature.

---

[11] The PES of the glycine chain is completely symmetric with respect to a mirror operation at the $\Theta = 180^\circ$-axis. This means that for each minimum of the PES with $\Theta < 180^\circ$ (right handed conformation) a corresponding second minimum with $\tilde{\Theta} = 360^\circ - \Theta$ (left handed conformation) exists with the same energy. This symmetric character of the glycine-PES is due to the fact that the glycine is not chiral. In contrast the alanine amino acids is chiral, and consequently the energy of the left-handed conformations is significantly higher than that of the corresponding right handed conformations. The origin of chirality is a PhD project on its own [151] and is beyond the scope of this thesis.

4.5.4 Helical propensities

We now determine the difference in helical propensities. The overall difference in the helix stability between L-alanine and glycine at room temperature is:

$$\Delta\Delta F = \Delta F^{\mathrm{f}}_{\mathrm{helix}\rightarrow\mathrm{unfolded}}[Gly] - \Delta F^{\mathrm{f}}_{\mathrm{helix}\rightarrow\mathrm{unfolded}}[Ala] = 0.15\,\mathrm{kcal/mol} \tag{4.36}$$

Here $\Delta F^{f}_{\mathrm{helix}\rightarrow\mathrm{unfolded}}[Gly]$ and $\Delta F^{f}_{\mathrm{helix}\rightarrow\mathrm{unfolded}}[Ala]$ are the stability of the helical state against unfolding for poly-glycine and poly-L-alanine, as given in Eqs. (4.35) and (4.11), respectively. The calculated value is thus in qualitative agreement with the experimental helix propensity scales, since $\Delta\Delta F > 0$. However, our results do not give the full explanation for the experimentally observed helical propensities, since $\Delta\Delta F$ is significantly smaller than the experimental values reported in the literature. We here compare to the values reported by Pace&Scholtz [27], those reported by Munoz&Serano [26], and those reported by Williams et al. [152], since these three works cover a broad range of possible determination techniques for helix propensities. Pace&Scholtz have based their helix propensity scale on an average including 11 systems, considering both proteins and peptides, all exposed to aqueous solvent. They find a difference $\Delta\Delta F = 1.12 \pm 0.43$ kcal/mol or $\Delta\Delta F = 0.98 \pm 0.07$ kcal/mol, depending on whether all 11 values are averaged or the 4 systems with the largest deviations are excluded from the average, respectively. Munoz&Serano have used the measured helicities of 423 peptides in solvent to derive parameters characterizing the helix coil transition. They find a difference of $\Delta\Delta F = 1.10$ kcal/mol. Williams et al. have based their propensity scale on the frequency of occurrence of the amino acids in α-helices found in the structure of 75 peptides. They find a $\Delta\Delta F = 0.85$ kcal/mol. All these values are significantly larger than our result.

The differences between our prediction and those reported in the literature might have the following reasons:

1. The differences might be explained by the fact that the experimental values have been obtained for solvent exposed peptides/proteins, while our approach is treating peptides in vacuum. If this is true then helical propensities are highly solvent dependent.

2. The free energy as estimated within the harmonic approximation might largely differ from the true free energy due to the neglected anharmonic contributions.

3. There might be a systematic error of our approach in describing the quantity $\Delta\Delta U^{\mathrm{el}}_{\alpha\rightarrow\mathrm{FES}}$ due to the deficiencies of the DFT-PBE functional in particular in describing van-der-Waals attractions (Sec. 2.4).

While it is currently not possible to directly check the possibilities one and three, we discuss the second possibility in the next section.

4.6 Anharmonic corrections

The differences in the free energies, on which our study is based on so far, are significant, but also small – without exception, smaller than 1.0 kcal/mol. While the numerical precision of our calculations is (after the implementations we have presented in Sec. 3.4) sufficient to resolve these delicate free energy differences and the high accuracy of the DFT-GGA approach has been verified in Sec. 4.1, a very important issue is still not clarified yet: The soft, low frequency modes of the peptide chain are expected to exhibit anharmonic contributions which might lead to significant deviations from the free energy calculated within the harmonic approximation.

The results for the thermodynamic stability as derived within the harmonic approximation thus have to be verified/corrected by estimating anharmonic corrections. In this section we first investigate the thermal expansion of the helices by employing the quasi-harmonic approximation (Eq. (2.118)) and solving the Grüneisen-Mie equation of state (Eq. (2.122), Sec. 3.4.5). Then we determine the range of validity for the quasi-harmonic approximation and the thermodynamic integration method. Based on these considerations the anharmonic free energy corrections are calculated using the thermodynamic integration approach.

4.6.1 Thermal expansion

To investigate the thermal dependence of the helical parameters we have determined the Grüneisen coefficients (Sec. 3.4.5) and solved the Grüneisen-Mie equation of state (Eq. (2.122)) for the three helical conformations of the poly-L-alanine chain and for the poly-glycine 3_{10}-helix. For the poly-L-alanine chain the temperature dependence of the pitch L results in an increase of about 3 % at room temperature for all three helical conformations (Fig. 4.17a). The thermal increase of the pitch of the poly-glycine 3_{10}-helix is smaller than that of the L-alanine helices and is about 0.3 % at room temperature. For the 3_{10}-helices a small thermal reduction (< 0.05 %) of the pitch L is observed for low temperatures, i.e., $T < 50$ K, for both poly-glycine and poly-L-alanine. Such an effect is not observed for the poly-L-alanine α- and π-helix. For the temperature dependence of the twist the differences between the helices are larger than for the pitch (Fig. 4.17b), as they may vary between 0.4 % and 1.8 % (at room temperature), depending on the helix type and amino acid.

The free energy gain at room temperature due to the thermal dependence of the helical parameters is rather small — about 0.05 kcal/mol for the poly-L-alanine helices and 0.01 kcal/mol for the poly-glycine the 3_{10}-helix (Fig. 4.17c, dashed lines).

The twist dependence of the vibrational spectrum gives, however, rise to a further correction to the harmonic free energies: For the phonon calculations we cannot choose the twist angle to be exactly at the equilibrium value, but we have to choose it, for the sake of computational efficiency, with a certain offset (see appendix, Sec. 6.6.1). This offset causes a deviation of the determined vibrational free energies from the true values corresponding to the equilibrium twist. By means of the Grüneisen parameters we may, nevertheless, correct these deviations. The corrections are very small for the α-helix and the π-helix, since for these systems the modeled twist is very close to the equilibrium twist. However, for the 3_{10}-helices the deviation is of the order of 0.15 kcal/mol per

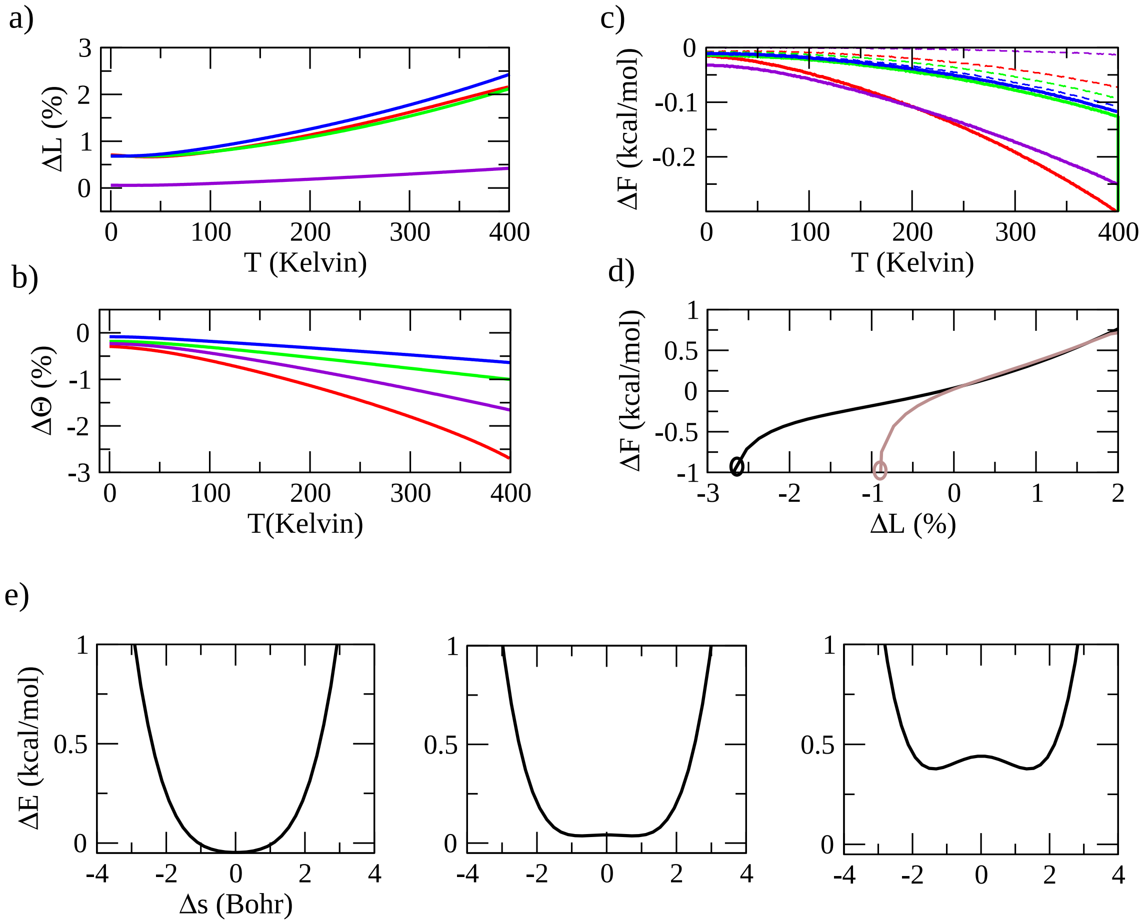

Figure 4.17: Results for the quasi-harmonic approximation: a) Thermal variation of the pitch L in percent of the static equilibrium pitch for the poly-L-alanine π- (blue line), α- (green line) and 3_{10}-helix (red line) and for the poly-glycine 3_{10}-helix (violet line). b) Respective plots for the thermal variation of the twist Θ. c) Free energy gain with respect to harmonic free energies obtained at lattice parameters given in Tab. 6.2 (solid lines). Free energy gain solely due to thermal expansion (dashed lines). d) Free energy surface at 300 K of the poly-glycine FES (brown line) and poly-L-alanine FES (black line) for fixed twist $\Theta = 180°$ and varying pitch. e) Lowest frequency branch of the poly-glycine FES for varying pitches: at the static equilibrium pitch (left plot) for a reduction of the pitch of 0.5 % (middle plot) and a reduction of 1% (right plot).

peptide unit at room temperature.

However, to summarize, the thermodynamic trends between the helices as derived in the harmonic approximations remain largely unaffected by the results of the quasi-harmonic approximation.

An attempt to determine the thermal expansion also for the fully extended structure failed due to the appearance of an effect, which is commonly referred to as the *guitar string effect* [153]. This effect may be described as a structural instability at finite temperatures which leads to the appearance of an imaginary branch in the frequency spectrum. Moreover we observe a negative thermal expansion, i.e., a reduction of the pitch with increasing temperatures. The reduction of the pitch is accompanied by a strong softening of the vibrational frequencies corresponding to deformations *perpendicular* to the chain axis. This softening is explained by the fact that the compressed peptide chain prefers to locally break the high symmetry enforced by the helical parameters. For pitch values commensurable with the symmetry break the corresponding phonon frequencies are close to zero (for pitch values larger than the transition pitch, Fig. 4.17e, left plot) or even imaginary (for pitch values smaller than the transition pitch, Fig. 4.17e, right plot). The quasi-harmonic free energy surface $F(L,\Theta)$ has a singularity at that transition pitch[12] and is ill-defined for pitches smaller than the transition pitch. The theoretical treatment of the FES, both for poly-L-alanine and poly-glycine, is particularly problematic due to the fact that the static equilibrium is very close to this structural instability. At 300 K, the free energy surface is actually concave (Fig. 4.17d). It is thus impossible to determine the free energy of the FES *within the quasi-harmonic approximation*.

These findings are artifacts of the *quasi-harmonic approximation* and disappear (of course) in the full anharmonic treatment. However, these findings also make the free energy values as derived for the FES within the *harmonic* approximation questionable. A major deficiency of both, the quasi-harmonic and the harmonic approximation, is that they are exclusively based on the determination of local curvatures of the PES. An option to get rid of the imaginary frequencies would be, to allow the structure to break the symmetry and to re-determine the dynamical matrix for the structure of lower symmetry. This approach is however only valid for small oscillations and still neglects the anharmonicity arising from the amplitude dependence of the vibrational modes (Sec. 2.7). Therefore, we have instead employed the thermodynamic integration approach. This approach allows to *fully* account for the anharmonicity, and is free of these deficiencies.

4.6.2 Thermodynamic phase stability in the classical approximation

The thermodynamic integration approach, as it is employed here, is based on the classical Langevin equations of motion (Sec. 3.5.4). Therefore, quantum effects for the movement of the ion cores are neglected, which makes this approach invalid at low temperatures. We are, however, interested in free energy corrections at room temperature, where quantum effects for the movement of the ion cores are certainly less important. To check for the validity of the classical equations of motion *at room temperature* we have determined the harmonic thermodynamic stability using the classical partition function. The comparison between the thermodynamic stabilities derived from the

---

[12] The quasi-harmonic free energy surface has a singularity at the transition pitch because the harmonic vibrational entropy is approaching infinity for a real frequency approaching zero.

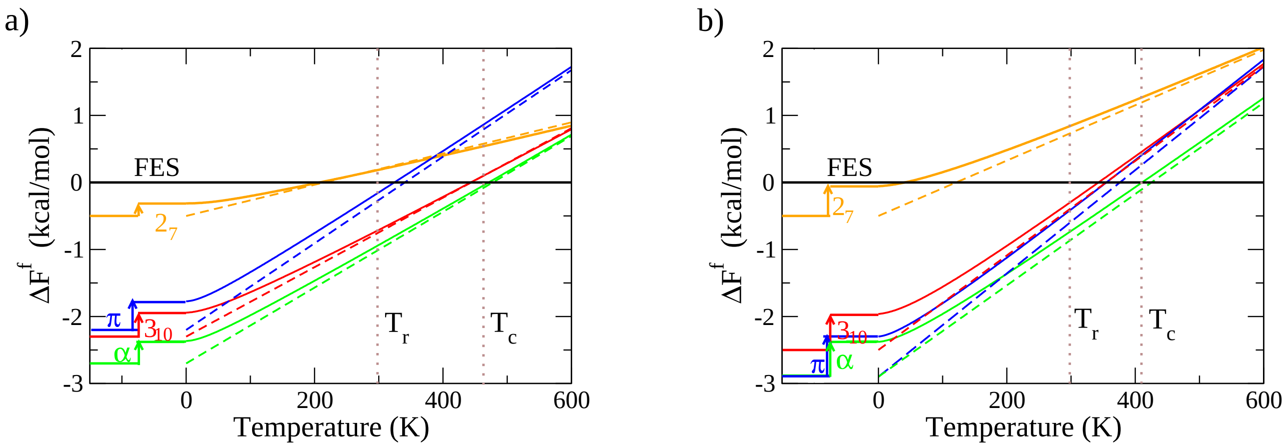

Figure 4.18: Comparison for the stability of the various conformations as derived from the quantum mechanic partition function (solid lines) and from the classical partition function (dashed lines) for a) poly-L-alanine and b) poly-glycine.

quantum mechanic partition function and the classical partition function reveals some differences at room temperature (Fig. 4.18). The differences are larger for glycine, but still rather small. Hence we expect that anharmonic corrections determined within the classical approximation to be valid at room temperature.

4.6.3 Explicit anharmonicity obtained with SCCDFTB

It is now interesting to check, how the quasi-harmonic approximation compares to the thermodynamic integration approach. To address this issue we have determined the quasi-harmonic free energy surface (in the classical approximation) and the free energy surface using the thermodynamic integration for the glycine 3_{10}-helix (Fig. 4.19a). For these *test* calculations we have used the SCCDFTB approach (Sec. 6.2.2).

For the helix we obtain a clear picture: The free energy corrections to the harmonic approximation (Fig. 4.19, solid black lines) as determined in the framework of the quasi-harmonic approximation (Fig. 4.19a, dashed red line) are essentially underestimated compared to those predicted with the thermodynamic integration approach (Fig. 4.19, solid red lines). This shows that the anharmonic corrections to the free energy of the helices stem from the amplitude dependence of the frequencies, i.e., the *explicit* anharmoncity, rather than from the dependence on the lattice parameters, i.e., the *implicit* anharmonicity.

A comparison of the curvatures of the static potential energy surface and the free energy surface determined with the thermodynamic integration furthermore reveals an interesting side aspect of the study. The latter has a significantly smaller curvature than the static potential energy surface. For the 3_{10}-helix the difference amounts to 20 % at room temperature (Fig. 4.19a), and for the FES the difference is even larger, reaching 50 % (Fig. 4.19b). This shows that the elastical properties of the peptide chain are strongly temperature dependent. The quasi-harmonic approximation does not reproduce this temperature dependence.

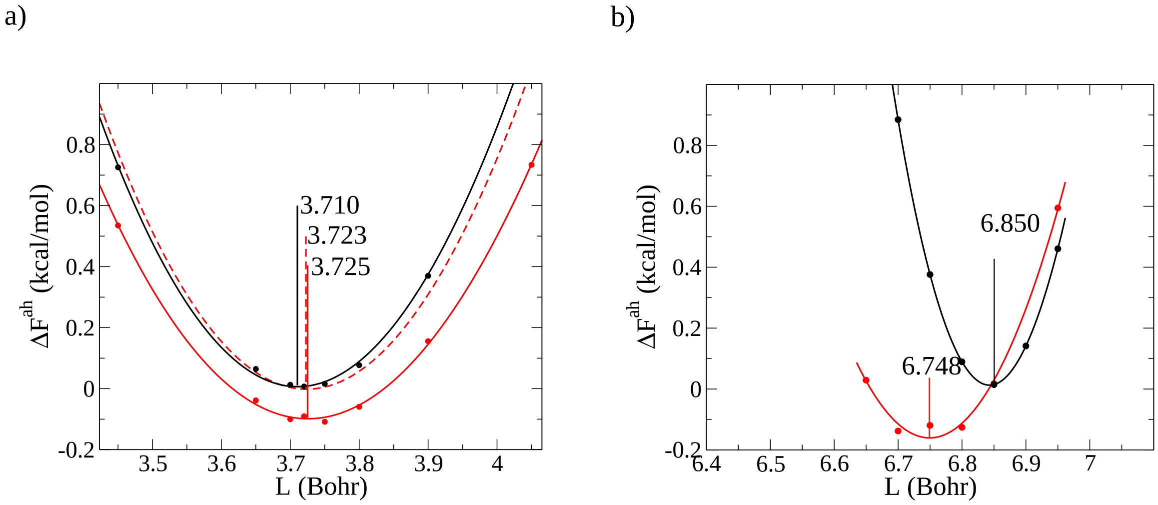

Figure 4.19: SCCDFTB-free-energy-surfaces (per peptide unit) along the helix pitch L of a) the poly-glycine 3_{10}-helix and b) the poly-glycine FES at various stages of approximation: The harmonic free energy surface (black lines), the free energy surface as calculated using the quasi-harmonic approximation (dashed red line, only for the 3_{10}-helix) and the free energy surface determined with the thermodynamic integration approach (solid red lines). The free energy surfaces are referred to the harmonic free energy at the equilibrium pitch L_0, i.e., $\Delta F^{\mathrm{ah}}(L) = F^{\mathrm{ah}}(L) - F^{\mathrm{harm}}(L_0)$.

	Ala-FES	Ala-3_{10}	Ala-α	Gly-FES	Gly-3_{10}
τ^{sim}	10000	10000	4300	9100	9000
ΔF^{ah}	-0.08	-0.36	-0.23	+0.02	-0.13
$\delta\Delta F^{\mathrm{ah}}$	0.13	0.04	0.06	0.15	0.04

Table 4.8: Anharmonic corrections, ΔF^{ah}, to the vibrational free energy as determined with DFT-GGA at room temperature denoted in kcal/mol per peptide unit. The anharmonic corrections are referred to the harmonic free energy determined with DFT-GGA at the equilibrium pitch L_0 and twist Θ_0, i.e., $\Delta F^{\mathrm{ah}} = F^{\mathrm{ah}} - F^{\mathrm{harm}}(L_0, \Theta_0)$. τ^{sim} denotes the number of simulation steps ($\Delta t = 1.5 \cdot 10^{-15}$ s) and the remaining statistical error bar is indicated by $\delta\Delta F^{\mathrm{ah}}$.

Despite the fact that we find a systematic anharmonic correction to the free energy with the thermodynamic integration approach, this correction is surprisingly small even for the FES at room temperature: The SCCDFTB free energy corrections for 3_{10}-helix is -0.1 kcal/mol per peptide unit (Fig. 4.19a), and for the FES it is -0.2 kcal/mol (Fig. 4.19b). However, to be sure that these findings are not an artifact of the SCCDFTB approach they have to be verified by performing corresponding DFT calculations.

4.6.4 Explicit anharmonicity obtained with DFT

Finally, the anharmonic free energies have been determined, by exclusively employing DFT-GGA, for selected conformations. These are the poly-L-alanine FES, 3_{10}- and α-helix and the poly-glycine FES and 3_{10}-helix. Based on the considerations obtained within the SCCDFTB approach we have performed these calculations at the equilibrium pitch for the helices, whereas for the FES a reduction in the pitch has been accounted for[13]. The anharmonic corrections we find are small (Tab. 4.8). These results verify, once more, the numerical reliability of our harmonic free energy study. Furthermore, these results verify the trends found already with the SCCDFTB approach above: The anharmonic corrections are negligible for the thermodynamic trends as derived with the harmonic approximation. The latter finding is particularly surprising, since a common expectation in the field of biological physics is that soft matter systems, like the peptide chain, exhibit a strong anharmonicity at room temperature (e.g. [154, 155, 156]).

---

[13] To determine the free energy corrections for the helices, we may perform the LD simulations at the lattice parameters corresponding to the minima of the PES, as can be inferred from Fig. 4.8. For the FES, in contrast, the free energy corrections have to be determined for a reduced pitch, performing the LD simulations for the static equilibrium pitch would result in an underestimation of the free energy corrections.

5 Summary

The present study delivers new insights into the temperature dependent stability of the helical secondary structure motif. Therefore it is expected that it will be relevant for protein science. In the following the main results are summarized.

The basic motivation for the project (Sec. 1.3) may be concentrated to the following questions:

1. Is the helical secondary structure motif intrinsically stable at room temperature?
2. Why are π-helices rarely observed in proteins (compared to α- and 3_{10}-helices)?
3. What is the origin of the difference in helical propensities between L-alanine and glycine?

Each of these questions addresses a fundamental aspect of helix stability. However, none of them could — on the basis of experimental studies — be satisfactorily answered so far. The reason is that a perfectly "clean" situation is required to study these intrinsic aspects of helix stability, i.e., the absence of environmental effects, such as solvent, helix endings and protein environment. Such a situation cannot be achieved within an experimental setup. In contrast, a computer simulation is able to fulfill these conditions, since it allows to study idealized, infinite structure motifs in vacuum. However, as discussed in the introduction, previous theoretical works, which were based on empirical force fields, turned out to be unsuitable due to their limited accuracy. The basic idea of this study was thus to tackle these questions by means of density functional theory (DFT).

In contrast to the force field approach previously used to study poly-peptides, DFT explicitly takes into account each electronic degree of freedom of the system and includes electronic many body effects based on the principal laws of quantum mechanics. Nonetheless, DFT still contains an approximation in form of the exchange-correlation functional and its accuracy has to be carefully validated for the given application. Indeed, recent comparative studies to more accurate post Hartree-Fock methods had already verified the high reliability in describing the *static/energetic* contributions of the hydrogen bonds to the helix stability. However, the performance of DFT-GGA to determine the *vibrational/thermodynamic* properties of the helix was essentially unknown before this project. We therefore have, as a first step, computed the phonon dispersion and specific heat of the poly-L-alanine α-helix and compared it to experimental literature data. The agreement with *available* experimental data is excellent and therefore verifies the overall high reliability of the DFT-PBE approach to predict the vibrational and thermodynamic properties.

Furthermore, the comparison underlines the complementary role DFT calculations can play to experimental studies in this field. Although spectroscopical methods, i.e., IR- and Raman spectroscopy, deliver precise information about the *optical* branches of peptide chains they cannot resolve the acoustical branches. As a consequence, also empirical force fields, which are fitted to experimental frequency spectra, largely fail to predict these branches. As will be discussed below the crucial interactions for the acoustical branches are the hydrogen bonds – it is thus tempting to conclude that the main shortcoming of the previous force field calculations is the inaccurate description of hydrogen bonds. The information available from DFT about the acoustical branches is complete and thus DFT can fill the knowledge gap left by experimental studies. The advantages of DFT calculations become even clearer when considering the importance of the low frequency branches for the thermodynamic properties. It is not only that the DFT results predict a qualitatively different shape of the low temperature specific heat curve than force fields – DFT provides a $\sim T^3$ dependence, whereas the force fields predict a linear dependence. Moreover, the acoustical branches contain, as also shown in this work, the elastical/mechanical deformations of the helix and determine to a major part the vibrational entropy. Hence, an improvement is expected for the description of the temperature dependence of the stability. These results have been published in Ref. [157].

Having verified the high accuracy of our approach, we were able to tackle the fundamental questions, which have been mentioned above.

- 1. Is the helical secondary structure motif intrinsically stable at room temperature?

Our results on poly-L-alanine clearly verify that vibrational contributions to the free energy play a key role for the stability of the helix in the biologically relevant temperature range. They strongly reduce the phase stabilities of the folded, helical conformations compared to the fully extended structure of the peptide chain. Thus they counteract the enthalpic stability of the helices arising from the formation of hydrogen bonds. We remark that this finding clearly contradicts a widespread assumption that the contribution of vibrational entropy to the helix stability is small (e.g. Refs. [158, 159]).

Nonetheless, we also have shown that, despite the strong impact of the vibrational entropy on the helix stability, the hydrogen bonds are still sufficiently strong to make the α-helix the most stable bulk phase at room temperature. We thus conclude that a poly-L-alanine α-helix is intrinsically stable at room temperature in the absence of environmental (solvent) effects. This fundamental finding remains valid, also if we replace the FES by a more realistic reference for the unfolded state, i.e., an ideal solution of the FES and the remaining bulk phases contributing to the unfolded state

Furthermore, our results clearly reveal a significant temperature dependence of the *relative* stability between the three helix types. Hence, our results may be used to rationalize why the relative population of π-, α- and 3_{10}-helices varies with temperature [10, 11]. This also explains

- 2. Why π-helices are rarely observed in proteins (compared to α- and 3_{10}-helices).

The π-helix exhibits the strongest temperature dependence amongst the three helix types. In contrast to the 3_{10}- and α-helix it is, with respect to the free energy, almost degenerated to the FES at room temperature (and higher in free energy than the unfolded state). Previous explanations mainly stressed ending effects to explain the rarity of the π-helix. Our results clearly reveal that an entropic “penalty” for the π-helix exists even in the *absence* of any ending effects.

To understand the pronounced differences in the entropic character among the helices and between the helices and the FES we have analyzed the vibrational entropy in detail. By mapping our DFT data on the ball-and-spring model, we could show that the observed differences in the low frequency branches in the α-helix and the π-helix and consequently the thermodynamic/entropic trends are exclusively due to the formation of hydrogen bonds, whereas changes in the backbone stiffness are practically negligible. Only for the 3_{10}-helix, the 2_7-structure, and the FES, the nearest neighbor peptide-peptide interactions, which stabilize the backbone and are influenced by the amino acid sequence, come into play. However, the main differences are still due to the hydrogen bonds. This result and the separation of backbone and hydrogen bonding interactions are novel contributions of this work. It has indeed been realized before that the acoustical branches of the helix are not only determined by the backbone of the helix but also depend sensitively on the hydrogen bonds [55, 56, 146]. Nevertheless, the employment of empirical force fields in these studies made it not possible to accurately quantify the influence of hydrogen bonds, e.g., compared to that of nearest neighbor interactions – this was only possible in our project through the application of DFT.

Furthermore, by employing the thin rod approximation for the helices, which correctly reproduces the low-energy long-wavelength modes dominating the thermodynamic properties, it has been demonstrated in this work that the strong temperature dependence of the π-helix is almost exclusively driven by its geometric peculiarities as compared to the α-helix and 3_{10}-helix. Since the geometric aspects of the three helix-types are roughly independent of the specific peptide sequence, the dominance of the geometric parameters may be used to rationalize why the π-helical motif is in *general* the least common of the helical conformations in proteins, independent of the amino acid sequence and the environmental aspects. These results have been published in Ref. [160].

We remark that the last question:

- 3. What is the origin of the difference in helical propensities between L-alanine and glycine?

could not be resolved conclusively. The comparison between L-alanine and glycine has delivered a *partial* explanation for the different helical propensities of the two amino acids: Vibrational free energy contributions lower the stability of the glycine helices relative to L-alanine — while the static contributions make the poly-glycine α-helix more stable than the poly-L-alanine α-helix at 0 K, the vibrational free energy contributions cause that at room temperature, vice versa, the poly-L-alanine α-helix is more stable than the poly-glycine α-helix. However, since the associated free energy differences are too small as compared to experimental values, additional reasons must exist for the different helical propensities. Likely candidates have been discussed in Sec. 4.5.

Regarding the methodology developed for achieving the objectives of this work, it was necessary to increase the numerical accuracy for determining the harmonic vibrational frequencies as provided by the standard methodology. At the outset of the project in particular the low frequency vibrations of the peptide chain had been found to be completely smeared by the numerical noise. Therefore, in order to achieve the high accuracy required for forces, vibrational frequencies and thermodynamic data, several extensions have been implemented in the S\PHI\nX code. The resulting method for calculating the dynamical matrix, the TSR scheme allowed us to reduce the numerical error on the frequencies to less than 3 cm^{-1}. We remark that this accuracy is fundamental for all the results derived in this project. Indeed, the basic ideas of the TSR scheme are not only applicable to the peptide chain but also in general for phonon calculations, whenever numerical noise significantly disturbs the determination of the dynamical matrix.

Another focus was on the determination of anharmonic corrections to the free energy of the peptide chain. It is believed that anharmonicity strongly influences the vibrations of molecular systems at elevated temperatures. In particular, the soft, low frequency modes of the peptide chain are expected to exhibit strong anharmonic contributions leading to significant deviations from the free energy as calculated within the quasi-harmonic approach. Determining anharmonic corrections for a relatively large system like the peptide chain (from the viewpoint of an ab-initio calculations) is challenging. Nonetheless, we have determined these corrections within reasonable statistical error bars by combining the thermodynamic integration approach with an efficient integration scheme for the ionic equations of motion (Langevin dynamics), an efficient extrapolation scheme for the electronic degrees of freedom, and adequate equilibration and parallelization schemes for the statistical average. In this regard it is important to mention that the determined anharmonic corrections for the peptide chain are rather small. Finally, we remark that the methodology developed here is completely general and can be employed to address in principle any material/system. For example it has been successfully employed to determine the anharmonic contributions to the specific heat of aluminum [161] and the temperature dependence of the bulk modulus of water [162].

Outlook

Although the present study constitutes a few steps on our path to a quantitative and systematic understanding of the stability of the secondary structure, a lot of work remains to be done. There are several fundamental issues to be clarified, which are challenging on their own. We would like here to mention only some of these:

The role of van-der-Waals interactions for the stability of the secondary structure is basically unknown. The deficiency of current exchange-correlation functionals for describing these interactions could result in an error of up to 1 kcal/mol per peptide unit for the stability. While the main results of this project, which address the temperature dependent, *vibrational* contributions to the stability, will remain largely unaffected by the (hypothetical) inclusion of van-der-Waals interactions, it is a valuable task for the future, to repeat the calculations for the static, *energetic* contributions with a theoretical approach, which is even more accurate than (conventional) DFT and accurately includes van-der-Waals interactions.

Another open issue is the quantitative and systematic understanding of the impact of solvent on the helix stability. In particular it is important to treat the solvated system using the high accuracy of the ab-initio approach but in the same way allow to properly include the complex interaction with the solvent.

The helix is the most abundant secondary structure motif in proteins – and also in available ab-initio studies. A complete picture of the secondary structure demands, however, to understand also the remaining secondary structure motifs, most prominently the β-sheet. Ab-initio studies on this motif are therefore highly desired. In particular the understanding of misfoldings in proteins requires a detailed understanding of the stability between the sheet and the helix structure.

A further interest is on the kinetic aspects of helix folding. To deal with this issue a viable approach could be to combine the ab-initio results for the regular secondary structure motifs with coarse grained statistical models, for instance the Lifson-Roig model [163]. Such approach would allow to simulate the helix-coil transition, and also to include interfaces between different secondary structure motifs, transitions between these motifs and finite size effects.

6 Appendix

6.1 Phonon dispersion relation and thermodynamic data

In this section we present additional material regarding the phonon dispersion relation and thermodynamic data. It includes a detailed numerical error analysis and convergence checks. Further, the complete data for the calculated phonon dispersion relations are presented. Finally, a detailed comparison of the phonon dispersion spectra of the poly-L-alanine α-helix and the poly-L-alanine FES is presented.

6.1.1 Error bars and convergence tests

The considerations of Sec. 3.4 clearly revealed that the vibrational spectrum is very sensitive to any perturbations arising from numerical inaccuracies. For a reliable interpretation of the obtained results it is important i) to reduce the influence of these perturbations as much as possible and ii) to estimate the remaining errors, in order to differentiate "true" physical effects from possible numerical artifacts. While the first issue has been treated in detail in Sec. 3.4, here the latter issue is discussed. A detailed analysis of the possible sources of numerical errors is presented and error bars are estimated. Further, convergence checks are presented for the important control parameters of the calculations. These are the cutoff energy E^{cut}, which limits the basis set size, the truncation parameter n^{max}, which limits the long-range interaction taken into account in the dynamical matrix, and the lateral supercell size c_{lat}, which controls the empty volume between the artificial periodic images of the peptide chain. All test calculations are performed employing the three-stage refinement scheme as explained in Sec. 3.4.

Convergence with respect to the basis set size (cutoff energy)

The electronic basis set convergence has been tested for two representative test systems: the poly-glycine 3_{10}-helix and the poly-glycine FES. Fig. 6.1 shows that the absolute values for the frequencies and thermodynamic properties are converged at ~110 Ry up to a remaining error, which is smaller than 2 cm^{-1} for the frequencies and 0.01 kcal/mol for the free energy at 300 K. The worst convergence is found for the highest frequency branches, which correspond to the $\mathrm{C-H}$ and $\mathrm{N-H}$ bond stretching modes, indicating that the "bottleneck" for cutoff-convergence is the non pseudized $1/r$ potential corresponding to the hydrogen species. We remark that the relative differences between the FES and the 3_{10}-helix are already converged at 70 Ry with a maximal error of $\sim 4\ \mathrm{cm}^{-1}$ and 0.01 kcal/mol, respectively. For applications, which exclusively deal with the relative properties (and most of the applications of this project are of this kind), it is therefore sufficient to use a cutoff

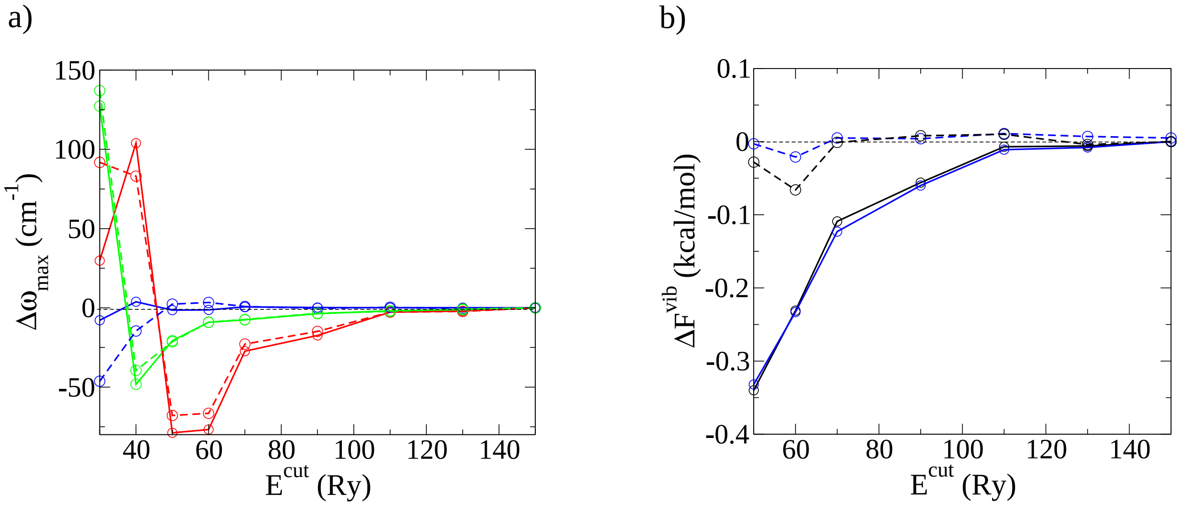

Figure 6.1: a) Maximal error $\Delta\omega_{\mathrm{max}}$ versus E^{cut} for the poly-glycine 3_{10}-helix (solid line) and the FES (dashed line). The error is plotted separately for the low frequency region ($\omega < 100\,\mathrm{cm}^{-1}$, blue line), the mid frequency region ($100\,\mathrm{cm}^{-1} < \omega < 2500\,\mathrm{cm}^{-1}$, green line), and the high frequency region ($\omega > 2500\ \mathrm{cm}^{-1}$, red line). The vibrational spectrum for $E^{\mathrm{cut}} = 150$ Ry serves as reference, where $\Delta\omega_{\mathrm{max}} \equiv 0$. b) Convergence for the free energy of the poly-glycine 3_{10}-helix at $T = 0$ K (blue line) and $T = 300$ K (black line). Shown are the absolute errors in the free energy (solid lines) and the error in the free energy difference to the FES (dashed line). The free energy for $E^{\mathrm{cut}} = 150$ Ry serves as reference, where $\Delta F^{\mathrm{vib}} \equiv 0$.

of 70 Ry. We have therefore used a cutoff energy of 110 Ry only for the comparison to experiment, as presented in Sec. 4.1, since this is the only application, for which convergence in the absolute frequencies is required. For all remaining calculations a cutoff of 70 Ry has been used.

Convergence with respect to the truncation of long-ranged Interactions

To determine the phonon dispersion relation, it is necessary to introduce a truncation radius for the long-ranged interactions taken into account for the dynamical matrix (Eq. (3.34)). Furthermore, at the long-wavelength limits of the acoustical branches the interpolation of Eq. (3.34) is replaced by a cubic spline interpolation (Sec. 3.4.4). To estimate the error in the thermodynamic properties arising from these two interpolations, convergence checks have been performed on two representative systems, the poly-glycine FES and the poly-glycine 3_{10}-helix. These convergence tests implicitly include the convergence with respect to the sampling of the electronic Brillouin zone, i.e., verify whether the Γ-point is sufficient to sample the electronic dispersion. As convergence parameter we choose here the number of turns n^{turns} rather than the parameter n^{max} in Eq. (3.34), since n^{turns} is a more natural convergence parameter, and allows for a direct transferability between the various helical conformations. The calculations are rather involved and have therefore been performed by employing the SCCDFTB approach (Sec. 6.2.2). We, however, expect the findings of these convergence calculations to be transferable to the DFT-PBE approach, since the long-range interactions are of electrostatic nature and thus qualitatively reproduced by the SCCDFTB

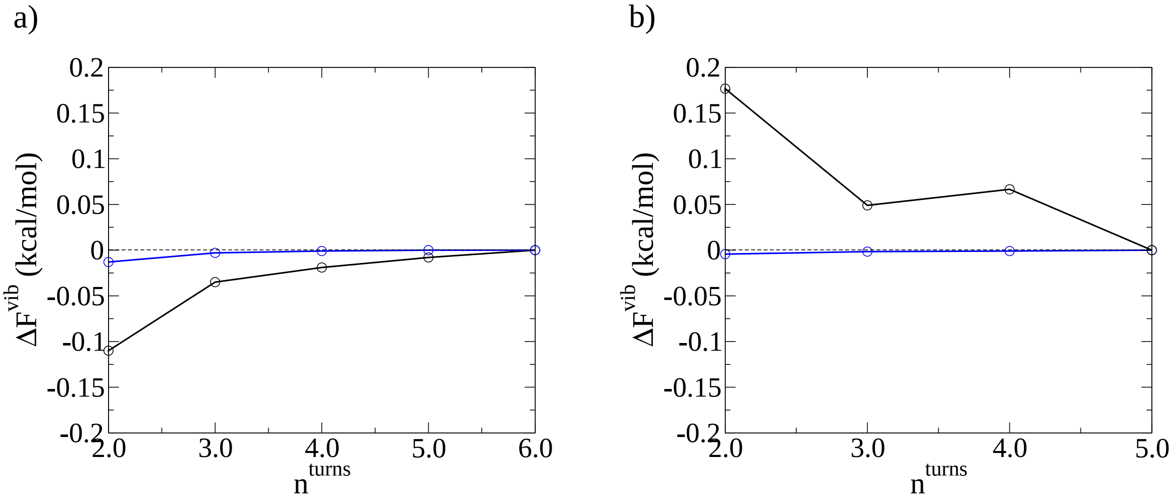

Figure 6.2: Error in the vibrational free energy ΔF^{vib} per peptide unit versus number of turns, n^{turns}, included in the supercell for a) the poly-glycine 3_{10}-helix and b) the FES. In both cases, the error for T=300 K (black lines) and T=0 K (blue lines) are shown. The references values (where $\Delta F^{\text{vib}} \equiv 0$) have been chosen to be the free energies, where the number of turns equals to 6 (for the 3_{10}-helix) or to 5 (for the FES). The calculations have been performed by employing the SCCDFTB approach.

approach. Fig. 6.2 shows that the free energy per peptide unit at room temperature is, for three turns, converged up to an error of 0.03 kcal/mol and 0.05 kcal/mol for the helix and the FES, respectively.

Convergence with respect to the lateral supercell size and remaining error bars due to the discretization of the XC contributions

The supercell approach implies that the peptide chain is not isolated, but is embedded in an artificial 2-dimensional crystal of identical peptide chains (Fig. 3.1). Hence, artificial interactions between the individual peptide chains of this crystal exist, which might modify the calculated frequency spectra. In order to determine the minimum lateral lattice parameter c_{lat} at which these artificial interactions are sufficiently small, we have performed convergence checks for a representative test system, the poly-L-alanine 3_{10}-helix. For this system we find convergence for c_{lat}=20 Bohr (Fig. 6.3). For $c_{\text{lat}} > 20$ Bohr the vibrational frequencies still show small fluctuation for varying c_{lat}, however, these fluctuations are exclusively related to remaining errors associated with the FFT mesh discretization. Therefore, a further increase of c_{lat} would not lead to a systematic improvement of the results. In this study, all helical systems have been treated with a lateral supercell extension of at least $c_{\text{lat}} = 22$ Bohr. For the extended structures, i.e., 2_7-structure and the FES a separate convergence test was performed and convergence was found for c_{lat}= 20 Bohr.

The remaining errors are due the XC wiggles and are estimated as follows: Five equivalent calculations of the vibrational spectrum are performed, each for a different relative rotational position of the geometry with respect to the FFT mesh (Fig. 6.4). The error bars are then estimated as the largest deviation which in between either two of these five vibrational spectra: or the frequency an

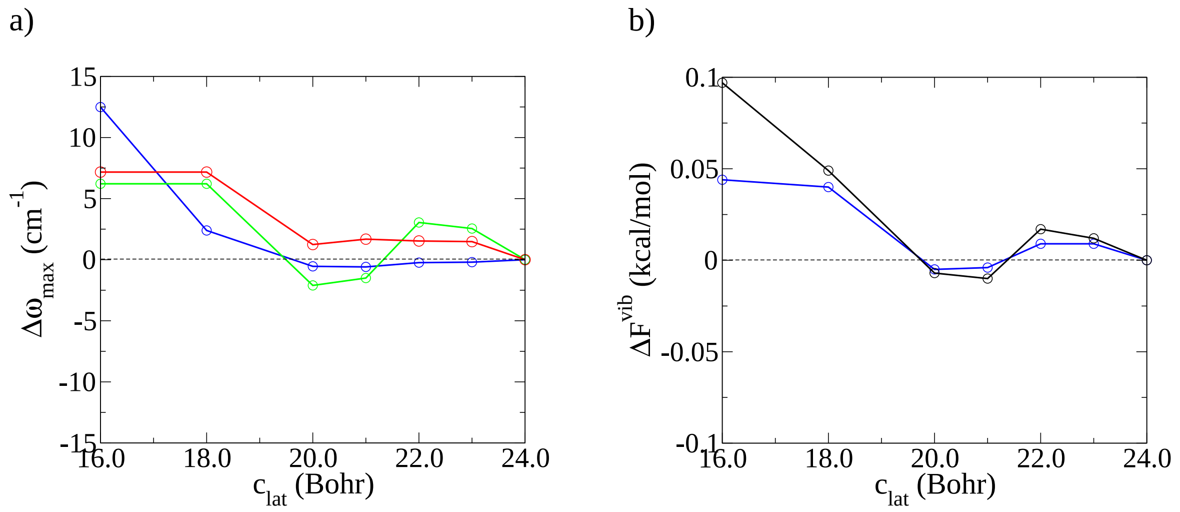

Figure 6.3: a) Maximum absolute errors $\Delta\omega_{\mathrm{max}}$ in the frequencies for increasing lateral supercell sizes c_{lat}. $\Delta\omega_{\mathrm{max}}$ has been determined separately for the low-frequency region (blue line), the mid frequency region (green line) and the high-frequency region (red line). The frequency spectrum for $c_{\mathrm{lat}} = 24.0$ Bohr serves as reference value (where $\Delta\omega_{\mathrm{max}} \equiv 0$). b) Respective errors in the free energies, i.e. ΔF^{vib}, for T=0 K (blue line) and T=300 K (black line)

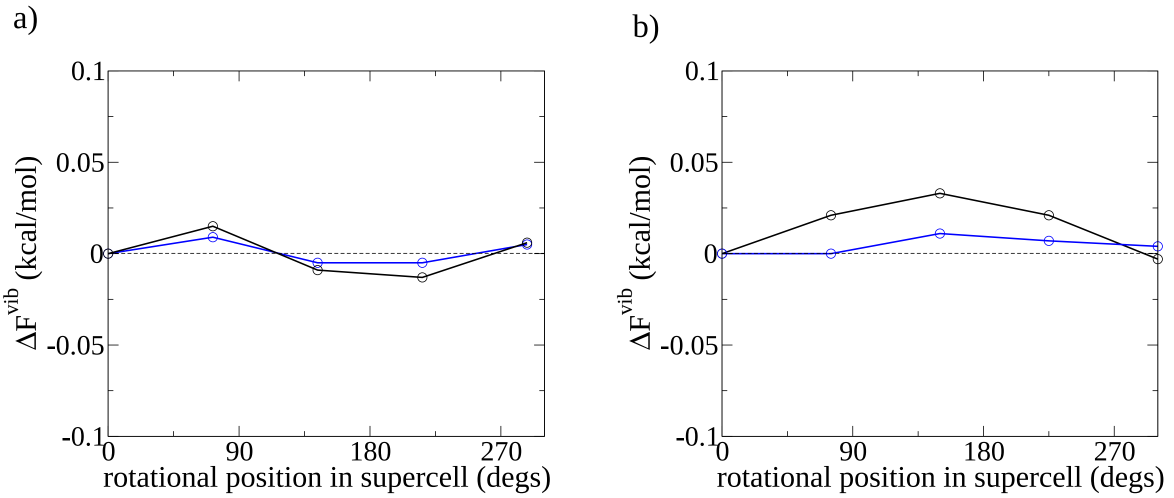

Figure 6.4: Deviations ΔF^{vib} in the vibrational free energy for 5 different (formally equivalent) rotational orientations of the poly-peptide in the supercell for a) the poly-glycine 3_{10}-helix and b) the poly-L-alanine FES. Shown are, in both cases, the error for T=300 K (black lines) and T=0 K (blue lines). The reference values (where $\Delta F^{\mathrm{vib}} \equiv 0$) have been (arbitrarily) chosen from the first rotational orientation.

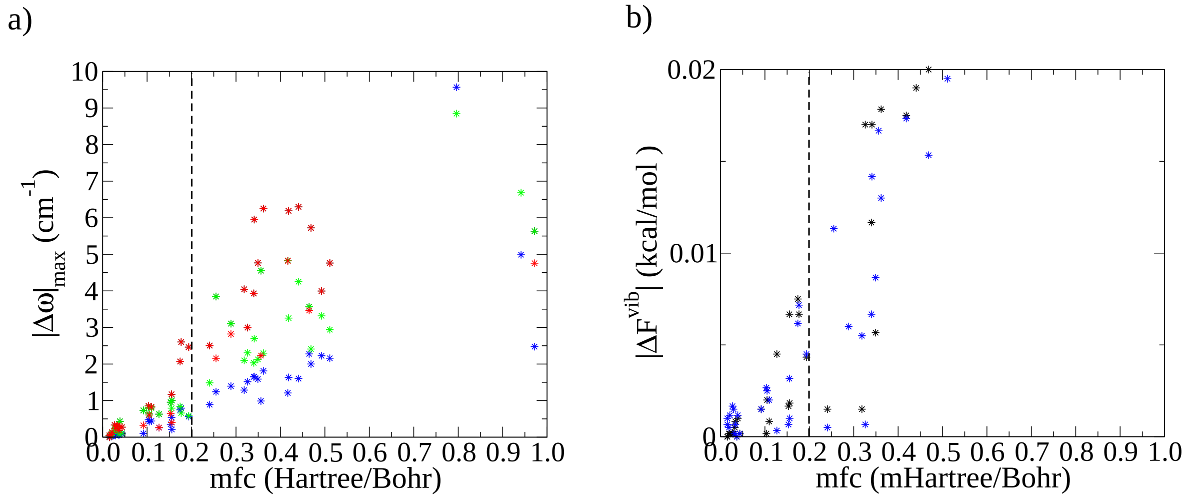

Figure 6.5: a) Maximum frequency deviation $|\Delta\omega|_{\max}$with respect to maximal force component (mfc) calculated with SCCDFTB for the poly-glycine 3_{10}-helix. Separately plotted for the low-frequency region (blue dots), the mid frequency region (green dots) and the high-frequency region (red dots) b) Deviation in the free energy at 300 K (black dots) and 0 K (blued dots)

error of about 2 cm^{-1} is found and for the free energy the error bar is 0.03 kcal/mol.

Convergence with respect to the accuracy of the geometry optimization

A geometry optimization, which is performed on a DFT potential energy surface, in general does not end up in a perfectly converged structure, but rather in a structure, which is slightly distorted from the equilibrium structure. For the determination of the vibrational spectra this circumstance may lead to deviations from the "true" values (which correspond to the perfectly converged structure). We have estimated this error by performing a test calculation on the poly-glycine 3_{10}-helix. As this test is computationally rather demanding, it has been performed again by using the SCCDFTB approach (Sec. 6.2.2) instead of the DFT-PBE approach.

The test is performed in the following way: First of all an artificial structure is generated by randomly displacing the atoms from their equilibrium positions. This artificial structure is then used as an input structure to start the geometry optimization scheme. At each step n of the geometry optimization the corresponding intermediate structure $\mathbf{X}(n)$ and maximal force component $f_{\max}(n)$ acting on the structures are determined. Each structure $\mathbf{X}(n)$ serves then as an input structure for an individual frequency calculation and a subsequent calculation of the thermodynamic data. Based on these calculations the maximum error in the frequency spectra is determined:

$$|\Delta\omega_{\max}(n)| = \max_i(|\omega_i(n) - \omega_i(n_{opt})|). \tag{6.1}$$

Here i goes over the vibrational spectrum and n_{opt} indicates the final step of the geometry opti-

a)

	low freq. region	mid freq. region	high freq. region
geom. optim.	1	1	3
XC wiggles	1	1	2
basis set (70 Ry)	1	5	30
basis set(110 Ry)	1	1	2
overall error (70 Ry)	3	7	35
overall error (110 Ry)	3	3	7

b)

	F^{vib}	$\Delta F^{\mathrm{vib}}_{\mathrm{helix-FES}}$	$\Delta F^{\mathrm{vib}}_{\mathrm{helix-helix}}$
geom. optim.	0.01 (0.01)	0.02 (0.02)	0.02 (0.02)
XC wiggles	0.03 (0.01)	0.06 (0.02)	0.06 (0.02)
truncation at n^{max}	0.05 (0.00)	0.08 (0.00)	0.03 (0.00)
basis set (70 Ry)	0.12 (0.12)	0.01 (0.01)	0.01 (0.01)
basis set(110 Ry)	0.01 (0.01)	0.01 (0.01)	0.01 (0.01)
absolute error (70 Ry)	0.21 (0.15)	0.18 (0.05)	0.10 (0.05)
absolute error (110 Ry)	0.10 (0.03)	0.18 (0.05)	0.10 (0.05)

Table 6.1: a) Compendium of the error bars in cm^{-1} for the low-frequency region with $\omega < 100$ cm^{-1}, the mid frequency region with 100cm^{-1} $< \omega <$ 2500cm^{-1} and the high-frequency region with $\omega >$ 2500cm^{-1} b) Compendium about of the error bars in kcal/mol for thermodynamic data at 300 K (and at 0 K in parentheses).

mization and corresponds to the most accurate structure. Further, the error in the free energies:

$$|\Delta F^{\mathrm{vib}}(n)| = |F^{\mathrm{vib}}(n) - F^{\mathrm{vib}}(n_{\mathrm{opt}})|, \tag{6.2}$$

is evaluated. To determine a correlation between the convergence parameter f_{max} and the errors $|\Delta\omega_{\mathrm{max}}|$ and $|\Delta F^{\mathrm{vib}}|$, the data points

$$(|f_{\mathrm{max}}(n)|, |\Delta\omega_{max}(n)|) \quad \text{and} \quad (|f_{\mathrm{max}}(n)|, |\Delta F^{\mathrm{vib}}(n)|), \tag{6.3}$$

respectively, are plotted on a 2-dimensional map (Fig. 6.5). We use this map to estimate the errors of the DFT calculations: All structures of the DFT calculations have been converged up to an accuracy corresponding to a maximal force component $f_{\mathrm{max}} \leq 0.25$ mHartree/Bohr. Therefore, the error in the frequencies arising from errors in the structure is smaller than 3 cm^{-1} and the error in the vibrational free energy is smaller than 0.01 kcal/mol per peptide unit (largely independent of the temperature).

Overall error bars for frequency and thermodynamic data

The error bars due to the various sources of error described above are summarized in Tab. 6.1. To estimate the overall (absolute) error bars for the frequency data and the vibrational free energy,

a)

L-alanine	Θ	L	R	Ψ	δ	D_1	$D_{\nu-1}$	D_ν	ζ
FES	180.00	6.74	0.961	148.16	180	7.01	-	-	-
2_7	180.00	5.35	2.608	91.5	180	7.47	7.47	10.7	0.31
3_{10}	120.00	3.71	3.48	85.04	84.56	7.07	9.56	11.13	0.22
α	98.18	2.83	4.1	93.16	51.26	6.82	9.59	11.54	0.20
π	80.00	2.21	5.03	105.9	30.4	6.83	9.48	11.57	0.08

b)

glycine	Θ	L	R	Ψ	δ	D_1	$D_{\nu-1}$	D_ν
FES	180.00	6.81	0.80	153.6	180	7.00	-	-
2_7	180.00	5.40	0.72	150.3	180	5.59	5.59	10.8
3_{10}	120.00	3.66	2.85	91.9	91.8	6.14	8.82	10.98
α	96.00	2.73	3.60	97.08	53.53	6.01	9.01	9.22
π	83.08	2.18	4.26	103.5	35.3	6.05	9.51	9.57

Table 6.2: Geometrical parameters for a) poly-L alanine and b) poly-glycine. Tabulated are the helical parameters, i.e., twist Θ, pitch L, and radius R, the backbone valence angle Ψ and dihedral angle δ, the nearest neighbor peptide-peptide distance D_1, and the peptide-peptide distances characterising the hydrogen bonds, i.e., $D_{\nu-1}$ and D_ν. Further shown is the Poisson ratio ζ (only for L-alanine)

the single contributions are summed up. For the relative differences in free energy $\Delta F^{\text{vib}}_{\text{helix}\rightarrow\text{FES}}$ and $\Delta F^{\text{vib}}_{\text{helix}\rightarrow\text{helix}}$ we consider that two different types of errors exist: i) errors which are of stochastic nature (geometry optimization, XC wiggles) and ii) errors which are of systematic nature (basis set, truncation at $n^{\max}$). While the first type of errors fully enters the relative quantities, for the second type of errors a partial error cancellation is expected. For example: The error bar according to the structure optimization is 0.01 kcal/mol, when calculating the (absolute) free energy of a given chain conformation. The error is of stochastic nature, therefore the error according to the structure optimization is 0.02 kcal/mol, when determining free energy differences between two chain conformations. Counter-example: The error due to the basis set truncation at E^{cut} is 0.12 kcal/mol at 70 Ry, when calculating the (absolute) free energy of a given chain conformation. This error is of systematic nature, the according error has been found to be only 0.01 kcal/mol, when determining free energy difference in between two chain conformations.

6.1.2 Phonon dispersion curves

The complete frequency data for all analyzed conformations, i.e., fully extended structure, 2_7-structure, 3_{10}-structure, α-helix, and π-helix are shown for poly-L-alanine in Fig. 6.7 and for poly-glycine in Fig. 6.6. These results have been obtained using the methodology described in Chapter 3 and a cutoff energy of 70 Ry.

A graphical illustration of the corresponding eigenmodes is given in Fig. 6.8

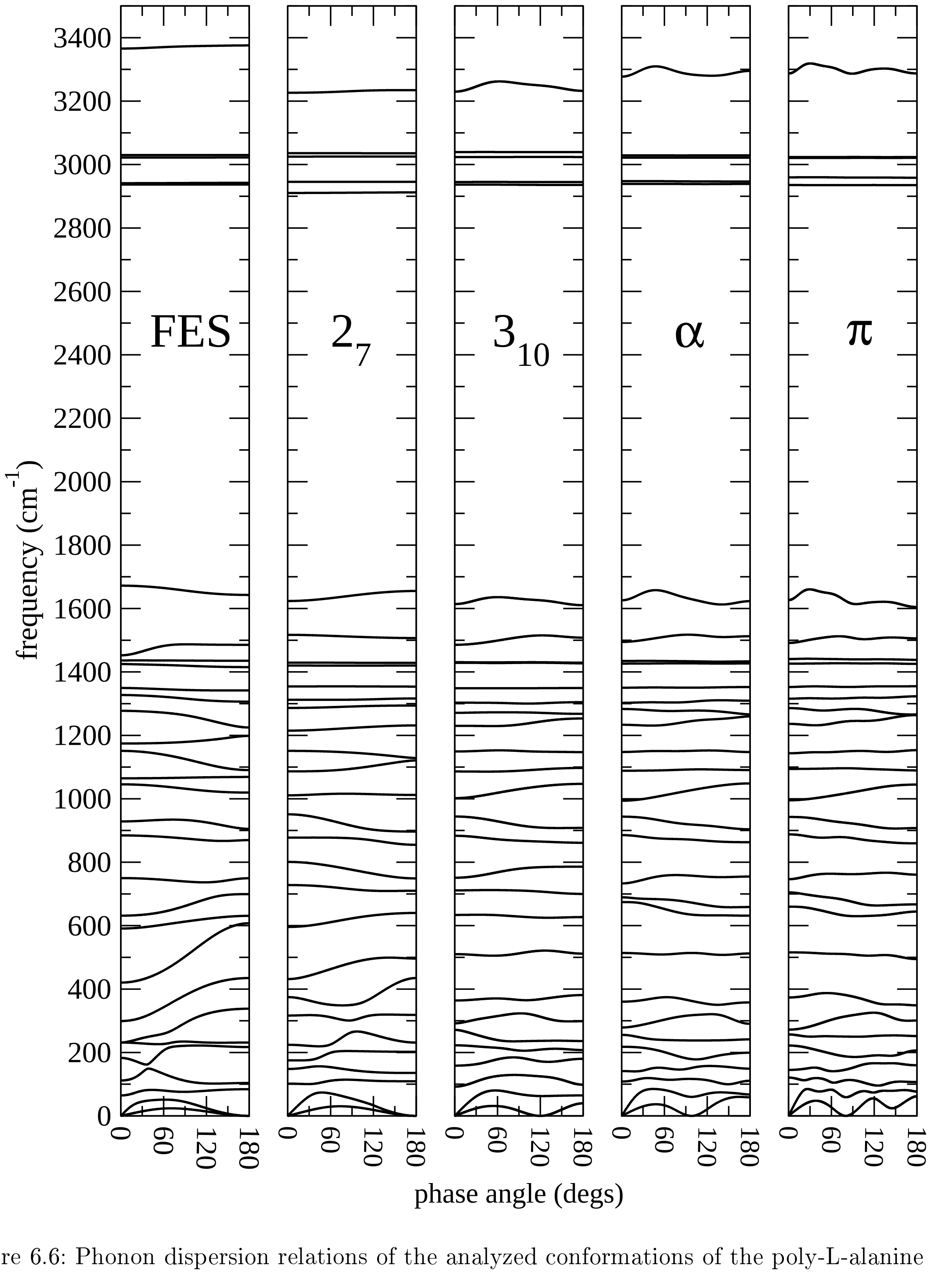

Figure 6.6: Phonon dispersion relations of the analyzed conformations of the poly-L-alanine chain.

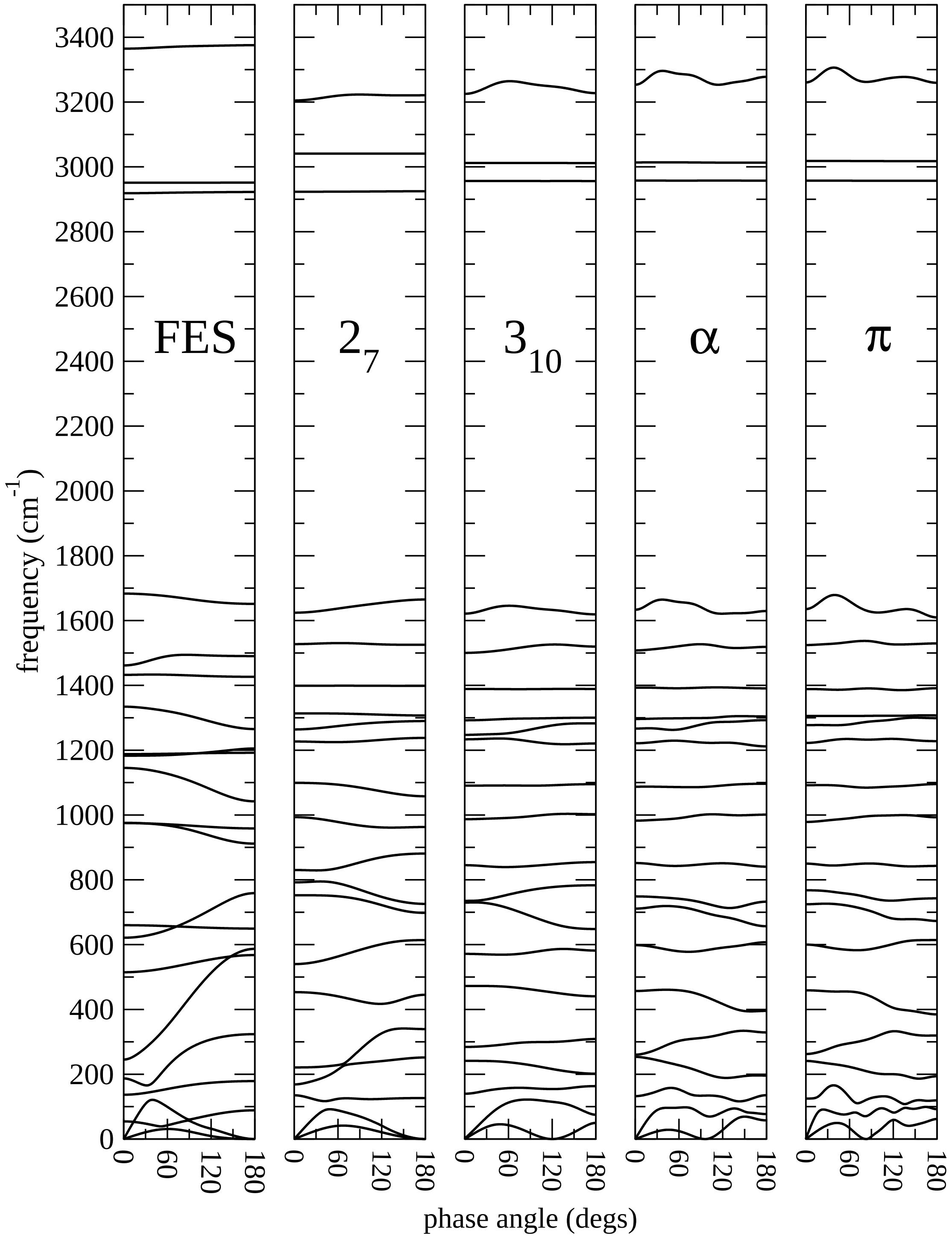

Figure 6.7: Phonon dispersion relations of the analyzed conformations of the poly-glycine chain.

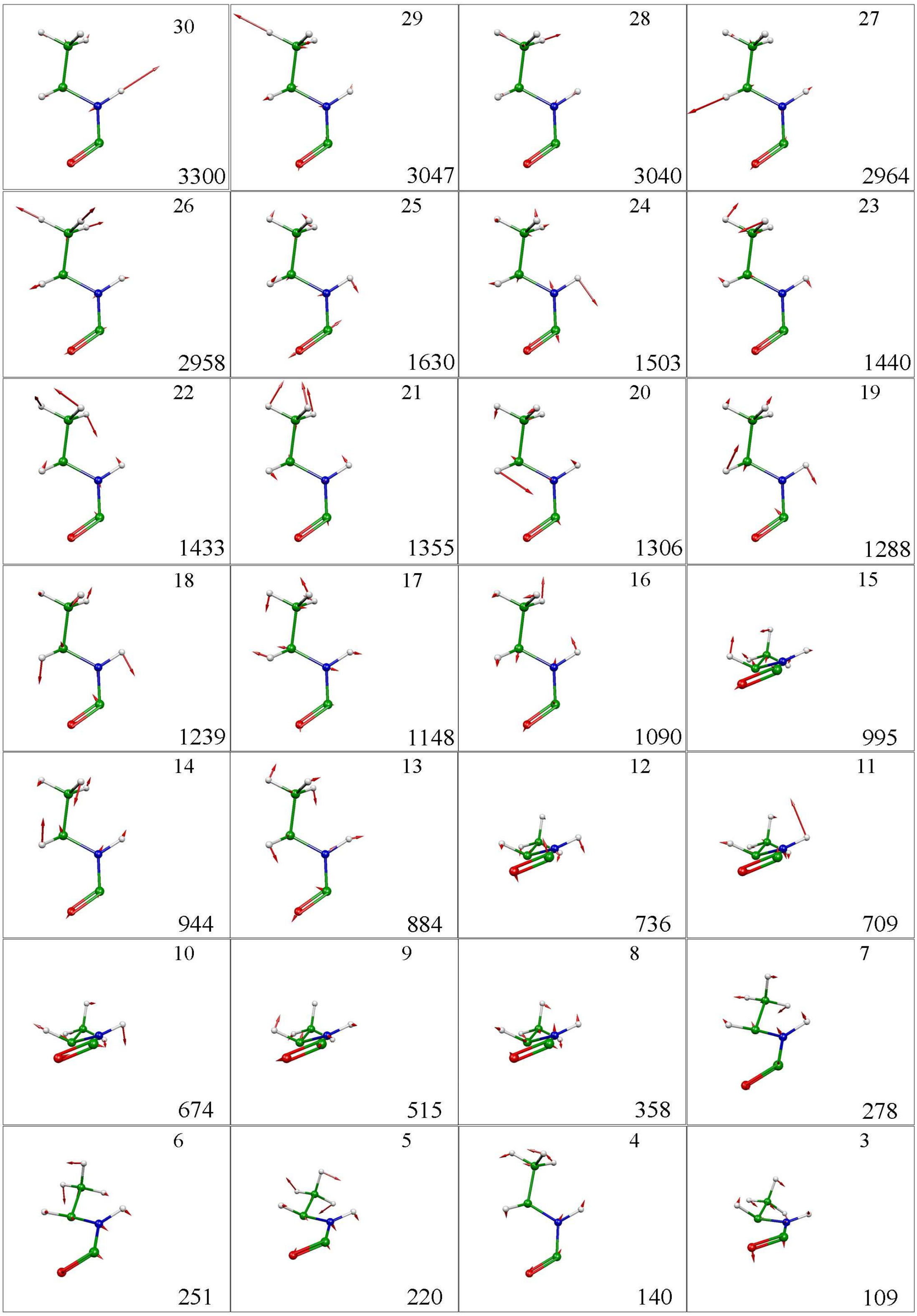

Figure 6.8: Vibrational eigenmodes corresponding to the 28 optical branches of the poly-L-alanine α-helix. Shown is the lattice-periodic part of the vibrational Bloch-states at the Γ-point, i.e., the quantity $\mathbf{l}_i^{\mathrm{c}}(\varphi = 0)$ in Eq. (2.94), expressed in Cartesian coordinates. The arrows depict the velocities of the particles at the zero-point. The numbers in the lower right corners denote the vibrational frequencies at the Γ-point in cm^{-1} and the labels in the upper right corners correspond to those used in Fig. 4.1 and Tab. 4.2.

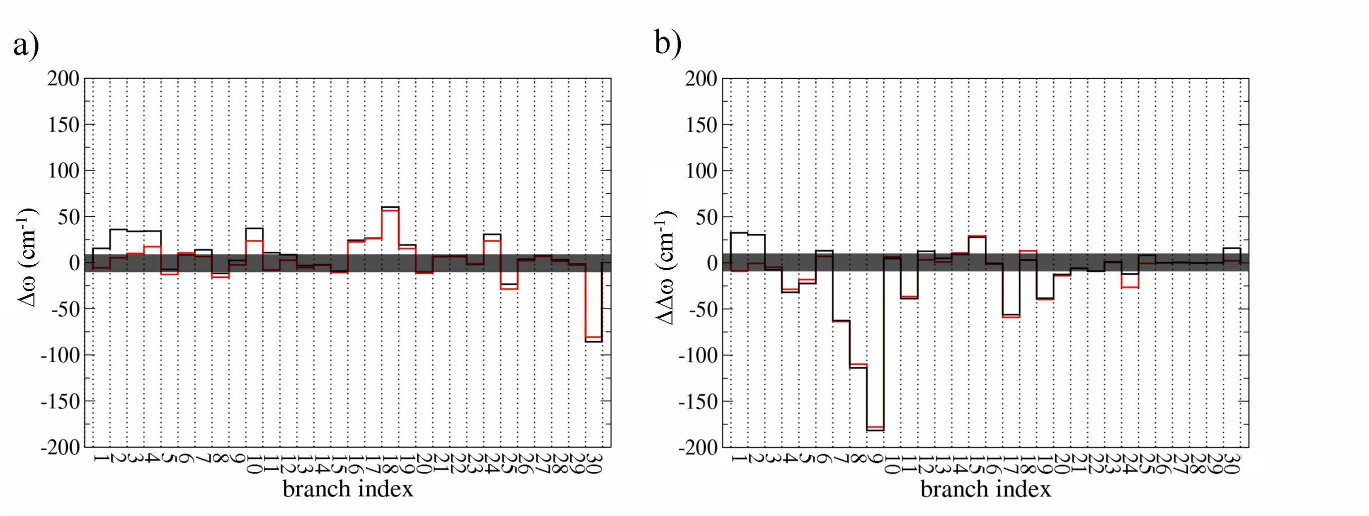

Figure 6.9: a) Band center shifts (Eq. (6.4)) in the α-helical conformation compared to the FES and b) the changes in the band widths (Eq. (6.5)). The black lines denotes the shifts for the un-manipulated dynamical matrix, whereas the red line shows the shift, when the long-ranged interactions are removed from the dynamical matrix (Sec. (4.3.2)). The dark, semi-transparent bar denotes an (arbitrarily defined) region of insignificance, where $\Delta\omega_i^{\text{bc}}, \Delta\Delta\omega_i^{\text{bw}} < 10\text{cm}^{-1}$.

6.1.3 Comparison between α-helix and FES

In order to identify the impact of the helix formation on the vibrational spectrum of the peptide chain we have compared the phonon dispersion relations for two conformations of the peptide chain. For this comparison, we have focused on the α-helix and the FES, since these two conformations are representative for the folded, helical state and the unfolded state, respectively.

To be able to quantify the differences we introduce two measures, firstly the band-center shift:

$$\Delta\omega_i^{\text{bc}} = \frac{1}{\pi}\int_0^{\pi} \omega_i^{\alpha}(\varphi)d\varphi - \frac{1}{\pi}\int_0^{\pi} \omega_i^{\text{FES}}(\varphi)d\varphi, \tag{6.4}$$

and, secondly, the change in the band-width:

$$\Delta\Delta\omega_i^{\text{bw}} = \mid \max_{\varphi=0..\pi} \omega_i^{\alpha}(\varphi) - \min_{\varphi=0..\pi} \omega_i^{\alpha}(\varphi) \mid - \mid \max_{\varphi=0..\pi} \omega_i^{\text{FES}}(\varphi) - \min_{\varphi=0..\pi} \omega_i^{\text{FES}}(\varphi) \mid . \tag{6.5}$$

We here define (arbitrarily) the differences according to these two quantities as significant, if they are larger 10 cm^{-1}. Then we obtain the following classification:

- Branches which show significant band center shifts: These are the branches with the indices 1-4, 6, 7, 10, 11, 16-20, 24, 25, 30 (indices refer to the notation as used in Figs. 6.8 and 4.5 and in Tab.4.2). We may identify them as, on the one hand, the low frequency branches, and as, on the other hand, the high frequency stretching/bending vibrations corresponding to the atoms, which are most directly involved in the hydrogen bonds stabilizing the helix.
- Branches which show significant changes in the dispersion but no band center shifts: These

are the branches with indices 5, 8, 9, 12, 14, and 15. We may identify them as the mid frequency branches corresponding to a deformation of the backbone and those corresponding to a collective motion of the side group with respect to the backbone.

- Branches which do not show significant changes at all: These are the branches with the indices 13, 21-23, and 26-29. We may identify them as the C-H stretching respectively bending vibrations in the methyl side group and in the C_β-H bond.

We thus get a qualitative impression of the impact the helix formation has for the vibrational spectrum of the peptide chain: While the internal vibrations of the side-group remain unaffected, significant changes can be found for the vibrational branches which correspond to a deformation of the backbone of the helix. For the latter type of modes, significant band-center shifts can be found for the acoustical branches and for the optical modes which are directly involved in the hydrogen bond formation, whereas those vibrational modes which do not involve a distortion of the hydrogen bonds exhibit only changes in their band-width.

6.2 Density functional theory

This section contains additional material on density functional theory. First details of the PBE functional, which is the XC functional employed in this project, are given. Then the SCCDFTB approach is presented. This approach denotes a simplified, approximated form of DFT, which has been used for many test calculations.

6.2.1 The PBE functional

The XC-energy is written in this approximation as:

$$E^{\mathrm{xc}}_{\mathrm{PBE}}[n] = \int d^3r f^{\mathrm{xc}}_{\mathrm{PBE}}(\mathbf{r}, |\nabla n(\mathbf{r})|) n(\mathbf{r}), \tag{6.6}$$

where:

$$f^{\mathrm{xc}}_{\mathrm{PBE}}(\mathbf{r}, |\nabla n(\mathbf{r})|) = f^{\mathrm{x}}_{\mathrm{PBE}}(\mathbf{r}, |\nabla n(\mathbf{r})|) + f^{\mathrm{c}}_{\mathrm{PBE}}(\mathbf{r}, |\nabla n(\mathbf{r})|). \tag{6.7}$$

The exchange part in the PBE functional is written as

$$f^{\mathrm{x}}_{\mathrm{PBE}}(\mathbf{r}, |\nabla n(\mathbf{r})|) = \epsilon^{\mathrm{x}}_{\mathrm{unif}}(n(\mathbf{r})) F^{\mathrm{x}}(s(\mathbf{r})), \tag{6.8}$$

where $\epsilon^{\mathrm{x}}_{\mathrm{unif}}(n)$ is the local exchange energy of a uniform electron gas with density n (see below, Eq. (6.19)), and

$$F^{\mathrm{x}}(s) = 1 + \kappa - \frac{\kappa}{(1 + \mu s^2/\kappa)}, \tag{6.9}$$

is the *gradient correction* with

$$s = \frac{|\nabla n|}{2 k_F n}, \tag{6.10}$$

$$k_F = \left(3\pi^2 n\right)^{1/3}, \tag{6.11}$$

$$\mu \simeq 0.235 \text{ and } \kappa \simeq 0.967. \tag{6.12}$$

The correlation part is given by

$$f^{\mathrm{c}}_{\mathrm{PBE}}(\mathbf{r}, |\nabla n(\mathbf{r})|) = n(\mathbf{r})(\epsilon^{c}_{\mathrm{unif}}(n(\mathbf{r})) + h(\mathbf{r})), \tag{6.13}$$

where $\epsilon^{\mathrm{c}}_{\mathrm{unif}}$ is the local correlation energy of a uniform electron gas with density n (see below, Eqs. (6.21) and (6.22)), and

$$h = \frac{e^2}{a_0}\gamma\phi^3 \ln[1 + \frac{\beta}{\gamma}t^2[\frac{1 + At^2}{1 + At^2 + A^2t^4}]], \tag{6.14}$$

h is the gradient correction with

$$A = \frac{\beta}{\gamma}[\exp\{-\frac{\epsilon^{\mathrm{c}}_{\mathrm{unif}}a_0}{\gamma\phi^3 e^2}\} - 1]^{-1}, \tag{6.15}$$

$$t = \frac{|\nabla n|}{2\phi k_{\mathrm{s}} n}, \tag{6.16}$$

$$k_{\mathrm{s}} = \sqrt{4k_{\mathrm{F}}/\pi a_0}, \tag{6.17}$$

$$\beta \simeq 0.066725, \text{ and } \gamma \simeq 0.031091. \tag{6.18}$$

Exchange energy of a uniform electron gas

The exchange energy of an uniform electron gas can be analytically derived via the Hartree-Fock equations:

$$\epsilon^{\mathrm{x}}_{\mathrm{unif}} = -\frac{3}{16}\left(\frac{3}{\pi}\right)^{1/3} r_{\mathrm{s}}^{-1}, \tag{6.19}$$

where r_s denotes the *Wigner-Seitz-radius*:

$$r_{\mathrm{s}} = (\frac{3}{4\pi n})^{1/3}. \tag{6.20}$$

Correlation energy of a uniform electron gas

In contrast to the exchange part an analytical expression for the correlation energy of a uniform electron gas does not exist. Instead, it is described by a parametrized expression, in which the parameters are optimized to fit the numerically exact correlation energy of the uniform electron gas. A widespread used parametrization, which also enters into the particular XC functional employed for this work, has been derived by Perdew&Zunger [69]. In this parametrisation the correlation energy follows for high electron densities, i.e. $r_{\mathrm{s}} < 1$, the expression:

$$\varepsilon^{\mathrm{c}}_{\mathrm{unif}} = A \ln r_{\mathrm{s}} + B + C r_{\mathrm{s}} \ln r_{\mathrm{s}} + D r_{\mathrm{s}}, \tag{6.21}$$

and for $r_s \geq 1$ it follows:

$$\varepsilon^{\mathrm{c}}_{\mathrm{unif}} = \frac{\gamma}{1 + \beta_1 \sqrt{r_{\mathrm{s}}} + \beta_2 r_{\mathrm{s}}}. \tag{6.22}$$

The parameters in the above two equations, $A, B, C, D, \gamma, \beta_1$ and β_2, have been optimized to fit the exact numerical results for a huge bandwidth of electron densities as have been calculated by Ceperley and Alder [63] using the QMC approach.

6.2.2 The self-consistent-charge density functional tight-binding method

For the determination of thermodynamic properties, harmonic free energies, and anharmonic corrections a variety of test calculations were required. Some of these tests are computationally too demanding to practically perform them using the DFT-PBE approach. An alternative, less computationally demanding approach was then required. We have chosen the self-consistent-charge density functional tight-binding method (SCCDFTB) approach as proposed by Elstner et al. [164]. This approach is by definition not able to achieve the accuracy of the DFT-PBE plane wave approach, since it is based on a minimal basis set and further severe approximations (e.g. restriction on two-center integrals). Therefore the SCCDFTB approach has not been applied to directly obtain results for this project. However, the SCCDFTB contains, in a qualitative manner, the ingredients to describe chemical and hydrogen bonds. In particular it accounts for long-ranged electrostatic interactions and partly includes hydrogen bond cooperativity due to long-range polarization effects. Most importantly it is about two orders of magnitude faster than the DFT-PBE approach. The SCCDFTB approach has therefore extensively been used to replace the DFT-PBE approach for *test calculations* and *convergence checks*.

According to Ref. [164] the method is based on a second order expansion of the LDA-Kohn-Sham total energy with respect to charge density fluctuations, which reveals the following expression for the total energy:

$$E_2^{\mathrm{el,TB}} = \sum_i^{\mathrm{occ}} \left\langle \Psi_i \mid \hat{H}_0 \mid \Psi_i \right\rangle + \frac{1}{2} \sum_{\alpha,\beta}^{N} \gamma_{\alpha\beta} \Delta q_\alpha \Delta q_\beta + E_{\mathrm{rep}}. \tag{6.23}$$

The first term in Eq. (6.23) contains the electronic band-structure and the third term is a parametrized repulsive potential, which is determined by fitting the SCCDFTB approach to reproduce cohesive energies and elastic constants of a set of suitable reference systems. These two terms (the first and the third) are the typical ingredients of a (non-self consistent) tight binding approach. The self-consistency of the here applied approach is contained in the second term of Eq. (6.23). In this term Δq_α denotes charge fluctuations as induced at the atom α and $\gamma_{\alpha\beta}$ is an approximated, parametrized Hubbard-type function to model the electrostatic interaction according to the charge fluctuations. The charges Δq_α are self-consistently updated, while solving the Kohn-Sham equations, which, according to Ref. [164], considerably improves the transferability of the approach compared to the non-self consistent tight binding approaches.

$n^{\text{turns}} \rightarrow$	2	3	4	6
FES	-0.24	-0.07	-0.11	0.13
3_{10}	-0.11	-0.13	-0.13	-

Table 6.3: Anharmonic corrections to the vibrational free energy as determined with the SCCDFTB approach for different number of turns n^{turns} in the supercell.

6.3 Thermodynamic integration

In this section we present additional material on the thermodynamic integration. It includes a method to determine the correlation time of a MD simulation (Sec. 6.3.2) and a method to parallelize Langevin dynamics runs (Sec. 6.3.3).

6.3.1 Calculational details

The calculations for the thermodynamic integration denote the numerically most demanding part of this project. Therefore, to ensure the maximum computational efficiency, careful convergence tests have been performed regarding each parameter.

Correspondingly to those convergence checks presented for the harmonic free energies in Sec. 6.1.1 we have also performed convergence checks regarding the lateral supercell size and the cutoff energy for the anharmonic corrections. We remark that it turned out to be sufficient to use a cutoff of 50 Ry. We used a lateral supercell size of 16 Bohr for the 3_{10}-helix, of 17.5 Bohr for the α-helix and of 20 Bohr for the FES. The convergence with respect to the chain lengths to be included in the supercell has also been checked: For the helices we found it sufficient to include 2 full turns in the supercell and for the FES we found it sufficient to include 3 full turns in the supercell (Tab. 6.3).

6.3.2 Method of minimum statistical inefficiency

To determine the correlation time and the variance of a given Langevin Dynamics simulation the time series $\{X_n\}$ obtained from the simulation was divided up into n_b blocks of length τ^{b}, where $n^{\text{b}} = \tau^{\text{sim}}/\tau^{\text{b}}$. The mean value is calculated for each block b:

$$\left\langle \frac{\partial U}{\partial \lambda} \right\rangle_b = \frac{1}{\tau_b} \sum_{\tau=1}^{\tau_{\text{b}}} \frac{\partial U}{\partial \lambda}(\tau). \tag{6.24}$$

The mean values for all the blocks are then used to estimate the variance:

$$s\left(\left\{\left\langle \frac{\partial U}{\partial \lambda} \right\rangle_b\right\}\right) = \frac{1}{n^{\text{b}}} \sum_{b=1}^{n^{\text{b}}} \left(\left\langle \frac{\partial U}{\partial \lambda} \right\rangle_b - \left\langle \frac{\partial U}{\partial \lambda} \right\rangle_{\text{sim}}\right), \tag{6.25}$$

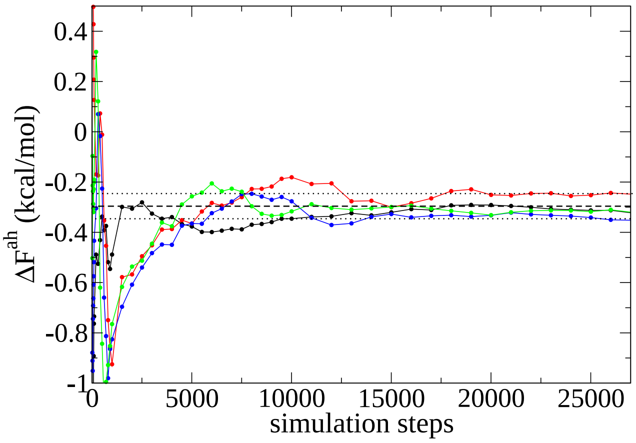

Figure 6.10: Evaluated anharmonic correction ΔF^{ah} for the poly-L-alanine FES versus total number of simulation steps: For a serial run (black lines) and for parallelized runs with each branch containing 500 simulation steps simulation time and a preceding equilibration of 0 (red line), 100 (blue line), and 200 steps (green line), respectively. The dashed black line corresponds to the (converged) value taken after 50000 simulation steps. The dotted lines denote an error bar of 0.05 kcal/mol.

where $\langle \frac{\partial U}{\partial \lambda} \rangle_{\mathrm{sim}}$ denotes the average over the entire time series $\{X_n\}$. According to Ref. [124] the *statistical inefficiency* is given by:

$$\kappa = \lim_{\tau^{\mathrm{b}} \to \infty} \frac{\tau^{\mathrm{b}} s\left(\left\{\left\langle \frac{\partial U}{\partial \lambda} \right\rangle_b\right\}\right)}{s\left(\{X_n\}\right)} \tag{6.26}$$

and the correlation time t^{cor} is given by the *smallest* blocksize τ^{b} for which the right hand quantity in Eq. (6.26) approaches its converged value κ, multiplied with the time step Δt. Eq. (6.26) thus may be used to determine the correlation time. The variance to substitute in Eq. (3.79) is calculated from Eq. (6.25) by setting the blocksize to $\tau^{\mathrm{b}} = t^{\mathrm{cor}}/\Delta t$.

6.3.3 Parallelization

The relatively long simulation times required to obtain statistical convergence for the peptide chain made it necessary to determine the quantity $\left\langle \frac{\partial U}{\partial \lambda} \right\rangle_\lambda$ not within one single serial run, but within a set of parallelized runs. To verify that the data series that is made from the combination of parallelized runs represents the canonical ensemble in the same way, as a data series that is made from one serial run it must be ensured that i) the individual runs of the parallelization are statistically independent from each other and ii) the individual runs are equilibrated for the given potential $U(\lambda)$, such that the starting conditions do not bias the results.

To satisfy these two conditions the following initialization scheme is applied: A set of statistically independent starting conditions, i.e., *random walkers*, is extracted from a sufficiently long Langevin dynamics (LD) run on the harmonic potential of the system of interest. The random walkers are then equilibrated for a certain time and the LD trajectories of the random walkers subsequent to the equilibration are merged to generate the data series for the statistical analysis. Fig. 6.10 shows that this scheme reproduces the results as obtained for a serial run (black line), provided that a equilibration period of at least 200 steps (green line) is used.

6.4 Analytical models

Here we present additional material to the analytical models discussed in Sec. 4.4. First the ball-and-spring model of Christiansen et al. [147] is discussed, which denoted the starting point of our work with model potentials. Then the thin rod approximation is introduced and analytical formulas for the long-wavelength limits of the acoustical branches of the helix are derived. Finally, these analytical formulas are simplified by means of approximations in order to obtain the formulas discussed in Sec. 4.4.2.

6.4.1 Ball-and-spring model

Recently, Christiansen et al. have proposed a simple model, which focuses on modeling the interactions of the peptide units in the helix [147]. In this approach the Hamiltonian of the peptide chain is written as:

$$H = \sum_n \left[\frac{1}{2} M(\dot{x}_n^2 + \dot{y}_n^2 + \dot{z}_n^2) + \sum_{j=1,2,\nu} U_j(r_{jn}) \right] . \tag{6.27}$$

Here, M is the mass of the peptide unit, the coordinates x_n, y_n and z_n describe the displacements of the n^{th} peptide unit from its equilibrium position, the dots denote the first derivative with respect to time and $r_{jn} =\mid \mathbf{R}_j - \mathbf{R}_n \mid$ is the spatial distance of the peptide units j and n, respectively. The three functions $U_j(r_{jn})$ describe the interactions between the first-nearest neighbor ($j = 1$), second-nearest neighbor ($j = 2$) and ν^{th}-nearest neighbor peptide units (ν is number of peptides to form a hydrogen bond, see Fig. 1.2). Christiansen et al. [147] argue that, since the regular helix structure is given uniquely by three geometric parameters, one needs to consider three types of interactions, which stabilize this structure. They identify the first-nearest neighbor interactions in Eq. (6.27) with valence bonds and second-nearest neighbor interaction they consider to take effectively into account the three-body interaction fixing the valence angle. The ν^{th}-nearest neighboring interactions are referred to as hydrogen bonds. Christiansen et al. have treated both the harmonic approximation and (anharmonic) Morse potentials to model the terms $U_j(r_{jn})$, the latter ones to study the propagation of solitons in the helix. Since we aim to understand the thermodynamic trends as derived from the harmonic phonon dispersion relation, we focus on the harmonic approximation[1], i.e., we write:

$$U_j(r_{jn}) = \frac{1}{2} K_j (r_{jn} - a_j)^2, \tag{6.28}$$

where a_j denote the peptide-peptide equilibrium distances. We have estimated the quality of the potential proposed by Christiansen et al. in fitting the vibrational branches of π-, α- and 3_{10}-helix.

---

[1] However, the new insights we have derived for the harmonic approximation are transferable to the anharmonic potentials, i.e., may be directly used to study soliton propagation.

For this purpose we have optimized the spring constants K_j separately for each of the three helical conformations by minimizing the following error measure:

$$E^{\text{err}}(T) = \sum_{i=1}^{3} \int_0^{\pi} d\varphi \left(F^{\text{vib}}(\omega_i^{\text{DFT}}(\varphi), T) - F^{\text{vib}}(\omega_i^{\text{model}}(\varphi), T) \right)^2 . \tag{6.29}$$

Here $\omega_i^{\text{DFT}}(\varphi)$ and $\omega_i^{\text{model}}(\varphi)$ are the vibrational branches from the DFT calculations and the model calculations, respectively, and $F^{\text{vib}}(\omega_i^{\text{DFT}}(\varphi), T)$ and $F^{\text{vib}}(\omega_i^{\text{model}}(\varphi), T)$ denote the corresponding harmonic oscillator free energies. For $T = 0\ K$ the error measure of Eq. (6.29) is equivalent to a least square fitting regarding the individual vibrational frequencies. We have used the error measure $E^{\text{err}}(T = 300\text{K})$, which emphasizes the importance of the lower frequencies. However, the differences of the obtained spring constants for $E^{\text{err}}(T = 0K)$, i.e., the "conventional" least square fitting, and $E^{\text{err}}(T = 300K)$ are rather small.

Fig. 4.8 shows that the model gives a good fit for the 3_{10}-helix. However, for the α-helix and in particular for the π-helix the model of Christiansen et al. gives a poor description: The first vibrational branch of the π-helix predicted by the model spuriously contains an additional nodal point, the slopes/curvatures at the long wavelength limits are strongly underestimated and the third vibrational branch is strongly blue shifted. A closer analysis of the free energies further revealed that the thermodynamic differences between the helices could not be reproduced by the model, since it strongly underestimates the vibrational free energy of the π-helix.

To have a model that describes well the vibrational spectra of *all* five investigated structures of the peptide chain, we have modified the model proposed by Christiansen et al. by improving both, the description of the backbone interactions and the description of the hydrogen bonding.

The model we developed to fulfill this task is discussed in Sec. 4.4.1.

6.4.2 Wave equations arising from the thin rod approximation

By considering the thin rod approximation (Sec. 4.4.2), the mechanical waves of the helix may be described by three separated homogeneous wave-equations. As a result one obtains three different kinds of mechanical waves in thin rods: longitudinal waves, torsional waves and bending waves. We first consider the longitudinal and the torsional waves. For simplification we identify the rod axis with the z-axis. The wave-equations for the longitudinal deformations $u_L(z)$ and torsional deformations $u_\varphi(z)$ may then be written as:

$$\frac{\partial^2 u_L}{\partial z^2} - \frac{\rho}{Y}\ddot{u}_L = 0 \quad \text{and} \quad \frac{\partial^2 u_\varphi}{\partial z^2} - \frac{\rho}{T}\ddot{u}_\varphi = 0 \tag{6.30}$$

respectively. Here, Y and T are the Young's and the torsional modulus, respectively, and are defined as:

$$Y = \frac{\sigma_{zz}}{\epsilon_{zz}} \quad \text{and} \qquad T = \frac{\sigma_{\Theta\Theta}}{\epsilon_{\Theta\Theta}}. \tag{6.31}$$

In Eq. (6.31) σ_{zz} and $\sigma_{\Theta\Theta}$ denote the longitudinal and the torsional stress, respectively, and ϵ_{zz} and $\epsilon_{\Theta\Theta}$ denote the longitudinal and the torsional strain. These four quantities will be evaluated below. A solution to Eq. (6.30) is given by plane waves:

$$u_L(z,t) = u_{0L} \exp(i(kz - \omega_L t)) \quad \text{and} \quad u_\varphi(z,t) = u_{0\varphi} \exp(i(kz - \omega_\varphi t)). \tag{6.32}$$

Here $k = \frac{2\pi}{\lambda}$ is the reciprocal wavelength and ω is the frequency of the wave. Inserting Eq. (6.32) into Eq.(6.30) gives the linear dispersion relations:

$$\omega_L(k) = v_L k \quad \text{and} \quad \omega_T(k) = v_T k. \tag{6.33}$$

Here v_L and v_T are the longitudinal and the torsional velocities of sound and are given by

$$v_L = \sqrt{\frac{Y}{\rho}} \quad \text{and} \quad v_T = \sqrt{\frac{T}{\rho}}. \tag{6.34}$$

For the bending waves we obtain, in the thin rod approximation, two (instead of one) wave equations:

$$\frac{\partial^4 x}{\partial z^4} - \frac{\rho S}{Y I_x}\ddot{x} = 0 \quad \text{and} \quad \frac{\partial^4 y}{\partial z^4} - \frac{\rho S}{Y I_y}\ddot{y} = 0. \tag{6.35}$$

These two wave equations arise from the assumption that the bending of the rod is small compared to its length. Thus the bending can, in any point of the rod be expanded by a (microscopic) stretching [150]. The quantities I_x and I_y are defined through the cross-sectional area S of the rod by:

$$I_y = \int_S x^2 df \quad \text{and} \quad I_x = \int_S y^2 df. \tag{6.36}$$

Solving the wave equations for the bending waves, results in two *quadratic* dispersion relations:

$$\omega = \frac{1}{2} a_{B,x} k^2 \quad \text{and} \quad \omega = \frac{1}{2} a_{B,y} k^2, \tag{6.37}$$

here $a_{B,x}$ and $a_{B,y}$ are connected to the *bending velocities of sound* by:

$$v_{B,x} = k a_{B,x} \quad \text{and} \quad v_{B,y} = k a_{B,y} \tag{6.38}$$

with amplitudes along I_x and I_y, respectively, and are given by:

$$a_{B,x} = \sqrt{\frac{Y I_x}{\rho S}} \quad \text{and} \quad a_{B,y} = \sqrt{\frac{Y I_y}{\rho S}}. \tag{6.39}$$

We apply an additional approximation to address the quantities I_x and I_y

$$I_x \approx I_y \approx I \equiv \int_S r^2 df, \tag{6.40}$$

and, considering the hollow-cylinder shape of the mass distribution in the helices, we obtain one single dispersion law for the bending waves:

$$\omega = \frac{1}{2} a_B k^2, \quad \text{where} \quad a_B = R\sqrt{\frac{Y}{\rho}} = R v_L. \tag{6.41}$$

We remark that the density ρ, the cross-sectional area S, the Young's and the torsional modulus are *not* well defined quantities for the peptide chain. However, for calculating the sound velocities they cancel out, as we will see below.

6.4.3 Analytical expressions for the elastical moduli

To calculate the Young's modulus we cut a long piece of length ξ_0 out of the peptide chain and assume that a force ΔF is acting uniformly on the cross-sectional area A at the ends of that piece. Then we may write for the tensile stress and strain:

$$\sigma_{zz} \quad := \quad \lim_{A\to 0} \frac{\Delta F^{||}(A)}{A} = \frac{\Delta F^{||}}{A} \quad \text{and} \quad \epsilon_{zz} = \frac{\Delta \xi}{\xi_0}. \tag{6.42}$$

and, correspondingly, for the torsional stress and strain:

$$\sigma_{\Theta\Theta} := \lim_{A\to 0} \frac{\Delta F^{\perp}(A)}{A} = \frac{\Delta F^{\perp}}{A} \text{and} \quad \epsilon_{\Theta\Theta} = \frac{\Delta x^{\perp}}{\xi_0} = \frac{\Delta \Theta R}{\xi_0}, \tag{6.43}$$

where $\Delta\xi$ is the change in the length of the helix as a result on a force, $\Delta F^{||}$, which is acting on the area A and pointing along the helix-axis. $\Delta\Theta$ is the change in the angle as result on a rotational force, $\Delta F^{\perp}$, acting on the area A and pointing perpendicular to the helix axis. Using these expressions we may rewrite the Young's and the torsional modulus:

$$Y \quad = \quad \left(\frac{\Delta F \xi}{A \Delta \xi}\right)_{\xi=\xi_0} = \frac{\xi_0}{A}\left(\frac{dF}{d\xi}\right)_{\xi=\xi_0} = \frac{\xi_0}{A}\left(\frac{d^2U}{d\xi^2}\right)_{\xi=\xi_0}, \tag{6.44}$$

and

$$T = \left(\frac{\Delta F \xi}{A R \Delta \Theta}\right)_{\Theta=0} = \frac{\xi_0}{A R^2}\left(\frac{d^2U}{d\Theta^2}\right)_{\Theta=\Theta_0}. \tag{6.45}$$

Here, U denotes the potential energy of the peptide chain. To calculate the quantities $\left(\frac{d^2U}{d\xi^2}\right)$ and $\left(\frac{d^2U}{d\Theta^2}\right)$ we neglect, by following the thin rod approximation the coupling of the helical parameters L, R and Θ. Hence, we may write:

$$\left(\frac{d^2U}{d\xi^2}\right)_{\xi=\xi_0} \quad = \quad \left(\left(\frac{\partial L}{\partial \xi}\right)^2 \left(\frac{\partial^2 U}{\partial L^2}\right)\right)_{\xi=\xi_0} = \frac{1}{N^2}\left(\frac{\partial^2 U}{\partial L^2}\right) = \frac{1}{N}\left(\frac{\partial^2 U^{\mathrm{pp}}}{\partial L^2}\right), \tag{6.46}$$

and

$$\left(\frac{d^2U}{d\Theta^2}\right)_{\Theta=0} = \frac{1}{N}\left(\frac{\partial^2 U^{\mathrm{pp}}}{\partial\Theta^2}\right) \tag{6.47}$$

respectively, where U denotes the potential energy of the whole chain segment, N denotes the number of peptide units, and U^{pp} denotes the potential energy per peptide unit.

We now substitute the ball-and-spring model (Eq. (4.18)) into this formula and obtain for the Young's modulus and the torsional modulus:

$$Y = \frac{L_0}{AN}\left(\frac{\partial^2 U^{\mathrm{pp}}}{\partial L^2}\right) \quad = \quad \frac{L}{A}\left(\frac{\partial^2 U^{\mathrm{bb}}}{\partial L^2}\right) + \frac{L}{A}\left(\frac{\partial^2 U^{\mathrm{hb}}}{\partial L^2}\right) = Y^{\mathrm{bb}} + Y^{\mathrm{hb}}, \tag{6.48}$$

and

$$T = \frac{L}{AR^2}\left(\frac{\partial^2 U^{\mathrm{bb}}}{\partial\Theta^2}\right) + \frac{L}{AR^2}\left(\frac{\partial^2 U^{\mathrm{hb}}}{\partial\Theta^2}\right) = T^{\mathrm{bb}} + T^{\mathrm{hb}}, \tag{6.49}$$

where Y^{bb} and T^{bb} denote the contribution of the backbone to the Young's and torsional modulus, respectively, and Y^{hb} and T^{hb} denote the contributions of the hydrogen bonds. The explicit analytical expressions for the Young's moduli are:

$$Y^{\mathrm{hb}} = \frac{L}{A}\sum_{i}^{\nu,\nu-1}\left[K_{r_i}\left(i^2\frac{L}{D_i}\right)^2\right], \tag{6.50}$$

and

$$\begin{aligned}
Y^{\mathrm{bb}} \quad &= \quad \frac{L}{A}\left(K_{r_1}\left(\frac{\partial\Delta r_{0_1}}{\partial L}\right)^2 + K_\Psi\left(\frac{\partial\Psi}{\partial L}\right)^2 + K_\delta\left(\frac{\partial\Psi}{\partial\delta}\right)^2\right)\\
&= \quad \frac{L}{A}\left(K_{r_1}\left(\frac{L}{D_1}\right)^2 + K_\Psi\left(\frac{2}{\sqrt{1-A^2}}\left(\frac{R}{D_1}\sin\Theta - R(1-\cos\Theta)\frac{L}{D_1^3}\right)\right)^2\right.\\
&+ \quad K_\delta\left(\frac{2L\left(\cos(\Theta)+h^2\cos(\Theta)+\sin^2(\Theta)\right)}{R^2\sqrt{1-A^2}\left(h^2+\sin^2\Theta\right)^2}\right)^2 .
\end{aligned} \tag{6.51}$$

For the hydrogen bonding part of the torsional modulus we find:

$$T^{\mathrm{hb}} \quad = \quad \frac{L}{A}\sum_{i}^{\nu,\nu-1} K_{r_i}\left(\frac{Ri}{D_i}\sin(i\Theta)\right)^2 \tag{6.52}$$

and for the backbone part we find:

$$\begin{aligned}
T^{\mathrm{bb}} \quad &= \quad \frac{L}{AR^2}\left(K_{r_1}\left(\frac{\partial\Delta r_{0_1}}{\partial\Theta}\right)^2 + K_\Psi\left(\frac{\partial\Psi}{\partial\Theta}\right)^2 + K_\delta\left(\frac{\partial\delta}{\partial\Theta}\right)^2\right)\\
&= \quad \frac{L}{A}\Bigg(K_{r_1}\left(\frac{R}{D_1}\sin(\Theta)\right)^2 + \frac{1}{R^2}K_\Psi\left(\frac{2}{\sqrt{1-A^2}}(\frac{R}{D_1}\sin\Theta(1-\frac{R^2}{D_1^2}) + \frac{R^3}{D_1^3}\cos\Theta\sin\Theta)\right)^2
\end{aligned}$$

a)

	Θ	L	R	Ψ	δ	D_1	$D_{\nu-1}$	D_ν
FES	180.00	6.74	0.961	148.16	180	7.01	-	-
2_7	180.00	5.35	2.608	91.5	180	7.47	7.47	10.7
3_{10}	120.00	3.71	3.48	85.04	84.56	7.07	9.56	11.13
α	98.18	2.83	4.1	93.16	51.26	6.82	9.59	11.54
π	80.00	2.21	5.03	105.9	30.4	6.83	9.48	11.57

b)

	$\left(\frac{\nu L}{D_\nu}\right)^2$	$\left(\frac{(\nu-1)L}{D_{\nu-1}}\right)^2$	$\frac{2\nu-1}{\nu^2}$	$(D_{\nu-1})^2$	$(D_\nu)^2$	$(D_1)^2$	$\sin^2((\nu-1)\Theta)$ $+\sin^2(\nu\Theta)$
id	1	2	3	4	5	6	7
2_7	1.00	0.52	0.75	55.8	114.5	55.8	1
3_{10}	1.00	0.61	0.56	91.4	123.9	50.0	0.75
α	0.96	0.79	0.44	92.0	133.2	46.5	1.26
π	0.92	0.86	0.36	89.9	133.9	46.6	0.82
avg	0.96	0.75	0.45	91.1	130.0	47.7	0.94

Table 6.4: a) Geometrical parameters for poly-L-alanine: twist Θ, pitch L, radius R, valence angle Ψ, dihedral angle δ and equilibrium distances D_1, D_ν and $D_{\nu-1}$. b) Geometrical approximations as employed in the Eqs. (6.57 to 6.59).

$$+ \quad \frac{1}{R^2} K_\delta \left(\frac{h^2 \sin(\Theta) \left(h^2 - 2\cos\Theta + \sin^2\Theta + 2\cos^2\Theta\right)}{\sqrt{1-A^2}\left(h^2 + \sin^2\Theta\right)^2} \right)^2 \Bigg) . \tag{6.53}$$

6.4.4 Geometrical approximations

The expressions for the speeds of sound have been obtained by substituting the analytical expressions for the elastical moduli Eqs. (6.48-6.53) into the Eqs. (6.34) and (6.41), respectively. As discussed in Sec. 4.4.2, the longitudinal speed of sound is determined exclusively by the hydrogen bonds, whereas the contributions of the backbone may be neglected:

$$v_L = \sqrt{\frac{Y^{\mathrm{hb}} + Y^{\mathrm{bb}}}{\rho}} \approx \sqrt{\frac{Y^{\mathrm{hb}}}{\rho}}. \tag{6.54}$$

Here Y^{hb} is given in Eq. (6.50), and ρ is the density (which is not well defined for the helix, but cancels out for the calculation of the speed of sound). The torsional speed of sound is determined by both, hydrogen bonding and backbone contributions:

$$\begin{aligned} v_T &= \sqrt{\frac{T^{\mathrm{bb}} + T^{\mathrm{hb}}}{\rho}} \\ &= \sqrt{\left(v_T^{\mathrm{bb}}\right)^2 + \left(v_T^{\mathrm{hb}}\right)^2}, \end{aligned} \tag{6.55}$$

where

$$v_T^{\rm bb} = \sqrt{\frac{T^{\rm bb}}{\rho}} \quad \text{and} \quad v_T^{\rm hb} = \sqrt{\frac{T^{\rm hb}}{\rho}}. \tag{6.56}$$

Here $T^{\rm bb}$ and $T^{\rm hb}$ are given by the Eqs. (6.53) and (6.52), respectively.

The expressions for the sound velocities have been further simplified considering some geometric approximations. For applying these approximations we utilized the important fact that the hydrogen bonding geometries, i.e., distances to the $\nu^{\rm th}$ and $\nu^{\rm th}$-1 nearest neighbor are largely the same in the three helical conformations (Tab. 6.4a). Thus we replaced the parameters describing the individual hydrogen bonding geometries of the helices by quantities averaged over the three helical conformations (Tab. 6.4b). We first simplified the expression for the longitudinal speed of sound (Eq. (4.26)).

$$\begin{aligned} v_L &= L\sqrt{\sum_i^{\nu,\nu-1} M^{-1}K_{r_i}\left(\frac{(iL)^2}{D_i}\right)} \approx^{[1,2]} L\sqrt{M(0.75(\nu-1)^2K_{r_{\nu-1}} + 0.96\nu^2M^{-1}K_{r_\nu})} \\ &= L\nu\sqrt{M^{-1}\left(\left(0.75K_{r_{\nu-1}} + 0.98K_{r_\nu}\right) - \left(\frac{2\nu-1}{\nu^2}\right)0.75K_{r_{\nu-1}}\right)} \\ &\approx^{[3]} L\nu\sqrt{K^{\rm l,hb}/M} \end{aligned} \tag{6.57}$$

where $K^{\rm l,hb} = 0.34K_{r_{\nu-1}} + 0.98K_{r_\nu}$. The super-scripted labels in Eq. (6.57) denote the approximations applied in the respective step and are explained in (Tab. 6.4b).

We then simplified the expressions for the torsional speed of sound. For the hydrogen bonding contributions we obtain:

$$\begin{aligned} v_T^{\rm hb} &= L \sqrt{\sum_i^{\nu,\nu-1} M^{-1}K_{r_i}\left(\frac{Ri}{D_i}\sin(i\Theta)\right)^2} \\ &= LR\nu\sqrt{M^{-1}\left(K_{r_{\nu-1}}\left(\frac{1-\frac{1}{\nu}}{D_{\nu-1}}\sin((\nu-1)\Theta)\right)^2 + K_{r_\nu}\left(\frac{1}{D_\nu}\sin(\nu\Theta)\right)^2\right)} \\ &\approx^{[3,4,5]} LR\nu\sqrt{M^{-1}0.006K_{r_{\nu-1}}\sin^2((\nu-1)\Theta) + 0.0077K_{r_\nu}\sin(\nu\Theta)^2} \\ &\approx LR\nu\sqrt{M^{-1}\frac{1}{2}(0.006K_{r_{\nu-1}} + 0.0077K_{r_\nu})(\sin^2((\nu-1)\Theta) + \sin^2(\nu\Theta)} \\ &\approx^{[6]} LR\nu\sqrt{M^{-1}\frac{1}{2}(0.006K_{r_{\nu-1}} + 0.0077K_{r_\nu})0.96} \\ &= LR\nu\sqrt{K^{\rm t,hb}/M} \end{aligned} \tag{6.58}$$

where $K^{\rm t,hb} = 0.0029K_{r_{\nu-1}} + 0.0037K_{r_\nu}$.

For the backbone contributions we found that we may neglect the contributions of the valence angle stiffness and those of the dihedral angle stiffness and hence may write:

$$\begin{aligned} v_T^{\mathrm{bb}} &\approx L\sqrt{\left(M^{-1}K_{r_1}\left(\frac{R}{D_1}\sin(\Theta)\right)^2\right.} \\ &\approx LR\ \sqrt{K^{\mathrm{t,bb}}/M}, \end{aligned} \tag{6.59}$$

where $K^{\mathrm{t,bb}} = 0.021K_{r_1}$.

6.5 Morse oscillator model

Here we estimate the anharmonic corrections for the lowest lying C-H stretching branch of the poly-L-alanine α-helix (with id=26, Figs. 4.1 and 6.8, Tab. 4.2). The eigenmodes corresponding to this branch are comparatively well localized exclusively in the corresponding C-H bonds of the peptide chain and are free of any vibrational dispersion. Thus we may describe these vibrations with a single degree of freedom, i.e., the bonding distance between the hydrogen atom and the carbon atom. For this particularly simple type of vibration we may employ a very simple and in the same way realistic model potential, the so called Morse potential:

$$V(r) = D_0(1 - \exp(-\alpha(r - r_0)))^2. \tag{6.60}$$

Here D_0 (dissociation energy) is the depth of the potential, r_0 is the equilibrium distance and α determines the steepness of the potential. The latter is related to the curvature at the equilibrium by:

$$k = 2D_0\alpha^2. \tag{6.61}$$

The Morse potential can be solved approximately [165]. The approximated eigenvalues are:

$$E(n) = -D + h\omega_0(n + \frac{1}{2}) - \frac{h^2\omega_0^2}{4D}(n + \frac{1}{2})^2. \tag{6.62}$$

Ref. [166] points out that the deviations to the exact solution are negligible.

The Morse potential has been found to give a perfect fit for the C-H bond. We found as anharmonic correction[2]:

$$\begin{aligned} \Delta\omega^{\mathrm{ah}} &= \omega^{\mathrm{harm}} - (E(1) - E(0)) \\ &= -115\,\mathrm{cm}^{-1}. \end{aligned} \tag{6.63}$$

6.6 Dynamical matrix

In this section technical aspects of the phonon calculations are presented and the employed supercells and equilibrium structures are tabulated. Furthermore, the employed scheme for the sum rules to

---

[2] We focus on the difference between the harmonic frequency and the transition energy from the ground state to the first excited state of the Morse oscillator, since these are the predominant transitions at room temperature.

L-alanine	a_{lat}	c_{lat}	N^{PPS}	N^{TPS}	Θ(used)	Θ(ideal)	L
FES	40.44	20	6	3	180.00	181.2	6.74
2_7	32.10	22	6	3	180.00	171.2	5.35
3_{10}	33.39	22	9	3	120.00	115.3	3.71
α	31.13	23	11	3	98.18	97.6	2.83
π	33.15	24	18	4	80.00	81.4	2.21

glycine	a_{lat}	c_{lat}	N^{PPS}	N^{TPS}	Θ(used)	Θ(ideal)	L
FES	40.86	20	6	3	180.00	180.0	6.81
2_7	32.40	22	6	3	180.00	164.9	5.38
3_{10}	32.94	23	9	3	120.00	116.2	3.66
α	40.95	23	15	4	96.0	94.8	2.73
π	28.34	24	13	3	83.1	83.9	2.18

Table 6.5: Relevant geometrical data for the modeling of the different conformations in the orthorhombic supercell. Shown are the supercell dimensions along the helix axis, a_{lat}, and orthogonal to it, c_{lat}, the number of peptides and the number of turns in the supercell, $N^{\text{PPS}}$and N^{TPS}, respectively. These values have been used to perform all phonon calculations for this work. Further, the used twist angles and pitches in comparison to the ideal twist angles and pitches, which correspond to the interpolated minimum of the (Θ, L)-PES (Fig. 1.5) are shown.

treat the long-wavelength limits of the acoustical branches is explained.

6.6.1 Modeling the helices in orthorhombic supercells

Here it will be described how the helical conformations of the peptide chain can be modeled in an orthorhombic supercell. According to Eq. (2.1) the structure of the peptide chain is defined by the helix pitch L and the helix twist Θ. The helix pitch can be straightforwardly modeled to arbitrary values within the supercell by tuning the corresponding cell extension z_{lat}, since this parameter is related to the helix pitch by:

$$\Delta z = \frac{z_{\text{lat}}}{N^{\text{PPS}}}, \tag{6.64}$$

where N^{PPS} denotes the number of peptide units contained in the supercell. The helix twist is more problematic in this sense: In contrast to the helix pitch it cannot be sampled continuously when employing the supercell approach. The helix twist is related to the number of full turns N^{TPS} of the peptide chains contained in the supercell by the relation:

$$\frac{\Theta}{360^o} = \frac{N^{\text{TPS}}}{N^{\text{PPS}}}. \tag{6.65}$$

Since N^{TPS} and N^{PPS} are integers, an arbitrarily precise sampling of the helix twist would require to put an arbitrarily high number of peptides and turns into the supercell, which is impracticable for reasons of the computational effort. The twist angle is therefore sampled at values commensurable to the smaller possible values for N^{PPS} and N^{TPS} and small deviations to the "real" twist angles, as obtained from the interpolation of the PES (Fig. 1.5) have to be accepted. A table of the used and the real pitch and twist values is given in Tab. 6.5.

6.6.2 Notation for the dynamical matrix

To explain the calculation of the dynamical matrix in Sec. 3.4.1 three different notations have been used, which will be briefly explained here.

The notation:

$$\mathbf{D}^{\mathrm{c}}(n) \tag{6.66}$$

denotes the dynamical matrix corresponding to the interaction of a representative peptide unit with its n'th nearest neighbor. $\mathbf{D}^{\mathrm{c}}(n)$ is a $(3N^{\mathrm{APP}} \times 3N^{\mathrm{APP}})$-dimensional matrix.

The notation:

$$\mathbf{D}^{\mathrm{c}}(\varphi) \tag{6.67}$$

denotes the symmetry reduced dynamical matrix corresponding to the vibrational phase difference φ between adjacent peptide units. $\mathbf{D}^{\mathrm{c}}(\varphi)$ is a $(3N^{\mathrm{APP}} \times 3N^{\mathrm{APP}})$-dimensional matrix and is related to $\mathbf{D}^{\mathrm{c}}(n)$ by Eq. (3.34).

The notation:

$$\mathbf{D}^{\mathrm{cell}}$$

denotes the dynamical matrix corresponding to the supercell. $\mathbf{D}^{\mathrm{cell}}$ is a $(3N^{\mathrm{APS}} \times 3N^{\mathrm{APS}})$-dimensional matrix, where N^{APS} is the number of atoms in the supercell. It can be constructed by a block-wise arrangement of the matrices $\mathbf{D}^{\mathrm{c}}(n)$, as described with Eq. (2.88).

The dynamical matrices can be converted to the *Hessian matrices*:

$$\mathbf{K}^{\mathrm{c}}(\varphi) = \sqrt{M_i M_j}\mathbf{D}^{\mathrm{c}}(\varphi);\ \mathbf{K}^{\mathrm{c}}(n) = \sqrt{M_i M_j}\mathbf{D}^{\mathrm{c}}(n);\ \mathbf{K}^{\mathrm{cell}} = \sqrt{M_i M_j}\mathbf{D}^{\mathrm{cell}}. \tag{6.68}$$

6.6.3 Sum rules

As mentioned in Sec. 3.4.4 a problem appeared for the calculation of the acoustical branches at the long-wavelength limits $\varphi \to 0$ and $\varphi \to \pm\Theta$. These branches were not found to be exactly zero at the long-wavelength limits (as they should be, according to Sec. 2.6.4)

To solve this problem with the long-wavelength limit the sum rules according to the three translational degrees of freedom and the rotational degree of freedom of the peptide chain (Eqs. (2.101) and (2.104)) are applied to the dynamical matrix (notation is explained in Sec. 6.6.2):

$$\mathbf{D}^{\mathrm{cell}'} = \mathbf{J}^{\dagger}\mathbf{J}\mathbf{D}^{\mathrm{cell}}. \tag{6.69}$$

Here $\mathbf{J}$ is a $(3 \cdot \mathrm{N}^{\mathrm{APS}} \times 3 \cdot \mathrm{N}^{\mathrm{APS}} - 4)$-dimensional matrix, which projects the dynamical matrix $\mathbf{D}^{\mathrm{cell}}$ on a set of internal coordinates. It is constructed in the following way: at first three $(3 \cdot \mathrm{N}^{\mathrm{APS}})$-dimensional vectors corresponding to the translation of the helix are constructed

$$\begin{aligned}
\mathbf{D}_1 &= (1/\sqrt{M_1}, 0, 0, 1/\sqrt{M_2}, ..., 1/\sqrt{M_{\mathrm{NAPS}}}, 0, 0), & (6.70)\\
\mathbf{D}_2 &= (0, 1/\sqrt{M_1}, 0, 0, 1/\sqrt{M_2}, ..., 0, 1/\sqrt{M_{\mathrm{NAPS}}}, 0), & (6.71)\\
\mathbf{D}_3 &= (0, 0, 1/\sqrt{M_1}, 0, 0, 1/\sqrt{M_2}, ..., 0, 0, 1/\sqrt{M_{\mathrm{NAPS}}}) & (6.72)
\end{aligned}$$

and one vector corresponding to the rotation of the helix around its axis:

$$\mathbf{D}_4 = (y_1/\sqrt{M_1}, -x_1/\sqrt{M_1}, 0, ..., y_{N^{\mathrm{APS}}}/\sqrt{M_{N^{\mathrm{APS}}}}, -x_{N^{\mathrm{APS}}}/\sqrt{M_{N^{\mathrm{APS}}}}, 0). \qquad (6.73)$$

These four vectors correspond to the *external* degrees of freedom, i.e., the translation of the geometry along these vectors does not displace the *internal* structure of the peptide chain. The $(3 * \mathrm{N}^{\mathrm{APS}} - 4)$ columns of the **J**-matrix are now constructed as an orthonormal basis of the subspace, which remains, when the subspace corresponding to the four external degrees of freedom is subtracted from the basis corresponding to the $(3 * \mathrm{N}^{\mathrm{APS}})$-dimensional configurational space by means of a Grahm-Schmidt orthonormalisation.

6.6.4 Transformation rules

Here the transformation formulas of the Hessian matrix between the Cartesian and the cylindrical coordinate basis are derived. The following notation is used: The atomic positions in Cartesian coordinates are written as

$$X_{I,a},$$

where I is the atomic index and a can be either x, y or z. The corresponding components of the gradient $\mathbf{g} := \frac{\partial}{\partial \mathbf{X}} E^{\mathrm{el}}$ are written as

$$g_{I,a} = \frac{\partial E^{\mathrm{el}}}{\partial X_{I,a}}, \qquad (6.74)$$

and the Hessian matrix:

$$\mathbf{K} = (\frac{\partial}{\partial \mathbf{X}})^t \mathbf{g} \qquad (6.75)$$

is written as

$$K_{ij,ab} = \frac{\partial}{\partial x_{I,a}} g_{J,b} = \frac{\partial^2 E^{\mathrm{el}}}{\partial x_{I,a} \partial y_{J,b}} = \frac{\partial}{\partial y_{J,b}} g_{I,a} = K_{ij,ba}. \qquad (6.76)$$

The notation to expand the respective quantities in cylindrical coordinates is in an analogous way. To differentiate the Cartesian from the cylindrical expansion, the quantities in cylindrical Coordinates is marked with a superscripted c.

Transformation from Cartesian to cylindrical coordinates

Provided the Hessian is known in Cartesian coordinates, the Hessian entries $K^{\mathrm{c}}_{IJ,ab}$ corresponding to the cylindrical coordinates ϕ and r may be calculated by:

$$
\begin{aligned}
K^{\mathrm{c}}_{IJ,ab} &= \frac{\partial^2 E^{\mathrm{el}}}{\partial X^{\mathrm{c}}_{I,a} \partial X^{\mathrm{c}}_{J,b}} \\
&= \frac{\partial}{\partial X^{\mathrm{c}}_{I,a}} \left(\frac{\partial}{\partial X^{\mathrm{c}}_{j,b}} E^{\mathrm{el}} \right) \\
&= \frac{\partial}{\partial X^{\mathrm{c}}_{I,a}} \left(\frac{\partial X_{J,x}}{\partial X^{\mathrm{c}}_{J,b}} \frac{\partial E^{\mathrm{el}}}{\partial X_{J,x}} + \frac{\partial X_{J,y}}{\partial X^{\mathrm{c}}_{J,b}} \frac{\partial E^{\mathrm{el}}}{\partial X_{J,y}} \right) \\
&= \frac{\partial^2 X_{J,x}}{\partial X^{\mathrm{c}}_{I,a} \partial X^{\mathrm{c}}_{J,b}} g_{J,x} + \frac{\partial^2 X_{J,y}}{\partial X^{\mathrm{c}}_{I,a} \partial X^{\mathrm{c}}_{j,b}} g_{J,y} \\
&+ \frac{\partial X_{j,x}}{\partial X^{\mathrm{c}}_{j.b}} \left(\frac{\partial X_{I,x}}{\partial X^{\mathrm{c}}_{j,a}} \frac{\partial^2 E^{\mathrm{el}}}{\partial X_{I,x} \partial X_{j,x}} + \frac{\partial X_{I,y}}{\partial X^{\mathrm{c}}_{I,a}} \frac{\partial^2 E^{\mathrm{el}}}{\partial X_{I,y} \partial X_{J,x}} \right) \\
&+ \frac{\partial X_{J,y}}{\partial X^{\mathrm{c}}_{J,b}} \left(\frac{\partial X_{I,x}}{\partial X^{\mathrm{c}}_{I,a}} \frac{\partial^2 E^{\mathrm{el}}}{\partial X_{I,x} \partial Y_{j,y}} + \frac{\partial X_{I,y}}{\partial X^{\mathrm{c}}_{I,a}} \frac{\partial^2 E^{\mathrm{el}}}{\partial X_{I,y} \partial X_{J,y}} \right) \\
&= \delta_{IJ} \left(\frac{\partial^2 X_{J,x}}{\partial X^{\mathrm{c}}_{I,a} \partial X^{\mathrm{c}}_{J,b}} g_{J,x} + \frac{\partial^2 X_{J,y}}{\partial X^{\mathrm{c}}_{I,a} \partial X^{\mathrm{c}}_{j,b}} g_{J,y} \right) \\
&+ T_{J,xb} T_{I,xa} K_{IJ,xx} + T_{J,xb} T_{I,ya} K_{IJ,yx} \\
&+ T_{J,yb} T_{I,xa} K_{IJ,xy} + T_{J,yb} T_{I,ya} K_{IJ,yy},
\end{aligned}
\tag{6.77}
$$

where each a and b can be either ϕ or r and:

$$
T_{I,xa} := \frac{\partial X_{I,x}(\phi_J, r_J)}{\partial X^{\mathrm{c}}_{I,a}}, \text{ and } T_{I,ya} := \frac{\partial X_{I,y}(\phi_J, r_J)}{\partial X^{\mathrm{c}}_{I,a}}
\tag{6.78}
$$

and coordinate transformations are:

$$
X_{I,x}(\phi_I, r_I) = \cos(X^{\mathrm{c}}_{I,\phi}) X^{\mathrm{c}}_{I,r} \text{ and } X_{I,y}(\phi_I, r_I) = \sin(X^{\mathrm{c}}_{I,\phi}) X^{\mathrm{c}}_{I,r}.
\tag{6.79}
$$

Hence for a vanishing gradient $g = 0$ the explicit transformation formulas are:

$$
\begin{aligned}
K^{\mathrm{c}}_{IJ,\phi\phi} &= T_{J,x\phi} T_{I,x\phi} K_{IJ,xx} + T_{J,x\phi} T_{I,y\phi} K_{IJ,yx} + T_{J,y\phi} T_{I,x\phi} K_{IJ,xy} + T_{J,y\phi} T_{I,y\phi} K_{IJ,yy} \\
&= r_I r_J (\sin(\phi_J) \sin(\phi_I) K_{IJ,xx} - \sin(\phi_J) \cos(\phi_I) K_{IJ,yx} - \\
&- \cos(\phi_J) \sin(\phi_I) K_{IJ,xy} + \cos(\phi_I) \cos(\phi_J) K_{IJ,yy})
\end{aligned}
\tag{6.80}
$$

$$
\begin{aligned}
K^{\mathrm{c}}_{IJ,rr} &= T_{J,xr} T_{I,xr} K_{IJ,xx} + T_{J,xr} T_{I,yr} K_{IJ,yx} + T_{J,yr} T_{I,xr} K_{IJ,xy} + T_{J,yr} T_{I,yr} K_{IJ,yy} \\
&= \cos(\phi_J) \cos(\phi_I) K_{IJ,xx} + \cos(\phi_J) \sin(\phi_I) K_{IJ,yx} + \\
&+ \sin(\phi_J) \cos(\phi_I) K_{IJ,xy} + \sin(\phi_J) \sin(\phi_I) K_{IJ,yy}
\end{aligned}
\tag{6.81}
$$

$$
\begin{aligned}
K^{\mathrm{c}}_{IJ,\phi r} &= T_{J,xr} T_{I,x\phi} K_{IJ,xx} + T_{J,xr} T_{I,y\phi} K_{IJ,yx} + T_{J,yr} T_{I,x\phi} K_{IJ,xy} + T_{J,yr} T_{I,y\phi} K_{IJ,yy} \\
&= -r_I (\cos(\phi_J) \sin(\phi_I) K_{IJ,xx} - \cos(\phi_J) \cos(\phi_I) K_{IJ,yx} +
\end{aligned}
$$

$$+ \quad \sin(\phi_J)\sin(\phi_I)K_{IJ,xy} - \sin(\phi_J)\cos(\phi_I)K_{IJ,yy}) \tag{6.82}$$

$$\begin{aligned} K^{\mathrm{c}}_{IJ,r\phi} &= T_{J,x\phi}T_{I,xr}K_{IJ,xx} + T_{J,x\phi}T_{I,yr}K_{IJ,yx} + T_{J,y\phi}T_{I,xr}K_{IJ,xy} + T_{J,y\phi}T_{I,yr}K_{IJ,yy} \\ &= -r_J(\cos(\phi_I)\sin(\phi_J)K_{IJ,xx} - \cos(\phi_I)\cos(\phi_J)K_{IJ,yx} + \\ &+ \sin(\phi_I)\sin(\phi_I)K_{IJ,xy} - \sin(\phi_I)\cos(\phi_J)K_{IJ,yy}). \end{aligned} \tag{6.83}$$

For the entries of the Hessian in cylindrical coordinates which correspond to terms related to the z-coordinates the transformation rules are:

$$K^{\mathrm{c},\alpha z}_{ij} = T_i^{x\alpha}K_{ij}^{xz} + T_i^{y\alpha}K_{ij}^{yz} \quad \text{and} \quad K_{ij}^{z\alpha} = T_j^{x\alpha}K_{ij}^{zx} + T_j^{ya}K_{ij}^{zy} \tag{6.84}$$

respectively. The explicitly calculated transformation rules are then:

$$\begin{aligned} K^{\mathrm{c}}_{IJ,\phi z} &= T_{I,x\phi}K_{IJ,xz} + T_{I,y\phi}K_{IJ,yz} \\ &= -r_I(\sin(\phi_I)K_{IJ,xz} - \cos(\phi_I)K_{IJ,yz}), \end{aligned} \tag{6.85}$$

$$\begin{aligned} K^{\mathrm{c}}_{IJ,rz} &= T_{I,xr}K_{IJ,xz} + T_{I,yr}K_{IJ,yz} \\ &= \cos(\phi_I)K_{IJ,xz} + \sin(\phi_I)K_{IJ,yz}, \end{aligned} \tag{6.86}$$

$$\begin{aligned} K^{\mathrm{c},z\phi}_{IJ} &= T_{J,x\phi}K_{IJ,zx} + T_{J,y\phi}K_{IJ,zy} \\ &= -r_J(\sin(\phi_J)K_{IJ,zx} - \cos(\phi_J)K_{IJ,zy}) \text{ and} \end{aligned} \tag{6.87}$$

$$\begin{aligned} K^{\mathrm{c}}_{IJ,zr} &= T_{J,xr}K_{IJ,zx} + T_{J,yr}K_{IJ,zy} \\ &= \cos(\phi_J)K_{IJ,zx} + \sin(\phi_J)K_{IJ,zy}. \end{aligned} \tag{6.88}$$

Transformation from cylindrical to Cartesian coordinates

The rules for the transformation from cylindrical to Cartesian coordinates have been obtained in an analogous way:

$$\begin{aligned} K_{IJ,xx} &= T_{J,\phi x}T_{I,\phi x}K^{\mathrm{c}}_{J,\phi\phi} + T_{J,\phi x}T_{I,rx}K^{\mathrm{c}}_{IJ,r\phi} + \\ &+ T_{J,rx}T_{I,\phi x}K^{\mathrm{c}}_{IJ,\phi r} + T_{J,rx}T_{I,rx}K^{\mathrm{c}}_{IJ,rr} \end{aligned} \tag{6.89}$$

$$\begin{aligned} K_{IJ,yy} &= T_{J,\phi y}T_{I,\phi y}K^{\mathrm{c}}_{IJ,\phi\phi} + T_{J,\phi y}T_{I,ry}K^{\mathrm{c}}_{IJ,r\phi} + \\ &+ T_{J,ry}T_{I,\phi y}K^{\mathrm{c}}_{IJ,\phi r} + T_{J,ry}T_{I,ry}K^{\mathrm{c}}_{IJ,rr} \end{aligned} \tag{6.90}$$

$$\begin{aligned} K_{IJ,xy} &= T_{J,\phi y}T_{I,\phi x}K^{\mathrm{c}}_{IJ,\phi\phi} + T_{J,\phi y}T_{I,rx}K^{;\mathrm{c}}_{IJ,r\phi} + \\ &+ T_{J,ry}T_{I,\phi x}K^{\mathrm{c}}_{IJ,\phi r} + T_{J,ry}T_{I,rx}K^{\mathrm{c}}_{IJ,rr} \end{aligned} \tag{6.91}$$

$$\begin{aligned} K_{IJ,yx} &= T_{J,\phi x}T_{I,\phi y}K^{\mathrm{c}}_{IJ,\phi\phi} + T_{J,\phi x}T_{I,ry}K^{\mathrm{c}}_{IJ,r\phi} + \\ &+ T_{J,rx}T_{I,\phi y}K^{\mathrm{c}}_{IJ,\phi r} + T_{J,rx}T_{I,ry}K^{\mathrm{c}}_{IJ,rr}, \end{aligned} \tag{6.92}$$

and:

$$K_{IJ,xz} = T_{I,\phi x} K^{\mathrm{c}}_{IJ,\phi z} + T_{I,rx} K^{\mathrm{c}}_{IJ,rz} \tag{6.93}$$

$$K_{IJ,yz} = T_{I,\phi y} K^{\mathrm{c},}_{IJ,\phi z} + T_{I,ry} K^{\mathrm{c}}_{IJ,rz} \tag{6.94}$$

$$K_{IJ,zx} = T_{J,\phi x} K^{\mathrm{c}}_{IJ,z\phi} + T_{J,rx} K^{\mathrm{c}}_{IJ,zr} \tag{6.95}$$

$$K_{IJ,zr} = T_{J,\phi y} K^{\mathrm{c}}_{IJ,z\phi} + T_{J,ry} K^{\mathrm{c}}_{IJ,zr}, \tag{6.96}$$

with:

$$T_{I,rx} = \frac{X_{I,x}}{\sqrt{X_{I,x}^2 + X_{I,y}^2}} \tag{6.97}$$

$$T_{I,ry} = \frac{X_{I,y}}{\sqrt{X_{I,x}^2 + X_{I,y}^2}} \tag{6.98}$$

$$T_{I,\phi x} = -\frac{X_{I,y}}{X_{I,x}^2} \left(\frac{1}{1 + \frac{X_{I,y}^2}{X_{I,x}^2}} \right) \tag{6.99}$$

$$T_{I,\phi y} = \frac{1}{X_{I,x}} \left(\frac{1}{1 + \frac{X_{I,y}^2}{X_{I,x}^2}} \right). \tag{6.100}$$

Bibliography

[1] C. Levinthal, *Mößbauer Spectroscopy in Biological Systems* (Univ. of Illinois Press, Urbana, 1969).

[2] C. Anfinsen, Science **181**, 223 (1973).

[3] P. Leopold, M. Montal, and J. Onuchic, Proc. Natl. Acad. Sci. USA **89**, 8721 (1992).

[4] S. Govindarajan and R. Goldstein, Proc. Natl. Acad. Sci. USA **95**, 5545 (1998).

[5] R. Ellis and S. ivan der Vies, Annu. Rev. Biochem **60**, 321 (1991).

[6] D. Selkoe, Nature **426**, 900 (2003).

[7] D. Barlow and J. Thornton, J. Mol. Biol. **201**, 601 (1988).

[8] T. Weaver, Prot. Sci. **9**, 201 (2000).

[9] J.-P. Cartailler and H. Luecke, Structure **12**, 133 (2004).

[10] A. Mikhonin and S. Asher, J. Am. Chem. Soc. **128**, 13789 (2006).

[11] A. Mikhonin, S. Asher, S. Bykov, and A. Murza, J. Phys. Chem. B **111**, 3280 (2007).

[12] L. Pauling, R. Corey, and H. Branson, Proc. Natl. Acad. Sci. USA **37**, 205 (1951).

[13] M. Huggins, Chem. Rev. **32**, 195 (1943).

[14] B. Low and H. Grenville-Wells, Proc. Natl. Acad. Sci. USA **39**, 785 (1953).

[15] S. Marqusee, V. Robbins, and R. Baldwin, Proc. Natl. Acad. Sci. USA **86**, 5286 (1989).

[16] R. Hudgins, M. Ratner, and M. Jarrold, J. Am. Chem. Soc. **120**, 12974 (1998).

[17] J. Villa, D. Ripoll, and H. Scheraga, Proc. Natl. Acad. Sci. USA **97**, 13075 (2000).

[18] M. Kohtani, T. Jones, J. Schneider, and M. Jarrold, J. Am. Chem. Soc. **126**, 7420 (2004).

[19] K. O'Neil and W. DeGrado, Science **250**, 646 (1990).

[20] B. Low and R. Baybutt, J. Am. Chem. Soc. **74**, 5806 (1952).

[21] G. Ramachandran and V. Sasisekharan, Adv. Prot. Chem. **23**, 283 (1968).

[22] C. Rohl and A. Doig, Prot. Sci. **5**, 1687 (1996).

[23] S. Padmanabhan, S. Marqusee, T. Ridgeway, T. Laue, and R. Baldwin, Nature **344**, 268 (1990).

[24] A. Horovitz, J. Mattews, and A. Fersh, J. Mol. Biol. **270**, 560 (1992).

[25] S. Park, W. Shalongo, and E. Stellwagen, Biochemistry **32**, 7048 (1993).

[26] V. Munoz and L. Serano, J. Mol. Biol. **245**, 275 (1995).

[27] C. N. Pace and J. Scholtz, Biophys. J. **75**, 422 (1998).

[28] J. D'Aquino, J. Gomez, V. Hilser, K. Lee, L. Amzel, and E. Freire, Proteins: Struct. Funct. Genet. **25**, 143 (1996).

[29] G. Nemethy, S. Leach, and H. Scheraga, J. Phys. Chem. **70**, 998 (1966).

[30] D. Pal and P. Chakrabati, Proteins: Struct. Functi. Genet. **36**, 332 (1999).

[31] M. Zaman, M. Shen, R. Berry, K. Freed, and T. Sosnick, J. Mol. Biol. **331**, 693 (2003).

[32] K. Scott, D. Alonso, S. Sato, A. Fersht, and V. Dagett, Proc. Natl. Acad. Sci. USA **104**, 2661 (2007).

[33] M. Blaber, X.-J. Zhang, and B. Mathews, Science **260**, 1637 (1993).

[34] A.-S. Yang and B. Honig, J. Mol. Biol. **252**, 351 (1995).

[35] F. DiCapua, S. Swaminathan, and D. Beveridge, J. Am. Chem. Soc. **113**, 6154 (1991).

[36] R. Hudgins and M. Jarrold, J. Phys. Chem. B **104**, 2154 (2000).

[37] L. Pauling, *The Nature of the Chemical Bond, 3rd. ed.* (Cornell University Press: Ithaca, New York, 1960).

[38] T. Creighton, *Proteins* (W.H. Freeman and Company, New York, 1993).

[39] C. Reid, J. Chem. Phys. **30**, 182 (1959).

[40] S. Grabowski, W. Sokalski, and J. Leszczynski, J. Phys. Chem. A **110**, 4772 (2006).

[41] P. Hohenberg and W. Kohn, Phys. Rev. **136**, B864 (1964).

[42] W. Kohn and L. Sham, Phys. Rev. **140**, A1133 (1965).

[43] L. Ismer, *Protonentransport in Wasserstoffbrückenbindungen* (Diploma Thesis, Technische Universität Berlin, 2002).

[44] J. Ireta, J. Neugebauer, and M. Scheffler, J. Chem. Phys. A **108**, 5692 (2004).

[45] R. Improta, V. Barone, K. Kudin, and G. Scuseria, J. Am. Chem. Soc. **61**, 3311 (2001).

[46] Y.-D. Wu and Y.-L. Zhao, J. Am. Chem. Soc. **123**, 5313 (2001).

[47] R. Wieczorek and J. Danneberg, J. Am. Chem. Soc. **125**, 14065 (2003).

[48] J. Ireta, J. Neugebauer, M. Scheffler, A. Rojo, and M. Galvan, J. Chem. Phys. B **107**, 1432 (2003).

[49] R. Kaschner and D. Hohl, J. Phys. Chem. A **102**, 5111 (1998).

[50] J. Ireta, J. Neugebauer, M. Scheffler, A. Rojo, and M. Galvan, J. Am. Chem. Soc. **127**, 17241 (2005).

[51] J. Ireta, *private communication*.

[52] A. Mackerell, J. Comp. Chem. **25**, 1584 (2004).

[53] M. Feig, A. MacKerell, and C. Brooks, J. Phys. Chem. B **107**, 2831 (2003).

[54] B. Fanconi, W. Small, and W. Peticolas, Biopolymers **10**, 1277 (1971).

[55] V. Datye and S.Krimm, J. Chem. Phys. **84**, 12 (1986).

[56] S. Lee and S. Krimm, Biopolymers **46**, 283 (1998).

[57] S. Franzen, J. Phys. Chem. A **107**, 9898 (2003).

[58] G. Papamokos and I. Demetropoulos, J. Phys. Chem. A **108**, 7291 (2004).

[59] R. Wieczorek and J. Danneberg, J. Am. Chem. Soc. **127**, 14524 (2005).

[60] U. Scherz, *Quantenmechanik* (Teubner Studienbücher, Stuttgart;Leipzig, 1996).

[61] P. Ayala and G. Scuseria, J. Chem. Phys. **110**, 3660 (1999).

[62] M. Schuetz, J. Chem. Phys. **116**, 8772 (2002).

[63] D. Ceperley and B. Alder, Phys. Rev. Lett. **45**, 566 (1980).

[64] J. Neugebauer, *private communication*.

[65] J. Perdew, K. Burke, and M. Ernzerhoff, Phys. Rev. Lett. **77**, 3865 (1996).

[66] R. Dreizler and E. Gross, *Density Functional Theory* (Springer, 1990).

[67] W. Kohn, Rev. Mod. Phys. **1253**, 71 (1999).

[68] P. Rinke, A. Qteish, J. Neugebauer, C. Freysoldt, and M. Scheffler, N. J. Phys. **7**, 126 (2005).

[69] J. Perdew and A. Zunger, Phys. Rev. B **23**, 5048 (1981).

[70] K. Laasonen, F.Csajka, and M. Parinello, Chem. Phys. Lett. **194**, 172 (1992).

[71] K. Laasonen, M. Parinello, R. Car, C. Lee, and D. Vanderbilt, Chem. Phys. Lett. **207**, 208 (1993).

[72] S. Kurth, J. Perdew, and P. Blaha, Int. J. Quant. Chem. **75**, 889 (1999).

[73] A. Becke, Phys. Rev. A **38**, 3098 (1988).

[74] C. Lee, W. Yang, and R. Parr, Phys. Rev. B **37**, 785 (1988).

[75] R. Adamson, P. Gill, and J. Pople, Chem. Phys. Lett **284**, 6 (1998).

[76] C. Lin, M. George, and P. Gill, Aust. J. Chem. **365**, 57 (2004).

[77] T. V. Voorhis and G. Scuseria, J. Chem. Phys. **109**, 400 (1998).

[78] P. Ziesche and H. E. (Editors), *Electronic Structure of Solids '91* (Akademie Verlag Berlin, 1991).

[79] J. Perdew, J. Chevary, S. Vosko, K. Jackson, M. Pederson, D. Singh, and C. Fiolhais, Phys. Rev. B **46**, 6671 (1992).

[80] J. Perdew, S. Kurth, A. Zupan, and P. Blaha, Phys. Rev. Lett. **82**, 2544 (1999).

[81] J. Krieger, J. Chen, G. Iafrate, and A. Savin, *Electron Correlations and Materials, edited by A.Gonis, and N. Kioussis* (Plenum, New York, 1999).

[82] A. Becke, J. Chem. Phys. **96**, 2155 (1992).

[83] J. Perdew, J. Chevary, S. Vosko, K. Jackson, M. Pederson, D. Singh, and C. Fiolhais, Phys. Rev. B **46**, 6671 (1992).

[84] B. Hammer, K. Jacobsen, and J. Norskov, Phys. Rev. Lett. **70**, 3971 (1993).

[85] B. Hammer and M. Scheffler, Phys. Rev. Lett. **74**, 3487 (1995).

[86] K. Riley, B. O. Holt, and K. Merz, J. Chem. Th. Comp. **3**, 407 (2007).

[87] S. Tsuzuki and H. Lüthi, J. Chem. Phys. **114**, 3949 (2001).

[88] Q. Wu and W. Yang, J. Chem. Phys. **116**, 515 (2002).

[89] R. Improta, V. Barone, K. Kudin, and G. Scuseria, J. Comp. Chem. **114**, 2541 (2001).

[90] D. Wallace, *Thermodynamics of Crystals* (Dover Publications, inc., Mineola, New York, 1972).

[91] E. Grüneisen, Ann. Phys. **12**, 257 (1912).

[92] M. Born and K. Huang, *Dynamical Theory of Crystal Lattices* (Oxford: Oxford Univerity Press, p. 51, 1954).

[93] G. de Wijs, G. Kresse, and J. Gillan, Phys. Rev. B **57**, 8223 (1998).

[94] D. Frenkel and B. Smit, *Understanding Molecular Simulation* (Academic Press, San Diego, California, 1996).

[95] P. Flory, *Statistical Mechanics of Chain Molecules* (Wiley, New York, 1969).

[96] C. Pisani and R. Dovesi, Int. J. Quant. Chem. **17**, 501 (1980).

[97] V. Saunders, Far. Symp. Chem. Soc. **19**, 79 (1984).

[98] M. Causa, R. Dovesi, C.Pisani, R. Colle, and A. Fortunelli, Phys. Rev. B. **36**, 891 (1987).

[99] M. Towler, M. Causa, and A. Zupan, Comp. Phys. Comm. **181**, 98 (1996).

[100] K. Kudin and G. Scuseria, Phys. Rev. B **61**, 16440 (2000).

[101] Q. Timerghazin, T. Nguyen, and G. Peslherbe, J. Chem. Phys. **116**, 6867 (2002).

[102] S. Boys and F. Bernardi, Mol. Phys. **19**, 553 (1970).

[103] M. Fuchs and M. Scheffler, Comp. Phys. Comm. **119**, 67 (1999).

[104] D. Hamann, M. Schlüter, and C. Chiang, Phys. Rev. Lett. **43**, 1494 (1979).

[105] G. Bachelet, D. Hamann, and M. Schlüter, Phys. Rev. B **26**, 4199 (1982).

[106] N. Troullier and J. Martins, Phys. Rev. B **43**, 1993 (1991).

[107] L. Kleinman and D. M. Bylander, Phys. Rev. Lett. **4**, 1425 (1982).

[108] M. Bockstedte, A. Kley, J. Neugebauer, and M. Scheffler, Comp. Phys. Comm. **107**, 67 (1997).

[109] A. Kley, Ph.D. thesis, Technische Universität Berlin (1997).

[110] M. Payne, M. Teter, D. Allen, M. Arias, and J. Joannopoulos, Rev. Mod. Phys. **2656**, 1045 (1992).

[111] S. Boeck, L. Ismer, A. Dick, M. Wahn, and J. Neugebauer, *S/phi/nx manual, www.sphinxlib.de.*

[112] H. Nyquist, Trans. AIEE **47**, 617 (1928).

[113] C. Broyden, J. Inst. Math. Appl. **6**, 76 (1970).

[114] R. Fletcher, Comp. J. **13**, 317 (1970).

[115] D. Goldfarb, Math. Comp. **24**, 23 (1970).

[116] D. Shanno, Math. Comp. **24**, 647 (1970).

[117] J. White and D. Bird, Phys. Rev. B **50**, 4954 (1994).

[118] W. Hastings, Biometrika **57**, 97 (1970).

[119] S. Nose, J. Chem. Phys. **81**, 511 (1984).

[120] W. Hoover, Phys. Rev. A **31**, 1695 (1985).

[121] S. Nose, Prog. Theor. Phys. Suppl. **103**, 1 (1991).

[122] G. Martyna, M. Tuckerman, and M. Klein, J. Chem. Phys. **97**, 2635 (1992).

[123] W. van Gunsteren and H. Berendsen, Mol. Phys. **45**, 637 (1982).

[124] M. Allen and D. Tildesley, *Computer Simulation of Liquids* (Oxford University Press, 1987).

[125] A. Bergstroem, Nor. Mat. Tid. **20**, 138 (1972).

[126] A. Xie, Q. He, L. Miller, B. Sclavi, and M. Chance, Biopolymers **49**, 591 (1986).

[127] K. Itohl, T. Nakahara, and T. Shimanouchi, Biopolymers **6**, 1759 (1968).

[128] J. Koenig and P. Sutton, Biopolymers **8**, 167 (1969).

[129] B. Fanconi, B. Tomlinson, L. Nafie, W. Small, and W. Peticolas, J. Chem. Phys. **51**, 3993 (1969).

[130] J. Pople, A. Scott, M. Wong, and L. Radom, Isr. J. Chem. **33**, 345 (1993).

[131] M. Wong, Chem. Phys. Lett. **256**, 391 (1996).

[132] X. Zhou, C. Wheeless, and R.Liu, Chem. Phys. Lett **256**, 391 (1996).

[133] S. Krimm and J. Bandekar, Adv. Prot. Chem. **98**, 5612 (1993).

[134] H. Zelsmann, J. Mol. Struct. **350**, 95 (1995).

[135] B. Johnson, P. Gill, and J. Pople, J. Chem. Phys. **98**, 5612 (1993).

[136] V. Gupta, S. Trevino, and H. Boutin, Nature **214**, 1325 (1967).

[137] W. Drexel and W. Peticolas, Biopolymers **14**, 715 (1975).

[138] H. Bordallo, M. Barthes, and J. Eckert, Physica B **1138**, 241 (1998).

[139] M. Daurel, P. Delhaes, and E. Dupart, Biopolymers **14**, 801 (1975).

[140] A. Adzhubei and M. Sternberg, J. Mol. Biol. **229**, 472 (1993).

[141] S. Hovmoller, T. Zhou, and T. Ohlson, Acta Crystallogr. D Biol. Cystallogr. **58**, 768 (1998).

[142] A. Jha, A. Colubri, M. Zaman, S. Koide, T. Sosnick, and K. Freed, Biochemistry **44**, 9691 (2005).

[143] Z. Shi, C. Olson, G. Rose, R. Baldwin, and N. Kallenbach, Proc. Natl. Acad. Sci. USA **99**, 9190 (2002).

[144] K. Chen, Z. Liu, and N. Kallenbach, Proc. Natl. Acad. Sci. USA **101**, 15352 (2002).

[145] K. Chen, Z. Liu, , Z. Shi, and N. Kallenbach, J. Am. Chem. Soc. **127**, 10146 (2005).

[146] J. Pleiss and F. Jähnig, Biophys. J. **59**, 795 (1991).

[147] P. Christiansen, A. Zolotaryuk, and A. Savin, Phys. Rev. E **56**, 877 (1997).

[148] A. Savin and L. Manevitch, Phys. Rev. E **61**, 7065 (2000).

[149] J. Cutnell and K. Johnson, *Physics* (Wiley, New York, 1997).

[150] L. Landau and J. Lifschitz, *Lehrbuch der theoretischen Physik, Bd. 7 - Elastizitätstheorie* (Verlag Harry Deutsch, 1997).

[151] F. Grzegorzewski, *in preparation*.

[152] R. Williams, D. Chang, D. Juretic, and S. Loughran, Biochim. Biophys. Acta. **916**, 200 (1987).

[153] G. Barrera, J. Bruno, T. Barron, and N. Allan, J. Phys.: Condens. Matt. **17**, 217 (2005).

[154] R. Gerber, B. Brauer, S. Gregurick, and G. Chaban, PhysChemComm **5**, 142 (2002).

[155] J. Roh, V. Novikov, R. Gregory, J. Curtis, Z. Chowdhuri, and A. Sokolov, Phys. Rev. Lett. **95**, 038101 (2005).

[156] J. Jezierska, J. Panek, U. Borstnik, J. Mavri, and D. Janezic, J. Phys. Chem. B **111**, 5243 (2007).

[157] L. Ismer, J. Ireta, S. Boeck, and J. Neugebauer, Phys. Rev. E **71**, 031911 (2005).

[158] Y. Ohkubo and C. Brooks, Proc. Natl. Acad. Sci. USA **100**, 13196 (2003).

[159] A. Yakubovich, I. Solov'yov, A. Solov'yov, and W. Greiner, Eur. Phys. J. D **40**, 363 (2006).

[160] L. Ismer, J. Ireta, and J. Neugebauer, J. Phys. Chem. B, accepted (2008).

[161] B. Grabowski, L. Ismer, T. Hickel, and J. Neugebauer, *to be published*.

[162] M. Todorova and J. Neugebauer, *to be published*.

[163] S. Lifson and A. Roig, J. Chem. Phys. **34**, 1963 (1961).

[164] M. Elstner, D. Porezag, G. Jungnickel, J. Elsner, M. Haugk, T. Frauenheim, S. Suhai, and G. Seifert, Phys. Rev. B **58**, 7260 (1998).

[165] P. Morse, Phys. Rev. **34**, 57 (1929).

[166] D. T. Haar, Phys. Rev. **70**, 222 (1946).